FEUP FACULDADE DE ENGENHARIA UNIVERSIDADE DO PORTO

U.PORTO

Transition Metals Thermal Crystal Physics:

Cu**-Sb-S, **Cu**-Li-Mg, Bi-Sn-**Zn** and Al-**Fe**-**Ti

José Jorge do Amaral Ferreira

Dissertation presented to obtain the degree of

DOCTOR IN ENGINEERING PHYSICS

by the

UNIVERSITY OF PORTO

SUPERVISOR:

Maria Helena Sousa Soares de Oliveira Braga, Assistant Professor

2012

FCT Fundação para a Ciência e a Tecnologia
MINISTÉRIO DA EDUCAÇÃO E CIÊNCIA

UNIÃO EUROPEIA
FEDER

LNEG

ACKNOWLEDGEMENTS

First of all, I would like to express here my gratitude to my supervisor, Prof. Helena Braga, for her endless support, guidance and advice throughout the time of my thesis. I would also like to acknowledge the discussions with Prof. Helena Braga; her expertise on Materials Physics was very helpful.

I would like to acknowledge Prof. Mario Machado Leite, Director of my laboratory for providing much of the material support for this work and for his enormous motivation and encouragement.

I would like to thank the members of the jury for their interest in this present work and for their in-depth reading of the manuscript.

I thank my colleagues of UCTM-Lab LNEG for their warm support.

I would like to acknowledge FCT – Portugal and the FEDER - EU, for the PTDC/CTM/099461/2008 project **Hydrogen Storage on New Metal Hydrides Based on the Cu-Li-Mg system**

CONTENTS

ABSTRACT

This thesis focuses four different systems containing at least one transition element. A transition element is an element whose atom it has an incomplete *d* sub-shell, or which can give rise to cations with an incomplete *d* sub-shell. This characteristic gives rise to some distinctive properties that were object of this study.

All the following systems **Cu**-Sb-S, **Cu**-Li-Mg, Bi-Sn-**Zn**, and Al-**Ti**-**Fe**, were studied by means of experimental and/or theoretical techniques. Differential Scanning Calorimetry (DSC), Scanning Electron Microscopy (SEM) or, alternatively, Electron Probe Micro Analysis (EPMA) and X-ray diffraction (XRD). Additionally, X-ray Absorption (XANES) experiments were performed for Tetrahedrite structures of the Cu-Sb-S system, and Neutron Scattering (diffraction and spectroscopy) and hydrogen absorption studies were performed for the Cu-Li-Mg (H, D) system.

The theoretical studies are of paramount importance, not only as a auxiliary technique used in the analysis of experimental data, but also to predict worth doing experiments and to tailor new materials.

Density Function Theory (DFT), as implemented in VASP codes, was used to optimize the crystal structure of the phases in study. Electrical, mechanical, and thermodynamic properties were also studied. For the latter PHONON code was additionally used.

Phase diagrams were furthermore assessed using Thermo-Calc code.

Cu-Sb-S

Tetrahedrite, $Cu_{12}Sb_4S_{13}$ is one of the ternary phases of the Cu-Sb-S system. This phase is interesting from the mineralogical point of view since Cu can be replaced by impurities like Zn, Fe, Ag, Cd, Mn, In, Tl and Ge and by that being able to store these elements. Bond distortion is the result of these replacements.

In this thesis, I've initiated the experimental and theoretical work leading to an understanding of the structural features conducing to this effect that is not verified in other phases like, for example, Chalcopyrite, $CuFeS_2$. Phase diagram experimental studies (including XRD, DSC and EPMA) were performed to characterize the Cu-Sb-S system.

Cu-Li-Mg (H, D)

The increasing need for materials that optimize the performance of fuel cells and batteries is becoming one of the major trends of Materials Research.

In this work, I've contributed for the experimental and theoretical study of $CuLi_{0.08}Mg_{1.92}H_5$ as a hydrogen storage material with applications in both fuel cells and Li batteries conversion electrodes. I was specially focused in studying the parent $CuLi_{0.08}Mg_{1.92}$ phase by means of XRD and presently I am complementing the neutron scattering studies on the Cu-Li-Mg-H system with XRD experiments. Furthermore, I am involved in the DFT and PHONON calculations developed for some of the phases of the mentioned system.

Van't Hoff plots were obtained by means of experimental hydrogen absorption experiments, the $CuLi_{0.08}Mg_{1.92}H_5$ phase was characterized mostly by neutron diffraction and spectroscopy and DSC in synchrony with thermogravimetric analysis.

The catalytic effect of the Cu-Li-Mg-H system over Li/LiH, Mg/MgH_2 and Ti/TiH_2 was moreover studied.

The first part of this work was devoted to the study of the $CuLi_{0.08}Mg_{1.92}$ compound and its thermodynamic and structural characteristics.

Bi-Sn-Zn

Lead and lead-containing compounds are considered toxic substances due to their detrimental effect to the well-being of humans and the environment. Suitable development policy has been implemented by many countries around the world and, in order to protect the environment, the restriction of lead used in industry has been strongly promoted. Sn-Zn is one of the systems that has been used as solder as a substitute of the traditional Sn-Pb solder.

We have studied the Sn-Zn and Bi-Sn-Zn systems experimentally. My main participation in these studies was related with the XRD studies at room and elevated temperatures.

The Sn-Zn and Bi-Sn-Zn systems were furthermore studied by means of DSC and SEM. The system was reassessed and liquid miscibility gap of the Bi-Zn system was moreover studied using phase field. Microstructures were determined as a function of temperature and composition and phase diagram assessed parameters.

Al-Fe-Ti

Both the Al-Fe and Al-Fe-Ti systems were experimentally studied. Nonetheless, I only present some of the results obtained for the Al-Fe system since the study of the Al-Fe-Ti system is still insipient and only contemplates experimental results (XRD, DSC and EPMA).

With respect to Al-Fe, I have mainly contributed with XRD and EPMA data and/or analysis and first principles calculations, including phonon calculations. Even if we do not present the complete study in this thesis, the study of the Al-Fe system, centered on the ε high temperature phase, is becoming mature and we just need a final reflection over the whole data (including the immediate neighbor phases such as AlFe and $AlFe_2$) to publish this work.

RESUMO

Na presente dissertação são abordados quatro sistemas diferentes, cada um destes sistemas contendo pelo menos um elemento de transição. Um elemento de transição é um elemento cujo átomo tem uma orbital *d* com preenchimento incompleto, ou que pode dar origem a catiões com uma orbital *d* com preenchimento incompleto. Esta configuração electrónica dá origem a elementos que exibem propriedades características e que foram objecto do meu estudo.

Os seguintes sistemas **Cu**-Sb-S, **Cu**-Li-Mg, Bi-Sn-**Zn** e Al-**Ti**-**Fe**, foram estudados por meio de técnicas experimentais e teóricas. Experimentalmente foram utilizadas, a Calorimetria Diferencial de Varrimento (DSC), Microscopia Electrónica de Varrimento (SEM) ou, alternativamente, a Microssonda Electrónica (EMPA) e a Difracção de Raios-X (XRD). Para o cálculo teórico recorremos aos primeiros princípios, segundo a teoria dos funcionais de densidade e fonões.

Experiências de espectroscopia de absorção de raios-X por sincrotrão foram realizadas para estudar a estrutura da tetraedrita pertencente ao sistema Cu-Sb-S.

Difracção e espectroscopia de neutrões e estudos de absorção de hidrogénio foram realizados para o sistema Cu-Li-Mg (H, D).

Os estudos teóricos são de extrema importância, não só como técnica auxiliar usada na análise dos dados experimentalmente obtidos, como também, para prever as experiências e para criar/adaptar novos materiais.

Teoria dos Funcionais de Densidade (DFT), como implementada no código VASP, foi utilizada para optimizar a estrutura cristalina das fases do estudo. Propriedades eléctricas, mecânicas e termodinâmicas também foram estudadas. O código Phonon foi utilizado em conjugação com o VASP.

Os diagramas de fase foram ainda avaliados usando o código Thermo-Calc.

Cu-Sb-S

A tetraedrite, $Cu_{12}Sb_4S_{13}$, é uma das fases pertencente ao sistema ternário Cu-Sb-S. Esta fase é interessante sob o ponto de vista mineralógico e tecnológico uma vez que o Cu pode

ser substituído por elementos como o Zn, Fe, Ag, Cd, Mn, Na, Tl e Ge na sua rede cristalina. Como resultado desta substituição ocorre uma distorção na ligação química.

Nesta tese, iniciou-se o trabalho experimental e teórico, que conduzira a uma melhor compreensão das características estruturais provocadas pelo efeito da substituição destes elementos em baixa concentração. Esta substituição não é tão amplamente verificada em outras fases, como por exemplo na calcopirite, $CuFeS_2$.

Estudos experimentais do diagrama de fase (incluindo XRD, DSC e EMPA) foram realizados para caracterizar o sistema Cu-Sb-S.

Cu-Li-Mg (H, D)

A crescente necessidade de materiais para otimizar o desempenho das células de combustível e baterias tornou-se um dos principais temas da investigação em materiais para armazenamento de energia.

Neste trabalho, contribuí para o estudo experimental e teórico do composto $CuLi_{0.08}Mg_{1.92}H_5$. Este material que tem propriedades de armazenamento de hidrogénio pode ser aplicado tanto em células de combustível como em eléctrodos de conversão baterias de Li. O meu trabalho esteve especialmente focado em estudar a liga "mãe", a fase de composição $CuLi_{0.08}Mg_{1.92}$ por meio de difracção de Raios-X e actualmente estou a complementar os estudos de difracção de neutrões do sistema Cu-Li-Mg-H, com experiências de difracção de Raios-X. Além disso, estou envolvido nos cálculos com fonões e primeiros princípios desenvolvidos para algumas das fases do sistema mencionado.

A primeira parte deste trabalho foi dedicada ao estudo do comportamento termodinâmico e características estruturais da fase $CuLi_{0.08}Mg_{1.92}$.

Os diagramas de van't Hoff foram obtidos por meio de experiências de absorção de hidrogénio. A fase $CuLi_{0.08}Mg_{1.92}H_5$ foi caracterizada por espectroscopia e difracção de neutrões e experiências de DSC em simultâneo com análise termogravimétrica.

O efeito catalítico do sistema Cu-Li-Mg-H ao longo de Li/LiH, Mg/MgH_2 e Ti/TiH_2 foi também objecto de estudo.

Bi-Sn-Zn

O chumbo e compostos contendo chumbo são considerados tóxicos devido ao seu efeito prejudicial para o bem-estar de seres humanos e para o ambiente. Uma política de desenvolvimento adequado foi implementada por muitos países do mundo, a fim de proteger o meio ambiente. Uma restrição no uso de chumbo na indústria tem sido fortemente promovida. Fases do sistema Sn-Zn têm sido utilizadas como substituto da solda de Sn-Pb tradicional.

Estudamos experimentalmente os sistemas Sn-Zn e Bi-Sn-Zn. A minha principal participação nestes estudos esteve relacionada com os estudos de difracção de Raio-X a temperaturas elevadas (XRD-HT).

Os sistemas Sn-Zn e Bi-Sn-Zn foram ainda estudados por meio de Calorimetria Diferencial de Varrimento (DSC) e Microscopia Electrónica de Varrimento (SEM). O sistema foi reavaliado e a lacuna miscibilidade na fase liquida do sistema Bi-Zn foi estudada usando a teoria de campo. Foram determinadas as microestruturas em função da temperatura, da composição e dos parâmetros otimizados do diagrama de fase (duas otimizações diferentes).

Al-Fe-Ti

Foram estudados experimentalmente tanto os sistemas Al-Fe como Al-Fe-Ti. No entanto, só são apresentados alguns dos resultados obtidos para o sistema Al-Fe, uma vez que o estudo do sistema Al-Fe-Ti é ainda insipiente e contempla apenas resultados experimentais obtidos por XRD, DSC e EMPA.

Em relação ao Al-Fe, contribuí principalmente com dados e análises obtidas por microssonda electrónica e difracção de raios-X e cálculos por primeiros princípios, incluindo cálculos com fonões. Apesar do estudo não se apresentar completo nesta tese, a análise da fase de alta temperatura, ε, está quase finalizada sendo necessária uma reflexão final sobre todos os dados (incluindo os das fases vizinhas AlFe e $AlFe_2$) para que este trabalho seja submetido para publicação.

ACRONYMS

Chapter 1. INTRODUCTION

IUPAC - International Union of Pure and Applied Chemistry
CIGS - Copper Indium Gallium Selenide
CZTS - Copper Zinc tin Sulfide
LED - Light Emitting Diode
DFT - Density Functional Theory
LDA - Local Density Approximation
GGA - Generalized Gradient Approximation
LUMO - Lowest Occupied Molecular Orbital
HOMO - Highest Occupied Molecular Orbital
XC - Exchange-Correlation
U - Hubbard parameter
J - Strength of the exchange interaction parameter
DFT+U - Density Functional Theory plus Hubbard parameter
LDA+U - Local Density Approximation plus Hubbard parameter
GGA+U - Generalized Gradient Approximation plus Hubbard parameter
MUE - Mean Unsigned Errors
GGA-PBE - Generalized Gradient Approximation-Perdew Burke Ernzerhof functional
HSE - Heyd Scuseria Ernzerhof hybrid functional
PBE0 - Perdew Burke Ernzerhof hybrid functional
EOS - Equation Of State
VASP - Vienna *Ab-initio* Simulation Package
PW - Planwaves

Chapter 2. Cu-Sb-S SYSTEM

Tet - Tetrahedrite
Enr - Enargite
Fam - Famantinite
XANES - X-ray Absorption Near Edge Struture

ESRF - European Synchrotron Research Facility

DSC - Differential Scanning Calorimetry

SEM - Scanning Electron Microscopy or, alternatively,

EPMA - Electron Probe Micro Analysis

XRD - X-ray diffraction

Chapter 3. Cu-Li-Mg (H, D) SYSTEM

DSC - Differential Scanning Calorimetry

WETO - World Energy Technology and Climate Policy Outlook

MEM - Maximum Entropy Method

HT- High-Temperature

LT - Low-Temperature

XRD - X-ray diffraction

ND - Neutron Diffraction

INS - Incoherent Inelastic Scattering

IR - Infrared Spectroscopy

TOF - Time-of-Flight

NPDF - Neutron Powder Diffractometer

GSAS - General Structure Analysis System

PDF - Pair Distribution Function

DFT - Density Functional Theory

DSC - Differential Scanning Calorimetry

TGA - Thermal Gravimetry Analysis

HIPD - High-Intensity Powder Diffractometer

LANSCE - Los Alamos Neutron Science Center

SMARTS - Spectrometer for Materials Research at Temperature and Stress

FDS - Filter Difference Spectrometer

Chapter 4. Bi-Sn-Zn SYSTEM

RoHS - Restriction of Certain Hazardous Substances

WEEE - Waste Electrical and Electronic Equipment Legislations

COST 531 EU - Lead-free Solder Materials –EU action

COST MP0602 EU - Advanced Solder Materials for High Temperature Application –EU action

HT-XRD - High Temperatures X-ray Diffraction

RT-XRD - Room Temperatures X-ray Diffraction

SEM - Scanning Electron Microscopy

DSC - Differential Scanning Calorimetry

Chapter 5. Al-Fe-Ti SYSTEM

COST 533 EU– Thermodynamics of Alloyed Aluminides –EU action

HT-XRD - High Temperatures X-ray Diffraction

RT-XRD - Room Temperatures X-ray Diffraction

SEM - Scanning Electron Microscopy

DSC - Differential Scanning Calorimetry

EMPA - Electron Microprobe Probe Analyzer

Chapter 1- INTRODUCTION

Chapter 1.

INTRODUCTION

1.1. Transition metals and their applications

The definition of the International Union of Pure and Applied Chemistry (IUPAC) for what a transition element is: "an element whose atom has an incomplete *d* sub-shell, or which can give rise to cations with an incomplete *d* sub-shell" (McNaughton & Wilkinson, 1997).

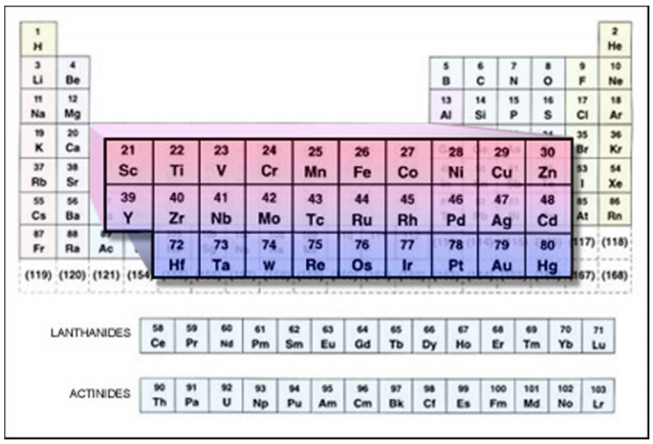

Fig. 1.1 Transition metals in the periodic table of elements (Glenbard West AP Chemistry Wiki, 2012).

The main characteristic of the transition elements, which can be referred as transition metals as well, is having a partially filled *d* sub-shell or to give rise to cations with an incomplete *d* sub-shell (e.g. Cu^{2+}). The transition elements belong to three rows in the periodic table which correspond to the progressive filling of *3d*, *4d*, and *5d* states. The presence of the *d* electrons changes the "picture" of bonding in these metals considerably. The transition metals usually have high melting points and several oxidation states; they usually form colored compounds and are often paramagnetic (McNaughton & Wilkinson, 1997).

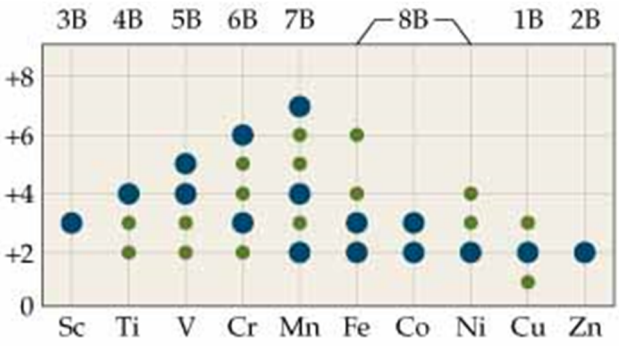

Fig. 1.2 Transition metals oxidation states. The most common is represented in bigger dots (Glenbard West AP Chemistry Wiki, 2012).

There is an extensive variety of materials that include transition metals. Such compounds, with transition metals can have different electronic behaviors. They can be conductors or semiconductors and more rarely insulators or superconductors. Materials having transition metals may have interesting magnetic, ferroelectric, antiferroelectric, and piezoelectric properties (Vaughan & Rosso, 2006), (Cramer & Truhlar, 2009).

When an anion of sulfur in its lowest oxidation state of -2 is bonded to a transition metal, a transition-metal sulfide is formed.

Transition-metal sulfides constitute an important class of inorganic compounds with diverse applications in industry, ranging from catalysis to lubrication, corrosion protection and photoconductivity. In important minerals containing sulfur, such as Chalcopyrite, Tetrahedrite (Fig. 1.3) and Blend, it is common to find some of latter properties.

These minerals can be doped with other elements enhancing the above mentioned properties (Rignanese, 2005).

Sulfides are also components of many thin-film devices and have been extensively investigated as part of the nanotechnology revolution.

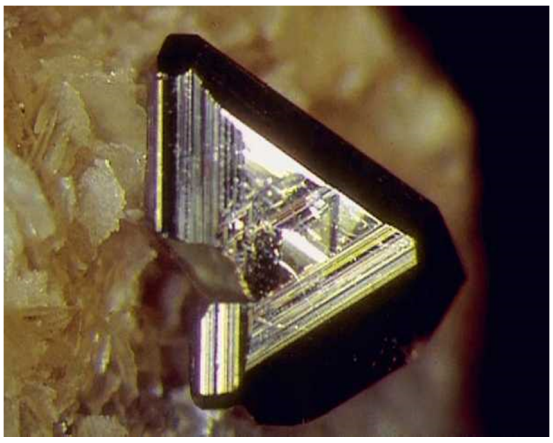

Fig. 1.3 Photograph of a Tetrahedrite mineral (School of Geology - University of Aristotle's – Greece, 2012).

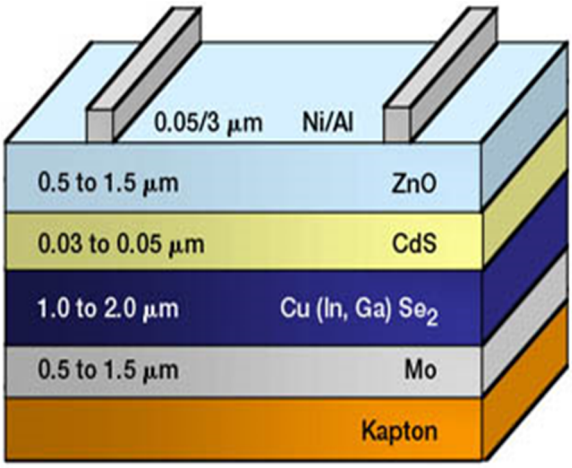

Fig. 1.4 Schematic representation of a sulfide thin-film solar cell deposited on Kapton substrate (Hepp et al, 2000)

A cross-section of a ZnO-CdS-CIGS solar cell is shown in Fig. 1.4. From bottom to top: Kapton foil, layer of Mo with 0.5-1.5 µm thick working as positive electrode, roughly 1-2 µm of CIGS functionalized as the positive semiconductor, layer of 3-5µm CdS functionalized as the negative semiconductor, and a layer with 0.5-1.5 µm of ZnO working as negative electrode. In the top cell, two wire conductors based on Ni/Al alloy.

Fig. 1.5 Photograph of park of thin film solar cell panels, (CNET, 2010)

Since the beginning of the 21st century the increasing demand for renewable energies, due to the limited availability of fossil fuels and to environmental problems, resulted in an extraordinary request for photovoltaic materials.

Currently, the high cost of the materials applied in photovoltaic solar cells, (e.g. Ga and In) Fig. 1.5, is one of the main obstacles for their production and application to a larger scale.

Ternary Chalcopyrite's with the general formula $A_IB_{III}X_2$ (A = Li, Na, Cu, Ag; B = Fe, Al, Ga, Ge, In; X = S, Se, Te; I is a +1 cation and III a +3 cation) are of considerable interest because of their potential optoelectronic applications as solar energy converters, nonlinear optical devices, Light Emitting Diodes (LED), and detectors. Chalcopyrite is a semiconductor. Polycrystalline solar cells with $Cu(In,Ga)Se_2$ - Chalcopyrite (Shafarman & Zhu, 2000) absorber are reach up to 18.8 % efficiency.

The importance and application of compounds based on transition-metal sulfides have many technological applications, ranging from lubrication to the use as catalysts in sulfo-reductive hydrotreating processes in the petroleum refining industry (Harris & Chianelli, 1984), (Topsoe et al., 1996), (Hobbs & Haffner, 1999)

In addition, transition-metal sulfides have also a fundamental scientific interest. The sulfides of the transition metals are intermediate between the transition-metal oxides, whose properties are determined by strong electronic correlation effects (Ansisimov et al., 1991), and the transition-metal selenides showing a variety of electronically induced structural phase transitions, including the formation of incommensurate phases (di Salvo & McMillan, 1977). The combined scientific and technological importance of these materials has motivated a substantial research effort directed towards an understanding of their properties at an atomistic level.

The electromagnetic properties of sulfide minerals are furthermore responsible for their contribution to geomagnetism and paleo-magnetism, since they become geophysical prospectors to be used as exploration tools in metalliferous ore deposits (Fig. 1.6). To the mineral technologist, these same properties provide methods for the separation of the metal-bearing sulfides from the associated waste minerals after mining and milling and before extraction of the metal by pyrometallurgical or hydrometallurgical treatment (Pearce et al., 2006).

Fig. 1.6 Chuquicamata sulfide ore deposit. Open pit in Andean Chile (CODELCO National Copper Corporation of Chile, 2012)

In this doctoral thesis we will explore several systems including transition metals, from minerals to light weight hydrogen storage, passing through lead free solders.

1.2. Theoretical tools supporting the materials study

A great approach for studying structural and electronic properties is the Density-Functional Theory (DFT). DFT is the most popular and robust theoretical approach currently available for solving the electronic structure of materials. Although far from an answer for all physical problems in this domain, no other theoretical approach has provided as much understanding of the electronic properties. DFT has proven to be capable of computing a multitude of properties of condensed matter with a reasonable accuracy (Michaelides & Scheffler 2012).

1.2.1 The Kohn-Sham equations

Hohenberg and Kohn, 1964, and Kohn and Sham, 1965, formulated a rather outstanding theorem which states that the total energy of a system such as a solid, surface or molecule depends only on the electron density of its *ground state*. In other words, one can express the total energy, E, of an atomistic system as a functional of its electron density, $E[\rho]$.

$$E = E[\rho] \tag{1.1}$$

The idea of using the electron density as the fundamental entity of a quantum mechanical theory for describing matter was developed in the early days of quantum mechanics,

particularly by the work of Fermi, 1928 and Thomas, 1929, (Slater, 1951). In the following decades, it was rather the Hartree-Fock approach Hartree, 1928; Fock, 1930; Fock, 1934 (Slater, 1951) which was developed and applied to small molecular systems. Calculations on realistic solid state systems were then out of reach.

Later Slater, 1951, used ideas from the electron gas with the intention to simplify the Hartree-Fock theory to a point in which electronic structure calculations on solids became feasible. Slater's work, which led to the so-called Xα-method (Slater, 1974) has contributed enormously to the progress of electronic structure calculations. The Xα-approach, combined with other simplifications in the entitled Scattered-Wave method have driven heated disputes about the "*ab initio*" character of this approach, which was carried over into the comparison of density functional theory *vs.* Hartree-Fock based methods. Today's density functional methods can be considered "*ab initio*" (Wimmer & Freeman, 2000).

In solid-state systems, molecules, and atoms, the electron density, ρ, is a scalar function defined at each point, **r,** in real space,

$$\rho = \rho(\mathbf{r}) \tag{1.2}$$

The electron density and the total energy, E, depend on the type and arrangements of the atomic nuclei. Therefore, E, can be expressed by,

$$E = E\,[\rho(\mathbf{r}),(\mathbf{R}_{\alpha})] \tag{1.3}$$

Conventionally ($\mathbf{R}_{\alpha}$), represents the positions of all atoms of the element, α, in the system under consideration. Equation (1.2) is the key to the atomic-scale understanding of electronic, structural, and dynamic properties of matter. If (1.2) can be evaluated, then the equilibrium structure of a solid, the reconstruction of a surface, and the equilibrium geometry of molecules adsorbed on surfaces, can be predicted (Wimmer & Freeman, 2000).

Moreover, the derivative of the total energy (1.3), with respect to the nuclear position, of an atom, is the absolute value of the force acting on that atom. This enables the efficient search for stable structures and, perhaps more importantly, the study of dynamical processes such as diffusion or the reaction of molecules on surfaces.

Most of the considerations presented here are based on the Born-Oppenheimer approximation in which it is assumed that the motions of the electrons are infinitely faster than those of the nuclei. This approximation rests on the fact that the nuclei are much more massive than the electrons, which allows us to say that the nuclei are nearly fixed with respect to electron motion (Sherrill, 2005). This means that the electronic structure is calculated for a fixed atomic arrangement and the atoms are then moved according to classical mechanics.

In density functional theory, the total energy is decomposed into three parts: a kinetic energy, T_0, an electrostatic or Coulomb energy, U, and exchange-correlation energy, E_{xc},

$$E = T_0 + U + E_{xc} \tag{1.4}$$

The most straightforward term is the Coulomb energy, U. It is purely classical and contains the electrostatic energy arising from the Coulomb attraction between electrons and nuclei, the repulsion between all electronic charges, and the repulsion between nuclei.

$$U = U_{en} + U_{ee} + U_{nn} \tag{1.5}$$

With

$$U_{en} = -e^2 \sum_\alpha Z_\alpha \int \frac{\rho(\boldsymbol{r})}{|\boldsymbol{r}-\boldsymbol{R}_\alpha|} d\boldsymbol{r} \tag{1.6}$$

$$U_{ee} = e^2 \int\int \frac{\rho(\mathbf{r})\rho(\mathbf{r}')}{|\boldsymbol{r}-\boldsymbol{r}'|} d\boldsymbol{r}\, d\boldsymbol{r}' \tag{1.7}$$

$$U_{nn} = e^2 \sum_\alpha \frac{Z_\alpha Z_{\alpha'}}{|\boldsymbol{R}_\alpha - \boldsymbol{R}_{\alpha'}|} \tag{1.8}$$

Where, e, *is* the elementary charge of a proton, and, Z_α, is the atomic number of the atom of α. The summations extend over all atoms and the integrations over all space. Once the electron density and the atomic numbers and positions of all atoms are known, equations (1.6)-(1.8) can be evaluated by using the techniques of classical electrostatics, were , U_{en}, is the the potential energy between the electrons and nuclei, U_{ee}, is the potential energy

giving from Coulombic electron-electron repulsions and , U_{nn}, is the the potential energy giving from Coulombic nuclei-nuclei repulsions.

The kinetic energy term, T_0, in density functional theory, the physical electrons of a system are substituted by electrons with the equal charge, mass, and density distribution. However, the electrons move as independent particles in an effective potential, where the motion of a real electron is connected with that of all other electrons. T_0 is the sum of the kinetic energies of all physical electrons moving as independent particles (Wimmer & Freeman, 2000). Frequently, one does not explicitly make this distinction between real and effective electrons.

If each effective electron is described by a single particle wave function, Ψ_i , then the kinetic energy of all effective electrons in the system is given by

$$T_0 = \sum_i n_i \int \Psi_i^* (\boldsymbol{r}) \left(-\frac{\hbar^2}{2m}\nabla^2\right) \Psi_i(\boldsymbol{r}) d\boldsymbol{r} \qquad (1.9)$$

Equation (1.9) is the sum of the expectation values of one-particle kinetic energies, *ni*, denotes the number of electrons in state, *I*, and Ψ_i^* designate the complex conjugate part of the wave function. By construction, dynamical correlations between the electrons are excluded from T_0.

The third term of equation (1.4), called exchange-correlation energy, E_{xc}, includes all remaining electronic contributions to the total energy. The most important of these contributions is the exchange term.

Electrons are Fermions and follow the Pauli Exclusion Principle. In real space, the Pauli principle implies that, around each electron with a given spin, all other electrons with the same spin tend to avoid that electron. As a consequence, the average Coulomb repulsion acting on that electron is reduced. This energy gain is called exchange energy. Effectively each electron is surrounded by a positive exchange hole (Slater, 1963). By definition, the additional many-body interaction terms between electrons of opposite spin are called correlation energy (Wimmer & Freeman, 2000).

The Hohenberg-Kohn-Sham theorem, which is a central part of density functional theory,

states that the total energy is at its minimum value for the ground state density and that the total energy is stationary with respect to first-order variations in the density.

$$\frac{\partial E[\rho]}{\partial \rho} \mid_{\rho=\rho_0} = 0 \tag{1.10}$$

In conjunction with the kinetic energy, we have introduced one-particle wave functions, Ψi($\boldsymbol{r}$) which generate the electron density

$$\rho(\boldsymbol{r}) = \sum_i n_i [\Psi_i(\boldsymbol{r})]^2 \tag{1.11}$$

As in the expression (1.9) for the kinetic energy, n_i denotes the occupation number of the eigenstate, *i*, which is represented by the one-particle wave function, Ψ_i. So far, one has a formally exact theory in the sense that no approximations have been made yet to the many-electron interactions. By construction, ***ρ(r)***, in eq. (1.11) is the exact many-electron density.

The next step is the derivation of equations that can be used for practical density functional calculations. Through equations (1.9) and (1.11) we have introduced one-particle wave functions. A change of these wave functions corresponds to a variation in the electron density (Wimmer & Freeman, 2000). Therefore, the variational condition (1.10) can be used to derive the conditions for the one-particle wave functions that lead to the ground state density. In order to accomplish that, one substitutes equation (1.11) in equation (1.10) and varies the total energy with respect to each wave function (Wimmer & Freeman, 2000). This procedure leads to the following equations:

$$\left[-\frac{\hbar^2}{2m}\nabla^2 + V_{eff}(\boldsymbol{r})\right]\Psi_i(\boldsymbol{r}) = \epsilon_i \Psi_i(\boldsymbol{r}) \tag{1.12}$$

With

$$V_{eff}(\boldsymbol{r}) = V_c(\boldsymbol{r}) + \mu_{xc}[\rho(\boldsymbol{r})] \tag{1.13}$$

Equations (1.12) and (1.13) are named the Kohn-Sham equations (Kohnn& Sham, 1965). The electron density, which corresponds to these wave functions, is the ground state (1.12) density which minimizes the total energy and the, $V_{eff}(\boldsymbol{r})$, is the Kohn–Sham potential, and, $V_c(\boldsymbol{r})$, is the Coulomb potential or electrostatic potential. The solutions of the Kohn-Sham equations form an orthonormal set, i.e.

$$\int \Psi_i^*(\boldsymbol{r})\Psi_j(\boldsymbol{r})d\boldsymbol{r} = \delta_{ij} \tag{1.14}$$

This additional constraint is achieved by introducing Lagrange multipliers, ε_i, in eq. (1.12). These Lagrange multipliers are effective one-electron eigenvalues and are used to determine the occupation numbers, n_i. The eigenstates are ordered according to increasing eigenvalues. For non-spin polarized systems each state is occupied by two electrons until all electrons are accommodated. In spin polarized systems, each state is occupied by at most one electron.

As a consequence of the partitioning of the total energy equation (1.4), the Hamiltonian operator in the Kohn-Sham equation (1.12) has three terms, one for the kinetic energy, the second for the Coulomb potential, and the third for the exchange-correlation potential.

The kinetic energy term is the standard second-order differential operator of one-particle Schrödinger equations and its construction does not require specific knowledge of a system. In contrast, the Coulomb potential, $V_c(\boldsymbol{r})$, and the exchange-correlation potential, μ_{xc}, depend on the specific electron distribution in the system under consideration (Wimmer & Freeman, 2000).

The Coulomb or electrostatic potential, $V_c(\boldsymbol{r})$, at point, **r**, is generated from the electric charges of all nuclei and electrons in the system. It can be evaluated directly in real space,

$$V_c(\boldsymbol{r}) = -e^2 \sum_\alpha \frac{Z_\alpha}{|\boldsymbol{r}-\boldsymbol{R}_\alpha|} + e^2 \int \frac{\rho(\boldsymbol{r}')}{|\boldsymbol{r}-\boldsymbol{r}'|} d\boldsymbol{r}' \tag{1.15}$$

In condensed systems it is more appropriate to use Poisson's equation

$$\nabla^2 V_c(\boldsymbol{r}) = -4\pi e^2 q(\boldsymbol{r}) \tag{1.16}$$

to calculate the electrostatic potential. Here, $q(\mathbf{r})$ denotes both the electronic charge distribution $\rho(\boldsymbol{r})$ and the positive point charges of the nuclei at positions, $\mathbf{R}_\alpha$. The exchange-correlation potential, μ_{xc} , is related to the exchange-correlation energy, $E_{xc}[\rho]$ by,

$$\mu_{xc} = \frac{\partial E_{xc}[\rho]}{\partial \rho} \tag{1.17}$$

Equation (1.17) is formally exact in the sense that it does not contain any approximations to the complete many-body interactions. In practice however, the exchange-correlation energy and thus the exchange-correlation potential, is not known and approximations must be done (Hutter, 2002).

As a result of the Kohn-Sham theorem, the exchange-correlation energy depends only on the electron density. As a simple and, as it turns out, surprisingly good approximation one can assume that the exchange-correlation energy depends only on the local electron density around each volume element, $d\boldsymbol{r}$, (Wimmer & Freeman, 2000). This is called the Local Density Approximation (LDA)

$$E_{xc}[\rho] = \int \rho\,(\boldsymbol{r}) \epsilon_{xc}\big(\rho(\boldsymbol{r})\big) d\boldsymbol{r} \tag{1.18}$$

There are various analytical forms with different coefficients in their representation of the exchange-correlation terms. These coefficients are not adjustable parameters, but rather are determined through first-principles theory. Hence, the LDA is a first-principles approach in the sense that the quantum mechanical problem is solved without any adjustable, arbitrary, or system depended parameters (Wimmer & Freeman, 2000).

Energy		Potential
$\epsilon_{xc} = \epsilon_x + \epsilon_c$		$\mu = \frac{\partial(\rho\epsilon)}{\partial\rho}$
Exchange	$\epsilon_x = \frac{-3}{2}\left(\frac{3}{\pi}\rho\right)^{\frac{1}{3}}$	$\mu_x = -2\left(\frac{3}{\pi}\rho\right)^{\frac{1}{3}}$
Correlation	$\epsilon_c = -c\left[(1+x^3)ln\left(1+\frac{1}{x}\right)+\frac{x}{2}-x^3-\frac{1}{3}\right]$	$\mu_c = -c\ ln\left(1+\frac{1}{x}\right)$
$c = 0.0225, \quad x = \frac{r_s}{21}, \quad r_s = \left(\frac{3}{4\pi\rho}\right)^{\frac{1}{3}}$		

Table 1.1 Explicit forms for the local density exchange (LDA) adapted from (Wimmer & Freeman, 2000)

Explicit forms for the local density exchange are given by (Kohn & Sham, 1965). Correlation terms are according to (Hedin & Lundqvist, 1971). Exchange and correlation energies per electron are denoted by, ϵ, and the corresponding potentials by, μ. Both quantities are given in Hartree atomic unit (1 Hartree = 2 Rydberg = 27.21165 eV). The units for the electron density are number of electrons/(Bohr radius)^3.

Note that there are two types of exchange-correlation terms, one term for the energy and other term for the potential. The energy, ϵ_{xc}, is needed to evaluate the total energy and the potential term, μ_{xc}, is required for the Kohn-Sham equations (Eschrig, 2003). The two terms are, following equations (1.17) and (1.18), related

$$\mu_{xc} = \frac{\partial(\rho\ \epsilon_{xc}(\rho))}{\partial\rho} \tag{1.19}$$

Using the explicit formulas given in the Table 1.1, the exchange-correlation potential for any electron density $\rho(\boldsymbol{r})$ can be evaluated. Thus, all terms of the effective one-particle operator in the Kohn-Sham equations are defined and one can proceed with a computational implementation (Eschrig, 2003).

Another approximation called Generalized Gradient Approximation (GGA) was proposed by (Perdew, 1986), (Becke, 1988), (Perdew & Wang, 1992) and (Perdew et al. 1996). The basic idea in these schemes is the inclusion of terms in the exchange-correlation expressions that depend on the gradient of the electron density and not only on its value at each point in space. Therefore, these corrections are also sometimes referred to as "non-local" potentials (Zeller, 2009).

The Table 1.2 gives the form proposed by (Becke, 1988) for the exchange part, the energy gradient corrected exchange, E_x^G, for the correlation (Perdew, 1986), the energy gradient corrected correlation, E_C^G , and where the energy for Local Spin Density (LSD) is designated by E_{LSD}. While dissociation energies calculated with these corrections competing in precision the best post-Hartree-Fock quantum chemistry approaches, gradient corrected density functional calculations are computationally much less demanding and more general. Gradient corrected density functional has been studied extensively for molecular systems, for example by (Andzelm & Wimmer, 1992). The results are very encouraging and this approach could turn out to be of great value in providing quantitative thermochemical data (Wimmer & Freeman, 2000).

The one-particle eigenvalues obtained from gradient-corrected exchange-correlation potentials are not significantly different from the LDA eigenvalues. Therefore, these potentials do not remove the discrepancy between calculated and measured energy band gaps.

exchange by Becke	**correlation by Perdew**
$E_{GGA} = E_{LSD} + E_x^G + E_c^G$	
$E_x^G = b\sum\int \frac{\rho_\sigma x_\sigma^2}{1 + 6bx_\sigma sinh^{-1}x_\sigma} dr$ $X_\sigma = \frac{\lvert\nabla\rho\rvert}{\rho^{\frac{4}{3}}} \quad \sigma = \uparrow or \downarrow$	$E_C^G = \int f(\rho_\uparrow, \rho_\downarrow) e^{-g(\rho)(\nabla\rho)} (\nabla\rho)^2 dr$

Table 1.2 Explicit forms for Gradient-correction to the total energy (GGA) (Wimmer & Freeman, 2000)

Energies are given in Hartree atomic units; the units for the electron and spin densities are number of electrons/(Bohr radius)^3. The constant b in Becke's formula is a parameter

fitted to the exchange energy of inert gases. The explicit form of the functions f and g in Perdew's expression for the correlation energy is given in the original paper (Perdew, 1986).

Modern DFT provides an extremely valuable tool for predicting structures, thermodynamic, mechanical and electronic properties of new materials for both finite and periodic systems. In theory, the electron affinity and ionization potential can be obtained exactly from the ground-state energy differences of the N+1 and N-1 electron systems versus the N electron system being N the number of electrons of the atom.

In practice, for periodic structures, the band gap, is the difference between the ionization potential and the electron affinity, and it is obtained from the difference in the orbital energies of the Lowest Occupied Molecular Orbital (LUMO) corresponding to the conduction band minimum - and the Highest Occupied Molecular Orbital (HOMO) corresponding to the valence band maximum from a single calculation.

It is well documented in (Xiao et al., 2011) that standard DFT exchange-correlation (XC) functionals, including various Generalized Gradient Approximations (GGA), dramatically underestimate the band gaps, Eg, for insulators due to the existence of a derivative discontinuity of the energy with respect to the number of electrons.

The study of the materials based on transition-metal sulfides, using DFT, began with the work of (Raybaud et al., 1997), in which a complete research of the structural, cohesive and electronic properties of transition-metal sulfides in the Local Density Approximation (LDA) is made. Raybaud et al., 1997, demonstrated the overbinding tendency of the LDA (prediction of too small atomic volumes and too large cohesive energies) pronounced, in particularly, for the transition-metal sulfides. For the 4d and 5d orbitals, in transition-metal sulfides, the overbinding is largely corrected by including non-local corrections in the form of a generalized gradient approximation (GGA) (Hobbs & Hafner, 1999), (Hafner, 2008).

An approximate description of strong intra-atomic correlation effects is provided by the DFT+U. The physical idea behind the LDA+U or GGA+U schemes comes from the Hubbard Hamiltonian. In practical implementations the on-site two-electron integrals, which would appear in Hartree-Fock, are expressed in terms of two parameters. These are the Hubbard parameter U, which reflects the strength of the on-site Coulomb interaction, and the parameter J, which adjusts the strength of the exchange interaction. In the somewhat simplified, yet rotationally invariant method of (Dudarev et al., 1998) these two

parameters are combined into a single parameter U_{eff} = U–J (Loschen et al., 2007) approach in which on-site Coulomb and exchange interactions, described in an unrestricted Hartree–Fock approximation, are added to the DFT Hamiltonian (Lichtenstein et al., 1995).

The DFT+U as formulated by (Dudarev et al., 1998), allows investigate the structural and electronic properties of several *3d* transition-metal sulfides to be calculated using both LDA and GGA as a starting point.

Using DFT+U, it is possible to deal more accurately, with electron correlations in transition metal and rare earth compounds. Its implementation within a PAW framework was developed by (Bengone et al., 2004).

The main important concept of DFT+U is to address the on-site Coulomb interactions in the localized *d* or *f* orbitals with an additional Hubbard-type term (Hafner, 2009). When DFT fails to account for the strong Coulomb repulsion between electrons occupying narrow bands, which leads to an enhanced exchange splitting between occupied and empty eigen states, The DFT+U method attempts to resolve this defect by adding a Hubbard-type Coulomb repulsion to the DFT Hamiltonian (Hafner, 2009).

The LDA functional already provides a good approximation for the calculation of properties in transition metal solids (Hathaway et al., 1985), and the GGA functional does not always necessarily improve the LDA results (Garcia et al., 1992). Some testes are made to evaluate the accuracy of the GGA PBE local functionals for the calculation of the unit cell volumes of Cu, Pd, W, Pt, and Au. The Mean Unsigned Errors (MUE) are 1.0% for LDA, 1.3–2.9% for GGA-PBE (Kurth et al., 1999).

In summary, according to (Kurth et al., 1999), LDA underestimates the volumes (over binding) whereas the GGA usually overestimate them (under binding). A similar effect was found for Cu, Rh, Pd, Ag, Ir, Pt, and Au with LDA and GGA. According to (Grabowski et al., 2007), the mean errors for the calculation of the bulk moduli are 19% for LDA and 8-34% for GGA (Kurth et al., 1999).

Relevant is also the work of (Heyd et al., 2005), in which they show that accurate lattice constants with the screened Coulomb hybrid functional Heyd-Scuseria-Ernzerhof (HSE) can be calculated. For example, the lattice constants of ZnS, ZnSe, and ZnTe are overestimated by HSE by an average of 0.7%, (Heyd et al., 2005), whereas the local GGA-PBE functional overestimates the same lattice constants by an average of 1.4% (Heyd et

al., 2005) . This is important because HSE predicts much more accurate band structures than do local functionals.

Chevier et al., 2010, compare the accuracy of conventional semilocal DFT, the DFT+U method and the Heyd-Scuseria-Ernzerhof (HSE06) (Heyd et al., 2005) hybrid functional for structural parameters, redox reaction energies, and formation energies of transition metal compounds.

As an example, (Sun et al., 2008) use the LDA with PBE to calculate the equation of state of Pt. The Helmholtz energy was determined as a function of the lattice constants and temperature by setting it equal to a sum of three terms: the ground-state electronic energy, the free energy of thermally excited electronic states and the vibrational free energy of the lattice (Li et al., 2007), (Sun et al., 2008).

Presently hybrids functionals like PBE0 (Perdew et al., 1996) and HSE (Heyd et al., 2003) can give more accurate band gap values, using the orbital-energy gap expression instead of using local functionals like PBE. For corroborating this assumption, (Heyd et al., 2005) presents an example, for ZnS, ZnSe, and ZnTe, in which HSE orbital energies underestimate the band gaps by an average of 0.27 eV while for the same three materials, the local PBE functional underestimates the band gaps by an average of 1.46 eV . (Heyd et al., 2005).

The ability to calculate band gaps more accurately allows us to study interesting problems such as the charge states of interstitial hydrogens in oxides like TiO_2, $SrTiO_3$, $PbTiO_3$, ZrO_2, $SrZrO_3$, $ZrSiO_4$, HfO_2, ZnO and CdO (Grabowski et al., 2007), (Cramer & Truhlar, 2009).

Theoretical studies are especially useful for studying materials under conditions that are hard to reproduce experimentally, for example, high-pressure conditions in the earth's mantle, and the GGA-PBE density functional was used to calculate the electronic energy, including core repulsion, as a function of volume at high pressure for three phases of FeH (Isaev et al., 2009).

Moreover, they extended their calculations to free energy as a function of pressure by adding a quasiharmonic vibrational (i.e., Phonon) contribution to the ground-state electronic energy.

Studies performed by (Umemoto et al., 2008) about the spin state of Fe in iron bearing magnesium silicate Perovskite, $(Mg,Fe)SiO_3$, under lower-mantle conditions, show that state is a crucial parameter for determining key mantle properties such as elastic and

seismic wave velocities, the post-Perovskite transition pressure, and electrical and thermal conductivities.

For calculation of phonon frequencies of solid materials with transition-metals, using full potentials or pseudo-potentials, LDA usually overestimates, and GGA-PBE usually underestimates (Grabowski et al., 2007). This author also shows that, for the calculation of thermal expansion, heat capacity, and free energy, LDA is usually more accurate than GGA-PBE (Grabowski et al 2007). For phonon dispersion curves, the experimental results generally lie between those calculated by LDA and GGA-PBE.

These same authors suggest that for improving the accuracy of calculated thermodynamic data of solids with transition metals, pure DFT data should be combined with temperature dependent data calculated with Phonons.

The Equation of State (EOS) of a material is determined by its Helmholtz free energy F(V,T), which consists of three parts:

$$F(V,T) = U(V) + F_{vib}(V,T) + F_{ele}(V,T) \quad (1.20)$$

$$F_{vib}(V,T) = k_B T \sum_{n,q} ln\left[2\sinh\left(\frac{h\,\omega_{nq}}{2k_B T}\right)\right] \quad (1.21)$$

where U(V) is the static energy of the lattice, $F_{vib}(V,T)$, is the vibrational free energy, and, $F_{ele}(V,T)$, accounts for the thermal excitation of the electrons, and, k_B, is the Boltzman constant, nq, is the frequency of the phonon mode for wave vector, **q**, and volume, V, (Isaev et al. 2007).

1.2.2 Phonon calculations, the PHONON code

The software PHONON was used to perform the Phonons calculations. PHONON (Parlinski, 1999), is a code for calculating phonon dispersion curves, and phonon density spectra of crystals, surfaces and adsorbed atoms on surfaces. From either a set of force constants or from a set of Hellmann-Feynman forces calculated within an Ab-initio code as Vienna *Ab-initio* Simulation Package (VASP), (Kresse & Hafner, 1993), (Kresse et al., 1994), (Kresse & Furthmüller, 1996), (Kresse & Furthmüller, 1996a). This code is capable to optimize a

supercell and calculate the Hellmann-Feynman forces. PHONON builds a crystal structure, using one of the 230 crystallographic space groups, finds the force constant from the Hellmann-Feynman forces, builds the dynamical matrix, diagonalizes it, and calculates the phonon dispersion relations, and their intensities.

PHONON finds the polarization vectors, and the irreducible representations, Gamma point of phonon modes, and calculates the total and partial phonon density of states. It plots the internal energy, free energy, entropy, heat capacity and tensor of mean square displacements, Debye-Waller factores (Parlinski, 1999). PHONON finds the dynamical structure factor for the coherent inelastic neutron scattering and the incoherent doubly differential scattering cross section for a single crystal and polycrystal.

A detailed knowledge of lattice vibrations is critical for the understanding and quantitative prediction of a wide variety of temperature dependent physical properties of solids. The fundamental thermodynamic functions of internal and free energy, entropy, heat capacity as well as non-linear properties such as thermal expansion and heat conduction are to a considerable extent determined by the vibrations of the constituent atoms in the lattice. Fortunately, the quantum theory of lattice dynamics is well developed and has proven to be one of the most successful theories of solid state physics (Müller et al., 2008).

1.2.3 Planewave pseudopotential method, the VASP code

The *ab initio* calculations are performed using the planewave pseudopotential code, the Vienna *Ab-initio* Simulation Package (VASP), (Kresse & Hafner, 1993), (Kresse et al., 1994), (Kresse & Furthmüller, 1996), (Kresse & Furthmüller, 1996a). The VASP codes have been used to determine the equilibrium lattice parameters, heats of formation, elastic constants. The Phonon dispersions are calculated together with PHONON code (Parlinski, 1999).

The VASP approach, is based on a finite-temperature local-density approximation, with the free energy as variational quantity, and an exact evaluation of the instantaneous electronic ground state at each calculation step using efficient matrix diagonalization schemes (Kresse & Furthmüller, 1996).

Planewaves (PAW) (Blöchl, 1994) and pseudopotentials form a natural alliance in this method, and they are fundamental when DFT calculations are used. In planewave pseudopotential method, the model system is constructed in a tridimensional periodic supercell which allows Bloch's theorem to be applied to the electron wavefunctions.

$$\psi_{n,k}\ (\boldsymbol{r}) = u_{n,k}(\boldsymbol{r})\exp(i\boldsymbol{k}.\boldsymbol{r}) \tag{1.22}$$

The function $u(\mathbf{r})$ has the periodicity of a supercell. It can be of any appropriate mathematical form and habitually one chooses a series expansion in terms of a set of basis function. In planewaves pseudopotential, planewaves are used for this expansion, so that each single-electron wavefuntion $\psi_{n,k}$ is written as (Segall et al., 2002).

$$\psi_{n,k}\ (\boldsymbol{r}) = \sum_G u_{n,k}(\boldsymbol{G})\exp(i(\boldsymbol{k}+\boldsymbol{G}).\boldsymbol{r}) \tag{1.23}$$

The $u_{n,k}$ are the expansion coefficients. The wavevectors $\boldsymbol{G}$ are such that the planewaves are commensurate with the supercell. Both the number of $\boldsymbol{G}$ vectors in the sum and the number of $\boldsymbol{k}$ considered should in principle be infinite (Kresse & Furthmüller, 1996a).

The exponential term is a planewave of wavevector $\boldsymbol{k}$ which must be commensurate with the entire system not just the periodically-replicated cell. For an infinite system there is an infinite number of $\boldsymbol{k}$ vectors, at each of which solutions for $\psi_{n,k}$ exist. This simply reflects the fact that the number of electrons is infinite (Segall et al., 2002).

1.3 References

Ansisimov, V., Zaanen, J., & Andersen, O., (1991.) Band theory and Mott insulators: Hubbard U instead of Stoner I Physical Review B, Vol.44, No.3 pp. 943-954, ISSN 1098-0121

Andzelm, J., & Wimmer, E., (1992). Density functional Gaussian-type-orbital approach to molecular geometries, vibrations, and reaction energies, Journal of Chemical Physics. Vol. 96 No. 2 , pp. 1280-1304, ISSN 0021-9606

Becke, A., (1988). Density-functional exchange-energy approximation with correct asymptotic behavior, Physical Review A, Vol.38, No. 6, pp. 3096–3100, ISSN 1050-2947

Bengone, O., Alouani, M., Blochl, P., & Hugel, J., (2000). Implementation of the projector augmented-wave LDA+U method: Application to the electronic structure of NiO. Physical Review B, Vol. 62, No.24, pp. 16392-16401, ISSN 1098-0121

Blöchl, P., (1994). Projector augmented-wave method, Physical Review B, Vol. 50, Vol.24, pp. 17953-17979, ISSN 1098-0121

Cramer, C., & Truhlar, D., (2009). Density Functional Theory for Transition Metals and Transition Metal Chemistry, Physical Chemistry Chemical Physics, Vol.11, No.44, pp. 10757-10816, ISSN 1463-9076

CODELCO National Copper Corporation of Chile, (2012). http://www.joeskitchen.com/chile/photos/norte/chuqui.htm

di Salvo F. & McMillan, W,. (1977). Electron–Phonon Interaction and Phase Diagrams, Ed. Risk, T., New York: Plenum, pp. 107

Dudarev, S., Botton, G., Savrasov, S., Humphreys, C., & Sutton, A. (1998). Electron-energy-loss spectra and the structural stability of nickel oxide: An LSDA+U study, Physical Review B, Vol. 57, No.3, pp. 1505-1509, ISSN 1098-0121

Eschrig, H., (2003) The Fundamentals of Density Functional Theory (revised and extended version), Institute for Solid State and Materials Research Dresden, University of Technology Dresden EAGLE Ed 2nd edition. pp224

Fermi, E., (1927). Un Metodo Statistico per la Determinazione di alcune Prioprietà dell'Atomo, Atti della Accademia Nazionale dei Lincei, Vol.6, pp.602–607, ISSN 0001-4435

Fock, V., (1930). Näherungsmethode zur Lösung des quantenmechanischen Mehrkörperproblems, Zeitschrift für Phisik Hadrons and Nuclei, Vol. 61, No. 1-2, pp. 126-148, ISSN 0939-7922

Garcia, A., Elsasser, C., Zhu, X.,. Louie, S., & Cohen, M., (1992). Use of gradient-corrected functionals in total-energy calculations for solids. Physical Review B, Vol. 46, No.15, pp. 9829-9832, ISSN 1098-0121

Glenbard, W., (2012) AP Chemistry Wiki,
http://gwapchem.wikispaces.com/23.7+Transition+Metals

Grabowski, B., Hickel, T. & Neugebauer, J., (2007). Ab initio study of the thermodynamic properties of nonmagnetic elementary fcc metals: Exange –correlation-related error bars and chemical trends, Physical Review B, Vol. 76, Vol.2, pp. 024309-16, ISSN 1098-0121

Grabowski, B., Ismer, L., Hickel, T., & Neugebauer J., (2009). Ab initio up to the melting point: Anharmonicity and vacancies in aluminum, Physical Review B, Vol. 79, No.13, pp. 134106-16, ISSN 1098-0121

Hafner, J., (2008). Ab-initio simulations of materials using VASP: Density-functional theory and beyond, Journal of Computational Chemistry, Vol. 29, No.13, pp. 2044-2078, ISSN 1096-987X

Hai, X., Tahir-Kheli, J., & Goddard, W., (2011). Accurate Band Gaps for Semiconductors from Density Functional Theory. Journal of Physical Chemistry Letters, Vol.2, No. 3, pp. 212-217. ISSN 1948-7185

Harris, S., & Chianelli R., (1984). Catalysis by transition metal sulfide: the relation between calculated electronic trends abd HDS activity, Journal of Catalysis. Vol.86, No- 2, pp. 400-412, ISSN: 0021-9517

Hartree, D., (1928). The Wave Mechanics of an Atom with a Non-Coulomb Central Field. Part I. Theory and Methods, Mathematical Proceedings of the Cambridge Philosophical Society Vol.24 pp. 89-110, ISSN 0068-6735

Hathaway, K., Jansen, H,. & Freeman, A., (1985). Total energy local spin density approach to structural and electronic properties of ferromagnetic iron. Physical Review B, Vol. 31, No.12, pp. 7603-7611, ISSN 1098-0121

Hedin, L., & Lundqvist, B., (1971). Explicit local exchange-correlation potentials, Journal of Physics C: Solid State Physics, Vol. 4, No. 14, ISSN 0953-8984

Hepp, A., Rybicki, G., Raffaelle, R., Harris, J., Hehemann, D.,Junek, W., Gorse, J., Thompson, T., Hollingsworth, J., & Buhro, W., (2000). Chemical Fabrication Used to Produce Thin-Film Materials for High Power-to-Weight-Ratio Space Photovoltaic Arrays, NASA, in, http:// www.grc.nasa.gov/ WWW/RT/RT1999/5000/5410hepp.html

Heyd, J., Peralta, J., Scuseria, G., & Martin, R., (2005). Energy band gaps and lattice parameters evaluated with the Heyd-Scuseria-Ernzerhof screened hybrid functional, Journal of Chemical Physics, Vol. 123, No. 17, pp.174101-8, ISSN 0021-9606

Heyd, J., Scuseria, G., & Ernzerhof, M., (2003). Hybrid functionals based on a screened Coulomb potential, Journal of Chemical Physics, Vol. 118, No.18, pp. 8207-8216, ISSN 0021-9606

Hobbs, D., & Hafner, J., (1999). Magnetism and magneto-structural effects in transition-metal sulphides, Journal of Physics: Condensed Matter, Vol. 11, No.42, pp. 8197-8222, ISSN 0953-8984

Hohenberg, P., & Kohn, W., (1964). Inhomogeneous Electron Gas, Physical Review, Vol. 136, No. 38, pp.864-871, ISSN 0031-899X

Hutter, J., (2002).Lecture Notes - Introduction to Ab Initio Molecular Dynamics, Physical Chemistry Institute of University of Zurich. pp 119

Isaev, E., Skorodumova, N., Ahuja, R., Vekilov, Y., Johansson, B., (2007) Dynamical stability of Fe-H in the Earth's mantle and core regions. Proceedings of the National Academy of Sciences, Vol. 104, No. 22, pp.9168-9171, ISSN 0027-8424

Kohn, W., & Sham, L., (1965). Self-Consistent Equations Including Exchange and Correlation Effects, Physical Review, Vol.140, pp.1133–1138, ISSN 0031-89

Kresse, G., & Hafner, J., (1993). Ab initio molecular dynamics for liquid metals, Physical Review B, Vol. 47, Vol.1, pp. 558-561, ISSN 1098-0121

Kresse, G., Furthmüller, J., & Hafner, J., (1994). Theory of the crystal structures of selenium and tellurium: The effect of generalized-gradient corrections to the local-density approximation, Physical Review B, Vol. 50, Vol.18, pp. 13181-13185, ISSN 1098-0121

Kresse, G., & Furthmüller, J., (1996). Efficient iterative schemes for ab initio total-energy calculations using a plane-wave basis set, Physical Review B, Vol. 54, Vol.16, pp. 11169-11186, ISSN 1098-0121

Kresse, G., & Furthmüller, J., (1996a). Efficiency of ab-initio total energy calculations for metals and semiconductors using a plane-wave basis set, Computational Materials Science, Vol. 6, No.1, pp. 15-50, ISSN 0927-02569X

Kurth, S., Perdew, J., & Blaha P., (1999). Molecular and solid-state tests of density functional approximations: LSD, GGAs, and meta-GGAs. International Journal of Quantum Chemistry, Vol. 75, No. 3, pp. 889-909, ISSN: 1097-461X

Li, Z., Bhatt, D., Schultz, N., Siepmann, J., & Truhlar, D., (2007). Free Energies of Formation of Metal Clusters and Nanoparticles from Molecular Simulations: Aln with n = 2-6, Journal of Physical Chemistry C, Vol. 111, No.44, pp. 16227-16242, ISSN 1932-7447

Liechtenstein, A., Anisimov, V., & Zaanen, J., (1995). Density-functional theory and strong interactions: Orbital ordering in Mott-Hubbard insulators. Physical Review B, Vol. 52, No.8, pp. 5467-5470, ISSN 1098-0121

Loschen, C., Carrasco, J., Neyman, K., & Illas, F. (2007). First-principles LDA+U and GGA+U study of cerium oxides: Dependence on the effective U parameter. Physical Review B, Vol. 75, No.3, pp. 035115-8, ISSN 1098-0121

McNaught, A. & Wilkinson, A., (1997) Compendium of Chemical Terminology, International Union of Pure and Applied Chemistry (IUPAC), 2nd ed. Blackwell Scientific Publications, Oxford, ISBN 0-86542-684-8

Michaelides, A., & Scheffler, M., (2012). An Introduction to the Theory of Crystalline Elemental Solids and their Surfaces. In Surface and Interface Science edited by K. Wandelt, Vol.1, pp. 13-72, ISBN 9783527411566

Müller S., Wolf, W., & Podloucky, R., (2008) Ab-initio methods and applications, Alloy Physics – A comprehensive Reference , Ed. Pfeiler, W., Wiley - Technology & Engineering – pp. 589-642, ISBN 978-3-527-31321-1

Parlinski, K., (1999). Calculation of phonon dispersion curves by the direct method, American Institute of Physics, Neutrons and numerical methods, AIP Conference Proceedings, ed. Johnson, M., Kearley, G, .& Buttner H., Vol. 479, pp. 121-126, ISBN 156396838X

Pearce, C., Pattrick, R., & Vaughan, D., (2006) Electrical and Magnetic Properties of Sulfides, Reviews in Mineralogy and Geochemistry. Vol.61, No. 1, pp.127-180, ISSN 1529-6466

Perdew, J., (1986). Density-functional approximation for the correlation energy of the inhomogeneous electron gas, Physical Review B, Vol.33, No. 12, pp. 8822–8824, ISSN 1098-0121

Perdew, J., Burke, K., & Wang, Y., (1992). Generalized gradient approximation for the exchange-correlation hole of a many-electron system, Physical Review B, Vol.54, No. 23, pp. 16533-16539, ISSN 1098-0121

Perdew, J., Burke, & Ernzerhof, M., (1996). Generalized Gradient Approximation Made Simple, Physical Review Letter, Vol.77, No. 18, pp. 3865–3868, ISSN 0031-9007

Perdew, J., & Wang, Y., (1992). Accurate and simple analytic representation of the electron-gas correlation energy, Physical Review B, Vol.45, No. 23, pp. 13244–13249, ISSN 1098-0121

Raybaud, P., Kresse, G., Hafner, J., & Toulhoat, H., (1997). Ab initio density functional studies of transition-metal sulphides: I. Crystal structure and cohesive properties, Journal of Physics: Condensed Matter, Vol. 9, No.50, pp. 11085-11106, ISSN 0953-8984

Rignanese G-M., (2005). Dielectric properties of crystalline and amorphous transition metal oxides and silicates as potential high-κ candidates: the contribution of density-functional theory Journal of Physics Condensed Matter, Vol. 17, No. 7, pp. 357-361, ISSN 0953-8984

Shafarman, W., & Zhu, J., (2000). Effect of substrate temperature and depostion profile on evaporated Cu(InGa)Se2 films and devices, Thin Solid Films, Vol. 361-362, pp. 473–477, ISSN 0040-6090

Sherrill, C., (2005). Bond Breaking in Quantum Chemistry, in Annual Reports, Computational Chemistry, Spellmeyer, D., Ed. Elsevier, Amsterdam, Vol. 1, pp. 45-54, ISBN 978-0-444-53835-2

School of Geology - University of Aristotle's – Greece, 2012
http://www.geo.auth.gr/106/2sulfides/tetrahedrite.htm

Slater, J., (1951). A Simplification of the Hartree-Fock Method, Physical Review, Vol.81, No.3, pp. 385–390, ISSN 0031-899X

Slater, J., (1963). Quantum Theory of Molecules and Solids, Electronic Structure of Molecules, New York, McGraw-Hill, Vol. 1, pp. 502, ISBN-10 0070580383

Slater, J., (1974). Quantum Theory of Molecules and Solids, The Self-Consistent Field for Molecules and Solids. New York, McGraw-Hill, Vol. 4, pp. 640 ISBN-13 978-0070580381

Segall, M., Lindan, P., Probert, M., Pickard, C., Hasnip, P., Clark, S., & Payne, M., (2002). First-principles simulation: ideas, illustrations and the CASTEP code, Journal of Physics.: Condensed Matter, Vol. 14, No.11, pp. 2717–2744, ISSN 1361-648X

Sun, T., Umemoto, K., Wu, A., Zheng, J., & Wentzcovitch, R., (2008). Lattice dynamics and thermal equation of state of platinum, Physical Review B, Vol. 78, No.2, pp. 024304-12, ISSN 1098-0121

Thomas, L., (1929). The calculation of atomic fields, Mathematical Proceedings of the Cambridge Philosophical Society. Vol.23, pp.542-548, ISSN 0068-6735

Topsoe, H, Clausen, B., & Massoth, F., (1996). Hydrotreating Cataylsis -Springer Series in Science and Technology, Berlin-Springer Vol. 11. ISBN 0-7923-5255-6

Umemoto, K., Wentzcovitch, R., Yu, Y., Requist, R., (2008). Spin transition in (Mg,Fe)SiO_3 perovskite under pressure, Earth and Planetary Science Letters, Vol. 276, No.1-2, pp. 198-206, ISSN 0012-821X

Vaughan, D., & Rosso, K., (2006) Chemical bonding in sulfide de minerals. Reviews in Mineralogy and Geochemistry Vol.61, No. 1, pp. 231-264, ISSN 1529-6466

Wimmer, E., & Freeman, A., (2000). Fundamentals of the electronic structure of surfaces, in Electronic Struture, Ed. Richardeson, N., & Holloway, S., North-Holland - Elsevier Science Amesterdam, Vol.2, pp. 1-93, ISBN 0-444-89291-5

Zeller, R., (2009) Density Functional Theory and Linear Scaling published in *Multiscale Simulation Methods in Molecular Sciences*, Grotendorst J., Attig N., Blugel S., Marx D. (Eds.), Institute for Advanced Simulation, Forschungszentrum Julich, NIC Series, Vol. 42, ISBN 978-3-9810843-8-2, pp. 121-144, 2009

Chapter 2- Cu-Sb-S System

Chapter 2.

Cu-Sb-S SYSTEM

2.1. Motivations

Chalcogenides are compounds primarily formed by chalcogen elements such as sulfur, selenium or tellurium. These compounds present interesting physical properties, like photosensitivity and photoconduction and therefore can be used as photovoltaic and photoconductor materials.

The solar energy is a natural resource that can be used without limitations since it is a non-polluent and it is powered by an infinite resource.

Some alternatives to the photovoltaic materials used in thin-films solar panels are going to be described and analyzed from the semiconductor behavior and mechanical properties point of view.

An ideal solar cell absorber material should have a direct band gap (around 1.0 - 2.2 eV) and being constituted of with abundant, inexpensive and nontoxic elements.

In this chapter the Cu-Sb-S system will be analyzed. The phases in which sulfur serves as the cationic coordinator were studied. One of the latter phases - belonging to the Cu-Sb-S and playing a major role as a photosensitive material - is the cubic phase, Tetrahedrite, I4-3m, $Cu_{12}Sb_4S_{13}$. This phase together with cubic phase Tennantite, I4-3m $Cu_{12}As_4S_{13}$, forms a complete solid solution series and is among the most frequent complex sulfides in Nature. The $Cu_{12}Sb_4S_{13}$ phase is important from the economical point of view, since it can be a carrier of minor useful elements (Ag, Ge, Se, Te, In).

The study of the phases, occurring in the natural form, allowed us to establish the grounds for a directional study with synthetic equivalents. These synthetics were used to improve the knowledge of the Cu-Sb-S system (Braga et. al, 2008), (Ferreira & Braga, 2010).

The Tetrahedrite-type structure, in its simplest elementary composition, can be studied within the Cu-Sb-S system. This ternary system encloses other variety of natural copper antimony Chalcogenides.

Recurrently, there are no experimental data available in the published literature or in databases. Therefore, we had to proceed with the experiments to obtain data. We have initiated the synthesis process of new samples with targeted compositions.

By relating specific properties of the elements with their position in the periodic table, we selectively manipulate the composition to obtain the optimal configuration for a particular physical property.

The electronic properties (e.g. band structure) are crucial to characterize photosensitive behaviors. For some different compositions it can be demonstrated that different elements, occupying certain crystallographic sites, will make a difference in what concerns the photosensitive behaviors of Tetrahedrites. The latter was taken into consideration and *ab initio* calculations were performed to show that the electronic properties of these compounds make them promising candidates as solar cells photovoltaic materials, since they possess a direct band gap and a band gap between 1.1 eV and 2.2eV. These properties can be further optimized by doping and substituting certain ions in the structure.

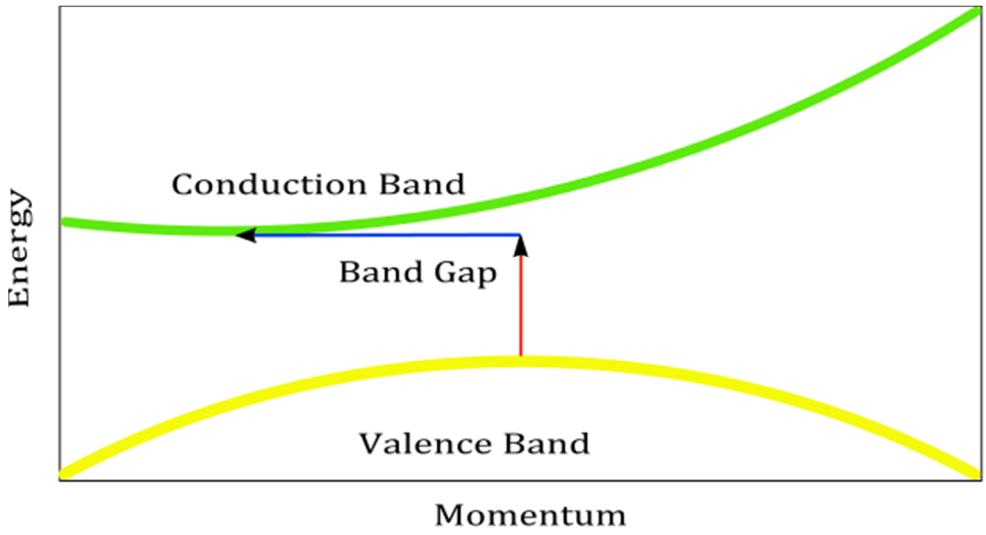

Fig 2.1 Energy vs. crystal momentum for a semiconductor with an indirect band gap (Adapted from: Wikipedia, 2012).

In Fig 2.1 it is illustrated the energy vs. crystal momentum for a semiconductor with an indirect band gap, showing that an electron cannot be removed from the lowest-energy state in the conduction band (green) to the highest-energy state in the valence band (yellow) without a change in momentum. Here, almost all the energy comes from

a photon (vertical red arrow), while almost all the momentum comes from a phonon (horizontal blue arrow) (Wikipedia, 2012)

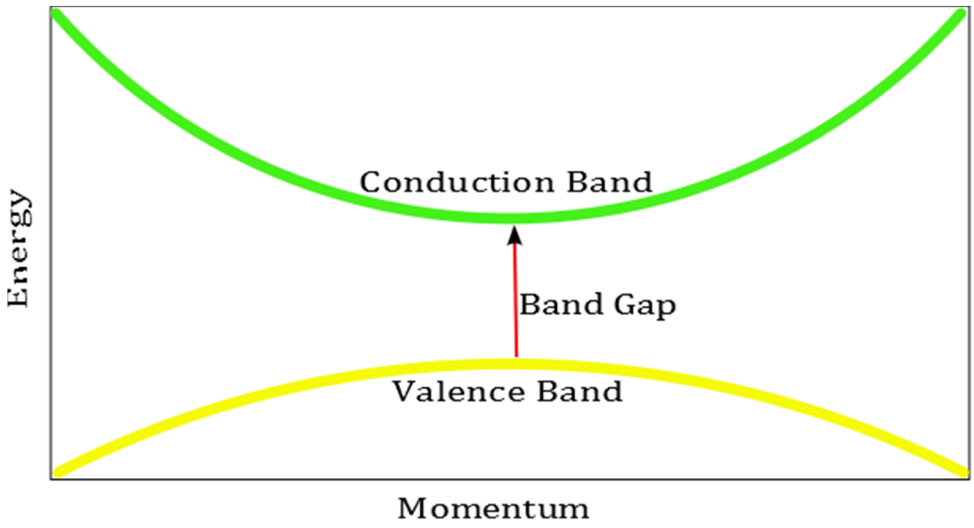

Fig 2.2 Energy vs. crystal momentum for a semiconductor with a direct band gap (Adapted from: Wikipedia, 2012).

In Fig 2.2 it is illustrated the Energy *vs.* Crystal Momentum for a semiconductor with a direct band gap, showing that an electron can shifted from the lowest-energy state in the conduction band (green) to the highest energy state in the valence band (yellow) without a change in crystal momentum. Depicted is a transition in which a photon excites an electron from the valence band to the conduction band (Wikipedia, 2012). .

This fact is very important for photovoltaics solar cells. Silicon is the most common solar-cell material, despite the fact that it has indirect-gap and therefore it does not absorb light very well. Silicon solar cells are typically hundreds of micrometres thick; if it was much thinner, much of the light, particularly in the infrared would simply pass through. On the other hand, thin-film solar cells are made of direct band gap materials such CIGS or CZTS, which absorb the light even if much thinner, and consequently can be made with a very thin active layer, often less than 1 micrometre thick (Miles et al. 2005).

The absorption spectrum of an indirect-band gap material usually depends more on temperature than that of a direct material, because at low temperatures there are fewer phonons, and therefore it is less likely that a photon and phonon can be simultaneously

absorbed to create an indirect transition. For example, silicon is opaque to visible light at room temperature, but transparent to red light at liquid helium temperatures, because red photons can only be absorbed in an indirect transition (Dresselhaus et al. 2008).

Although $Cu_{12}Sb_4S_{13}$ presents an electronic band gap of 1.24 eV, verifying the band gap condition, we want to replace the antimony in the Tetrahedrite structure since this element and its compounds are toxic.

Chalcopyrite (Cpy), $CuFeS_2$ which crystallizes in a tetragonal scalenohedral P-42m structure was furthermore studied. Based on our calculations, the band gap of this compound is 0.89 eV; but by doping and by high-pressure synthesis this value can be changed to be within the optimal band gap energy range (Hossain, 2012).

The most common elements used to dope Fe, are In or Ga and to dope S, is Se. In reality, $Cu(In,Ga)Se_2$ (CIGS) is one of the most promising thin-film solar cell materials, demonstrating an efficiency of about 20% (Contreras et al., 2005; Chen et al., 2009). Nonetheless, In and Ga are expensive and toxic elements and the band gap is usually not optimal for high efficiency CIGS solar cells. We want to design and synthesize new, high-efficient and low cost solar absorbers to replace CIGS.

The Enargite-Famatinite (Enr-Fam) Cu_3AsS_4-Cu_3SbS_4 is inexpensive; Enargite presents photosensitive properties (Pauporté & Lincot, 1995). These systems are constituted by the toxic antimony, Sb, and arsenic, As, elements. Nonetheless, these systems are interesting to be used as control for the structural and electronic properties.

Mechanical properties were additionally calculated for all compounds and were compared.

It is clear, from the recent published literature (Chirilă et al., 2010), the continuing interest in the study of Chalcogenide materials constituted by multielement and coordinated by sulfur.

2.2. The Cu-Sb-S system and the Tetrahedrite, $Cu_{12}Sb_4S_{13}$.

Sulfur is one of the most abundant elements in the universe and the 14th most abundant element in the Earth's crust. It plays a critical role in biology, atmospheric and ocean chemistry. Sulfur is the protagonist in multiple processes in different geochemical settings (Mandeville, 2010).

Sulfur is distributed throughout the mantle and crust mainly in sulfide or sulfate minerals and it finds its way into deep geologic fluids when these mineral reservoirs are perturbed by tectonic processes. The study of the sulfur behavior in the geochemical cycle provides the understanding of the origins of these mineral phases and their different formation conditions (Wallace & Carmichael, 1994).

The latter variations of the formation conditions are due to temperature differences, or more importantly due to sulfur oxidation or reduction reactions. The oxidation or reduction reactions can occur at high temperature, such as in igneous systems, at intermediate temperatures, such as in hydrothermal systems and at low temperature during sedimentary digenesis. At high temperatures, the reactions tend to occur under equilibrium conditions, whereas at low temperatures, non-equilibrium is prevalent.

The chemical speciation of sulfur in geological fluids is a controlling factor of the geochemical processes. The two major chemical forms of sulfur in crustal fluids, over a wide range of temperature and pressure are believed to be sulfate (SO_4^{2-}) and sulfide (S^{2-}). Using Raman spectroscopy it is possible to show that the dominant stable form of sulfur in aqueous solution above 250°C and 0.5 GPa is the trisulfur ion (S_3^-) (Pokrovski, & Dubrovinsky, 2011). The large stability range of (S_3^-) enables efficient transport and concentration of sulfur by geological fluids in deep metamorphic and subduction-zone settings.

Understanding the solubility of sulfur in molten silicate masses, together with the solubility of other volatile components, is a key factor for understanding the oxidation state of magma and recycling of global elements in subduction zones. It can contribute to the interpretation of the genesis of the deposits of metallic sulfides and allows evaluating the influence of volcanic sulfur emissions on the climate (Carroll & Webster, 1994).

It is known that sulfur plays a role in diagenesis and preservation of the organic matter and its conversion into oil fields (Vairavamurthy et al., 1993).

Sulfur occurs in silicate liquids in extreme states of formal valence (Connolly & Haughton, 1972; Carroll & Rutherford, 1988); oxidized as sulfate S^{6+}, and reduced in the form of sulfide S^{2-}.

The absorption spectroscopy using X-ray synchrotron radiation, XANES (X-ray Absorption Near Edge Structure), allows us to obtain the discontinuities in the absorption. A XANES edge discontinuity occurs when a core electron absorbs energy that is equal to or greater

than its binding energy. Edges are labeled according to the shell from which the electron was excited. Sulfur K-edge correspondent energy range is 2.45 to 2.53 keV.

XANES spectroscopy is a non-destructive technique and additionally it is strongly sensitive to the chemistry (formal oxidation state and geometry) of the absorbing atom; this allows us to make inferences about the coordination state of the environment of the absorbing atom (Li et al., 1995; Morra et al., 1997; Paris et al., 2001).

The microbeam XANES consents furthermore to realize studies in fluid inclusions in crystals of Olivine and Pyroxene (Gurenko & Schmincke, 2000; Bonin-Mosbach et al., 2002) which have shown the presence of intermediate oxidation states, namely S^{4+} in basaltic magmas rich in water (Métrich et al., 2002).

A spectroscopic study in order to characterize the sulfur state of speciation was performed but not yet published. In this work we present the first results of the analysis of the fine structure of the S K-edge absorption discontinuity of this element by XANES.

X-ray absorption experiments at ESRF (European Synchrotron Research Facility) had the purpose of studying the influence of the environment on sulfur ions and characterizing the geometry of metal ions coordinating sulfur and their bonding effects (e.g. the local order). These goals are achieved by comparing the observed sulfur K-edge profile of the minerals in study with the correspondent profile of well-known structures, which constitute model compounds for different binding situations. Native sulfur was used to characterize the molecule S = S (double bond) in S_8, Fig. 2.1; Pyrite was used to characterize the dimer S_2^{2-}, Fig. 2.2, and Chalcopyrite to characterize the sulfide ion S^{2-}, Fig. 2.3. The following sulfide minerals were also studied as model compounds: Galena, PbS, Fig. 2.4, Blend, ZnS, Fig. 2.5, Chalcopyrite, $CuFeS_2$, Fig. 2.3, and Tetrahedrites $Cu_{12}Sb_4S_{13}$, Fig. 2.6. These phases have a very well defined structure resulting in characteristic absorption spectra. The comparison of the latter with the samples' spectra permits a better interpretation of these spectra. In this particular case we can understand the conjugated influence of the nature of the coordinating metal atoms and the geometry of their arrangement over the electronic configuration of sulfur.

The goal of our study is to determine how impurities - replacing Cu - in the Tetrahedrite structure, will induce changes in the ideal bond lengths and geometries when compared to the ideal.

Tetrahedrite, conversely to other structures like for example the Chalcopyrite, can hold a big variety of impurities that replace Cu, such as: Zn, Fe, Ag, Cd, Mn, In, and Ge. We want to

understand why this phenomenon occurs in Tetrahedrite making it so different with this respect.

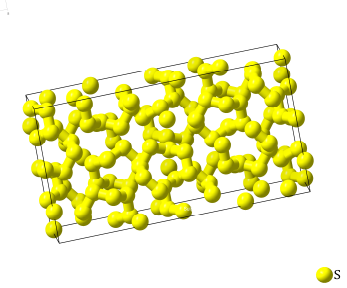

Fig. 2.1 Crystal structure of the molecular sulfur. Space group: Fddd.

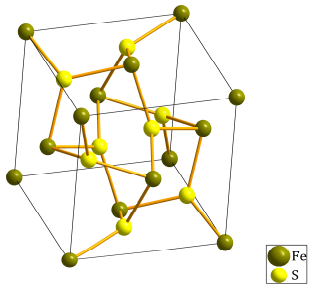

Fig. 2.2 Crystal structure of the Pyrite, FeS_2. Space group: Pa3.

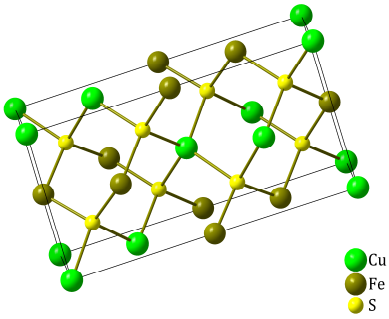

Fig. 2.3 Crystal structure of the Chalcopyrite, $CuFeS_2$. Space group: I-42d.

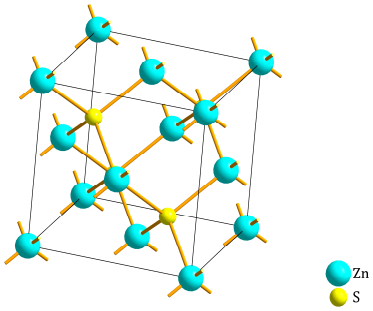

Fig. 2.4 Crystal structure of the Blend, ZnS. Space group: F-43m.

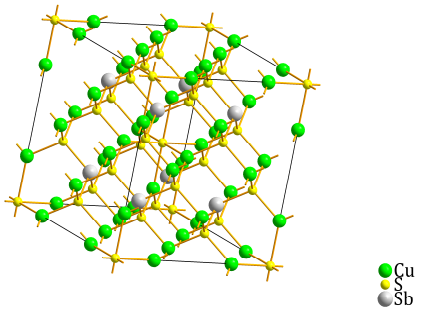

Fig. 2.5 Crystal structure of the Tetrahedrite, $Cu_{12}Sb_4S_{13}$. Space group:I-43m.

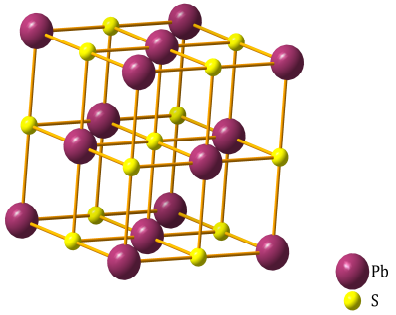

Fig. 2.6 Crystal structure of the Galena, PbS. Space group: Fm3m.

Scans between 2.45 and 2.53 KeV were performed to collect S K-edge XANES spectra. Fig. 2.7 illustrates the general trend of S K-edge XANES spectra of natural, synthetic and simulated Tetrahedrite.

The white line shown in the spectra reproduced in Fig. 2.7 (corresponding to the maximum absorption energy which in the Tetrahedrite XANES spectra is due to the Cu-S bond - an overlap of the tetrahedral and octahedral coordination contributions), does not seem to occur with similar intensity in the spectra collected from pure synthetic Tetrahedrite. This is eventually due to the presence of non-ideal structures in which there are slightly different bond lengths.

Furthermore, the presence of a small absorption peak (in the pre-edge region of the natural Tetrahedrite) is indicative of the presence of an element that replaces Cu in Cu-S bonds. This impurity element is likely to be zinc in natural Tetrahedrites.

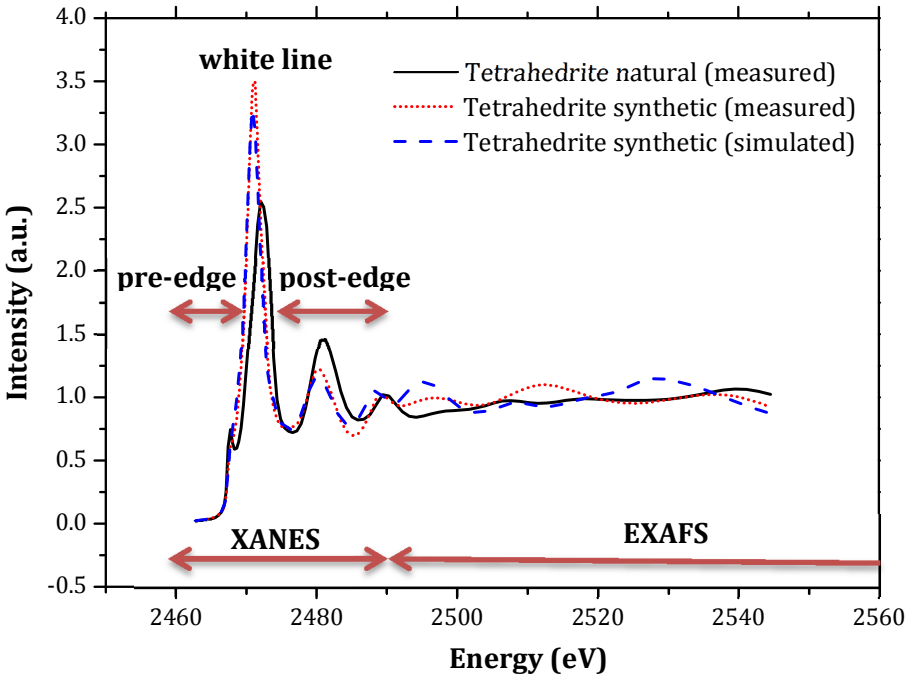

Fig. 2.7 Absorption spectra obtained in XANES region for natural, synthetic and simulated Tetrahedrite.

The cubic crystal structure of Tetrahedrite has two formula units per cell, being derived from the Blend structure by replacing a *tetrahedral cluster of packing vacancies* (4[vac.]) in each 16 packing positions by one single S-atom according to the sequence (Figueiredo & Ferreira, 2002).

$$[S^{t}_{16}] \rightarrow [S_{12}\,[vac.]_{4}] \rightarrow \{[S^{t}_{12}]\,[S^{o}]\}$$

The general crystal chemical formula of Tetrahedrite may then be written (t, tetrahedral; tr, triangular; π, pyramidal; o, octahedral), clearly specifying the particular situation of one out of thirteen sulphur atoms in the crystal structure (Figueiredo & Ferreira, 2002).

$$(Cu,Zn,Ag,Fe,Hg,Cd)^{t}_{6}(Cu,Ag)^{tr}_{6}(Sb,As,Bi,Te)^{\pi}_{4}\{[S^{t}_{12}][S^{o}]\}$$

This process provides pyramidal and triangular coordinations respectively to four As/Sb/Bi and to six Cu/Ag ions hosted in former tetrahedral sites within the original non-lacunar closest packing; the remaining six Cu ions are hosted in true tetrahedral interstices within the closest packing of sulfide anions, Fig. 2.8.

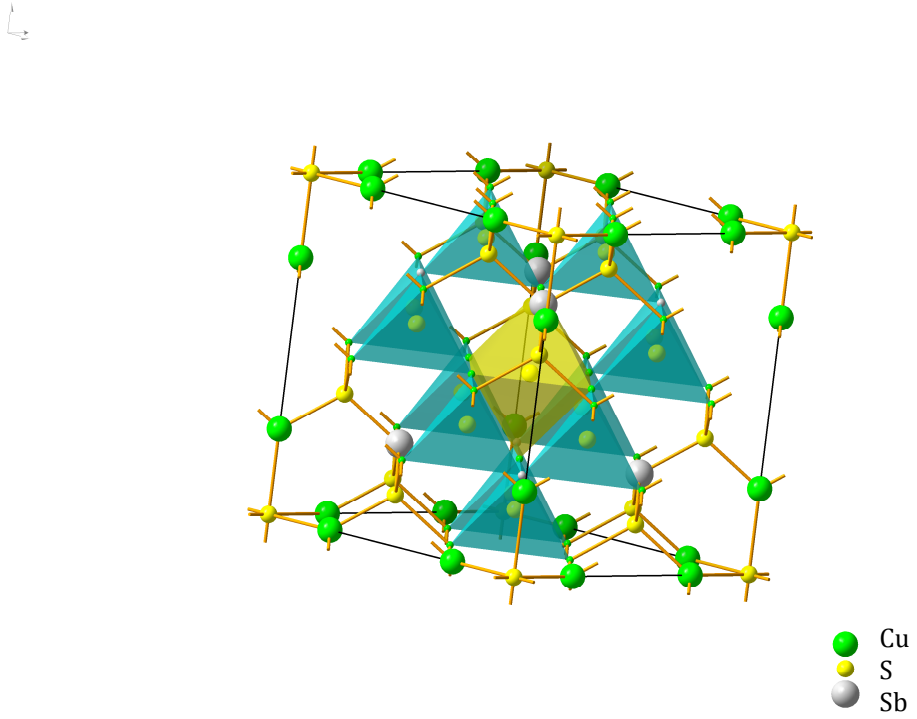

Fig. 2.8 Tetrahedral and octahedral arrangements in the Tetrahedrite structure.

Theoretical calculations and spectra modeling were performed with the codes FEFF 8.40 (Ankudinov et al., 1998) and FEFF 9.05 codes (Rehr et al., 2010). We want to compare FEFF simulations on DFT optimized impure Tetrahedrites with synthetic and then natural samples measurements. Spectroscopic data for Sb and Ag atoms were also recorded using XANES spectra and will be the subject of our near future study.

2.3. References

Ankudinov, A., Ravel, B., Rehr, J., & Conradson, S., (1998). Real-space multiple-scattering calculation and interpretation of x-ray-absorption near-edge structure, Physical Review B Vol. 58, No. 12, pp. 7565-7576, ISSN 1098-0121

Bonin-Mosbach, M., Métrich, N., Susini, J., Salomé, M., Massare, D., & Menez, B., (2002). Micro X-ray absorption near-edge structure at the sulfur and iron K–edges in natural silicate glasses, Spectrochimica Acta, Part B, Vol. 57, No. 4, pp. 711-725, ISSN 0584-8547

Braga, M., Ferreira J., & Malheiros L., (2008). Phase transitions in the Cu-Sb-S system, Materials Science Forum, Vol. 587-588, pp. 435-439, ISSN 0255-5476

Carroll, M., & Rutherford, M., (1988). Sulfur speciation in hydrous experimental glasses of varying oxidation state: results from measured wavelength shifts of sulfur X-rays, American Mineralogist, Vol. 73, No. 7-8, pp. 845-849, ISSN 1945-3027

Carroll, M. & Webster, J. (1994). Solubilities of sulfur, noble gases, nitrogen, chlorine and fluorine in magmas. In Volatiles in Magmas, Edts. Carroll, M., & Holloway, J., Reviews in Mineralogy, Vol. 30, No. 1, pp. 231-27, ISSN 1529-6466

Chen, S., Gong, G., Walsh, A., Wei, S., (2009). Crystal and Electronic band structure of Cu_2ZnSnX_4 (X=S and Se) photovoltaic absorbers: First-principles insights, Applied Physics Letters, Vol. 94, No.4, pp. 041903-3, ISSN 1077-3118

Chirilă, A., Buecheler, S., Pianezzi, F., Bloesch, P., Gretener,C., Alexander, Uhl, A., Fella, C., Kranz, L., Perrenoud, J., Seyrling, S., Verma, R., Nishiwaki, S., Romanyuk, Y., Bilger, G., & Tiwari, A., (2011). Highly efficient Cu(In,Ga)Se_2 solar cells grown on flexible polymer films, Nature Materials, Vol.10, No. 11, pp 857-861, ISSN 1476-1122

Connolly, J., & Haughton, D., (1972). The valence of sulfur in glass of basaltic composition formed under conditions of low oxidation potential, American Mineralogist, Vol. 57, No.9, pp. 1515-1517, No. 9, ISSN 1945-3027

Contreras, M., Ramanathan, K., Shama, J., Hasoon, F., Young, D., Egass B., & Noufi, R., (2005). Diode characteristics in state-of-the-art ZnO/CdS/Cu(In1−xGax)Se_2 solar cells, Progress in Photovoltaics: Research and Applications, Vol. 13, No. 3, pp. 209-216, ISSN 1099-159X

Dresselhaus, M., Dresselhaus, G., & Jori A., (2008). Group Theory: Application to the Physics of Condensed Matter, Springer, pp. 598, ISBN-10: 3540328971

Gurenko, A. & Schmincke, H-U. (2000). S concentrations and its speciation in miocenic basaltic magmas north and south of Gran Canaria (Canary Islands): constraints from glass inclusions in olivine and clinopyroxene, Geochimica et Cosmochimica Acta, Vol. 64, No. 13 pp. 2321-2337, ISSN 0016-7037

Hossain, M., (2012). Prospects of CZTS solar cells from the perspective of material properties, fabrication methods and current research challenges, Chalcogenide Letters, Vol. 9, No. 6, pp. 231 – 242, ISSN 1584-8663

Ferreira, J., & Braga, M., (2010). Ab initio simulations for the Cu-Sb-S system, oral, TOFA-Thermodynamics of alloys, FEUP, Portugal, 12th-17th Sept., ISBN 978-989-96696-1-1

Figueiredo, M., Ferreira, J., (2002). Crystal Chemistry of tetrhedrites revisited: Considerations on significant geochemical outputs: Nineth International Symposium on Experimental Mineralogy Petrology and Geochemistry, Cambridge Publications EMPG IX Abstract Volume, Zurich 24-27 March, pp 34,

Li, D., Bancroft, M., Kasrai, M., Fleet, M., Feng, X., & Tan, K., (1995). S K– edge and L–edge X-ray absorption spectroscopy of metal sulfides and sulfates: applications in Mineralogy and Geochemistry, The Canadian Mineralogist, Vol. 33, No. 5, pp. 949-960, ISSN 0008-4476

Mandeville, C., (2010). Sulfur: A ubiquitous and useful tracer in earth and planetary sciences, Elements, Vol.6, No. 2 pp. 75-80, ISSN 1811-5209

Métrich, N., Bonnin-Mosbach, M., Susini, J., Menez, B., & Galoisy, L., (2002). Presence of sulfite (S^{IV}) in arc magmas: implications for volcanic sulfur emissions, Geophysical Research Letters, Vol. 29, No. 11, pp, 331-334, ISSN 0094–8276

Miles, R., Hynes, K., & Forbes, I., (2005). Photovoltaic solar cells: An overview of state-of-the-art cell development and environmental issues, Progress in Crystal Growth and Characterization of Materials, Vol. 51, No. 1-3 , pp. 1-42, ISSN 0960-8974

Morra, M., Fendorf, S., & Brown, D., (1997). Speciation of sulfur in humic and fulvic acids using X-ray absorption near-edge structure (XANES) spectroscopy. Geochimica et Cosmochimica Acta, Vol. 61, No.3, pp. 683-688, ISSN 0016-7037

(Wikipedia, 2012) http://en.wikipedia.org/wiki/Direct_and_indirect_band_gaps

Paris, E.; Giuli, G.; Carroll, M. R. & Davoli, I. (2001). The valence and speciation of sulfur in glasses by X-ray absorption spectroscopy, The Canadian Mineralogist, Vol. 39, No.2, pp. 331-339, ISSN 0008-4476

Pauporté, Th., & Lincot, D., (1995). Electrical, Optical and Photoelectrochemical Properties of Natural Enargite, Cu3AsS4, Advanced Materials for Optics and Electronics, Vol. 5, No. 6, pp.289-298, ISSN 1099-0712

Pokrovski, G., & Dubrovinsky, L., (2011). The S3– ion is stable in geological fluids at elevated temperatures and pressures, Science, Vol. 331, No. 6020, pp. 1052-1054, ISSN 1095-9203

Rehr, J., Kas, J., Vila, F., Prange, M., & Jorissen, K., (2010). Parameter-free calculations of x-ray spectra with FEFF9, Physical Chemistry Chemical Physics, Vol. 12, No. 21, pp. 5503-5513, ISSN 1463-9084

Vairavamurthy, A., Manowitz, B., Luther G., & Jeon, Y., (1993). Oxidation state of sulfur in thiosulfate and implications for anaerobic energy metabolism, Geochimica et Cosmochimica Acta, Vol. 57, No. 13, pp. 1619-1623, ISSN 0016-7037

Wallace, P., & Carmichael, I., (1994). S speciation in submarine basaltic glasses as determined by measurements of S Kα X-ray wavelength shifts., American Mineralogist, Vol. 79, No.2 , pp. 161-167, ISSN 1945-3027

Papers on the Cu-Sb-S system

2.3. First Principles Study of Copper Sulfides (for applications as photoconductors)

2.4. Phase transitions in the Cu-Sb-S System

Materials Science Forum Vols. 730-732 (2013) pp 111-116

doi:10.4028/www.scientific.net/MSF.730-732.111

First Principles Study of Copper Sulfides (for applications as photoconductors)

J.A. Ferreira[1,a], M.H. Braga[2,3,b]

[1]LNEG, Laboratório Nacional de Energia e Geologia, S. Mamede Infesta, Portugal

[2]Los Alamos Neutron Scattering Center, Los Alamos National Laboratory, NM, USA

[3]CEMUC, Engineering Physics Dep., Engineering Faculty, Porto University, Portugal

[a]jorge.ferreira@lneg.pt (corresponding author), [b]mbraga@fe.up.pt

Keywords: Band Structures, Mechanical Properties, Sulfides, Photovoltaics

Abstract. The Tetrahedrite's family constitutes a complete solid-solution series, and is among the most frequent complex sulfides in Nature. This kind of structure can be generically expressed by the composition, $Cu_{12}Sb_4S_{13}$. We have calculated the electronic band structure of $Cu_{12}Sb_4S_{13}$ and $Ag_6Cu_6Sb_4S_{13}$ (with band gaps of 1.24 and 1.20 eV, respectively) to demonstrate that different elements occupying certain sites of the crystal structure will make a difference in what concerns the conduction process in Tetrahedrites. We will use this effect and *ab initio* calculations to show that the electronic properties of these compounds make them promising candidates as solar cells photovoltaic materials since not only they possess a direct band gap but their energy falls within the range of energies of photovoltaics. Moreover, we can optimize these properties by doping and substituting ions furthermore. Mechanical properties were also calculated for both compounds and will be compared.

Introduction

Tetrahedrite is a copper antimony sulfosalt mineral, $Cu_{12}Sb_4S_{13}$, with I -43m crystal symmetry, seeming to be a promising candidate for solar cells photovoltaics. The Copper-Antimony-Sulfur compound can occur as a stable mineral [1] (Fig. 1) (at ambient conditions), or being synthesized from the constituent elements in stoichiometric proportion [2,3].

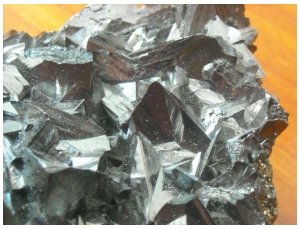

Fig1: A specimen of natural Tetrahedrite, from Huaron Mine, Peru.

The crystal structure of the Tetrahedrite can be interpreted as a derivation of the crystal structure of the Sphalerite, which presents a cubic structure F -43m, with composition ZnS. This compound can be transformed into a Tetrahedrite, I -43m. This transformation can be explained and supported by the principles assisting the geometrical crystallography. It only implies a transformation from F to I cell type, keeping the point group (-43m). The latter transformation requires doubling the unit cell size from a_0= 5.25 Å to a = 10.50 Å. The transformation is described as following: the cubic crystal structure of the Tetrahedrite has two formula units per cell, being derived from the Sphalerite structure by replacing a tetrahedral cluster of sulfur atoms by four packing vacancies (4Vac) in each sixteen packing sulfur positions. Then the vacancies, 4Vac, are replaced by one single S-atom according to the sequence (1), where S^t corresponds to the generic tetrahedral position and S^o is the final octahedral position assumed by one in sixteen atoms of sulfur (Fig. 2).

$$[S^t_{16}] \rightarrow [S^t_{12}\ Vac_4] \rightarrow \{[S^t_{12}][S^o]\} \quad (1)$$

This process provides pyramidal and triangular coordination, respectively, to four Sb and to six Cu^{+} cations hosted in former tetrahedral sites within the original non-lacunar closest packing; the remaining six Cu^{2+} cations are hosted in true tetrahedral interstices within the closest packing of sulfide anions (Fig. 2).

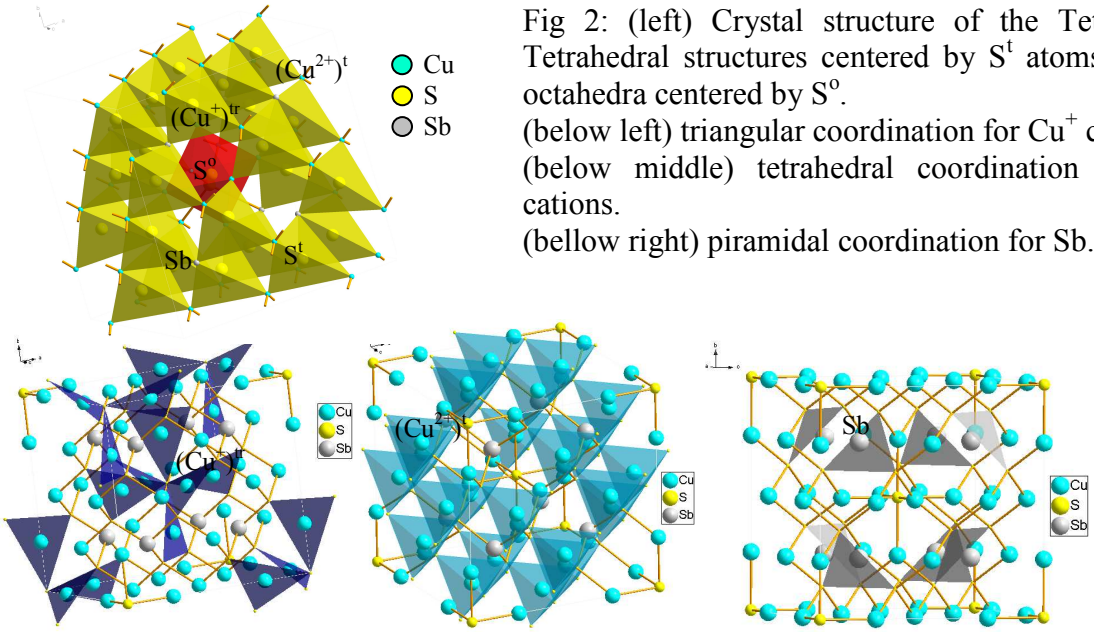

Fig 2: (left) Crystal structure of the Tetrahedrite. Tetrahedral structures centered by S^{t} atoms, and the octahedra centered by S^{o}.
(below left) triangular coordination for Cu^{+} cations.
(below middle) tetrahedral coordination for Cu^{2+} cations.
(bellow right) piramidal coordination for Sb.

The general crystal chemical formula of the Tetrahedrite may then be written (tr, triangular; t, tetrahedral; π, pyramidal; o, octahedral), as in the following expression:

$$(Cu^{+})^{tr}_{6}(Cu^{2+})^{t}_{6}(Sb)^{\pi}_{4}[(S)^{t}_{12}(S)^{o}] \quad (2)$$

The copper tetrahedral sites accommodate Cu^{2+} (Fig. 2 – bellow middle) as well as all tetrahedral coordinated divalent cations that can eventually substitute Cu^{2+} in the center of the tetrahedra. Cu^{+} occupies the center of a triangle (Fig. 2 – bellow left) of sulfur atoms and additionally, in a more distant position, in pyramidal coordination and oriented towards the central octahedra, is the Sb cation (Fig. 2 – bellow right). The $(Cu^{+})^{tr}$ sites share a single S^{o} atom belonging to the central octahedra (Fig. 2 – bellow left) and each $(Cu^{+})^{tr}$ is coordinated with two additional S^{t} atoms belonging to the tetrahedral framework.

Such crystal chemical insight illustrates the decisive role that *ab initio* simulations have in providing a comprehensive interpretation of the Tetrahedrite behavior since substitutions in different sites will perturb different arrangements; furthermore since the panoply of substituting ions is comprehensive, *ab initio* calculations deliver valuable information on the properties of the various Tetrahedrites.

Crystal engineering will be performed by substituting ions with the same valence in Tetrahedrites and eventually by creating vacancies in order to optimize electrical properties with the ultimate motivation of developing suitable photovoltaic materials.

The 89,000TW of sunlight reaching the Earth's surface is plentiful – almost 6,000 times more than the 15TW equivalent of average power consumed by humans [4,5]. Additionally, solar electric generation has the highest power density (global mean of 170 W/m²) [4,6] among renewable energies.

Photovoltaic materials are semiconductors used to convert solar radiation into direct current electricity. Solar photons colliding with electrons will make them jump to a higher energy state (an excited state); creating positively charged holes that in turn generate electrical current. An ideal solar cell absorber material should have a direct electronic band gap around 1.0 - 2.2 eV (in a direct band gap semiconductor, the top of the valence band and the bottom of the conduction band occur at the same value of momentum) with abundant, inexpensive and nontoxic elements. Materials

presently used for photovoltaics include monocrystalline, polycrystalline and amorphous silicon, cadmium telluride, and copper indium selenide/sulfide [7]. Among these materials, Cu_2ZnSnS_4 (CZTS) is one of the most promising materials as it consists of abundant and relatively cheap elements. This semiconductor combines the properties for an ideal absorber layer for photovoltaic applications, like a direct band gap of about 1.4-1.5 eV and an optical absorption coefficient higher than 10^4 cm^{-1} [7,8].

In this work we are going to calculate the structural and electronic properties of Tetrahedrite, $Cu_{12}Sb_4S_{13}$, and compare them with those of $Ag_6Cu_6Sb_4S_{13}$ to prove the viability of crystal engineering towards photovoltaics optimization.

Calculation Methods

The electronic band structures for the cubic crystalline Tetrahedrite, I -43m, were calculated using *ab initio* Density Functional Theory (DFT) and exchange correlation functionals. The calculations were performed using Vienna *Ab initio* Simulation Package code, VASP 5.2. [9] based on the DFT approach employing the Projector-Augmented Wave (PAW) method [10,11] within the Generalized Gradient Approximation and the Perdew-Burke-Ernzerhof (GGA-PBE) [12] functional. The PBE functional presents a simple derivation of the GGA, in which all parameters are fundamental constants, and is usually applied for calculation under periodic boundary conditions. The wave functions were expanded in the plane waves up to the kinetic energy cutoff of 500 eV, which ensures the convergence with respect to basis set for this structure. The Monkhorst–Pack [13] *k*-point generation scheme was used with a grid of 5×5×5 points in the irreducible part of the Brillouin zone. All calculations were performed in the 1×1×1 cell containing 58 atoms. The model structure was fully optimized (atomic and cell parameters) at hydrostatic pressures equal to 0 GPa. The electronic optimizations were continued until the energy differences between the successive electronic and ion cycles were less than 10^{-5} eV.

Electronic Properties

The band gap is a critical property for understanding the optical and electrical properties of the materials and for the design of semiconductor devices. The accurate calculation of band gaps is an active and important research area in Solid-State Physics and Theoretical Chemistry. Although Kohn–Sham DFT has been very successful in Theoretical Physics and Quantum Chemistry [14], the local density functionals such as the generalized gradient approximations GGA-PBE must be engaged in order to perform the calculation of electronic properties with greater accuracy.

Calculation results

The energy bands of electrons in semiconductors consist of a valence band fully occupied by electrons at low energy levels, a vacant conduction band at high energy levels and a forbidden band called - band gap - which separates the former two bands and which is not so high as that of an insulator. Fig. 2 shows the high symmetry lines within the first Brillouin zone of a cubic body centered lattice.

The band gap of $Cu_{12}Sb_4S_{13}$ was calculated to be 1.24 eV and 1.20 eV for $Ag_6Cu_6Sb_4S_{13}$ (Fig. 3). Generally, in $Cu_{12}Sb_4S_{13}$ and $Ag_6Cu_6Sb_4S_{13}$ the 3d orbitals of Cu (or Ag, respectively) and the 3p of S occupy the upper region of the valence band denoting that there is bonding between Cu (or Ag) and S atoms. The orbitals 3s and 3p of S compose the bottom of the conduction band. The peaks in the interval -7 eV to -2 eV are due to the S 3p orbital. The Cu 3d orbital is located at -7 to 0 eV. The S 1s orbital on the lower region of the valence band is divided into two intervals from -12.5 eV to -12 eV and from -16 eV to 13 eV.

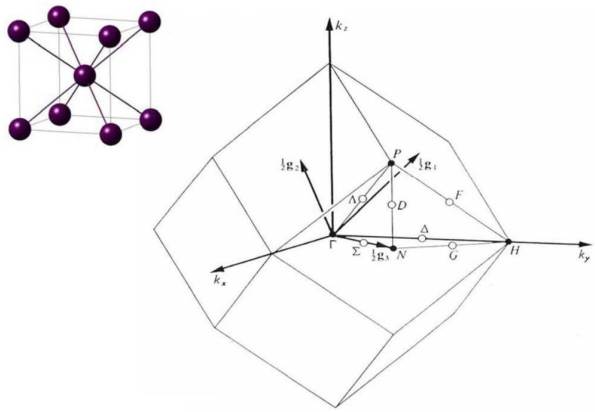

Point coordinates: (g_1,g_2,g_3)
Γ (0,0,0)
H (1/2,-1/2,1/2)
P (1/4,1/4,1/4)
N (0,0,1/2)

Fig 2: High symmetry lines within the first Brillouin zone of a cubic body centered lattice, as the Tetrahedrite structure.

Most of the states in the valence band, which is located from -5 eV to 0 eV, are mainly occupied by the Cu 3d orbital and in a small percentage by S 3p orbitals (Fig. 4b).

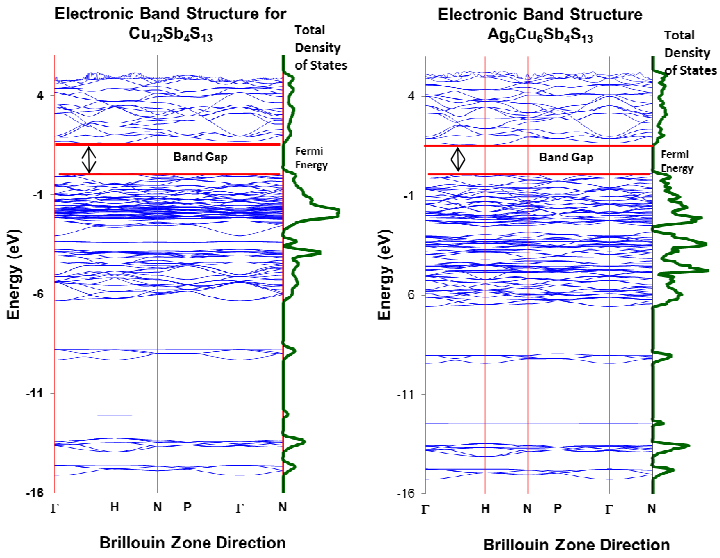

Fig 3: The calculated band gap is 1.24 eV for $Cu_{12}Sb_4S_{13}$ (left) and 1.20 eV for $Ag_6Cu_6Sb_4S_{13}$ (right) and can be both considered direct band gaps. In vertical, at each right side, the total Density of States (tDOS) spectra. The Fermi energy corresponds to E = 0 eV.

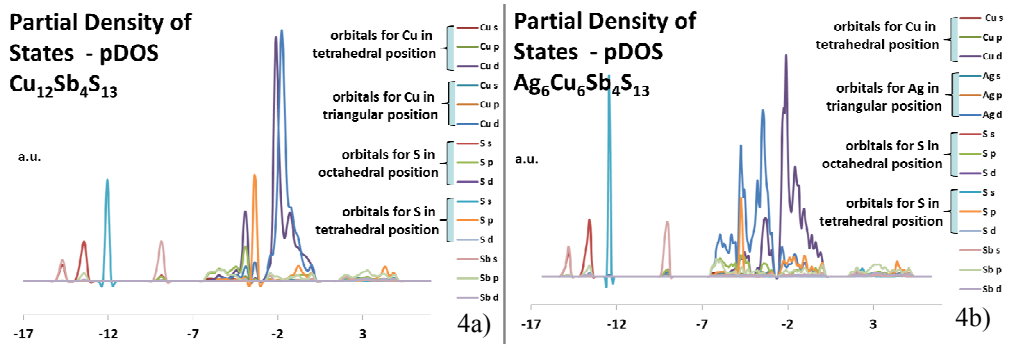

Fig 4a, 4b: The partial Density of States (pDOS) was calculated for each atom occupying a different site in $Cu_{12}Sb_4S_{13}$ and $Ag_6Cu_6Sb_4S_{13}$ crystal structures and for s, p and d orbitals.

Following the previous analysis but now focusing only on the use of the partial density of states (pDOS), we will be able to understand the orbital contribution for the promotion of electrons to the conduction band thus facilitating the occurrence of the photovoltaic effect. Essentially, from the analysis of the partial density of states (pDOS), one can infer the contribution of the electronic valence orbitals of the atoms occupying a given crystal position as well as all its equivalent positions existing in the unit cell.

By observing the data in the Fig 4a), it can be understood that both the 3d orbitals of copper that is in tetrahedral coordination, which are formally in the divalent state (Cu^{2+}) (2), as the electrons of the 3d orbitals of copper in triangular coordination, which are in the monovalent state (Cu^{+}) (2),

have equivalent probability to contribute to the promotion of these electrons to the conduction band, although the electrons of the 3d orbitals, which arise from the triangular positions, have a slightly more favorable electronic energy to promote the electrons to the conduction band.
The 3p and 3d valence orbitals of the Cu^{2+} cation (2) are filled with fifteen electrons in the following way: $3p^6\ 3d^9$, while the 3p and 3d valence orbitals of Cu^{+} cation (2), are filled with sixteen electrons in the following way: $3p^6\ 3d^{10}$. As it can be perceived, the difference in one electron, which induces a decoupling in a 3d orbital, facilitates the photo excitation.

In $Ag_6Cu_6Sb_4S_{13}$, there is a substitution of the Cu^{+} cation by Ag^{+} in the positions corresponding to the triangular coordination (2). In Fig 4b) it can be observed that the 3d orbitals of copper in the divalent state (Cu^{2+}), in tetrahedral coordination, are much more likely to contribute with electrons to the conduction band. The promotion of the monovalent silver (Ag^{+}) electrons to the conduction band is obtained from the 4d orbitals.
In the 3d orbitals of Cu^{2+}, the electronic filling of the valence orbitals is made as following: $3p^6\ 3d^9$, while for the 4d orbitals of Ag^{+}, the electronic filling of the valence orbitals is obtained by: $4p^6\ 4d^{10}$. It is clear from the analysis of the Fig 4b) that the Ag^{+} valence electrons correspond to orbitals that will contribute less to conduction, since they have lower energy. What makes them not so favorable to lose electrons capable of reaching the conduction band is, possibly, the different lengths of chemical bonds with the neighboring atoms. As shown in Table 1, the bond distances between copper and sulfur are smaller for both S^t and S^o.

Table 1. Bond distances of Cu^{+}-S^t, Cu^{+}-S^o, Ag^{+}-S^t and Ag^{+}-S^o when the cations Cu and Ag are in triangular coordination and the anion S in tetrahedral and octahedral positions.

	S^t	S^o
$(Cu^{+})^{tr}$	2.254 Å	2.291 Å
$(Ag^{+})^{tr}$	2.264 Å	2.304 Å

First principles calculations allow the characterization of band gaps as direct / indirect which is of paramount importance for photovoltaic applications.

Debye model

Elastic properties of solids are very important due to the fundamental solid-state phenomena such as equation of state, phonon spectra and atomic potentials. Elastic rigidity coefficients are essential for achieving the comprehension of the mechanical properties of a solid; such as internal strain, thermoelastic stress and load deflection. Measurements of the deformations of a solid are dependent of the coefficients of elastic rigidity (Table 2).

Table 2: Lattice parameter, enthalpy of formation at 0 K (with respect to the atomic state), elasticity tensor components C_{ij}, and bulk, shear, and young's modulus calculated using Voigt, Reuss and Hill approximations, obtained from the VASP optimization of the experimental structure.

Tetrahedrite	**P (GPa)**	**a(Å) (0 K)**	**$H_{formation}$ (kJ/mol; 0 K)**	***C_{11} (GPa)***	***C_{12} (GPa)***	***C_{44} (GPa)***	***Modulus (GPa)***	*Voigt*	*Reuss*	*Hill*
$Cu_{12}Sb_4S_{13}$	0	10.340	-425.9	80.46	52.99	19.61	***Bulk***	62.1	62.1	62.1
							Shear	17.3	16.7	17.0
							Young's	47.4	46.1	46.7
							Longitudinal	--	--	84.8
$Ag_6Cu_6Sb_4S_{13}$	0	10.374	-172.0	106.3	87.4	18.9	***Bulk***	93.7	93.7	93.7
							Shear	15.1	13.5	14.3
							Young's	43.1	38.6	40.8
							Longitudinal	--	--	112.8

It can be observed in Table 2. that the enthalpy of formation at 0 K is considerably different for each Tetrahedrite; $Ag_6Cu_6Sb_4S_{13}$ is much less stable than $Cu_{12}Sb_4S_{13}$. Conversely, the bulk modulus which measures the substance's resistance to uniform pressure is much higher in $Ag_6Cu_6Sb_4S_{13}$ although Cu (140 GPa), as a pure metal, has higher bulk modulus than Ag (100 GPa), in the same conditions [15]. The latter properties and differences highlight the necessity of first principles calculations to determine the properties of photovoltaic materials candidates, prior to synthesis and measurements. Furthermore, because both electronic band gap and mechanical properties change with the external pressure, it is important to correlate these properties if pressure is to be used as an additional tool to develop crystal engineering.

Conclusions

In this study, we present *ab initio* calculations using DFT and GGA-PBE to prove the usefulness of the latter in the selection of a particular substituting/doping element/ion and obtain new and optimized photovoltaic materials. Using the electronic band structures, density of states and correspondent orbital energies, the probability of certain electrons to be excited from the valence to the conduction band can be inferred. It can also be determined the energy cost of such a jump. Our results for the band structure and DOS for $Cu_{12}Sb_4S_{13}$ and $Ag_6Cu_6Sb_4S_{13}$ show that both the compounds have similar band gaps even if the electrons that will jump to the conduction band, are formerly from atoms occupying different sites.

The energy to overcome the band gap of these semiconductors – Tetrahedrites – falls within the photovoltaic operational range of 1.0 - 2.2 eV and the band gaps can be considered direct, as required.

References

[1] B.J. Wuensch, The crystal structure of Tetrahedrite, $Cu_{12}Sb_4S_{13}$. Z. Kristallogr. 119, (1964) 437-453

[2] K.Tatsuka, N. Morimoto, Tetrahedrite stability in the Cu-Fe-Sb-S system, Am. Min. 62 (1977) 1101-1109.

[3] C. An, Y. Jin, K. Tang, Y. Qian, Selective Synthesis and Characterization of Famatinite Nanofibers and Tetrahedrite Nanoflakes, J. Mater. Chem., 13 (2003) 301-303.

[4] V. Smil, Energy at the Cross Roads, Global Science Conference on Scientific Challenges for Energy Research, Paris, May 17-18, 2006.

[5] U.S. Climate Change Technology Program – Technology Options for the Near and Long Term, November 2003 – pg. 35

[6] M. Jacobson, Review of Solutions to Global Warming, Air Pollution, and Energy Security, Ener. Environ. Sci., 2 (2009) 148-173.

[7] S. Chen, X. G. Gong, A. Walsh, S.-H. Wei, Crystal and Electronic band structure of Cu_2ZnSnX_4 (X=S and Se) photovoltaic absorbers: First-principles insights, Appl. Phys. Let., 94 041903 (2009).

[8] Th. Pauporté, D. Lincot, Electrical, Optical and Photoelectrochemical Properties of Natural Enargite, Cu_3AsS_4, Adv. Mat. Opt. Elect., 5 (1995) 289-298.

[9] G. Kresse, J. Furthnüller, Efficiency of *ab-initio* total energy calculations for metals and semiconductors using a plane-wave basis set, Comp. Mater. Sci. 6 (1996) 15-50.

[10] P. E. Blöchl, Projector augmented-wave method, Phys. Rev. B 50 (1994) 17953-17979.

[11] G. Kresse, D. Joubert, From ultrasoft pseudopotentials to the projector augmented-wave method, Phys. Rev. B 59 (1999) 1758-1775.

[12] J. P. Perdew, K. Burke, M. Ernzerhof, Generalized gradient approximation made simple, Phys. Rev. Lett. 77 (1996) 3865-3868.

[13] H. J. Monkhorst, J. D. Pack, Special points for Brillouin-Zone integrations Phys. Rev. B (1976) 5188-5192.

[14] W. Kohn, L.J. Sham, Self-Consistent Equations Including Exchange and Correlation Effects, Phys. Rev.140 (1965) 1133-1138.

[15] Information on: Wolfram research, http://periodictable.com/Elements/029/data.html

Materials Science Forum Vols. 587-588 (2008) pp 435-439
online at http://www.scientific.net

Phase Transitions in the Cu-Sb-S System

M. H. Braga[1,a], J. A. Ferreira[2,b], C. Lopes[3,c] and L. F. Malheiros[3,d]

[1]GMM-IMAT, Dep. of Physics, Faculty of Engineering of the University of Porto, Portugal

[2]INETI Laboratory, S. Mamede Infesta, Portugal

[3]GMM-IMAT, Dep. of Metallurgical and Materials Engineering, FEUP, Portugal

[a]mbraga@fe.up.pt, [b]jorge.ferreira@ineti.pt, [c]ctlopes@fe.up.pt [d]lfmf@fe.up.pt,

Keywords: Cu-Sb-S, Tetrahedrite, Phase diagrams, XRD, DTA/DSC, EPMA

Abstract. The aim of this study is to determine the thermodynamic influence of the presence of Cu_3SbS_3, Cu_2S and Sb_2S_3 in the formation of $Cu_{12}Sb_4S_{13}$ - equivalent to mineral tetrahedrite. Thus, the Cu-Sb-S system is studied. Twenty three samples, with compositions that essentially lay along the vertical section Cu_2S-Sb_2S_3, were prepared. The samples were analyzed by Electron Microprobe (EPMA) in order to determine the room temperature phases' composition. Samples were also analyzed by Differential Thermal Analysis (DTA/DSC) in order to establish thermal transitions, and by X-Ray Diffraction (XRD), at room and high temperatures, so as to determine the phases that are present in the equilibria at certain temperatures. The experimental phase diagram was established and the results were compared with those available in the literature.

Introduction

This study aims to improve the knowledge about the Cu-Sb-S system by comparing synthetic with natural materials. The compositional variation and thermodynamic properties of the synthetic phases can help to establish relations with the natural equivalent composition.

The synthetic tetrahedrite type structure, in its simplest elementary composition, can be studied with the Cu-Sb-S system. This ternary system encloses, as well, synthetics with the same composition as a large variety of natural copper antimony chalcogenides. In nature, one of these phases is a very common sulphide, and crystallises in cubic system space group ($I\bar{4}3m$) [1], with nominal composition $M_{12}X_4S_{13}$ M = Cu, Ag, Bi, Hg, Fe, Zn, Pb X = Sb, As. This phase is very important by economic reasons because it can carry in its structure useful minor elements. It can show, as well, an interesting semiconductive electronic behaviour [2]. The comprehension of the mobility and accommodation of minor elements, like Ag, Bi, Hg, Fe, Zn, Pb,…, that can replace the copper positions or form an independent nanostructure in tetrahedrite lattice, will permit to explore the applicability of this structure.

Experimental

For studying the thermodynamic behaviour of the phases, belonging to the system Cu-Sb-S, synthetic samples were prepared: analytical powder (99.9995%) pure elements of Cu, Sb and S, from Alfa Aesar Puratronic, were weighed to obtain charges of 1 g.

Twenty three samples, with compositions that lay essentially along the vertical section Cu_2S-Sb_2S_3, were sealed in evacuated silica glass containers and melted at 630±2ºC for 6 h after a slow heating that took 4h. After melting, the temperature slowly dropped to room temperature in 4h in order to allow samples' homogenisation.

The samples were mounted in epoxy resin and successively observed in reflected-light optical microscopy and analysed in an Electron Microprobe (EPMA) JEOL JXA 8500F with WDS (Wavelength-Dispersive crystal Spectrometer). Samples were also analyzed by Differential Thermal Analysis (DTA) / Differential Scanning Calorimeter (DSC) in a Setaram Labsys TG/DTA/DSC apparatus, in order to determine thermal transitions. Room (RT - XRD) and high temperature X-ray

Diffraction (HT - XRD) were performed in a Panalytical X'Pert Pro MPD with an Anton Parr chamber apparatus in order to determine the phases present in equilibrium at certain temperatures.

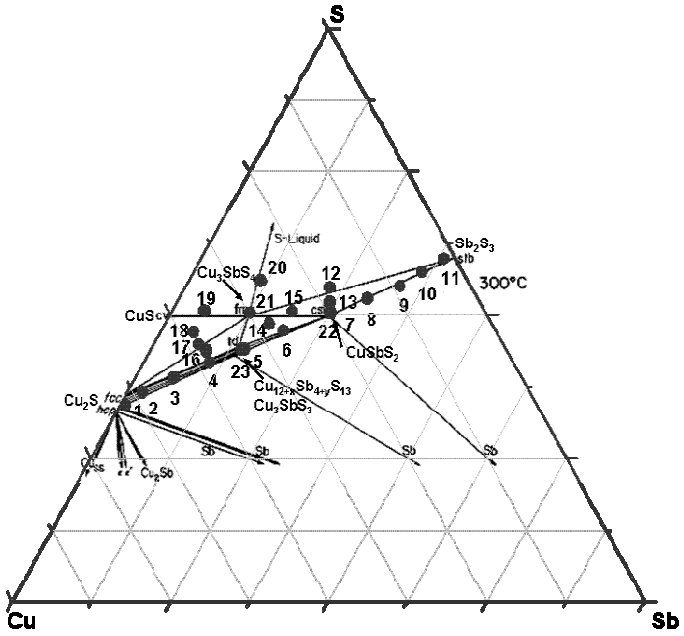

Fig. 1. (left) Cu-Sb-S system at 300 ºC, focussed essentially on the pseudo-binary Cu_2S - Sb_2S_3, as it was proposed by Skinner et al. [2]. Bullets represent the composition of the prepared samples and number its reference.

Fig. 2. (below) Photomicrographs of the samples, 23, 21 and 10.
Sample 23: light grey - (Sb), dark grey - Cu_2S, and medium grey - $Cu_{12.3}Sb_{4.3}S_{13}$.
Sample 21: light grey - $CuSbS_2$, dark grey - $Cu_{11.5}Sb_4S_{13}$ and medium grey - Cu_3SbS_4
Sample 10: dark grey - $CuSbS_2$, and medium grey - Sb_2S_3

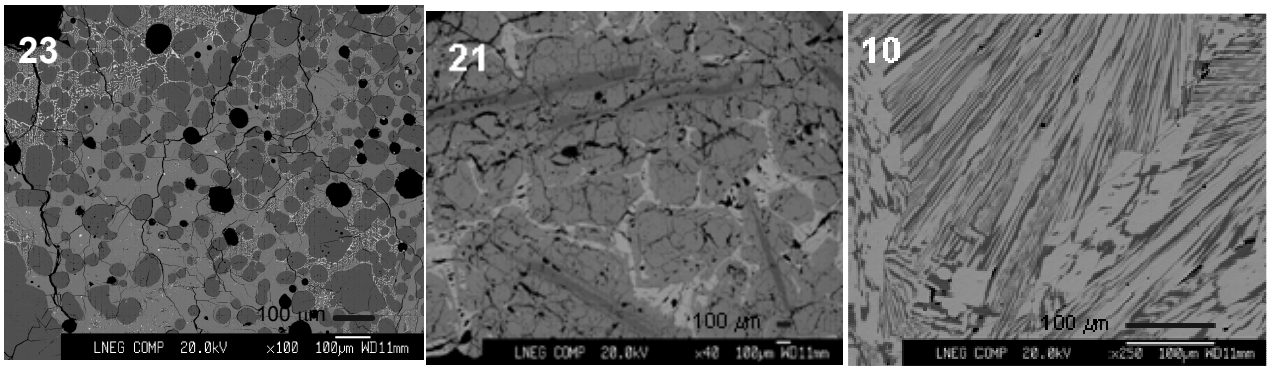

Results and discussion

EPMA/WDS. Almost every sample was analysed by means of EPMA and the composition of each phase was determined by WDS (using pure Cu, Sb and ZnS as standards). In Fig. 2 it can be seen three of the photomicrographs taken. It was observed that samples 1, 3, 4, 5, 7, 10, 14, 15, 16, 21, 22, and 23 presented the expected phases, at room temperature, after the work of [3] (see Table 1), although in the latter work samples were obtained by solid state synthesis. Samples 8, 9, 17, 18, 19 and 20 showed phases that were not expected to be found, at room temperature. This discrepancies are, in the case of samples 8 and 9, may be due to a composition shift caused by a small loss of sulphur and, in the case of sample 9, also due to a certain heterogeneity (Sb was not completely dissolved in the sample). For the other samples, the latter discrepancies are maybe due to the fact that the samples melt at higher temperatures than 630 ± 2 ºC (they have compositions close to those of the binary Cu-S whose compounds melt between ~813 and ~1127 ºC). Hence, as S melts at 115.2 ºC and Sb at 630.6 ºC, the first compounds to be formed are richer than expected in Sb. The remaining sulphur was probably accumulated at the container walls above 444.7 ºC (boiling point of S) Although in the literature, almost all synthesis, concerning the Cu-Sb-S system, were performed in the solid state (because solid state synthesis is closer to the natural process of formation of the chalcogenides), the homogenization was not sufficient for this kind of process. For the other samples, this problem could not be detected, since the samples reach the liquid state.

Table 1. The samples and its constituent phase's compositions, at room temperature, after EPMA/WDS and RT-XRD measurements.

	x(Cu) (%)	x(Sb) (%)	x(S) (%)	EPMA / WDS phases at room temperature ±1.0 at. (Cu); ±1.2 at. (Sb); ±0.9 at. (S)		
1.	64.9	0.8	34.3	$Cu_{64.6}Sb_{0.0}S_{35.4}$ (Cu_2S)	$Cu_{43.0}Sb_{13.8}S_{43.2}$ (Cu_3SbS_3)	
3.	54.9	6.1	39.0	$Cu_{64.4}Sb_{0.0}S_{35.6}$ (Cu_2S)	$Cu_{41.9}Sb_{14.3}S_{43.8}$ (Cu_3SbS_3)	
4.	47.8	10.4	41.8	$Cu_{63.5}Sb_{1.0}S_{35.5}$ (Cu_2S)	*	$Cu_{0.4}Sb_{99.5}S_{0.1}$ (Sb)
5.	41.3	14.7	44.0	$Cu_{41.6}Sb_{14.2}S_{44.2}$ (Cu_3SbS_3)	$Cu_{24.5}Sb_{24.6}S_{50.9}$ ($CuSbS_2$)	** probably (Sb)
6.	33.5	19.2	47.3	$Cu_{42.2}Sb_{14.3}S_{43.5}$ (Cu_3SbS_3)	$Cu_{24.5}Sb_{24.9}S_{50.6}$ ($CuSbS_2$)	$Cu_{0.3}Sb_{99.7}S_{0.0}$ (Sb)
7.	24.6	25.1	50.3	$Cu_{36.8}Sb_{12.3}S_{50.9}$ (Cu_3SbS_4)	$Cu_{24.0}Sb_{24.9}S_{51.1}$ ($CuSbS_2$)	$Cu_{0.7}Sb_{38.7}S_{60.6}$ (Sb_2S_3)
8.	17.4	29.7	52.9	$Cu_{24.2}Sb_{25.0}S_{50.8}$ ($CuSbS_2$)	$Cu_{0.3}Sb_{99.7}S_{0.0}$ (Sb)	
9.	11.1	33.8	55.1	$Cu_{24.8}Sb_{25.0}S_{50.2}$ ($CuSbS_2$)	$Cu_{0.3}Sb_{99.7}S_{0.0}$ (Sb)	
10.	6.4	36.0	57.6	$Cu_{24.8}Sb_{25.0}S_{50.2}$ ($CuSbS_2$)	$Cu_{0.2}Sb_{39.9}S_{59.9}$ (Sb_2S_3)	
11.	1.9	38.3	59.8	**	**	**
12.	22.4	22.8	54.8	**	**	**
13.	23.6	24.1	52.3	**	**	**
14.	35.2	16.4	48.4	$Cu_{40.9}Sb_{14.0}S_{45.1}$ ($Cu_{11.8}Sb_4S_{13}$)	$Cu_{37.1}Sb_{12.5}S_{50.4}$ (Cu_3SbS_4)	$Cu_{25.0}Sb_{25.1}S_{49.9}$ ($CuSbS_2$)
15.	30.4	19.0	50.6	$Cu_{36.2}Sb_{12.2}S_{51.6}$ (Cu_3SbS_4)	$Cu_{24.5}Sb_{24.5}S_{51.0}$ ($CuSbS_2$)	$Cu_{2.1}Sb_{36.1}S_{61.8}$ (Sb_2S_3)
17.	48.1	7.1	44.8	$Cu_{62.6}Sb_{0.0}S_{37.4}$ (Cu_2S)	$Cu_{36.4}Sb_{12.6}S_{51.0}$ (Cu_3SbS_4)	$Cu_{24.9}Sb_{24.6}S_{50.5}$ ($CuSbS_2$)
18.	47.7	5.2	47.1	**	**	**
19.	44.2	5.1	50.7	$Cu_{42.5}Sb_{14.6}S_{42.9}$ (Cu_3SbS_3)	$Cu_{25.1}Sb_{25.1}S_{49.8}$ ($CuSbS_2$)	$Cu_{1.1}Sb_{98.4}S_{0.5}$ (Sb)
20.	32.7	11.3	56.0	$Cu_{39.8}Sb_{14.1}S_{46.1}$ ($Cu_{11.2}Sb_{4.1}S_{13}$)	$Cu_{36.3}Sb_{12.4}S_{51.3}$ (Cu_3SbS_4)	$Cu_{24.5}Sb_{24.6}S_{50.9}$ ($CuSbS_2$)
21.	37.2	12.4	50.4	$Cu_{40.4}Sb_{14.0}S_{45.6}$ ($Cu_{11.5}Sb_4S_{13}$)	$Cu_{36.5}Sb_{12.3}S_{51.2}$ (Cu_3SbS_4)	$Cu_{24.7}Sb_{24.5}S_{50.8}$ ($CuSbS_2$)
22.	24.3	25.3	50.3	$Cu_{42.3}Sb_{14.5}S_{43.2}$ (Cu_3SbS_3)	$Cu_{24.6}Sb_{25.0}S_{50.4}$ ($CuSbS_2$)	$Cu_{0.3}Sb_{99.6}S_{0.1}$ (Sb)
23.	41.8	14.2	44.0	$Cu_{64.8}Sb_{0.0}S_{35.2}$ (Cu_2S)	$Cu_{41.6}Sb_{14.4}S_{44.0}$ (Cu_3SbS_3)	$Cu_{3.9}Sb_{94.6}S_{1.5}$ (Sb)

* According to XRD measurements, this phase is Cu_3SbS_3.
** Not measured.

DSC/DTA. DTA/DSC measurements were performed on a heat flux instruments with the possibility of determining the latent heat. Alumina crucibles with covers were used and the measurements were performed under flowing argon atmosphere at approx. 2.2 bar and approx. 40 cm^3 min^{-1}). The heating rates used were: 2, 5, 10 and 20 ºC/min. At least three different samples of the same composition were studied. A calibration factor: $C = b_0 + b_1*T + b_2*R + b_3*R^2$ (T – temperature in ºC, R – heating rate in ºC/min.) was evaluated after performing eleven calibrations with five different elements. Different heating rates (from 2 to 20 ºC/min.) were also used for determining the coefficients b_0, b_1, b_2 and b_3. The accuracy of all of the given temperatures is ±1 °C. The temperatures of the invariant phase reactions were taken from the extrapolated onset temperatures on heating. The liquidus surface temperatures were taken from the peaks on heating (Fig. 3). The obtained results are presented in Table 2.

Table 2. Expected transitions after [3,4], and DTA/DSC and HT-XRD measurements.

N.	Expected transitions (ºC) (from [3, 4] and this work)	Transition Temperatures (ºC) (from DTA/DSC and HT-DRX)
1	α - Cu_2S + $Cu_{1.96}S$ → β - Cu_2S + $Cu_{1.96}S$ (90) [4]; $Cu_{1.96}S$ → β - Cu_2S + $Cu_{2-\delta}S$ (93) [4]; Cu_3SbS_3' → Cu_3SbS_3 (122 ± 3) [3]; β - Cu_2S + $Cu_{2-\delta}S$ → $Cu_{2-\delta}S$; $Cu_{2-\delta}S$ + Cu_3SbS_3 → Liq.2 + $Cu_{2-\delta}S$ (607 ± 3) [3]; Liq.2+ $Cu_{2-\delta}S$ → Liq.2 + Liq.1 (1105) [4]; Liq.1 + Liq. 2 → Liq. [4]	85, 122, 172, 597, 1108, 1111
3	α - Cu_2S + $Cu_{1.96}S$ → β - Cu_2S (90) [4]; $Cu_{1.96}S$ → β - Cu_2S + $Cu_{2-\delta}$ (93) [4]; Cu_3SbS_3' → Cu_3SbS_3 (122 ± 3) [3]; β - Cu_2S + $Cu_{2-\delta}S$ → $Cu_{2-\delta}S$; $Cu_{2-\delta}S$ + Cu_3SbS_3 → Liq.2 + $Cu_{2-\delta}S$ (607 ± 3) [3]; Liq.2 + $Cu_{2-\delta}S$ → Liq.2 + $Cu_{2-\delta}S$ + Liq.1; Liq.2 + $Cu_{2-\delta}S$ + Liq.1 → Liq.2 + Liq.1	90, 123, 142, 604, 611, 911
4	Cu_3SbS_3' → Cu_3SbS_3 (122 ± 3) [3]; $Cu_{2-\delta}S$ + Cu_3SbS_3 + (Sb) → $Cu_{2-\delta}S$ + Cu_3SbS_3; $Cu_{2-\delta}S$ + Cu_3SbS_3 → Liq.2 + $Cu_{2-\delta}S$ (607 ± 3) [3]; Liq.2 + $Cu_{2-\delta}S$ → Liq.2 + $Cu_{2-\delta}S$ + Liq.1	125, 511, 604, 611
5	Cu_3SbS_3' → Cu_3SbS_3 (122 ± 3) [3]; Cu_3SbS_3 + $CuSbS_2$ + (Sb)→ Cu_3SbS_3 + (Sb) + Liq.2 (531 ± 2); Cu_3SbS_3 + (Sb) + Liq.2 → Liq.2 (607 ± 2)	109, 472, 539, 603
6	Cu_3SbS_3' → Cu_3SbS_3 (122 ± 3) [3]; Cu_3SbS_3 + $CuSbS_2$ + (Sb) → Cu_3SbS_3 + (Sb) + Liq.2 (531 ± 2); Cu_3SbS_3 + (Sb) + Liq.2 → Cu_3SbS_3 + $Cu_{2-\delta}S$ + Liq.2; Cu_3SbS_3 + $Cu_{2-\delta}S$ + Liq.2 → $Cu_{2-\delta}S$ + Liq.2 + Liq.1 (607 ± 2) [3]; $Cu_{2-\delta}S$ + Liq.2 + Liq.1 → Liq.2	108, 460, 522, 582, 604, 613
7	Cu_3SbS_4 + $CuSbS_2$ + Sb_2S_3 → Cu_3SbS_4 + $CuSbS_2$ + Liq.2 (476.5 ± 2); Cu_3SbS_4 + $CuSbS_2$ + Liq.2 → Cu_3SbS_4 + Liq.2 + Liq.1 (553 ± 2); Cu_3SbS_4 + Liq.2 + Liq.1 → Liq.2 + Liq.1; Liq.2 + Liq.1 → Liq.2	472, 495, 531, 537
8	$CuSbS_2$ + (Sb) → (Sb) + Liq.2 (531 ± 2); (Sb) + Liq.2 → Liq2 + Liq.1; Liq2 + Liq.1 → Liq.2	464, 520, 525, 533
9	$CuSbS_2$ + (Sb) → (Sb) + Liq.2 (531 ± 2); (Sb) + Liq.2 → Liq2 + Liq.1; Liq.2 + Liq.1 → Liq.2	454, 524, 530, 538
10	$CuSbS_2$ + Sb_2S_3 → Sb_2S_3 + Liq.2 (476.5 ± 2); Sb_2S_3 + Liq.2 → Liq.2 + Liq.1; Liq.2 + Liq.1 → Liq.2	465, 477, 495, 508
14	$Cu_{12}Sb_4S_{13}$ + Cu_3SbS_4 + $CuSbS_2$ → Cu_3SbS_4+ Cu_3SbS_3 + $CuSbS_2$ (522 ± 2); Cu_3SbS_4+ Cu_3SbS_3 + $CuSbS_2$ → Cu_3SbS_4+ Cu_3SbS_3 + Liq.2 (553 ± 2); Cu_3SbS_4+ Cu_3SbS_3 + Liq.2 → Cu_3SbS_4 + Liq.2; Cu_3SbS_4 + Liq.2 → Liq.2	530, 542, 572
15	Cu_3SbS_4 + $CuSbS_2$ + Sb_2S_3 → Cu_3SbS_4 + $CuSbS_2$ + Liq.2 (476.5 ± 2); Cu_3SbS_4 + $CuSbS_2$ + Liq.2 → Cu_3SbS_4 + Liq.2 + Liq.1 (553 ± 2); Cu_3SbS_4 + Liq.2 + Liq.1 → Liq.1 + Liq.2; Liq.1 + Liq.2 → Liq.2	495, 538, 600, 618
19	The composition is not absolutely accurate, despite the fact that the present phases at room temperature are known	462, 536, 538, 613, 616
20	The composition is not absolutely accurate, despite the fact that the present phases at room temperature are known	63, 72, 541, 549, 601, 603, 605
21	$Cu_{12}Sb_4S_{13}$ + Cu_3SbS_4 + $CuSbS_2$ → Cu_3SbS_4+ Cu_3SbS_3 + $CuSbS_2$ (522 ± 2); Cu_3SbS_4+ Cu_3SbS_3 + $CuSbS_2$ → Cu_3SbS_4+ $Cu_{2-\delta}S$ + Liq.2 (553 ± 2); Cu_3SbS_4+ $Cu_{2-\delta}S$ + Liq.2 → $Cu_{2-\delta}S$ + Liq.2 + Liq.1; $Cu_{2-\delta}S$ + Liq.2 + Liq.1 → Liq.2	543, 560, 607, 610
22	Cu_3SbS_3' → Cu_3SbS_3 (122 ± 3); Cu_3SbS_3 + $CuSbS_2$ + (Sb)→ Cu_3SbS_3 + (Sb) + Liq.2 (553 ± 2); Cu_3SbS_3 + (Sb) + Liq.2 → (Sb) + Liq.2 (607.5 ± 3); (Sb) + Liq.2 → Liq.2	463, 540, 612, 615
23	α - Cu_2S + $Cu_{1.96}S$ → β - Cu_2S (90) [4]; $Cu_{1.96}S$ → β - Cu_2S + $Cu_{2-\delta}$ (93) [4]; Cu_3SbS_3' → Cu_3SbS_3 (122 ± 3) [3]; β - Cu_2S + $Cu_{2-\delta}S$→ $Cu_{2-\delta}S$; $Cu_{2-\delta}S$ + Cu_3SbS_3 + (Sb) → $Cu_{2-\delta}S$ + (Sb) + Liq.2 (588 ± 2); $Cu_{2-\delta}S$ + (Sb) + Liq.2 → $Cu_{2-\delta}S$ + Liq.2; $Cu_{2-\delta}S$ + Liq.2 → Liq.2;	90, 109, 155, 586, 595, 600

RT-XRD/HT-XRD. Powder RT-XRD measurements were performed to identify the present phases. For some samples, powder HT-XRD measurements were also performed, under a secondary vacuum of 10^{-5} mbar. CuKα radiation was used to collect patterns from 10 to 90º (2θ) with steps of 0.008º and counting time of 17 s (Fig. 4). This study complemented the DTA/DSC experiments.

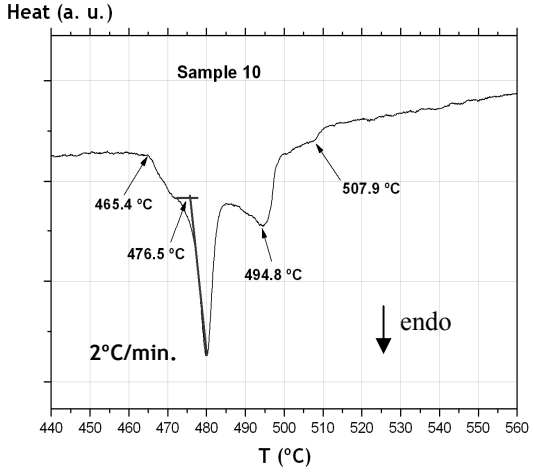

Fig. 3. (left) DTA/DSC curve on heating for sample 10, for a heating rate of 2 ºC/min.
Four transitions can be observed. The first two seem to correspond to invariant transitions and the last one seems to correspond to the liquidus point.

Fig. 4. (below) RT-XRD for Sample 7. The phases identified, using the ICDD PDF 2, 2003, database, are Cu_3SbS_4 (Famatinite, syn: 00-035-0581), $CuSbS_2$ (Chalcostibite: 00-002-0557) and Sb_2S_3 (Stibnite, syn: 01-078-1347).

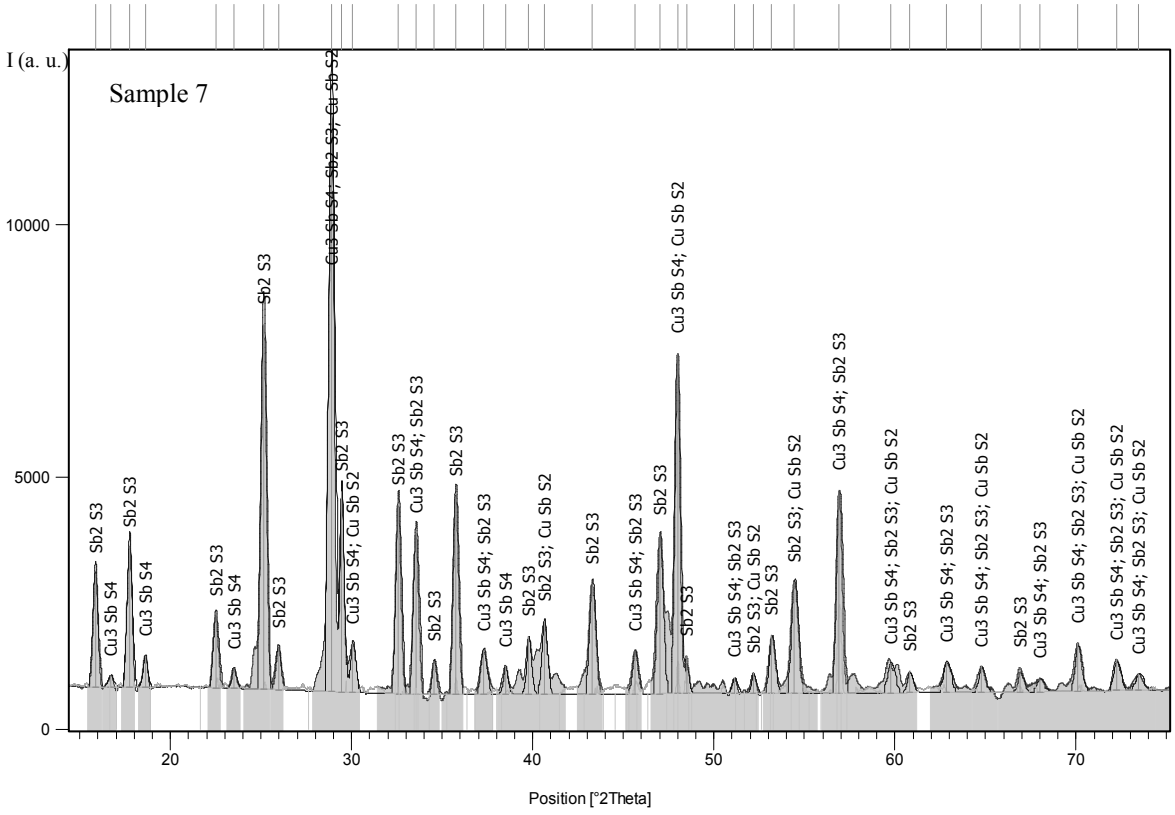

Summary

Although in the literature all studies concerning the system Cu-Sb-S were obtained after solid synthesis, the present results show that the samples can be studied after being melted and homogenized. The EPMA/WDS and XRD room temperature data for the samples' equilibrium phases are in good agreement with the ternary from [3], at 300 ºC. The DTA/DSC results are also generally in agreement with those from [3, 4]. Nevertheless, some transitions, like that at ~465 ºC (for samples 5, 6, 22, 8, 9 and 10), are still not well determined.

References

[1] A. Pfitzner, M. Evain and V. Petricek: Acta Crystallogr. B Vol. 53 (1997), p. 337.
[2] N. Hisayuki, E. Saburo and I. Taizo: Jpn. J. Appl. Phys. Vol. 8 (1969), p. 443.
[3] B. J. Skinner, F. D. Luce and E. Makovicky: Econ. Geol. Vol. 67 (1972), p. 924.
[4] D. J. Chakrabarti and D. E. Laughlin: Bull. Alloy Phase Diagrams Vol. 4, N. 3 (1993).

Chapter 3- Cu-Li-Mg (H, D) System

Chapter 3.

Cu-Li-Mg (H, D) SYSTEM

3.1 Introduction to Cu-Li-Mg system

The Cu-Li-Mg system was studied under the scope of the COST 507 - EU Action, since it is one of the ternaries of the quaternary, Al-Cu-Li-Mg system. The Al-Cu-Li-Mg system is one of the light weight reference systems with applications in the airplane and automotive industry.

Only one ternary phase coexists in the Cu-Li-Mg ternary phase diagram, $CuLi_xMg_{2-x}$ (x = 0.08). Lithium substitutes Mg in the ternary structure which is hexagonal, $P6_222$, although to the binary $CuMg_2$ crystallizes in an orthorhombic Fddd structure.

The fact that $NiMg_2$ crystallizes with a hexagonal structure, $P6_222$, made us hypothesize that, as $NiMg_2$, $CuLi_xMg_{2-x}$ (x = 0.08) would also form a hydride (Braga & Malheiros, 2007a) conversely to what happens with $CuMg_2$ that reacts with H_2: $2CuMg_2 + 3H_2 \rightarrow Cu_2Mg + 3MgH_2$.

The latter motivated the following study and all publications.

The following text resulted in the book chapter:

M.H. Braga, M.J. Wolverton, M.H. Sá**, J.A. Ferreira**

"Hydrides of Cu and Mg Intermetallic Systems: Characterization, Catalytic Function and Applications"

Keywords: Hydrides, Neutron Diffraction, Catalysis, First Principles Calculations, Phonons, Gibbs Energies, DSC/TGA, Van't Hoff plots

in **Neutron Diffraction**, published by Intech, ISBN: 979-953-307-475-6

2012

3.2 Introduction to hydrogen storage

The worldwide demand for energy in the 21st century is growing at an alarming rate. The European "World Energy Technology and Climate Policy Outlook" [WETO] predicts an average growth rate of 1.8% per annum for the period 2000-2030 for the world energy

demand (European Commission, 2003). The increased demand is being met largely by reserves of fossil fuel that emit both greenhouse gases and other pollutants. Since the rate of fossil fuel consumption is higher than the rate of fossil fuel production by nature, these reserves are diminishing and they will become increasingly expensive.

Against this background, the transition towards a sustainable, carbon-free and reliable energy system capable of meeting the increasing energy demands becomes imperative. Renewable energy resources, such as wind, solar, water, wave or geothermal, can offer clean alternatives to fossil fuels. Despite of their obvious advantages renewable energy sources have also some drawbacks in their use because they are unevenly distributed both over time and geographically. Most countries will need to integrate several different energy sources and an advanced energy storage system needs to be developed.

3.3 Hydrogen storage: a brief overview

Hydrogen has also attracted intensive attention as the most promising secure energy carrier of the future (Jain, 2009) due to its prominent advantages such as being:

1. Environmentally friendly. It is a "clean, green" fuel because when it burns in oxygen there is no pollutants release, only heat and water are generated:

$$2H_2\,(g) + O_2\,(g) \leftrightarrows 2H_2O\,(g) \qquad \triangle H = 120\ kJ/g \tag{3.1}$$

2. Easy to produce. Hydrogen is the most abundant element in the Universe and is found in great abundance in the world, allowing it to be produced locally and easily from a great variety of sources like water, biomass and organic matter;

3. Light. Hydrogen is the Nature's simplest and lightest element with only one proton and one electron with high energy per unit mass.

Nonetheless, opposing to the advantages of hydrogen as an energy carrier is the difficulty in storing it. Hydrogen storage remains a problem, in particular for mobile/vehicular applications (Felderhoff et al., 2007). High-pressure hydrogen gas requires very large volumes compared to petrol, for producing the same amount of energy. On the other hand, liquid hydrogen storage systems are not viable for vehicular applications due to safety concerns in addition to volumetric constraints. Thus, hydrogen storage viability has prompted an extensive effort to develop solid hydrogen storage systems but no fully satisfactory solutions have been achieved to date (Churchard et al., 2011).

The goal is to find a material capable of simultaneously absorbing hydrogen strongly enough to form a stable thermodynamic state, but weakly enough to release it on-demand with a small temperature rise (Jeon et al., 2011) in a safe, compact, robust, and efficient manner. There have been many materials under development for solid hydrogen storage, including metal hydrides (MH_x), via the chemical reaction of H_2 with a metal or metal alloy (M):

$$(x/2)\ H_2\ (g) + M\ (s) \leftrightarrows MH_x\ (s) \qquad (3.2)$$

Generally, a typical hydrogenation reaction is known to involve several steps: (3.1) gas permeation through the particle bed, (3.2) surface adsorption and hydrogen dissociation, (3.3) migration of hydrogen atoms from the surface into the bulk, (3.4) diffusion through the particle and finally (3.5) nucleation and growth of the hydride phase. Any delay in one of these steps will reduce the kinetic properties of the process (Schimmel et al., 2005).

3.4 Magnesium hydride

Magnesium-based hydrogen storage alloys have been considered most promising solid hydrogen storage materials due to their high gravimetric hydrogen storage densities and volumetric capacity (see Table 3.1 adapted from (Chen & Zhu, 2008) for comparison) associated to the fact that magnesium is abundant in the earth's crust, non-toxic and cheap (Grochala & Edwards, 2004; Jain et al., 2010; Schlapbach & Züttel, 2001).

Metal	Hydrides	Structure	Mass %	P_{eq}, T
$LaNi_5$	$LaNi_5H_6$	Hexagonal	1.4	2 bar, 298 K
$CaNi_3$	$CaNi_3H_{4.4}$	Hexagonal	1.8	0.5 bar, 298 K
ZrV_2	$ZrV_2H_{5.5}$	Hexagonal	3.0	10^{-8} bar, 323 K
TiFe	$TiFeH_{1.8}$	Cubic	1.9	5 bar, 303 K
Mg_2Ni	Mg_2NiH_4	Monoclinic (LT) / Cubic (HT)	3.6	1 bar, 555 K
Ti-V-based	Ti-V-based-H_4	Cubic	2.6	1 bar, 298 K
Mg	MgH_2	Tetragonal	7.6	1 bar, 573 K

Table 3.1 Structure and hydrogen storage properties of typical metal hydrides

Magnesium can be transformed in a single step to MgH_2 hydride with up to 7.6 wt% of hydrogen with a volumetric storage efficiency of 110g H_2/l (Milanese et al., 2010a), according to:

$$Mg\ (s) + H_2\ (g) \leftrightarrows MgH_2\ (s) \qquad (3.3)$$

Magnesium metal is hexagonal with $P6_3/mmc$ space group (α-structure) but the absorption of hydrogen induces a structural change into the tetragonal rutile-type structure α-MgH_2 ($P4_2/mnm$) (Aguey-Zinsou & Ares-Fernández, 2010) (see Fig. 3.1).

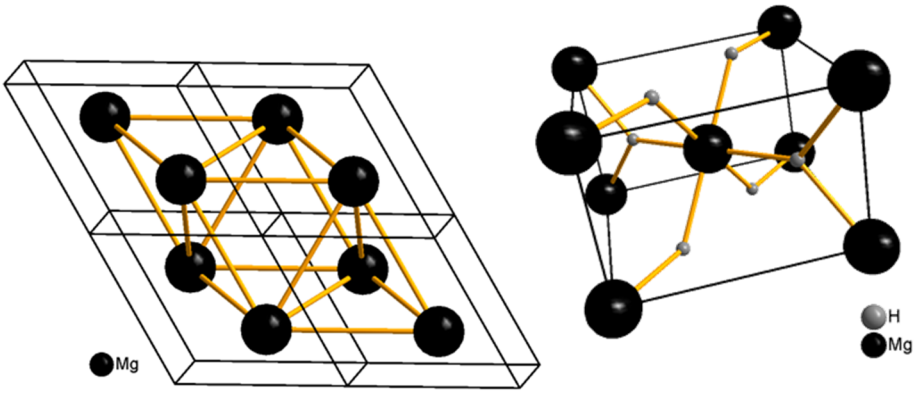

Fig. 3.1 Crystal structure of magnesium (left) and magnesium hydride (right).

At high temperature and pressure, the latter phase undergoes polymorphic transformations to form two modifications: γ-MgH_2 and β-MgH_2, having an orthorhombic structure and a hexagonal structure, respectively (Schlapbach & Züttel, 2001). Other high-pressure metastable phases have also been reported (Cui et al., 2008; Ravindran et al., 2004). The charge density distribution in these materials has also been investigated and revealed a strong ionic character. The charge density determination of MgH_2 by means of synchrotron X-ray powder diffraction at room temperature, the maximum entropy method (MEM) and Rietveld refinement revealed that the ionic charge of Mg and H can be expressed by $Mg^{1.91+}$ and $H^{0.26-}$, respectively, denoting that Mg in MgH_2 is fully ionized, but the H atoms are in a weak ionic state (Noritake et al., 2003). The high strength of these bonds results however in an unacceptably high thermodynamic stability which diminishes the potentialities of using MgH_2 in practical applications. The hydrogen desorption temperature is well above 573 K, which is related to its high dissociation enthalpy (75 kJ/mol H_2) under standard conditions of pressure (Schlapbach & Züttel, 2001). In addition,

the high directionality of the ionic bonds in this system leads to large activation barriers for atomic motion, resulting in slow hydrogen sorption kinetics (Vajo & Olson, 2007).

Several solutions were envisaged to circumvent these drawbacks. They can be accomplished to some extent by changing the microstructure of the hydride by ball-milling it (Huot et al., 1999; Zaluski et al., 1997). In this process the material is heavily deformed, and crystal defects such as dislocations, stacking faults, vacancies are introduced combined with an increased number of grain boundaries, which enhance the diffusivity of hydrogen into and out of the material (Suryanarayana, 2008).

Alloying the system with other metallic additives, like 3d elements (Ti, Fe, Ni, Cu or Al), or $LaNi_5$, FeTi, Pd, V among others and oxides like V_2O_5 or Nb_2O_5 can also be a way of improving kinetic and/or thermodynamic properties by changing the chemical interaction between the atoms (Reule et al., 2000; Rude et al., 2011; Tan et al., 2011a). The use of a proper destabilization or catalyst element/alloy into the system has also been shown to improve adsorption/desorption kinetics and to lower the adsorption temperature (Beattie et al., 2011).

Furthermore, substantial improvements in the hydriding-dehydriding properties can be achieved by nanoengineering approaches using nanosized reactants or by nanoconfinement of it (Jeon et al., 2011; Jurczyk et al., 2011; Vajo, 2011; Zaluska et al., 1999a; Zhao-Karger et al., 2010). The latter allows shorter diffusion distances and larger surface area, resulting in faster reaction kinetics. It can also introduce alternative mechanisms to hydrogen exchange modifying the thermodynamic stability of the process.

As previously referred, an alternative approach for altering the thermodynamics of hydrogenation-dehydrogenation is achieved by using additives that promote hydride destabilization by alloy or compound formation in the dehydrogenated state. This approach is known as chemical destabilization. The principle underlying this approach is that the additives are capable to form compounds or alloys in the dehydrogenated state that are energetically favourable with respect to the products of the reaction without additives. Destabilization occurs because the system can cycle between the hydride and the additive instead of the elemental metal.

A generalized enthalpy diagram illustrating this approach - destabilization of the generic hydride AH_2 through alloy formation (AB_x) promoted by the presence of the alloying species B - was given by Vajo and Olson (Vajo & Olson, 2007), and is shown in Fig. 3.2

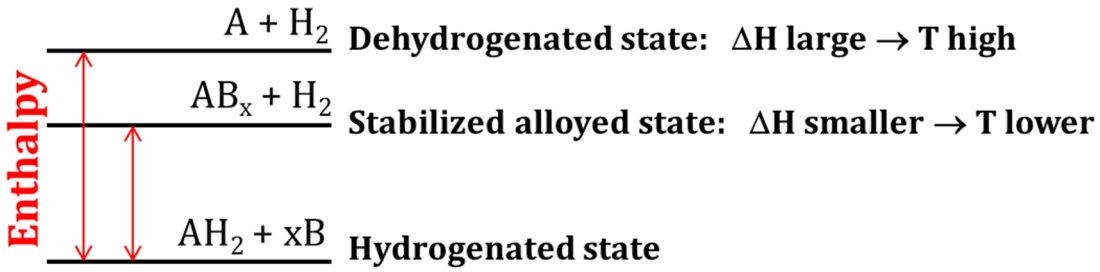

Fig. 3.2 Generalized enthalpy diagram illustrating destabilization through alloy formation upon dehydrogenation (adapted from Vajo & Olson, 2007)

3.5 Cu-Mg, Ni-Mg and other MgH_2 destabilizing systems

The work of Reilly and Wiswall provided the first evidences of this concept (Reilly & Wiswall, 1967, 1968). In their work, they showed that MgH_2 can be destabilized by Cu_2Mg. The formation of $CuMg_2$ occurs upon dehydrogenation at lower reaction temperatures than those obtained with just pure MgH_2. The compound $CuMg_2$ crystallizes in the orthorhombic structure (Braga et al., 2010c) and has a hydrogen capacity of 2.6 wt. % at 573 K (Jurczyk et al., 2007). The hydride formation enthalpy is approximately 5 kJ/mol H_2 lower than that of the hydrogenation of MgH_2 from Mg and this process obeys to the following scheme (Reilly & Wiswall, 1967):

$$2CuMg_2\,(s) + 3H_2\,(g) \rightleftarrows 3MgH_2\,(s) + Cu_2Mg\,(s) \qquad (3.4)$$

The intermetallic cubic compound Cu_2Mg does not hydrogenate under conventional hydrogenation conditions and seems to improve dehydrogenation kinetics (as compared to MgH_2) due to improve resistance towards oxygen contamination (Andreasen et al., 2006; Kalinichenka et al., 2011; Reilly & Wiswall, 1967). As to the hexagonal intermetallic compound $NiMg_2$, Reilly and Wiswall (Reilly & Wiswall, 1968) established that it reversibly reacts with hydrogen to form a ternary hydride Mg_2NiH_4, with a hydrogen content of 3.6 wt. %, according to the following scheme:

$$NiMg_2Ni\,(s) + 2H_2\,(g) \rightleftarrows NiMg_2H_4\,(s) \qquad (3.5)$$

Results obtained by A. Zaluska and co-workers (Zaluska et al., 1999b) showed that ball-milling the mixtures MgH_2 and $NiMg_2H_4$ results in a synergetic effect of desorption, allowing the mixture to operate at temperatures as low as 493K – 513K, with good

absorption / desorption kinetics and with total hydrogen capacity exceeding 5 wt.%. They point out however that the ball-milled mixtures of the hydrides behave differently from two metal phases that are firstly ball-milled and then hydrogenated. In the latter case volume changes occur during hydrogenation with associated volume expansion of the material, in contrast to what happen in their study in which $NiMg_2H_4$ promoted the hydrogen release from an adjacent MgH_2 matrix since they undergo a significant volume contraction, which facilitates their dehydrogenation.

Many more studies have focused on changes in the hydriding/dehydriding properties of Ni-Mg binary alloys with compositional changes and changes in processing variables. Nonetheless, we highlight the study of C. D. Yim and collaborators (Yim et al., 2007) that showed that the $NiMg_2$ compound acted as a catalyst in the dissociation of the hydrogen molecule, which resulted in a faster nucleation of magnesium hydride compared to pure Mg. It revealed also that the capacity and kinetics of hydriding were larger and faster when the average size of the hydriding phase was smaller and the volume fraction of the phase boundary was larger, since phase boundaries between the eutectic α-Mg and $NiMg_2$ phases acted as a fast diffusion path for atomic hydrogen.

In the full hydrogenated state, the $NiMg_2H_4$ structure consists of tetrahedral $[NiH_4]^{4-}$ complexes in a framework of magnesium ions and two different forms exist, high-temperature (HT) and low-temperature (LT). Under the partial pressure of 0.1 MPa of hydrogen, the HT cubic structure phase transforms into a LT monoclinically distorted structure between 518 and 483 K (Zhang et al., 2009).

The LT phase has also two modifications the untwined (LT1) and micro-twinned (LT2), which depend on the thermomechanical history of the sample (Cermak & David, 2011). The hydride formation enthalpy for the $NiMg_2H_4$ has been determined experimentally for the HT form, and it is in the range from -64.3 to -69.3 kJ/mol H_2, for the LT form this value ranges from -68.6 to -81.0 kJ/mol H_2 (Tan et al., 2011b).

In the pioneer work of Reilly and Wiswall (Reilly & Wiswall, 1968) it was pointed out the catalytical effect of $NiMg_2$ on the hydrogen desorption characteristics of MgH_2. Recently, Cermak and David (Cermak & David, 2011) showed that $NiMg_2$, and more efficiently the LT1 phase of $NiMg_2H_4$, were responsible for the catalytic effect of Ni reported in the literature. The fact that $NiMg_2$ is a metal whereas $NiMg_2H_4$ behaves like a semiconductor has opened the way to the possibility of using this system also as a switchable mirror upon hydrogenation and dehydrogenation (Setten et al., 2007). A switchable mirror will switch

from mirror to transparent material upon hydrogenation. A more detailed study of Ni-Mg-based hydrides can be found in (Orimo & Fujii, 2001).

Despite all the interest and extensive research on the above referred systems, a problem still remains; the hydrogen holding capacities of these materials are considerably less than that of MgH_2 (Sabitu et al., 2010). A way to overcome this limitation was found by combining MgH_2 with $LiBH_4$ (which involves the formation of MgB_2 and Li-Mg alloy (Yu et al., 2006)) since pure $LiBH_4$ has high gravimetric and volumetric hydrogen densities, 18.5 wt. % and 121 kg H_2/m^3, respectively (Bösenberg et al., 2010; Xia et al., 2011). However, although the reaction enthalpy is lowered and the hydrogen storage capacity increases (10.5 wt. %), the sorption and absorption processes occurs at high temperatures with relatively slow kinetic even though more additives are being tested in order to overcome this problem (Fernández et al., 2011; Xia et al., 2011). Alternatively, the study of the destabilization of MgH_2 with TiH_2 has also been taken experimentally (Choi et al., 2008; Sohn et al., 2011). Observations point to a substantially reduced apparent activation energy of 107-118 kJ/mol and significantly faster kinetics, compared with the 226 kJ/mol for the similarly milled MgH_2. The latter system constitutes a promising material to be used in practical applications for hydrogen storage.

The combined destabilization effect of Ni-Mg and Cu-Mg intermetallics towards MgH_2 was also tested and the Mg-rich ternary Cu-Ni-Mg alloys were recognized to have high potential for solid state hydrogen storage and have attracted many research interests. The study recently reported by Tan and co-workers (Tan et al., 2011b) elucidates about the influence of Cu substitution on the hydrogen sorption properties of magnesium rich Ni-Mg films. This study shows a two-step hydrogen absorption process. The first step is due to the absorption of Mg not alloyed in the form of $NiMg_2$ and/or $CuMg_2$, hereafter denoted as "free Mg" and is very quick, because it is mainly catalyzed by the intermetallic phase, $NiMg_2$. But the second step, due to the hydrogen absorption of intermetallic $NiMg_2$ and/or $CuMg_2$ ("bonded Mg") is significantly slow.

The Cu substitution shows positive effects on desorption kinetics during full capacity hydrogen cycling, but shows strongly negative effects on absorption kinetics, particularly for the second absorption step, due to the segregation of $CuMg_2$ towards the grain boundaries of MgH_2, forming a closed shell that traps the hydrogen in MgH_2. The authors also reported that the Cu substitution has no thermo-destabilization for MgH_2, but since a significant amount can be dissolve in $NiMg_2$, even at elevated temperatures, thermo-destabilization of $NiMg_2H_4$ and better desorption kinetics are observed. Hong and

collaborators (Hong et al., 2011) on their study on the hydrogen storage properties of x wt.% Cu-23.5 wt.% Ni-Mg (x = 2.5, 5 and 7.5) prepared by rapid solidification process and crystallization heat treatment have also reported that the $NiMg_2$ phase has higher hydriding and dehydriding rates than Mg under similar conditions and that the addition of a smaller amount of Cu is considered favourable to the enhancement of the hydriding and dehydriding rates of the sample. The 2.5 wt.% Cu-23.5 wt.% Ni-Mg alloy had the highest hydriding and dehydriding rates. These observations are in line with the ones previously reported by the group of Milanese (Milanese et al., 2010b; 2008), who also observed the high sorption capacity and good sorption performance of Cu-Ni-Mg mixtures and proposed a two steps sorption process with different kinetics.

The first step corresponds to the quick hydrogenation of "free Mg", according to reaction (3.3). After this step, absorption keeps on with a slower rate corresponding to the second step, hydrogenation of the "bonded Mg" phases, $NiMg_2$ and $CuMg_2$, according to reactions (3.4) and (3.5). They also showed that Ni is more effective than Cu in catalyzing the desorption reactions and that $NiMg_2H_4$ and Cu_2Mg phases destabilized each other with the beneficial effect of decreasing the dissociation temperature of about 50 K in comparison to the MgH_2, from "free Mg". The positive effect of Cu as a catalyst on the hydrogenation and thermodynamic properties of $NiMg_2$ mixed by ball milling technique was also studied and recently reported by Vyas and co-workers (Vyas et al., 2011) showing that hydrogen storage capacity and enthalpy of formation of $NiMg_2$ with 10 wt.% Cu reduces to 1.81 wt.% and 26.69 kJ $(mol\ H)^{-1}$ from 3.56 wt.% and 54.24 kJ $(mol\ H)^{-1}$ for pure $NiMg_2$ at 573 K, respectively. They attributed the decrement in the absorption capacity to the formation of the intermetallic phase Cu_2Mg, which does not absorb the hydrogen but itself behaves like a catalyst.

However, in the case of nanocrystalline $Cu_xNi_{10-x}Mg_{20}$ (x = 0-4) alloys synthesized by melt-spinning technique, it was found (Zhang et al., 2010a, 2010b) that the substitution of Ni by Cu does not change the major phase $NiMg_2$ although it leads to a refinement of grains with increased cell volume and the formation of a secondary phase $CuMg_2$. This in turn leads to a decrease of the hydride stability with a clear improve of the hydrogen desorption capacity and kinetics of the alloys.

The presence of $CuMg_2$ seems to act as a catalyst for the hydride-dehydride reactions of Mg and Mg-based alloys. Similar behaviour was found in $Cu_{0.25}Ni_{0.75}Mg_2$ and $Cu_{0.4}Ni_{0.6}Mg_2$ alloys that were prepared by mechanical alloying and subsequent thermal treatment (Simičić et al., 2006). The latter effect was also investigated on $Cu_{1-x}Ni_xMg_2$ (x = 0-1) alloys

by Hsu and collaborators (Hsu et al., 2010). They observed that by substituting Cu by Ni in $CuMg_2$, the cell volume decreased (since the radius of Cu atom is slightly larger than Ni atom) and with increasing Ni content , the effect of Ni is actually effective in MgH_2 and Mg_2NiH_4 destabilization, leading to a decrease of desorption temperature in these two phases. They also showed that substituted nickel caused the hydriding reaction because absorption kinetics and hydrogen storage capacity increased with the rise of Ni-substitution contents.

3.6 Lithium hydride

An alternative route to be considered is to explore other hydrates besides MgH_2 for solid hydrogen storage. One of most interesting is lithium hydride, because it contains 12.5 wt.% hydrogen. Nonetheless, the desorption temperature is 1183 K for an equilibrium pressure of 1 bar (Vajo et al., 2004). However, it has been shown (Chen et al., 2003) that when LiH (see Fig. 3.3) reacts with lithium amide ($LiNH_2$) by thoroughly mixing the substances, hydrogen is released at temperatures around 423 K, with formation of lithium imide (Li_2NH) or Li-rich imide (Li_xNH_{3-X}) and lithium nitride (Li_3N) depending on the temperature and molar ratio of ($LiH/LiNH_2$) according to the following schemes:

- Below 593 K: $LiH\,(s) + LiNH_2\,(s) \rightarrow 2H_2\,(g) + Li_2NH\,(s)$ (3.6)

$2LiH\,(s) + LiNH_2\,(s) \rightarrow (x\text{-}1)\,H_2\,(g) + Li_xNH_{3-X}\,(s) + (3\text{-}x)\,LiH(s)$ (3.7)

- At higher temperatures: $2LiH\,(s) + LiNH_2\,(s) \rightarrow H_2\,(g) + Li_3N\,(s)$ (3.8)

From a detailed analysis of high-resolution synchrotron x-ray diffraction data for the lithium amide ($LiNH_2$) - lithium imide (Li_2NH) hydrogen storage system (David et al., 2007), the authors were able to propose an alternative mechanism that does not need to have the materials mechanically milled to enhance mixing, as previously recognized by Chen and collaborators (Chen et al., 2003) as essential.

The mechanism they propose for the transformation between lithium amide and lithium imide during hydrogen cycling is a bulk reversible reaction that occurs in a non-stoichiometric manner within the cubic anti-fluorite-like Li-N-H structure, based on both Li^+ and H^+ mobility within the cubic lithium imide. Concluding that increasing the Li+

mobility and/or disorder it is likely to improve the hydrogen cycling in this and related Li-based systems. Recently, further systematical evaluation of the decompositions of $LiNH_2$ and Li_2NH was carried out by Zhang and Hu (Zhang & Hu, 2011), who also examined the effect of Cl^- anion on the decomposition process. Cl^- is widely employed as a promoter to improve various catalysts. As a result, decomposition mechanisms were established.

The decomposition of $LiNH_2$ producing Li_2NH and NH_3 occurs in two steps at the temperature range of 573-723 K. $LiNH_2$ decomposes into a stable intermediate species ($Li_{1.5}NH_{1.5}$) and then into Li_2NH. Furthermore, Li_2NH is decomposed into Li, H_2, and N_2 without formation of Li_3N at the temperature range of 823-1023 K. The introduction of Cl^- can decrease the decomposition *temperature of Li_2NH by about 110 K.*

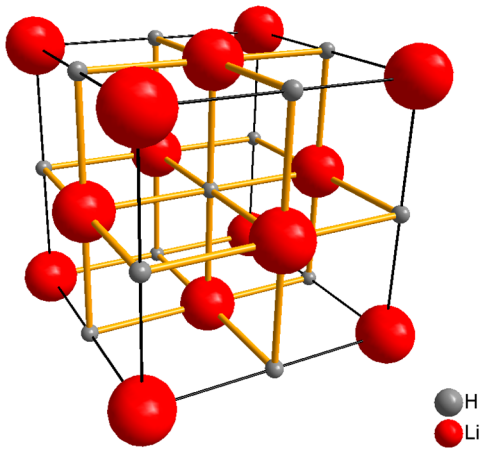

Fig. 3.3 Crystal structure of lithium hydride.

3.7 Neutron techniques associated with hydrogen solid storage

Though some progresses have been made, the state-of-art materials are still far from meeting the aimed targets for hydrogen solid storage material (Churchard et al., 2011). This huge task can be facilitated by employing state-of-the-art techniques like, computational first-principles calculations to evaluate the thermodynamic properties of the potential materials (Alapati et al., 2007; Siegel et al., 2007; Yang et al., 2007). This allows a quick screen of a large number of potential candidates, searching for thermodynamically suitable ones (saving time and money).

Once thermodynamic appropriate materials have been found other considerations such as structure and dynamics of the materials during hydrogenation/dehydrogenation will

become crucial in order to understand the fundamental properties of hydrogen storage, in realistic conditions and hence design new hydrogen storage materials.

Neutron scattering techniques are highly suitable for structure and dynamics studies related to hydrogen in solids and bound on surfaces. The energy distribution of thermal neutrons is nearly ideal for the study of condensed matter in general because it is of the same order of magnitude as most molecular and lattice excitations and the de Broglie wavelengths of thermal neutrons match quite well with interatomic distances in most solids (Squires, 1978).

Neutrons have some unique advantages over photons and electrons as scattering media which are of particular use for the analysis of hydrides. For these purposes the two most useful neutron scattering interactions are coherent elastic scattering for Neutron Diffraction (ND) and incoherent inelastic scattering (INS) to measure vibrational density of states.

The distinction of coherent and incoherent scattering interactions is important to the unique advantages offered by ND and INS respectively. This is because the relative scattering intensity of a given interaction is dependent highly upon the nucleus involved, and as such is isotope dependant. Each isotope has a different scattering cross section for both coherent (σ_{coh}) and incoherent (σ_{inc}) interactions measured in barns (1 barn = 10^{-28} m^2).

In general these scattering cross sections do not follow any specific trend regarding nucleus size.

INS has numerous advantages to other common techniques of obtaining vibrational spectra such as infrared (IR) and Raman spectroscopy. INS spectroscopy is hyper sensitive to the presence of hydrogen. The protium (^1H) nucleus has respective scattering cross sections of σ_{coh} = 1.8 and σ_{inc} = 80.2 barns respectively. This means neutron scattering in materials containing natural abundance hydrogen is largely inelastic.

Additionally, the incoherent cross section of ^1H is one to two orders of magnitude higher than any other isotope (Ross, 2008). This means that in hydrides INS spectra are dominated by vibrational modes of hydrogen almost exclusively. This hyper sensitivity to hydrogen means that hydride phases are detectible even with present in miniscule relative concentration.

Another advantage of INS is the complete absence of selection rules for the excitation of vibrational modes. External modes (lattice modes, i.e. phonons) are excited with equal opportunity to molecular vibrations. Because both IR and Raman spectroscopy rely upon different types of charge symmetry interactions, a number of vibrational modes cannot be excited in the majority of solids and molecules. In particular lattice modes are far more easily observable in INS spectra than any other type of vibrational spectroscopy.

INS is also more useful for comparison with *ab initio* calculated density of states because relative excitation amplitudes are simply dependent upon the magnitude of motion and σ_{inc} of the excited nucleus (Squires, 1978; Ross, 2008). Free codes, such as a-Climax is available to generate a theoretical INS spectrum from the density of states output files from numerous common *ab initio* packages such as Gaussian, AbInit and Dmol (Ramirez, 2004).

For these reasons INS is extremely useful in identifying the presence of different hydride phases which may not be structurally apparent (for example, due to structural disorder). A good example is the INS study of Schimmel et al. on MgH_2 produced from Mg processed by high energy ball milling. Ball milling of Mg to reduce particle size, and introduce fractures, defects, and faults has a beneficial effect of increasing hydride formation rate, and reducing the temperature required for absorption. Comparison of the INS spectra of the MgH_2 produced from ball milled Mg with well-ordered MgH_2 revealed a partial composition of γ-MgH_2, which is metastable and normally exists only at high temperatures (Schimmel et al., 2005). Presence of γ-MgH_2 was indicative of internal stress from mechanical processing. However after hydrogen sorption cycling, γ-MgH_2 was no longer observable in the INS spectrum of the ball milled material, while the fast kinetics and low sorption temperature remained. In this way INS was indispensable in revealing that the particle size reduction is more significant in the role of lowering temperature and increasing sorption kinetics than the creation of faults and internal stresses after the high energy ball milling of Mg (Schimmel, 2005; Ross, 2008).

Neutron diffraction also provides some unique advantages versus more conventional diffraction methods such as X-ray diffraction (XRD). Elastic neutron and X-ray scattering are similar in that both result in interference patterns according to Bragg scattering conditions (Squires, 1978).

In XRD the intensity of a given Bragg reflection varies with the atomic number (Z) of the atom at the lattice site. This means that the exact position of hydrogen in a structure is practically impossible to determine with XRD. In ND the relative intensities of reflections

are independent of Z, and instead depend on the coherent scattering cross section (σ_{coh}). This means that deuterium (^2H; σ_{coh} = 5.6, σ_{inc} = 2.0) is just as readily observable as most metal atoms. This allows for the observation of hydride phase transitions which differ only by the hydrogen occupation sites, such as in interstitial hydrides.

ND also allows metals with similar Z values such as Ni (Z=28, σ_{coh} = 13.4) and Cu (Z=29, σ_{coh} = 7.5) to be easily distinguished, unlike in XRD. A great deal of caution must be taken to ensure that ^2H is not displaced by ^1H during sample preparation and handling, as the large σ_{inc} of ^1H will create a substantial background signal.

Another advantage of ND is that intensity does not diminish greatly with scattering angle as it does in XRD (Massa, 2004). Beyond these differences, crystal structure determination techniques are very similar for ND and XRD. Common approaches include a combination of a structure solution method and the Rietveld refinement method.

ND and INS carry some common advantages and disadvantages intrinsic with the use of neutrons as a scattering medium. Common advantages are associated with the highly penetrating quality of neutron radiation through most materials. This provides some possibilities for variable depth of measurements. If the neutron beam is directed at a relatively thin portion of the sample, a greater quantity of surface and shallow depth material is surveyed, whereas in relatively thick segments predominantly material deep within the sample is surveyed. The high penetration of neutrons also allows for relatively clear in-situ measurements in a wide range of sample environments such as high pressure gas cells, furnaces, cryogenic refrigerators, anvil cells and other environments requiring obtrusive equipment. This allows for detailed structure and dynamics studies of metastable hydride phases, and phase transitions which occur only in extreme conditions.

There are numerous inconveniences associated with neutrons as well. The most prevalent and obvious is the relative scarcity and cost of neutron sources, which typically take two forms: a research reactor or a spallation source (fed by a high energy proton accelerator).

Another drawback is the time required to conduct a measurement, which can range from hours to days (per measurement). This is due to the short range of nuclear forces and relatively low probability of a scattering event, which is the same reason neutron radiation penetrates so effectively. For these reasons beam time is allocated very carefully at neutron sources, and flight paths are rarely left idle during neutron production.

ND and INS require larger sample sizes, often multiple grams, to increase the scatting rate.

3.8 Hydrides of Cu and Mg intermetallic systems

We have studied the Cu-Li-Mg system as a hydrogen storage system and, at the same time, as a catalyst of the hydrogen storage process, namely for the Ti/TiH_2 system (Braga & Malheiros, 2007a, 2007b; Braga et al., 2010a, 2010b).

The only ternary compound the Cu-Li-Mg system holds is $CuLi_xMg_{2-x}$ (x = 0.08) with hexagonal $P6_222$ structure (Braga et al., 2010c). Since the phase diagrams of Cu-Mg and Ni-Mg are similar (see Fig. 3.4), and Cu and Ni have similar electron affinities, it was thought in the sixties that $CuMg_2$ would store hydrogen, too.

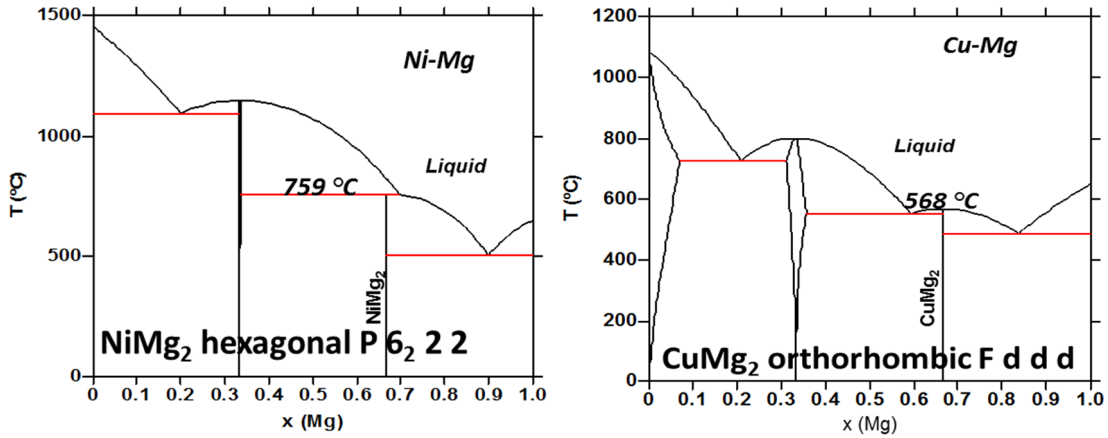

Fig. 3.4 Phase diagrams of Ni-Mg and Cu-Mg (Ansara et al., 1998)

However this is not the case (Reilly & Wiswall, 1967). $NiMg_2$ has a hexagonal structure ($P6_222$), but $CuMg_2$ has an orthorhombic structure (Fddd), and this structural difference is assumed to be the reason that $NiMg_2$ stores H_2 forming a hydride, but $CuMg_2$ does not. $CuMg_2$ decomposes into Cu_2Mg and MgH_2 (Reilly & Wiswall, 1967) upon hydrogen loading as previously referred (3.4). As a result of this reaction and since $CuMg_2$ does not form a hydride, $CuMg_2$ was abandoned as a candidate material for hydrogen storage (Reilly & Wiswall, 1967; Schlapbach & Züttel, 2001) until the late destabilization studies that were previously cited. The hexagonal structure of $CuLi_xMg_{2-x}$, suggested the possibility of using this phase as a hydrogen storage material (Braga & Malheiros, 2007a, 2007b) because $CuLi_xMg_{2-x}$ has the same space group ($P6_222$) as $NiMg_2$ and $NiMg_2(H,D)_{0.3}$ (lattice parameters are almost identical: a = b = 0.5250 nm and c = 1.3621 nm (at 300 K) for $CuLi_xMg_{2-x}$ and a = b = 0.5256 nm and c = 1.3435 nm for $NiMg_2(H,D)_{0.3}$ (Senegas et al., 1984)). Therefore, we hypothesized that $CuLi_xMg_{2-x}$ (x = 0.08) would be a hydrogen storage material, just like $NiMg_2$ - a hypothesis that has been confirmed by now (Braga & Malheiros, 2007a, 2007b; Braga et al., 2010a).

The change of the $CuMg_2$ orthorhombic (Fddd) structure to a hexagonal structure ($P6_222$) upon addition of a small amount of Li has been firmly established (Braga et al., 2007). Isostructural phases to $CuLi_xMg_{2-x}$ are the hexagonal phase $NiMg_2H_{0.24-0.30}$ and $NiMg_2$ (Senegas et al., 1984). For the NiMg-hydrides, several hydrogen positions were reported: In $NiMg_2H_{0.29}$ the hydrogen atoms occupy Wyckoff 6f positions and could occupy the interstitial Wyckoff 6h position (Senegas et al., 1984). Other possibilities would be that the H atoms would just occupy interstitial Wyckoff 12k position (in $NiMg_2H_{0.26}$) or the Wyckoff 12k and 6j positions in $NiMg_2H_{0.24}$ (Senegas et al., 1984). This suggests a number of possible sites for Li in $CuLi_xMg_{2-x}$.

Interestingly V. Hlukhyy and collaborators (Hlukhyy et al., 2005) have reported a result closely related to our observations in the Sn-doped Ni-Mg system. These authors show that the synthesis of alloys in the Ni-Mg system is affected by the presence of small amounts of Sn (forming $NiMg_{2-x}Sn_x$ with x = 0.22 and 0.40). The replacement of Mg by Sn produces changes in the structure of $NiMg_2$, this time making the alloy change from the $NiMg_2$ type (hexagonal) to the $CuMg_2$ type (orthorhombic). While the structure of $NiMg_{1.85}Sn_{0.15}$ is still of $NiMg_2$ type, the structure of $NiMg_{1.78}Sn_{0.22}$ and $NiMg_{1.60}Sn_{0.40}$ is already of the $CuMg_2$ type. These results represent obviously the converse of our own observations in the $CuMg_2$ structure, and reaffirm our results with respect to $CuLi_xMg_{2-x}$.

3.9 The $CuLi_{0.08}Mg_{1.92}$ compound

We have used neutron diffraction to refine the composition of $CuLi_xMg_{2-x}$, site occupancies and lattice parameters at different temperatures. In Fig. 3.5, results from the Time-of-flight (TOF) Neutron Powder Diffractometer (NPDF) at the Los Alamos Neutron Scattering Center are shown. It was analyzed a sample containing 37.5 at.% of $CuLi_{0.08}Mg_{1.92}$, 45.1 at.% of $CuMg_2$ and 17.4 at.% of Cu_2Mg. The structure was refined using the General Structure Analysis System (GSAS), a Rietveld profile analysis code developed by A. C. Larson and R. B. von Dreele (Larson & von Dreele, 2004).

Furthermore, we've fitted the NPDF data using the Pair Distribution Function (PDF) in which G(r) was obtained via the Fourier Transform of the total diffraction pattern as indicated below:

$$G(r) = 4\pi r[\rho(r) - \rho_0] = \frac{2}{r}\int_0^\infty Q[S(Q)-1]\sin(Qr)dQ \qquad (3.9)$$

where $\rho(r)$ is the microscopic pair density, ρ_0 is the average atomic number density, and *r* the radial distance. Q is the momentum transfer ($Q = 4\pi\sin(\theta)/\lambda$). $S(Q)$ is the normalized structure function determined from the experimental diffraction intensity (Egami & Billinge, 2003). PDF yields the probability of finding pairs of atoms separated by a distance *r*. PDF fittings were performed using the code PDFgui (Farrow et al., 2007).

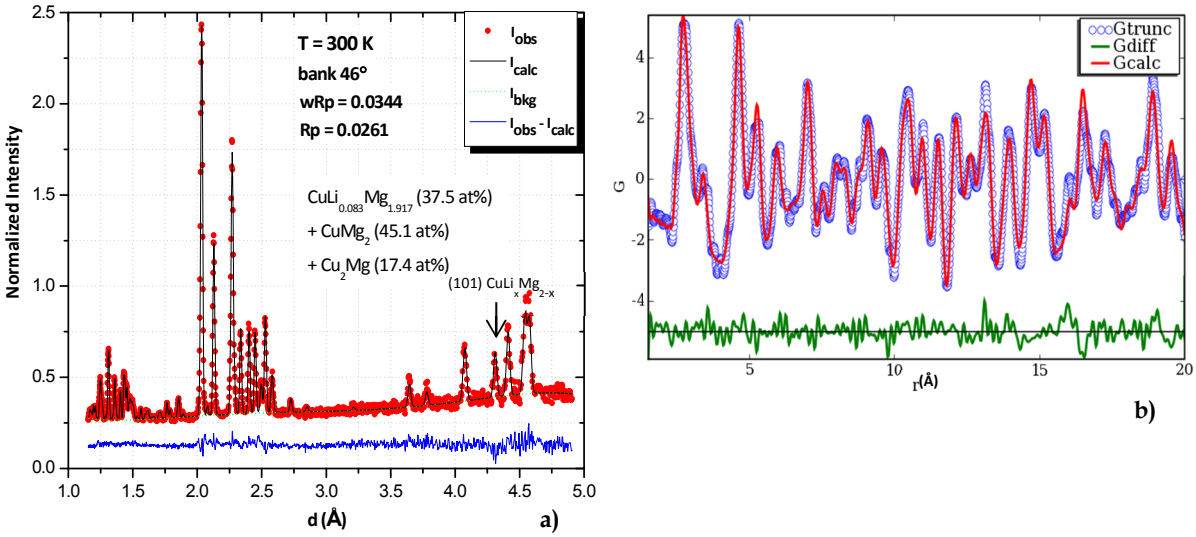

Fig. 3.5 a) Neutron diffraction pattern of a sample containing $CuLi_{0.08}Mg_{1.92}$, $CuMg_2$ and $CuMg_2$. The highlighted peak corresponds to the (101) reflection for the $CuLi_{0.08}Mg_{1.92}$ compound which is not overlapped by other phases. b) Pair Distribution Function (PDF) fitting for the same conditions of the pattern in a).

Besides Neutron Diffraction, we have used theoretical complementary methods to determine the stoichiometry of the $CuLi_xMg_{2-x}$ compound. We relied on the Density Functional Theory (DFT) (Hohenberg & Kohn, 1964) to calculate the structure that minimized the Electronic Energy at 0 K, without accounting for the zero point energy.

The latter energy gives us a good estimation of the Enthalpy of Formation at 0 K especially since we were relating data for stoichiometries that did not differ too much and for similar crystal structures. The results obtained are in close agreement with those obtained from ND after Rietveld refinement - $CuLi_xMg_{2-x}$ (x = 0.08).

Nonetheless, no conclusions about Li site occupancies could be drawn from the use of the referred means. DFT shows that there isn't a clear preference, in terms of energy, for the different Li site occupancies. Then again, a technique that gives information about the average site occupancies - like the Rietveld refinement - is also inadequate to clarify this

problem; therefore we have used PDF to determine Li preferred sites. With PDF fittings we were allowed to go further (see Fig. 3.5b). PDF does not see the average but the local structure and with PDF, all results but those in which Li would substitute Mg1 sites (1/2, 0, z), gave negative occupancies for Li. For Li substituting Mg1 we've obtained an average composition for $CuLi_xMg_{2-x}$ (x = 0.07) which is in agreement with the other obtained results. For further information please see (Braga et al., 2010c).

3.10 Hydrogen storage in the Cu-Li-Mg-H(D) system

To study the hydrogen storage in the Cu-Li-Mg system several techniques were used (Braga et al., 2010a). Besides absorption/desorption, Differential Scanning Calorimetry, Thermal Gravimetry Analysis (DSC/TGA), X-ray Diffraction (XRD) both at the laboratory and at the Synchrotron, we have used Neutron Diffraction and Inelastic Neutron Scattering. Owing to the low X-ray scattering power of hydrogen, neutron diffraction experiments on deuterides are necessary as previously highlighted in section 1.5.

Most atomic arrangements were determined on powders of different samples yet we have also used a bulk sample machined into a cylinder to obtain ND data in both the surface and the center of the sample during deuterium uptake.

The data were usually analyzed by the Rietveld method, yet in some cases in which the background was noisier we have used the biased method (Larson & von Dreele, 2004). For better convergence, the number of refined parameters in particular those of the atomic displacement amplitudes are reduced by constraints.

ND results obtained at HIPD at LANSCE, Los Alamos National Laboratory, for a sample initially containing 78 wt.% $CuLi_{0.08}Mg_{1.92}$ + 22 wt.%Cu_2Mg (from here on "initially containing" means before hydrogen/deuterium absorption) and that was deuterated *ex situ* at 473 K at P ≤ 5MPa in order to determine the crystal structure of the first deuteride phase formed in the sample (see Fig. 3.6 left). This pattern was refined using Rietveld's method.

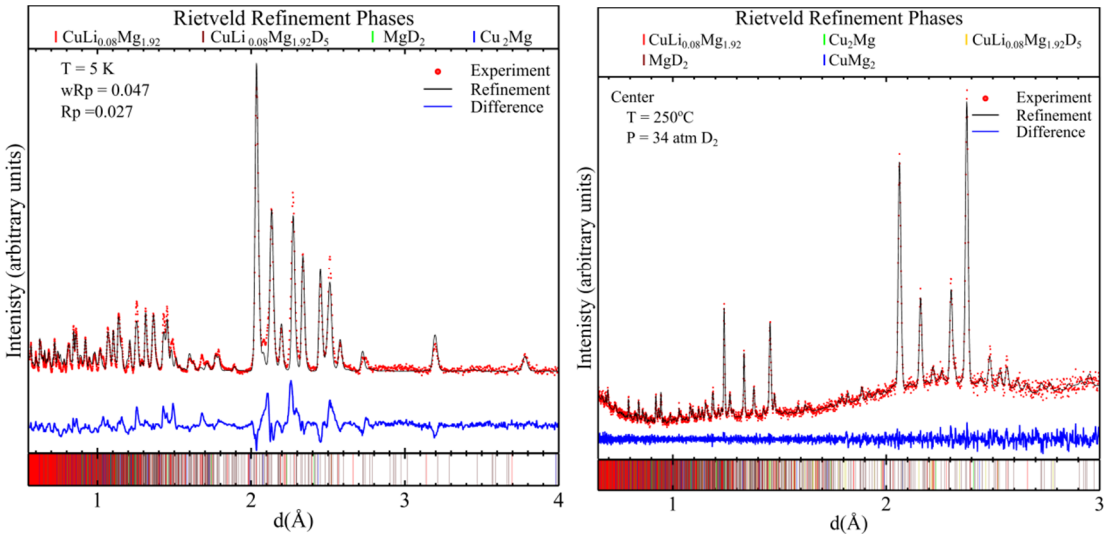

Fig. 3.6 (left) Rietveld refinement of a sample containing $CuLi_{0.08}Mg_{1.92}$, Cu_2Mg, MgD_2 and $CuLi_{0.08}Mg_{1.92}D_5$ obtained in HIPD. wRp and Rp are the reliability factors as defined in (Larson & von Dreele, 2004). (right) ND pattern of the center of a bulk cylinder sample containing $CuLi_{0.08}Mg_{1.92}$, Cu_2Mg, $CuMg_2$ obtained in SMARTS during an *in situ* reaction with D_2 at 523 K and ~3.4 MPa. Both patterns show experimental, refined and difference between experimental and calculated intensities.

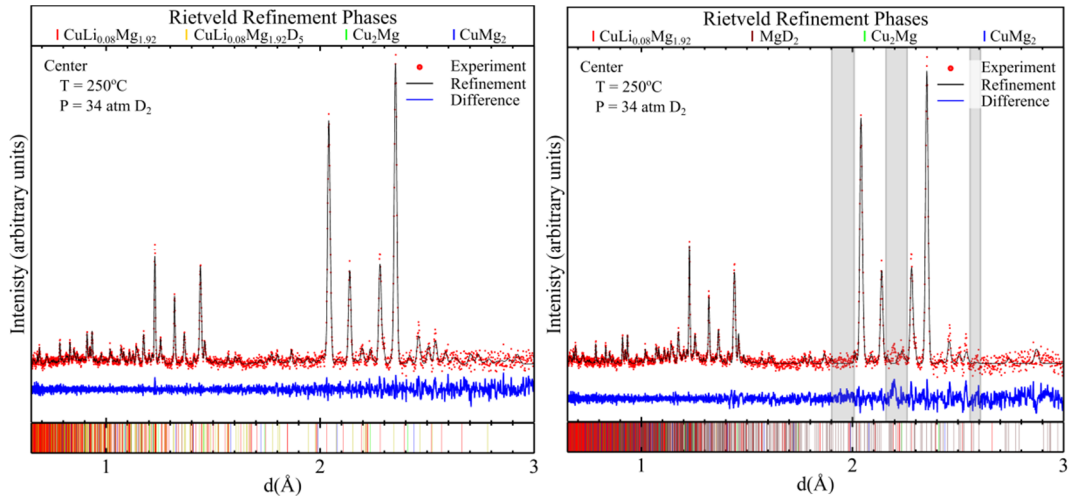

Fig. 3.7 (left and right) ND pattern of the surface of a bulk cylinder sample initially containing $CuLi_{0.08}Mg_{1.92}$, Cu_2Mg, and $CuMg_2$ obtained in SMARTS during an *in situ* reaction with D_2 at 523 K and ~3.4 MPa. (right) it is highlighted that MgD_2 cannot justify some existing peaks. Both patterns show experimental, refined and difference between experimental and calculated intensities.

The $CuLi_{0.08}Mg_{1.92}D_5$ crystal structure was determined to be monoclinic P121, with a = 1.514 nm., b = 0.688 nm, c = 0.555 nm and β = 91.73° according to the formula $CuLi_{0.08}Mg_{1.92}D_5 = 0.5(Mg_3^{2+}.[CuH_4]_2^{3-}.MgD_2)$ corresponding to 4.4 wt% D per formula unit. $CuLi_{0.08}Mg_{1.92}D_5$ is the first deuteride/hydride to be formed. This result is interesting by itself, but the presence of MgD_2 in the diffraction pattern, highlights even further the possibilities of applications of this compound. According to these results, it can be obtained $MgH(D)_2$ from a sample that did not contain "free" Mg or $CuMg_2$. Furthermore, the deuteration process occurred at 473 K, which is considerably lower than the hydrogen absorption temperature reported for $CuMg_2$ (3.4) (Reilly & Wiswall, 1967).

The experiments with the bulk sample at SMARTS, LANSCE, Los Alamos National Laboratory, show that before MgD_2 is observed, $CuLi_{0.08}Mg_{1.92}D_5$ is already distinguishable at the surface even in a sample that initially contained $CuMg_2$ (see Fig. 3.7). Therefore, it seems that $CuLi_{0.08}Mg_{1.92}D_5$ will have a catalytic and destabilizing roll that was additionally observed with the Ti/TiH_2 systems (Braga et al., 2010b).

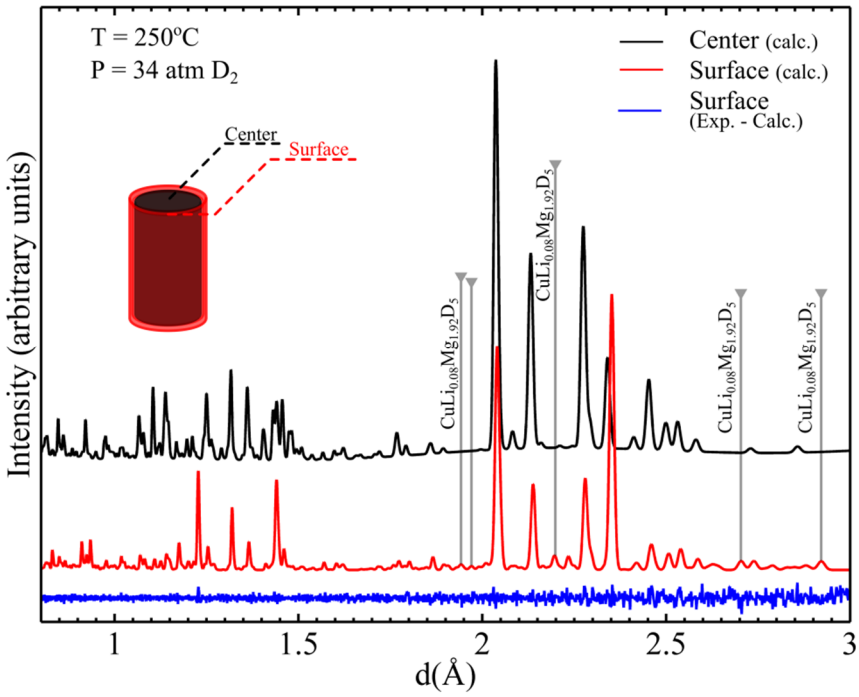

Fig. 3.8 ND refined pattern of the center and surface of a bulk cylinder sample initially containing $CuLi_{0.08}Mg_{1.92}$, Cu_2Mg, and $CuMg_2$ obtained in SMARTS during an *in situ* reaction with D_2 at 523 K and ~3.4 MPa. Besides the texture effect that might be present in a bulk sample, it seems that the center initially contained more $CuLi_{0.08}Mg_{1.92}$ than the surface.

Experimental information about the metal–hydrogen interactions can be obtained by measuring lattice vibrations via INS, as previously highlighted in section 3.5.

Because of the large difference between the masses of metal and H atoms in transition-metal–hydrogen systems, the acoustic dispersion branches of the phonon spectra can be attributed to the motion of the metal atoms, the optic branches to the vibrations of the light H atoms relative to the metal lattice. The densities of states of optic phonons typically show a pronounced maximum at the energy of the lattice vibrations at the Γ point in the center of the phonon Brillouin zone ($\boldsymbol{q}$ = 0) e.g. in (Fukay, 1993). These phonon modes describe the vibration of the undistorted H sublattice relative to the rigid metal sublattice. Hence, they contain the metal–hydrogen interaction only.

This is usually stronger than the H–H interaction, which leads to the dispersion of the optic branches. In the limit of very low H concentrations, the H vibrations can be imagined as independent vibrations of local Einstein oscillators at interstitial H sites. For both the lattice vibrations at the Γ point and the local vibrations, one can observe transitions from the ground state, the quantum-mechanical zero-point vibration of the H atoms, to the first excited states, e.g. by measuring optic phonon excitations, and transitions to higher excited states.

Their energies, intensities and symmetry splittings yield an insight into the shapes of the potential and the wavefunctions for the vibrations of the light particles (Elsasser et al., 1998).

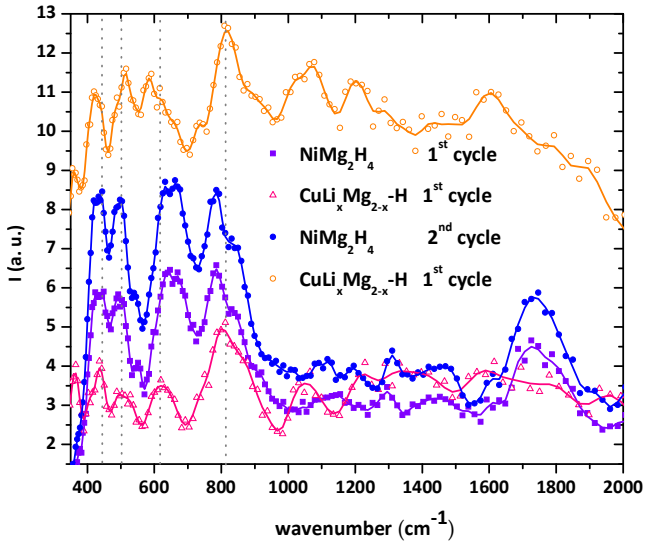

Fig. 3.9 INS spectra for $NiMg_2H_4$ (1st and 2nd hydrogenation cycles) and for two samples containing $CuLi_{0.08}Mg_{1.92}$ (triangles correspond to a sample also contained Cu_2Mg and the circles correspond to sample that contained Cu_2Mg and $CuMg_2$ as well). All samples show the formation of a similar monoclinic structure. As in $NiMg_2H_4$, in which Ni is bonded to four atoms of H forming the tetrahedral complex $[NiH_4]^{4-}$, Cu is also bonded to four atoms

of H forming the tetrahedral complex $[CuH_4]^{3-}$, which was previously referred on (Yvon & Renaudin, 2005).

We have measured samples of the Cu-Li-Mg-H system by means of INS at FDS, LANSCE, Los Alamos National Laboratory. There is no doubt about the sequence of events; first there is the formation of $CuLi_{0.08}Mg_{1.92}H_5$ (see Fig. 3.9) and then in subsequent cycles the formation of MgH_2, either for disproportionation of $CuLi_{0.08}Mg_{1.92}H_5$ or from hydrogenation of $CuMg_2$.

DSC/TGA experiments show that $CuLi_{0.08}Mg_{1.92}H_5$ starts desorbing hydrogen at 313 K to 328 K. In this range of temperatures the sample can release up to 1.3 wt.% (results for a isothermal experiment with a sample initially containing approximately 78 wt.% of $CuLi_{0.08}Mg_{1.92}$ and 22 wt.% of Cu_2Mg - which does not absorb hydrogen at the temperature and pressure that were used). In Fig. 3.10 it can be seen that 0.5 wt.% of a sample initially containing 61 wt.% of $CuLi_{0.08}Mg_{1.92}$, 23 wt.% of $CuMg_2$ and 16 wt.% of Cu_2Mg can be released at T < 350 K.

In spite of the fact that there was some visible oxidation during this run, we think it was worth showing this initial desorption. This initial desorption seems to be due to $CuLi_{0.08}Mg_{1.92}H_5$. At ~473 K, hydrogen starts to be desorbed at a different rate, probably due to the disproportionation of $CuLi_{0.08}Mg_{1.92}H_5$, with the formation of MgH_2, which will start releasing hydrogen at 553-573 K.

Additionally, MgH_2 can be formed upon hydrogenation of $CuMg_2$.

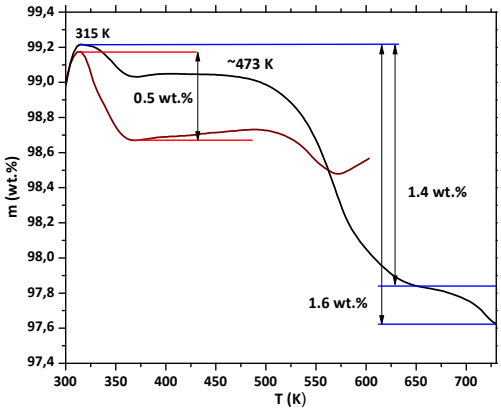

Fig. 3.10 TGA of two samples initially containing approximately 61 wt.% of $CuLi_{0.08}Mg_{1.92}$, 23 wt.% of $CuMg_2$ and 16 wt.% of Cu_2Mg. Samples were measured after hydrogenation but they are not expected to be saturated in hydrogen prior to the experiment (this figure refers to the same sample composition, where the lower curve seems to have oxidized).

The DSC/TGA results show that the system containing $CuLi_{0.08}Mg_{1.92}$ and Cu_2Mg can destabilize MgH_2 in a more efficient way than Cu_2Mg by itself can. In fact, in a DSC experiment in which kinetics must be accounted for, MgH_2 will release hydrogen at 553-573 K, which can only be obtained when particles are reduced to nanopowders.

3.11 Conclusion

The hydrogen storage world still offers a considerable amount of challenges since no universal solution has been found. Eventually, different solutions will be found to suite different applications.

The Cu-Li-Mg system provides other possibilities for catalytic and destabilization effects yet not fully explored.

There are several techniques that can be employed to study systems containing hydrogen. Nonetheless, Neutron Scattering is a very useful resource, in particular, Neutron Diffraction. In the latter, crystal structure of deuteride phases are directly studied since deuterium can be detected by ND and more accurate results can be obtained either in *ex situ* and *in situ* as shown previously.

3.12 References

Aguey-Zinsou, K. & Ares-Fernández, J. (2010). Hydrogen in magnesium: new perspectives toward functional stores. Energy & Environmental Science, Vol. 3, No. 5, pp. 526-543, ISSN 1754-5706

Alapati, S., Johnson, J. & Sholl, D. (2007). Using first principles calculations to identify new destabilized metal hydride reactions for reversible hydrogen storage. Physical Chemistry Chemical Physics, Vol. 9, No. 12, pp. 1438-1452, ISSN 1463-9084

Andreasen, A., Sørensen, M., Burkarl, R., Møller, B., Molenbroek, A., Pedersen, A., Vegge, T. & Jensen, T. (2006). Dehydrogenation kinetics of air-exposed MgH_2/Mg_2Cu and $MgH_2/MgCu_2$ studied with in situ X-ray powder diffraction. Applied Physics A, Vol. 82, No. 3, pp. 515-521, ISSN 1432-0630

Ansara, I., Dinsdale, A. & Rand, M. (Ed(s)). (1998). COST 507, Thermochemical database for light metal alloys, Vol. 2, pp. 170-174, Office for Official Publications of the European Communities, ISBN 92-828-3902-8, Luxembourg

Beattie, S., Setthanan, U. & McGrady, G. (2011). Thermal desorption of hydrogen from magnesium hydride (MgH2): An in situ microscopy study by environmental SEM and TEM. International Journal of Hydrogen Energy, Vol. 36, No. 10, pp. 6014-6021, ISSN 0360-3199

Bösenberg, U., Ravnsbæk, D., Hagemann, H., D'Anna, V., Minella, B., Pistidda, C., Beek, W., Jensen, T., Bormann, R. & Dornheim, M. (2010). Pressure and Temperature Influence on the Desorption Pathway of the $LiBH_4$–MgH_2 Composite System. The Journal of Physical Chemistry C, Vol. 114, No. 35, pp. 15212-15217, ISSN 1932-7455

Braga, M., Acatrinei, A., Hartl, M., Vogel, S., Proffen, T. & Daemen, L. (2010a). New Promising Hydride Based on the Cu-Li-Mg system. Journal of Physics: Conference Series, Vol. 251, pp. 012040 [4 pages], ISSN 1742-6596

Braga, M., Wolverton, M., Llobet, A. & Daemen, L. (2010b). Neutron Scattering to Characterize Cu/Mg(Li) Destabilized Hydrogen Storage Materials. Materials Research Society Symposium Proceedings, Vol. 1262, pp. 1262-W03-05, ISSN 0272-9172

Braga, M., Ferreira, J., Siewenie, J., Proffen, Th., Vogel, S. & Daemen, L. (2010c). Neutron powder diffraction and first-principles computational studies of $CuLi_xMg_{2-x}$ ($x \cong 0{,}08$), $CuMg_2$, and Cu_2Mg. Journal of Solid State Chemistry, Vol. 183, No. 1, pp. 10-19, ISSN 0022-4596

Braga, M. & Malheiros, L. (2007a). $CuMg_{2-Y}Li_X$ alloy for hydrogen storage. International patent, WO 2007046017 (A1)

Braga, M. & Malheiros, L. (2007b). $CuMg_{2-Y}Li_X$ alloy for hydrogen storage. National patent, PT 103368 (A)

Braga, M., Ferreira, J. & Malheiros, L. (2007). A ternary phase in Cu–Li–Mg system. Journal of Alloys and Compounds, Vol. 436, No. 1-2, pp. 278-284, ISSN 0925-8388

Cermak, J. & David, B. (2011). Catalytic effect of Ni, Mg_2Ni and Mg_2NiH_4 upon hydrogen desorption from MgH_2. International Journal of Hydrogen Energy, Vol. 36, No. 21, pp. 13614-13620, ISSN 0360-3199

Chen, P. & Zhu, M. (2008). Recent progress in hydrogen storage. Materials Today, Vol. 11, No. 12, pp. 36-43, ISSN 1369-7021

Chen, P., Xiong, Z., Luo, J., Lin, J. & Tan, K. (2003). Interaction between lithium amide and lithium hydride. The Journal of Physical Chemistry B, Vol. 107, No. 37, pp. 10967-10970, ISSN 1520-5207

Choi, Y., Hu, J., Sohn, H. & Fang, Z. (2008). Hydrogen storage properties of the Mg–Ti–H system prepared by high-energy–high-pressure reactive milling. Journal of Power Sources, Vol. 180, No. 1, pp. 491-497, ISSN 0378-7753

Churchard, A., Banach, E., Borgschulte, A., Caputo, R., Chen, J., Clary, D., Fijalkowski, K., Geerlings, H., Genova, R., Grochala, W., Jaroń, T., Juanes-Marcos, J., Kasemo, B., Kroes, G., Ljubić, I., Naujoks, N., Nørskov, J., Olsen, R., Pendolino, F., Remhof, A., Románszki, L., Tekin, A., Vegge, T., Zäch, M., & Züttelc, A. (2011). A multifaceted approach to hydrogen storage. Physical Chemistry Chemical Physics, Vol. 13, No. 38, pp. 16955-16972, ISSN 1463-9084

Cui, S., Feng, W., Hu, H., Feng, Z. & Wang, Y. (2008). Structural phase transitions in MgH_2 under high pressure. Solid State Communications, Vol. 148, No. 9-10, pp. 403-405, ISSN 0038-1098

David, W., Jones, M., Gregory, D., Jewell, C., Walton, A. & Edwards, P. (2007). A mechanism for non-stoichiometry in the lithium amide/lithium imide hydrogen storage reaction. Journal of the American Chemical Society, Vol. 129, No. 6, pp. 1594-1601, ISSN 0002-7863

Egami, T. & Billinge, S. (2003). Underneath the Bragg-Peaks: Structural Analysis of Complex Materials (First edition), Pergamon Press, Elsevier Ltd, ISBN 0-08-042698-0, Amsterdam

Elsasser, C., Krimmel, H., Fahnle, M., Louie, S. & Chan, C. (1998). Ab initio study of iron and iron hydride: III. Vibrational states of H isotopes in Fe, Cr and Ni. Journal of Physics: Condensed Matter, Vol. 10, No. 23, pp. 5131 [16 pages], ISSN 0953-8984

European Commission (2003). World energy, technology and climate policy outlook 2030 —WETO, in: Directorate-General for Research Energy, EUR 20366, Available from: http://ec.europa.eu/research/energy/pdf/weto_final_report.pdf

Farrow, C., Juhas, P., Liu, J., Bryndin, D., Božin, E., Bloch, J., Proffen, T. & Billinge, S. (2007). PDFfit2 and PDFgui: computer programs for studying nanostructure in crystals. Journal of Physics: Condensed Matter, Vol. 19, No. 33, pp. 335219 [7 pages], ISSN 0953-8984

Felderhoff, M., Weidenthaler, C., von Helmoltb, R. & Eberleb, U. (2009). Hydrogen storage: the remaining scientific and technological challenges. Physical Chemistry Chemical Physics, Vol. 9, No. 21, pp. 2643-2653, ISSN 1463-9084

Fernández, A., Deprez, E. & Friedrichs, O. (2011). A comparative study of the role of additive in the MgH_2 vs. the $LiBH_4$–MgH_2 hydrogen storage system. International Journal of Hydrogen Energy, Vol. 36, No. 6, pp. 3932-3940, ISSN 0360-3199

Fukai, Y. (1993). The Metal-Hydrogen System: Basic Bulk Properties (First edition), Springer-Verlag, ISBN 3540-556370, Berlin

Grochala, W. & Edwards, P. (2004). Thermal Decomposition of the Non-Interstitial Hydrides for the Storage and Production of Hydrogen. Chemical Reviews, Vol. 104, No. 3, pp. 1283-1315, ISSN 0009-2665

Hlukhyy, V., Rodewald, U. & Pöttgen, R. (2005). Magnesium-Tin Substitution in $NiMg_2$. Zeitschrift für anorganische und allgemeine Chemie, Vol. 631, No. 15, pp. 2997–3001, ISSN 1521-3749

Hohenberg, P. & Kohn, W. (1964). Inhomogeneous Electron Gas. Physical Review B, Vol. 136, No. 3B, pp. B864-B871, ISSN 1098-0121

Hong, S., Bae, J., Kwon, S. & Song, M. (2011). Hydrogen storage properties of Mg-23.5Ni-xCu prepared by rapid solidification process and crystallization heat treatment. International Journal of Hydrogen Energy, Vol. 36, No. 3, pp. 2170-2176, ISSN 0360-3199

Hsu, F., Hsu, C., Chang, J., Lin, C., Lee, S. & Jiang, C. (2010). Structure and hydrogen storage properties of $Mg_2Cu_{1-x}Ni_x$ (x = 0–1) alloys. International Journal of Hydrogen Energy, Vol. 35, No. 24, pp. 13247-13254, ISSN 0360-3199

Huot, J., Liang, G., Boily, S., Neste, A. & Schulz, R. (1999). Structural study and hydrogen sorption kinetics of ball-milled magnesium hydride. Journal of Alloys and Compounds, Vol. 293-295, pp. 495-500, ISSN 0925-8388

Jain, I., Lal, C. & Jain, A. (2010). Hydrogen storage in Mg: A most promising material. International Journal of Hydrogen Energy, Vol. 35, No. 10, pp. 5133-5144, ISSN 0360-3199

Jain, I. (2009). Hydrogen the fuel for 21st century. International Journal of Hydrogen Energy, Vol. 34, No. 17, pp. 7368-7378, ISSN 0360-3199

Jeon, K., Moon, H., Ruminski, A., Jiang, B., Kisielowski, C., Bardhan, R. & Urban, J. (2011). Air-stable magnesium nanocomposites provide rapid and high-capacity hydrogen storage without using heavy-metal catalysts. Nature Materials, Vol. 10, No. 4, pp. 286-290, ISSN 1476-4660

Jurczyk, M., Nowak, M., Szajek, A. & Jezierski, A. (2011). Hydrogen storage by Mg-based nanocomposites. International Journal of Hydrogen Energy, (In press - available online 27 April 2011), ISSN 0360-3199

Jurczyk, M., Okonska, I., Iwasieczko, W., Jankowska, E. & Drulis H. (2007). Thermodynamic and electrochemical properties of nanocrystalline Mg_2Cu-type hydrogen storage materials. Journal of Alloys and Compounds, Vol. 429, No. 1-2, pp. 316-320, ISSN 0925-8388

Kalinichenka, S., Röntzsch, L., Riedl, T., Gemming, T., Weißgärber, T. & Kieback, B. (2011). Microstructure and hydrogen storage properties of melt-spun Mg–Cu–Ni–Y alloys. International Journal of Hydrogen Energy, Vol. 36, No. 2, pp. 1592-1600, ISSN 0360-3199

Larson, A., von Dreele, R. (2004). GSAS Generalized Structure Analysis System, LANSCE, Los Alamos.

Massa, W. (2008). Crystal Structure determination. Springer-Verlag, Berlin Heidelberg. ISBN 978-3540206446

Milanese, J., Girella, A., Garroni, S., Bruni, G., Berbenni, V., Matteazzi, P. & Marini, A. (2010a). Effect of C (graphite) doping on the H_2 sorption performance of the Mg–Ni storage system. International Journal of Hydrogen Energy, Vol. 35, No. 3, pp. 1285-1295, ISSN 0360-3199

Milanese, C., Girella, A., Bruni, G., Cofrancesco, P., Berbenni, V., Matteazzi, P. & Marini, A. (2010b). Mg-Ni-Cu mixtures for hydrogen storage: A kinetic study. Intermetallics, Vol. 18, No. 2, pp. 203-211, ISSN 0966-9795

Milanese, C., Girella, A., Bruni, G., Cofrancesco, P., Berbenni, V., Villa, M., Matteazzi, P. & Marini, A. (2008). Reactivity and hydrogen storage performances of magnesium–nickel–copper ternary mixtures prepared by reactive mechanical grinding. International Journal of Hydrogen Energy, Vol. 33, No. 17, pp. 4593-4606, ISSN 0360-3199

Noritake, T., Towata, S., Aoki, M., Seno, Y., Hirose, Y., Nishibori, E., Takata, M. & Sakata, M. (2003). Charge density measurement in MgH_2 by synchrotron X-ray diffraction. Journal of Alloys and Compounds, Vol. 356-357, pp. 84-86, ISSN 0925-8388

Orimo, S. & Fujii, H. (2001). Materials science of Mg-Ni-based new hydrides. Applied Physics A, Vol. 72, No. 2, pp. 167-186, ISSN 1432-0630

Ramirez-Cuesta, A. (2004). aCLIMAX 4.0. 1, The new version of the software for analyzing and interpreting INS spectra. Computer Physics Communications. Vol. 157, No. 3, pp. 226-238.

Ravindran, P., Vajeeston, P., Fjellvåg, H. & Kjekshus, A. (2004). Chemical-bonding and high-pressure studies on hydrogen-storage materials. Computational Materials Science, Vol. 30, No. 3-4, pp. 349-357, ISSN 0927-0256

Reilly, J. & Wiswall, R. (1967). The Reaction of Hydrogen with Alloys of Magnesium and Copper. Inorganic chemistry, Vol. 6, No. 12, pp. 2220-2223, ISSN 0020-1669

Reilly, J. & Wiswall, R. (1968). The Reaction of Hydrogen with Alloys of Magnesium and Nickel and the Formation of Mg_2NiH_4. Inorganic chemistry, Vol. 7, No. 11, pp. 2254-2256, ISSN 0020-1669

Reule, H., Hirscher, M., Weißhardt, A. & Kronmüller, H. (2000). Hydrogen desorption properties of mechanically alloyed MgH_2 composite materials. Journal of Alloys and Compounds, Vol. 305, No. 1-2, pp. 246-252, ISSN 0925-8388

Ross, D. (2008). Neutron scattering studies for analysing solid state hydrogen storage, in: Solid State Hydrogen Storage Materials and Chemistry Walker, G. Ed. CRC Woodhead Publishing: Cambridge, England, pp. 135-172. ISBN 9781845692704

Rude, L., Nielsen, T., Ravnsbæk, D., Bösenberg, U., Ley, M., Richter, B., Arnbjerg, L., Dornheim, M., Filinchuk, Y., Besenbacher, F. & Jensen, T. (2011). Tailoring properties of borohydrides for hydrogen storage: A review. Physica Status Solidi A, Vol. 208, No. 8, pp. 1754-1773, ISSN 1862-6300

Sabitu, S., Gallo, G. & Goudy, A. (2010). Effect of TiH_2 and Mg_2Ni additives on the hydrogen storage properties of magnesium hydride. Journal of Alloys and Compounds, Vol. 499, No. 1, pp. 35-38, ISSN 0925-8388

Schimmel, H., Huot, J., Chapon, L., Tichelaar, F. & Mulder, F. (2005). Hydrogen Cycling of Niobium and Vanadium Catalyzed Nanostructured Magnesium. Journal of the American Chemical Society, Vol. 127, No. 41, pp. 1438-14354, ISSN 0002-7863

Schlapbach, L. & Züttel, A. (2001). Hydrogen-storage materials for mobile applications. Nature, Vol. 414, pp. 353-358, ISSN 0028-0836

Senegas, J., Mikou, A., Pezat, M. & Darriet, B. (1984). Localisation et diffusion de l'hydrogene dans le systeme Mg_2Ni-H_2: Etude par RMN de $Mg_2NiH_{0,3}$ et Mg_2NiH_4. Journal of Solid State Chemistry, Vol. 52, No. 1, pp. 1-11, ISSN 0022-4596

Setten, M., Wijs, G. & Brocks, G. (2007). Ab initio study of the effects of transition metal doping of Mg_2NiH_4. Physical Review B, Vol. 76, pp. 075125 [8 pages], ISSN 1098-0121

Siegel, D., Wolverton, C. & Ozoliņš, V. (2007). Thermodynamic guidelines for the prediction of hydrogen storage reactions and their application to destabilized hydride mixtures. Physical Review B, Vol. 76, No. 13, pp. 134102 [6 pages], ISSN 1098-0121

Simičić, M., Zdujić, M., Dimitrijević, R., Nikolić-Bujanović, L. & Popović N.(2006). Hydrogen absorption and electrochemical properties of Mg_2Ni-type alloys synthesized by mechanical alloying. Journal of Power Sources, Vol. 158, No. 1, pp. 730-734, ISSN 0378-7753

Sohn, H. & Emami, S. (2011). Kinetics of dehydrogenation of the Mg–Ti–H hydrogen storage system. International Journal of Hydrogen Energy, Vol. 36, No. 14, (July 2011), pp. 8344-8350, ISSN 0360-3199

Squires, G. (1978). Introduction to the theory of Thermal Neutron Scattering. Dover Publications Inc., Mineola, New York, ISBN 978-0486694474

Suryanarayana, C. (2008). Recent developments in mechanical alloying. Reviews on Advanced Materials Science, Vol. 18, No. 3, pp. 203-211, ISSN 1605-8127

Tan, Z., Chiu, C., Heilweil, E. & Bendersky, L. (2011a). Thermodynamics, kinetics and microstructural evolution during hydrogenation of iron-doped magnesium thin films. International Journal of Hydrogen Energy, Vol. 36, No. 16, pp. 9702-9713, ISSN 0360-3199

Tan, X., Danaie, M., Kalisvaart, W. & Mitlin, D. (2011b). The influence of Cu substitution on the hydrogen sorption properties of magnesium rich Mg-Ni films. International Journal of Hydrogen Energy, Vol. 36, No. 3, pp. 2154-2164, ISSN 0360-3199

Vajo, J. (2011). Influence of nano-confinement on the thermodynamics and dehydrogenation kinetics of metal hydrides. Current Opinion in Solid State & Materials Science, Vol. 15, No. 2, pp. 52-61, ISSN 1359-0286

Vajo, J. & Olson, G. (2007). Hydrogen storage in destabilized chemical systems. Scripta Materialia, Vol. 56, No. 10, pp. 829-834, ISSN 1359-6462

Vajo, J., Mertens, F., Ahn, C., Bowman Jr., R. & Fultz, B. (2004). Altering Hydrogen Storage Properties by Hydride Destabilization through Alloy Formation: LiH and MgH_2 Destabilized with Si. The Journal of Physical Chemistry B, Vol. 108, No. 37, pp. 13977-13983, ISSN 1520-5207

Vyas, D., Jain, P., Khan, J., Kulshrestha, V., Jain, A. & Jain, I. (2012). Effect of Cu catalyst on the hydrogenation and thermodynamic properties of Mg_2Ni. International Journal of Hydrogen Energy, Vol. 37, No. 4, pp. 3755-3760, ISSN 0360-3199

Xia, G., Leng, H., Xu, N., Li, Z., Wu, Z., Du, J. & Yu, X. (2011). Enhanced hydrogen storage properties of $LiBH_4$—MgH_2 composite by the catalytic effect of $MoCl_3$. International Journal of Hydrogen Energy, Vol. 36, No. 12, pp. 7128-725, ISSN 0360-3199

Yang, J., Sudik, A. & Wolverton, C. (2007). Destabilizing $LiBH_4$ with a Metal (M) Mg, Al, Ti, V, Cr, or Sc) or Metal Hydride (MH_2) MgH_2, TiH_2, or CaH_2). The Journal of Physical Chemistry C, Vol. 111, No. 51, pp. 19134-19140, ISSN 1932-7455

Yim, C., You, B., Na, Y. & Bae, J. (2007). Hydriding properties of Mg–xNi alloys with different microstructures. Catalysis Today, Vol. 120, No. 3-4, pp. 276-280, ISSN 0920-586

Yvon, K. & Renaudin, G. (2005). Hydrides: Solid State Transition Metal Complexes, In: Encyclopedia of Inorganic Chemistry, pp. 1814–1846, John Wiley & Sons Ltd, ISBN 0-470-86078-2, Chichester

Yu, X., Grant, D. & Walker, G. (2006). A new dehydrogenation mechanism for reversible multicomponent borohydride systems—The role of Li–Mg alloys. Chemical Communications, No. 37, pp. 3906-3908, ISSN 1359-7345

Zaluska, A., Zaluski, L., & Strom-Olsen, J. (1999a). Nanocrystalline magnesium for hydrogen storage. Journal of Alloys and Compounds, Vol. 288, No. 1-2, pp. 217-225, ISSN 0925-8388

Zaluska, A., Zaluski, L., & Strom-Olsen, J. (1999b). Synergy of hydrogen sorption in ball-milled hydrides of Mg and Mg_2Ni. Journal of Alloys and Compounds, Vol. 289, No. 1-2, pp. 197-206, ISSN 0925-8388

Zaluski, L., Zaluska, A. & Strom-Olsen, J. (1997). Nanocrystalline metal hydrides. Journal of Alloys and Compounds, Vol. 253-254, pp. 70-79, ISSN 0925-8388

Zhang, J. & Hu, Y. (2011). Decomposition of Lithium Amide and Lithium Imide with and without Anion Promoter. Industrial & Engineering Chemistry Research, Vol. 50, No. 13, pp. 8058–8064, ISSN 0888-5885

Zhang, Y., Li, B., Ren, H., Guo, S., Zhao, D. & Wang, X. (2010a). Microstructure and hydrogen storage characteristics of melt-spun nanocrystalline $Mg_{20}Ni_{10-x}Cu_x$ (x=0-4) alloys. Materials Chemistry and Physics, Vol. 124, No. 1, pp. 795-802, ISSN 0254-0584

Zhang, Y., Li, B., Ren, H., Guo, S., Zhao, D. & Wang, X. (2010b). Hydrogenation and dehydrogenation behaviours of nanocrystalline $Mg_{20}Ni_{10-x}Cu_x$ (x = 0−4) alloys prepared by melt spinning. International Journal of Hydrogen Energy, Vol. 35, No. 5, pp. 2040-2047, ISSN 0360-3199

Zhang, J., Zhou, D., He, L., Peng, P. & Liu J. (2009). First-principles investigation of Mg_2Ni phase and high/low temperature Mg_2NiH_4 complex hydrides. Journal of Physics and Chemistry of Solids, Vol. 70, No. 1, pp. 32-39, ISSN 0022-3697

Zhao-Karger, Z., Hu, J., Roth, A., Wang, D., Kübel, C., Lohstroh, W. & Fichtner, M. (2010). Altered thermodynamic and kinetic properties of MgH_2 infiltrated in microporous scaffold. Chemical Communications, Vol. 46, No. 44, pp. 8353-8355, ISSN 1359-7345

Papers on the Cu-Li-Mg system

3.13 A ternary phase in Cu-Li-Mg system

3.14 HT-XRD in the study of Cu-Li-Mg

3.15 Neutron powder diffraction and first-principles computational studies of CuLixMg_{2-x} ($x \cong 0.08$), $CuMg_2$, and Cu_2Mg

3.16 Study of the Cu–Li–Mg–H system by thermal analysis

3.17 First Principles Calculations and Experiments to Determine the Hydrogenation Process of Cu-Li-Mg

ELSEVIER

Journal of Alloys and Compounds 436 (2007) 278–284

Journal of ALLOYS AND COMPOUNDS

www.elsevier.com/locate/jallcom

A ternary phase in Cu–Li–Mg system☆

M.H. Braga [a,*], J. Ferreira [b], L.F. Malheiros [c]

[a] GMM-IMAT, Department of Physics, FEUP, R. Dr. Roberto Frias s/n, 4200-465 Porto, Portugal
[b] INETI Laboratory, R. da Amieira, P.O. Box 1089, 4466-956 S. Mamede de Infesta, Portugal
[c] GMM-IMAT, Department of Metallurgical and Materials Engineering, FEUP, R. Dr. Roberto Frias s/n, 4200-465 Porto, Portugal

Received 23 December 2005; received in revised form 10 March 2006; accepted 7 July 2006
Available online 17 August 2006

Abstract

A previous study on Cu–Li–Mg system pointed out the existence of $Cu_8Li_2Mg_{15}$, with an orthorhombic structure. The authors of the present paper also detected the existence of a ternary phase similar to the one mentioned. Due to some doubts on the phase's structure, a study of Cu–Li–Mg was focused in an area near to the composition of that phase. SEM/EDS measurements of the phases' compositions in equilibrium, as well as XRD powder patterns were obtained at room temperature. It was concluded that the ternary phase in Cu–Li–Mg system corresponds to $CuMg_{2-x}Li_x$ ($x \approx 0.11$), with a hexagonal structure, space group $P6_222$ (1 8 0), and lattice parameters $a = b = 0.5260$ nm, and $c = 1.3649$ nm. The structure was refined by Rietveld method; a Bragg reliability factor $R_B = 6.36\%$ was obtained. Similarities between $CuMg_{2-x}Li_x$ ($x \approx 0.11$) and $NiMg_2(H, D)_x$ ($x \approx 0.3$) structures are detailed.

Keywords: Intermetallics; Crystal structure; Phase diagram; X-ray diffraction; Scanning electron microscopy

1. Introduction

Cu–Li–Mg system has not been, up to now, object of many studies although it is one of the ternaries of the Al–Cu–Li–Mg system which has been deeply studied, at least near the quasicrystalline T2 (Al_6Li_3Cu) phase, and which has many applications in the aeronautic industry.

Mel'nik et al. [1] referred the existence of a ternary phase in the Cu–Li–Mg system: $Cu_8Li_2Mg_{15}$ with orthorhombic structure ($a = 0.524$ nm, $b = 0.899$ nm, and $c = 5.433$ nm). In a previous work, the present authors pointed out the existence of a phase with a stoichiometry close to that of $Cu_8Li_2Mg_{15}$, but some doubts concerning its structure still prevailed. This work was developed to confirm the crystal structure and the lattice parameters of that phase, as well as, determining the crystal structure.

A comparison between Cu–Li–Mg and H–Mg–Ni systems was established because, even if $NiMg_2$ presents, at room temperature, a hexagonal structure with space group $P6_222$ [2], and $CuMg_2$ an orthorhombic structure with space group $Fddd$ [3], the solid solution of hydrogen in $NiMg_2$, $NiMg_2(H, D)_x$ ($x \approx 0.3$) [4–8], and $CuMg_{2-x}Li_x$ seem to have the same space group $P6_222$ and very similar lattice parameters: $a = b = 0.5256$ nm and $c = 1.3435$ nm for $NiMg_2(H, D)_x$ ($x \approx 0.3$), and $a = b = 0.5260$ (1) nm and $c = 1.3649$ (1) nm for $CuMg_{2-x}Li_x$ ($x \approx 0.11$). Furthermore, metallic sublattices of $NiMg_2(H, D)_x$ ($x \approx 0.3$) and $CuMg_{2-x}Li_x$ ($x \approx 0.11$), $NiMg_2$ and $CuMg_2$, respectively, are isostructural.

2. Experimental

For this study, the alloys (Table 1 and Fig. 1) were prepared in Baikov Institute of Metallurgy from Cu > 99.97%, Li > 99.8% and Mg > 99.96% pure elements. The alloys melting was performed in a resistance furnace using alumina crucibles under a flux, consisting of a salt mixture of 75% LiCl + 25% LiF, in order to prevent oxidation of the melt and Li losses during processing. The melting was initialized by Mg; Cu and Li were added to the Mg bath. After smelting, the molten alloys were stirred and cast into a stainless steel mould; small ingots of 15 mm in diameter and 110 mm in length were obtained.

Chemical composition of the samples was also determined in Baikov Institute of Metallurgy. Li was analysed by flame emission spectrometer using a Varian – Switzerland spectrometer (model V-875). Cu was analysed by atomic-emission spectroscopy with inductive plasma (Jobin Yvon, model JY-38 plus); Mg content was obtained by difference.

Ingots were cut into ~10 g samples which were homogenised at 673 K for 3 h, using alumina crucibles, under an Ar atmosphere.

All samples were studied by SEM/EDS in a JEOL JFM 6301 F. Li could not be detected directly by EDS; its content was determined by difference [8].

☆ Patent pending number: PT103368.

* Corresponding author. Tel.: +351 225081420; fax: +351 225081447.
E-mail address: mbraga@fe.up.pt (M.H. Braga).

0925-8388/$ – see front matter © 2006 Elsevier B.V. All rights reserved.
doi:10.1016/j.jallcom.2006.07.023

Table 1
Chemical composition (in atomic fraction) of the studied samples of the Cu–Li–Mg system

Samples	x(Cu)	x(Li)	x(Mg)
1	0.313	0.032	0.655
2	0.304	0.056	0.640
3	0.312	0.066	0.622
4	0.355	0.067	0.578
5	0.290	0.096	0.614

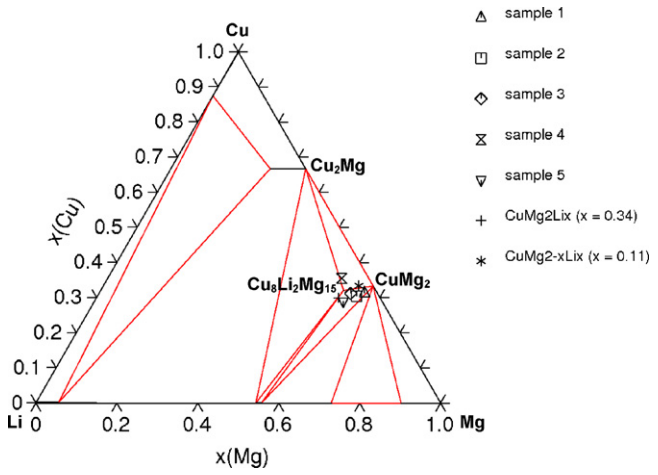

Fig. 1. Isothermal section, at room temperature (293 K), of the Cu–Li–Mg system [8]. The symbols represent the compositions of the studied samples as well as of $CuMg_2Li_x$ ($x \approx 0.34$) and $CuMg_{2-x}Li_x$ ($x \approx 0.11$).

Samples were milled to powder of <200 # and studied by XRD on a Philips X'Pert Pro MPD using primary monochromated radiation $CuK\alpha_1$ ($\lambda = 0.154060$ nm) by a symmetric Ge (1 1 1) crystal alpha 1R. Patterns were collected from 5° to 120° (2θ) under steps of 0.01° and counting time of 10 s.

Reflections of the compound under analysis were present on the XRD patterns of all the samples studied and indexed (after removal of the corresponding peaks of the other phases present in each sample). Crysfire [9] and McMaille [10] softwares were used for indexing and hence determining the phase cell and lattice parameters. In Crysfire, the hexagonal cell was found by Dicvol [11], Taup [12] and Treor [13].

It was used Checkcell [14] and Le Bail method [15], implemented on FullProf [16], for obtaining the "best solution" for the space group. For the refinement it was used Rietveld method, after Le Bail fitting, also implemented by FullProf software.

Peaks profiles were modelled using pseudo-Voigt functions, whereas the background was firstly interpolated using WinPLOTR [17] and refined at the end.

The presence of $CuMg_{2-x}Li_x$, as well as of Cu_2Mg, was detected in all samples (Figs. 2–6); Cu_2Mg was even present in sample 1 although in a rather lower content (Fig. 3).

Even if the presence of $CuMg_2$ in samples 1 (Fig. 6), 2 and 3 could not be detected from SEM/EDS analysis, the XRD patterns revealed its presence. On the other hand, no $CuMg_2$ phase could be detected on samples 4 and 5.

As in the XRD pattern of sample 4 only two phases were observed: $CuMg_{2-x}Li_x$ and Cu_2Mg (with a known cubic Laves-C15 structure and space group Fd-3m (2 2 7) – origin choice 2 with cell parameters $a = b = c = 7.034$ nm) [18], this sample was chosen for determining the structure of the ternary phase.

3. Results and discussion

Table 2 presents the crystallographic data for sample 4 and, for comparison, the crystallographic data of $NiMg_2(H, D)_x$

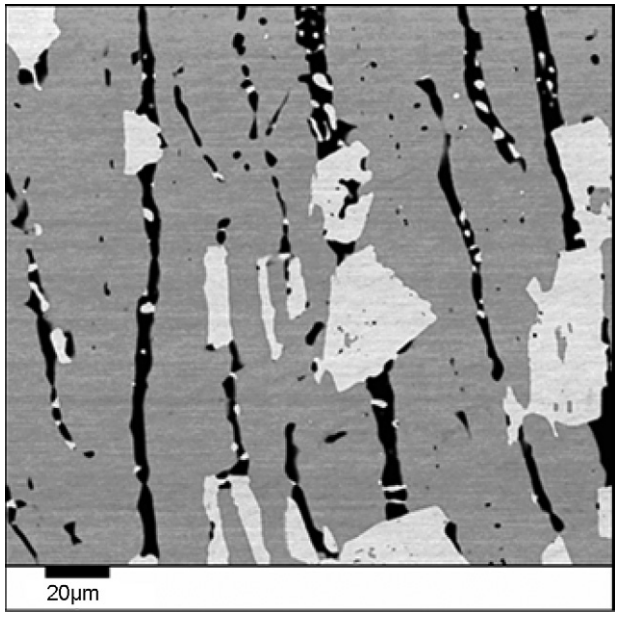

Fig. 2. Microstructure of sample 4 (magnification 500×, energy 15 keV)—Cu_2Mg: light grey and $CuMg_{2-x}Li_x$ ($x \approx 0.11$):medium grey (sample's micro porosity: dark grey).

(with $x \approx 0.3$); Fig. 4 is a zoom of the obtained XRD pattern ($2\theta = 10°$–$90°$).

Indexing results for $CuMg_{2-x}Li_x$ pointed out a hexagonal cell. The best fit was obtained with Dicvol (figures of merit M(20) = 50.8 and F(20) = 47.7) and with McMaille (figures of merit M(20) = 40.7 and F(20) = 40.5).

It was used Checkcell for obtaining the "best solution" for the space group, based on the ratio between the observed and the calculated peaks for a particular cell/space group combination.

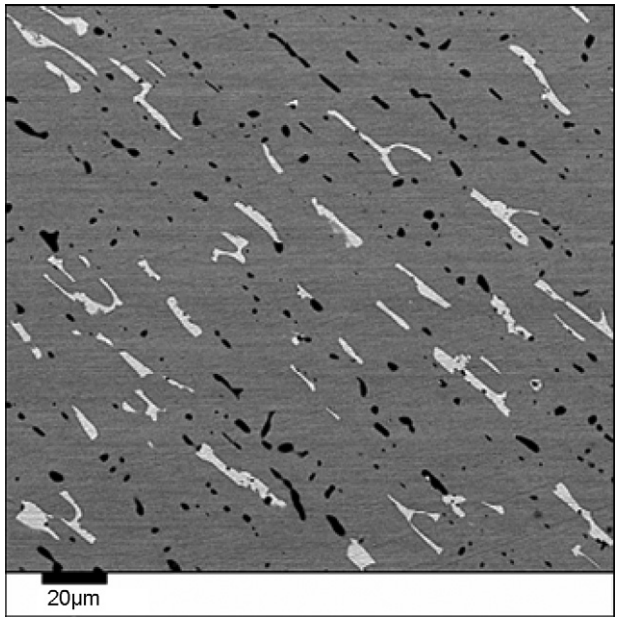

Fig. 3. Microstructure of sample 1 (magnification 500×, energy 15 keV)—Cu_2Mg: light grey and $CuMg_{2-x}Li_x$ ($x \approx 0.11$) + $CuMg_2$: medium grey (sample's micro porosity: dark grey).

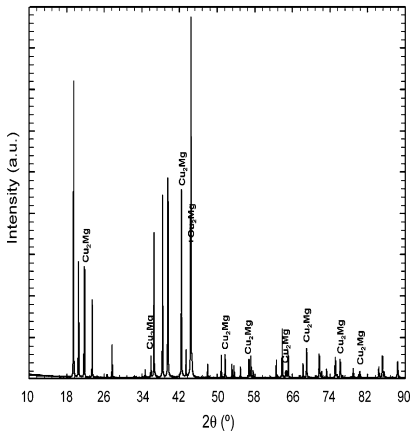

Fig. 4. Zoom of the XRD pattern for sample 4. Reflections of $CuMg_{2-x}Li_x$ ($x \approx 0.11$) (not assigned) and Cu_2Mg phases.

The space groups obtained for the "best solution" were those for which there were no extinguished reflections due to the lattice type, although there were limiting reflections due to the space group symmetry corresponding to 0 0 1 with $l = 3n$. $P6_222$ space group was in the assigned group.

Another method, Le Bail method implemented on FullProf software, was used for obtaining the space group: it was realized an extraction of intensities in a space group without extinctions ($P6_222$). Extracted intensities were very carefully checked in order to determine systematic extinctions if any. The visual examination of a zoomed part of the pattern showing the refinement results was essential for concluding to the absence or presence of a reflection. For the obtained space groups, extracted structure factors were calculated. If the cell was false, this step of extracting structure factors would reveal it by a very bad correspondence between the observed and cell-constrained calculated patterns.

The space group was found to be $P6_222$ (1 8 0) (Tables 2 and 3) and the corresponding structure was refined, as previously mentioned, using the Rietveld method also implemented in Fullprof.

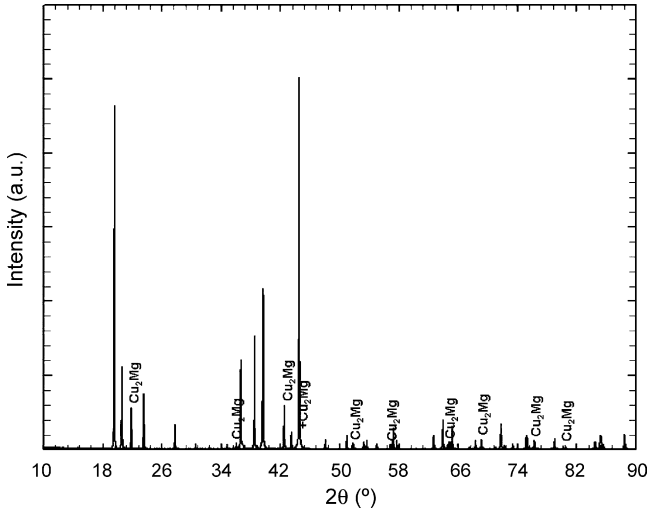

Fig. 5. Zoom of the XRD pattern for sample 5. Reflections of $CuMg_{2-x}Li_x$ ($x \approx 0.11$) (not assigned) and Cu_2Mg phases.

Table 2
Crystallographic data for $CuMg_{2-x}Li_x$ ($x \approx 0.11$) (on sample 4) and for $NiMg_2(H, D)_x$ ($x \approx 0.3$), from Ref. [22], obtained by neutron diffraction (converted to Cu $K\alpha_1$ in (PDF-2 01-085-0910, 1997))

h k l	*d* (nm) calc. for $CuMg_{2-x}Li_x$[a]	I/I_0 obs. by XRD	I/I_0 obs. for $NiMg_2(H, D)_x$ from [5] converted in Ref. [22]
1 0 0	0.4556 (7)	18.7	20.3
0 0 3	0.4550 (7)	65.4	59.2
1 0 1	0.4321 (6)	32.9	31.2
1 0 2	0.3789 (5)	21.7	14.3
1 0 3	0.3219 (3)	9.4	4.6
1 0 4	0.2731 (2)	0.1	1.6
1 1 0	0.2630 (2)	0.3	0.1
1 1 1	0.2583 (2)	2.9	4.1
1 1 2	0.2454 (2)	42.7	38.3
1 0 5	0.2342 (2)	52.3	39.7
2 0 0	0.2278 (2)	48.2	51.1
1 1 3	0.2277 (2)	11.6	31.2
0 0 6	0.2275 (2)	22.5	19.0
2 0 1	0.2247 (2)	0.0	0.0
2 0 2	0.2161 (1)	0.0	0.1
1 1 4	0.2083 (1)	7.6	5.6
2 0 3	0.2037 (1)	100.0	100.0
1 0 6	0.2035 (1)	14.8	10.3
2 0 4	0.1895 (1)	0.0	0.0
1 1 5	0.1894 (1)	4.7	2.8
1 0 7	0.1793 (1)	7.5	3.2
2 0 5	0.1749 (1)	0.0	0.1
2 1 0	0.1722 (1)	2.5	1.2
1 1 6	0.1721 (1)	2.4	–
2 1 1	0.1708 (1)	4.3	3.4
2 1 2	0.1670 (1)	3.8	1.7

[a]The *d*-spacings were determined from the best fitting of the raw data using the appropriate structural model.

A Rietveld refinement was carried out between 17° and 115° (2θ). Although the refinement of the structure of the Cu_2Mg phase was not the aim of this work, it was done together with $CuMg_{2-x}Li_x$, only by control reasons, during the process. $CuMg_{2-x}Li_x$ and Cu_2Mg were refined out of 133 and 21 reflections, respectively; five reflections (with $I/I_0 < 1$) were discarded due to the contribution (compare Fig. 7 with Fig. 4) of some impurities present in low contents.

For Cu_2Mg, with Cu (Wyck = 16d) for $x = y = z = 1/2$, and Mg (Wyck = 8a) for $x = y = z = 1/8$, it was obtained, after the above mentioned Rietveld refinement for control, a Bragg reliability factor $R_B = 7.34\%$.

$NiMg_2$ and $CuMg_2$ metallic sublattices were found to be isostructural.

Several alternatives were tried for possible Li positions on the ternary phase studied:

(I) (x, y, z) Wyck = 12k, with $x = 0.031$ (1) nm, $y = 0.018$ (1) nm, $z = 0.0515$ (3) nm and Biso = 0.0213 (4) nm^2;
(II) (1/2, 0, z) Wyck = 6f, with $z = 0.01081$ (1) nm, Biso = 0.0106 (4) nm^2 (with Li occupying Mg_1 atomic positions);

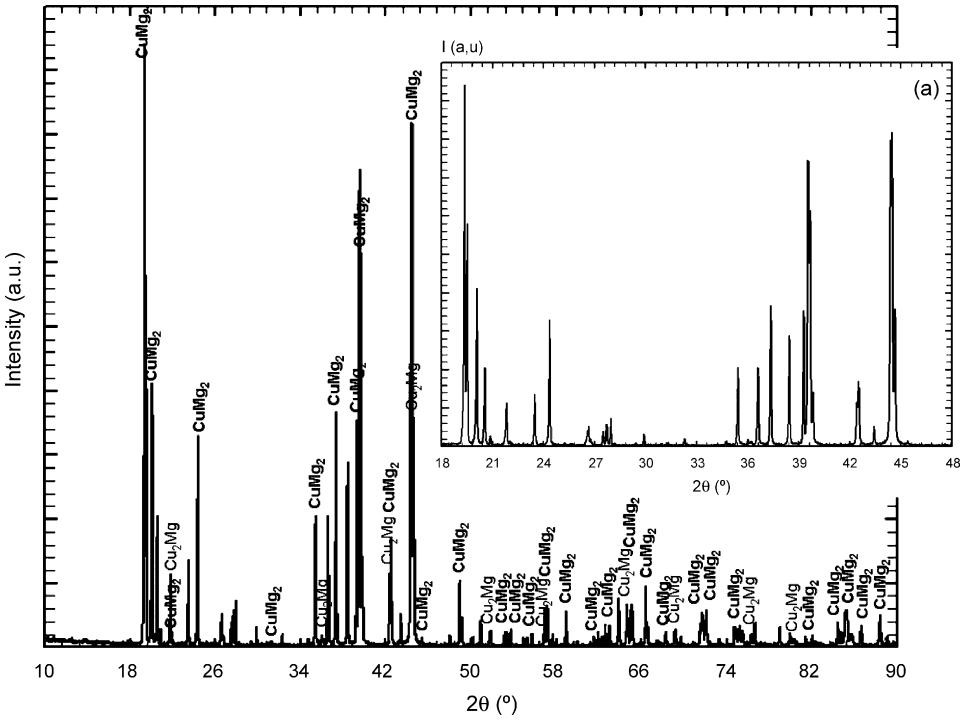

Fig. 6. Zoom of the XRD pattern for sample 1. Reflections of $CuMg_{2-x}Li_x$ ($x \approx 0.11$) (not assigned), $CuMg_2$ and Cu_2Mg phases (a) Zoom between 18° and 48° (2θ).

(III) (1/2, 0, z) Wyck = 6f (with Li occupying Mg_1 atomic positions) and (x, 0, 1/2) Wyck = 6h;
(IV) (x, y, z) Wyck = 12k and (x, 2x, 1/2) Wyck = 6j;
(V) (1/2, 0, z) Wyck = 6f (with Li occupying Mg_1 atomic positions) and (x, 2x, 1/2) Wyck = 6i (with Li occupying Mg_2 atomic positions).

Options I, III and IV are the same as those for hydrogen in $NiMg_2(H, D)_x$ ($x \approx 0.3$) [4].

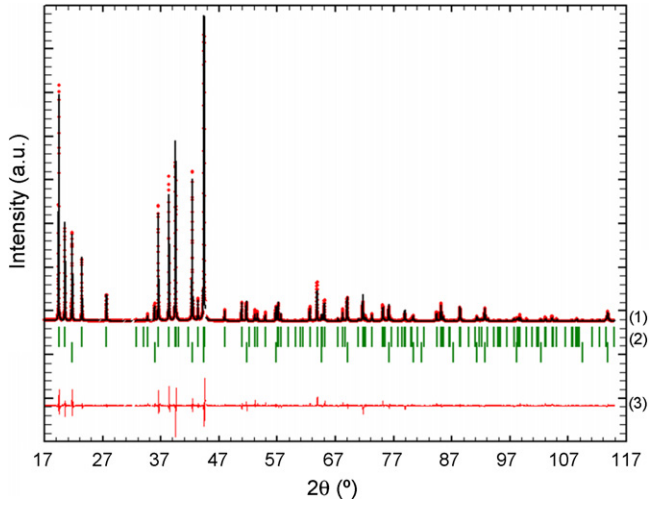

Fig. 7. XRD pattern for sample 4 after the refinement of $CuMg_{2-x}Li_x$ ($x \approx 0.11$). (1) observed—points, and calculated—continuous line (discontinuities correspond to the reflections not considered in the refinement), (2) Bragg positions, and (3) difference between observed and calculated patterns.

The best reliability factors and the most stable parameters were obtained with alternatives I and II (Table 3).

Final results of Rietveld refinement for $CuMg_2Li_x$ ($x \approx 0.34$) – I and $CuMg_{2-x}Li_x$ ($x \approx 0.11$) – II were obtained at the same time as Le Bail fit was being performed on Cu_2Mg.

From SEM/EDS and XRD experiments, it can be concluded that samples 4 and 5 belong to the two-phase region:

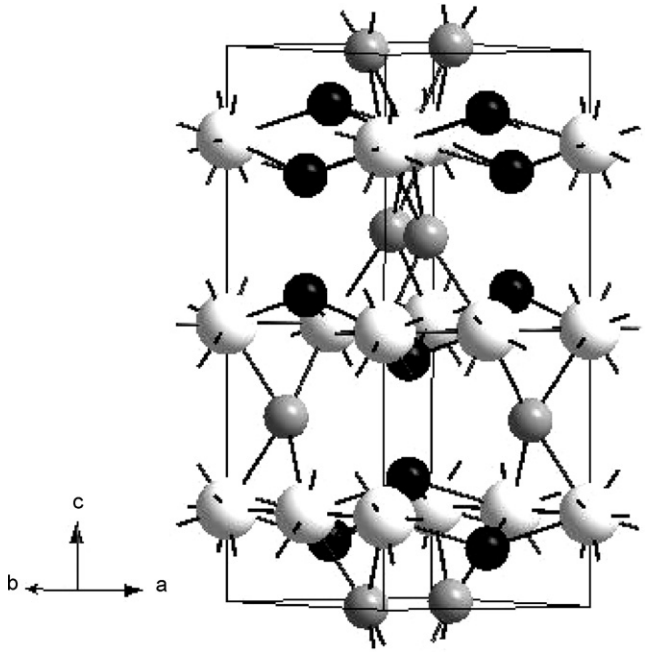

Fig. 8. Schematic representation of $Cu_6Mg_{11.367}Li_{0.633}$ structure. White spheres denote Cu, grey Mg_2 and black Mg_1/Li.

$Cu_2Mg + CuMg_2Li_x$ (Figs. 2, 4 and 5); on the other hand, the three remaining samples are located in the three-phase region $Cu_2Mg + CuMg_{2-x}Li_x + CuMg_2$ (Figs. 3 and 6). These observations are more consistent with a ternary compound's stoichiometry like $CuMg_2Li_x$ ($x \approx 0.34$) – I than with one like $CuMg_{2-x}Li_x$ ($x \approx 0.11$) – II (Fig. 1).

Results from SEM/EDS of the relation x(Mg)/x(Cu), for the present samples and for those that were studied in Ref. [19], lead to the conclusion that $x(Mg)/x(Cu)_{av.} = 1.87$ which is more in agreement with the presence of a phase with stoichiometry $CuMg_{2-x}Li_x$ ($x \approx 0.11$) – II.

The average content of Li in the phase in study, $x(Li)_{av.} = 0.04$ (from SEM/EDS results), has to be considered carefully because Li was obtained by difference, as detailed in Ref. [8].

In the refinement of the structure of Cu–Li–Mg ternary's phase, the best reliability and the most stable parameters concerning Li position were obtained for (x, y, z) Wyck = 12k corresponding to $CuMg_2Li_x$ ($x \approx 0.34$) – I (Table 3). Neverthe-

Table 3
Details of the refinement of the structure of $CuMg_2Li_x$ ($x \approx 0.34$)—I and $CuMg_{2-x}Li_x$ ($x \approx 0.11$)—II

	$CuMg_2Li_x$ (x ≈ 0.34)	**$CuMg_{2-x}Li_x$ (x ≈ 0.11)**
Formula sum	$Mg_{12}Cu_6Li_{2.049}$	$Mg_{11.367}Cu_6Li_{0.633}$
Formula weight (g/mol)	687.161	661.94
Crystal system	hexagonal	hexagonal
Space group	P 6_2 2 2	P 6_2 2 2
Unit cell lengths, in nm	a = b = 0.5260 (1), c = 1.3649 (1)	a = b = 0.5260 (1), c = 1.3649 (1)
V (nm^3)	0.32707 (9)	0.32708 (9)
Z	6	6
ρ_{calc} (g/cm^3)	3.489	3.360
Radiation type	CuKα_1	CuKα_1
Wavelength (nm)	0.154056	0.154056

Atomic parameters

$CuMg_2Li_x$ (x ≈ 0.34)

Atom	x	y	z	Biso (nm^2)	occ.
Mg1	1/2	0	0.1089 (1)	0.0190 (4)	1
Mg2	0.1657 (3)	0.3313 (7)	0	0.0155 (5)	1
Cu1	0	0	1/2	0.0125 (3)	1
Cu2	1/2	0	1/2	0.0097 (3)	1
Li	0.31 (1)	0.18 (1)	0.515 (3)	0.0213 (4)	0.17 (1)

$CuMg_{2-x}Li_x$ (x ≈ 0.11)

Atom	x	y	z	Biso (nm^2)	occ.
Mg1	1/2	0	0.1081 (1)	0.0105 (4)	0.894 (2)
Mg2	0.1631 (4)	0.3261 (7)	0	0.0191 (4)	1
Cu1	0	0	1/2	0.0126 (3)	1
Cu2	1/2	0	1/2	0.0122 (3)	1
Li	1/2	0	0.1081 (1)	0.0106 (4)	0.106 (2)

Bond distances (nm)

	$CuMg_2Li_x$ (x ≈ 0.34)				**$CuMg_{2-x}Li_x$ (x ≈ 0.11)**			
Mg1	Li	2x	0.17698 (2)	Mg1/Li	Cu1	2x	0.27489 (5)	
	Cu1	2x	0.27456 (5)		Cu2	2x	0.27489 (3)	
	Cu2	2x	0.27456 (3)		Mg1/Li	1x	0.29514 (2)	
	Li	2x	0.29244 (4)	Mg2	Cu1	2x	0.27170 (2)	
	Mg1	1x	0.29738 (2)		Cu2	2x	0.27443 (2)	
Mg2	Li	2x	0.20771 (2)		Mg2	1x	0.29716 (6)	
	Cu1	2x	0.27300 (2)	Cu1	Cu2	2x	0.26302 (5)	
	Cu2	1x	0.27375 (2)		Mg2	4x	0.27170 (2)	
	Cu2	1x	0.29418 (2)		Mg1/Li	4x	0.27489 (5)	

Table 3 (*Continued*)

Cu1	Li	4x	0.14301 (2)	Cu2	Cu1	2x	0.26302 (5)
	Cu2	2x	0.26302 (5)		Mg2	4x	0.27443 (2)
For Cu1-Mg1 and Cu1-Mg2 data on Mg1-Cu1 and Mg2-Cu1, respectively.							
Cu2	Li	4x	0.17027 (3)				
For Cu2-Cu1, Cu2-Mg1 and Cu2-Mg2 data on Cu1-Cu2, Mg1-Cu2 and Mg2-Cu2, respectively.							
Li	Li	1x	0.16928 (3)				
	Li	1x	0.23415 (4)				
	Li	1x	0.28309 (5)				
	Li	1x	0.29309 (5)				
	Li	1x	0.29829 (6)				
For Li-Cu1, Li-Cu2, Li-Mg1, and Li-Mg2 data on Cu1-Li, Cu2-Li, Mg1-Li, and Mg2-Li, respectively.							

Data collection	
Diffractometer	Philips X´Pert Pro MPD
Monochromator type	primary beam symmetrical Ge (111) – Johansson
Filter (for Kβ suppressing)	Ni
2θ range	5°– 120°
Step size	0.01°
Time per step (s)	10
Refinement	
Number of observations	14374
Number of contributing reflections	133
Number of refined profile parameters	12
FWHM (2θ)	0.05° to 0.15°
$CuMg_2Li_x$ (x ≈ 0.34)	
R_p (%) (without background correction)	9.34
R_{wp} (%) (without background correction)	12.4
R_p (%)	12.8
R_{wp} (%)	15.5
R_B (%)	6.68
R_f (%)	5.91
$CuMg_{2-x}Li_x$ (x ≈ 0.11)	
R_p (%) (without background correction)	9.34
R_{wp} (%) (without background correction)	12.3
R_p (%)	13.3
R_{wp} (%)	15.6
R_B (%)	6.36
R_f (%)	6.11

Refinement was done together with Le Bail fit of Cu_2Mg (both present in sample 4).

less, bond distances between Cu–Li seem to be rather small (Cu1–Li = 0.143 nm, Cu2–Li = 0.170 nm—Table 3). Hence, this compound was discarded at the last analysis, in spite of the fact that the literature values vary: for Li covalent radius from 0.068 nm [20] to 0.134 nm [21], and for Cu covalent radius from 0.138 nm [21] to 0.152 nm [20], making this last compound (II) as the chosen one (Fig. 8).

4. Conclusions

1. The results for the ternary phase of the Cu–Li–Mg system, when put in comparison with those for $NiMg_2(H, D)_x$ ($x \approx 0.3$), seem to confirm the analogy between space groups, lattice parameters and crystal structures of the metallic sublattices ($CuMg_2$ and $NiMg_2$, respectively).

   $NiMg_2$ presents, at room temperature, a hexagonal structure (space group $P6_222$) and $NiMg_2(H, D)_x$ ($x \approx 0.3$) is a solid solution of hydrogen in $NiMg_2$ that preserves the structure of the $NiMg_2$. However, in the Cu–Li–Mg system, $CuMg_2$ has an orthorhombic structure, with space group $Fddd$, with $a = 0.9044$ nm, $b = 0.5275$ nm, $c = 1.8328$ nm and $CuMg_{2-x}Li_x$ is hexagonal, with space group $P6_222$. It seems that Li stabilizes $CuMg_2$ into a hexagonal structure.
2. Mel'nik et al., [1] refers the existence of a ternary phase on the Cu–Li–Mg system: $Cu_8Li_2Mg_{15}$, with a composition of $x(Cu) = 0.34$, $x(Li) = 0.08$ and $x(Mg) = 0.60$.

   Results obtained in this work pointed the existence of a phase $CuMg_{2-x}Li_x$ ($x \approx 0.11$) with composition: $x(Cu) = 0.333$, $x(Li) = 0.035$ and $x(Mg) = 0.632$ corresponding to a formula sum $Cu_6Mg_{11.367}Li_{0.633}$.

Acknowledgments

The authors appreciate very much Dr. Armel Le Bail's contribution on helpful discussions and Dr. M. Hämäläinen's help for the supply of the samples.

References

[1] E.V. Mel'nik, M.F. Mitrofanova, P.I. Kripyakevich, M.Yu. Teslyuk (decd.), A.N. Malinkovich (L'vov), Russ. Metall. 3 (1976) 152–156.
[2] K. Schubert, K. Anderko, Z. Metallkd. 42 (1951) 321–325.
[3] F. Gingl, P. Selvam, K. Yvon, Acta Cryst. 49B (1993) 201–203.
[4] J. Schefer, P. Ficher, W. Hälg, F. Stucki, L. Schlapbach, J.J. Didisheim, K. Yvon, A.F. Andresen, J. Less-Common Met. 7 (1980) 65–73.
[5] J. Senegas, A. Mikou, M. Pezat, B. Darriet, J. Solid State Chem. 52 (1984) 1–11.
[6] B. Darriet, J.L. Soubeyroux, M. Pezat, D. Fruchart, J. Less-Common Met. 103 (1984) 153–162.
[7] K. Zeng, T. Klassen, R. Oelerich, R. Bormann, J. Alloys Comp. 283 (1999) 213–224.
[8] M.H. Braga, L.F. Malheiros, M. Hämäläinen, Thermochim. Acta 34 (2000) 47–54.
[9] R. Shirley, The Crysfire 2002 System for Automatic Powder Indexing: User's Manual, The Lattice Press, Guildford, Surrey, England, 2002.
[10] A. Le Bail, http://www.cristal.org/McMaille/index.html (2002).
[11] A. Boultif, D. Louër, J. Appl. Cryst. 24 (1991) 987–993.
[12] D. Taupin, J. Appl. Cryst. 6 (1973) 380–385.
[13] P.-E. Werner, L. Eriksson, M. Westdahl, J. Appl. Cryst. 18 (1985) 367–370.
[14] J. Laugier, B. Bernard, http://www.inpg.fr/LMGP, 2002.
[15] A. Le Bail, H. Duroy, J.L. Fourquet, Mater. Res. Bull. 23 (1988) 447–452.
[16] J. Rodriguez-Carvajal, Program Fullprof (version 3.0, Nov 2004), D.B. Wiles, R. A. Young, A. Sakthivel, J. Appl. Cryst. 14 (1981) 149–151.
[17] T. Roisnel, J. Rodríguez-Carvajal, in: R. Delhez, E.J. Mittenmeijer (Eds.), Proceedings of the Seventh European Powder Diffraction Conference (EPDIC 7), 2000, pp. 118–123.
[18] T. Ohba, Y. Kitanoÿ, Y. Komuraÿ, Acta Cryst. C40 (1984) 1–5.
[19] M.H. Braga, PhD Thesis, Faculty of Engineering of the University of Porto, 1999.
[20] Cambridge Crystallographic Data Centre, http://www.ccdc.cam.ac.uk/products/csd/radii/, 2005.
[21] M. Winter, The University of Sheffield and WebElements Ltd., UK, http://www.webelements.com/, 1993–2005.
[22] J.L. Soubeyroux, D. Fruchart, A. Mikou, M. Pezat, B. Darriet, Mater. Res. Bull. 19 (7) (1984) 895–904, 01-085-0910 ICDD PDF-2 2003; from 030715 ICSD using POWD-12++, 1997.

Z. Kristallogr. Suppl. **26** (2007) 299-304

HT-XRD in the study of Cu-Li-Mg

M. H. Braga[1,*], J. Ferreira[2], L. F. Malheiros[3], M. Hämäläinen[4]

[1]GMM-IMAT, Dep. of Physics, FEUP, R. Dr. Roberto Frias s/n, 4200-465 Porto, Portugal
[2]INETI Laboratory, R. da Amieira – P.O. Box 1089, 4466-956 S. Mamede de Infesta, Portugal
[3]GMM-IMAT, Dep. of Metallurgical and Materials Engineering, FEUP, R. Dr. Roberto Frias s/n, 4200-465 Porto, Portugal
[4]Laboratory of Materials Processing and Powder Metallurgy, HUT, Espoo, P.O. Box 6200, 02150 HUT, Finland
[*]Contact author; e-mail: mbraga@fe.up.pt

Keywords: powder diffraction (RT and HT), Cu-Li-Mg, DSC/DTA, SEM/EDS

Abstract. In a previous study on Cu-Li-Mg system, the authors of the present paper concluded that the ternary phase in that system corresponds to $CuMg_{2-x}Li_x$ ($x \sim 0.11$), with a hexagonal structure, space group $P6_222$ (180), and lattice parameters a = b = 0.5260 nm, c = 1.3649 nm [1]. The structure was refined by the Rietveld method [2]. In order to characterize the thermal behaviour of the ternary compound and to assess the Cu-Li-Mg phase diagram [3], HT-XRD measurements were performed on samples whose compositions were close to the one corresponding to the ternary compound. SEM/EDS measurements of the phases' compositions in equilibrium, as well as DSC/DTA heating curves, contributed to the identification of the transition temperatures and the phases present in equilibrium. It was concluded that the ternary phase decomposes at ~ 702 ± 2K.

Introduction

The Cu-Li-Mg system has not been, till now, the object of many studies although it is one of the ternaries of the Al-Cu-Li-Mg system which has been deeply studied, at least near the quasicrystalline T2 (Al_6Li_3Cu) phase, and which has many applications in the aeronautic industry.

Mel'nik *et al.* [4] referred to the existence of a ternary phase in the Cu-Li-Mg system: $Cu_8Li_2Mg_{15}$ with an orthorhombic structure (a = 0.524 nm, b = 0.899 nm, and c = 5.433 nm). Hämäläinen *et al.* [3] assessed the phase diagram of the system. Figure 1 presents two vertical sections for x(Li) = 0.04 and x(Li) = 0.07 from the Gibbs energy parameters obtained in [3]. In previous work, the present authors pointed out the existence of a phase with a stoichiometry close to that of $Cu_8Li_2Mg_{15}$ [5] and, in recent work, the latter phase was defined as being $CuMg_{2-x}Li_x$ ($x \sim 0.11$) [1]. Taking into account that there were no experimental data about the thermal behaviour of the ternary phase, nor the high temperature equilibria,

and that quenching seemed ineffective for such a narrow temperature range, some HT-XRD studies were developed.
On the other hand, an important feature for a successful assessment is the crystallographic data; thus the models used to describe the phases should be supported by the phase's crystal structure.

Experimental

DSC/DTA measurements
In the first part of this work, thirty samples were prepared in a resistance furnace and their compositions were analysed by AAS [5]. DSC/DTA experiments were performed on samples belonging to the vertical sections $x_{Mg} \sim 0.512$, $x_{Cu} \sim 0.097$, $x_{Cu} \sim 0.039$ and $x_{Li} \sim 0.050$ of the Cu-Li-Mg system under Ar atmosphere using quasi-hermetic stainless steel crucibles. Figure 1 presents some experimental data and figure 2 shows a DSC/DTA curve for a sample with x(Cu) = 0.088, x(Li) = 0.19, x(Mg) = 0.717.
In the second part of this work, samples were prepared in order to have compositions close to $Cu_8Li_2Mg_{15}$. Those samples were prepared and analysed in a similar way to the previous ones [1].

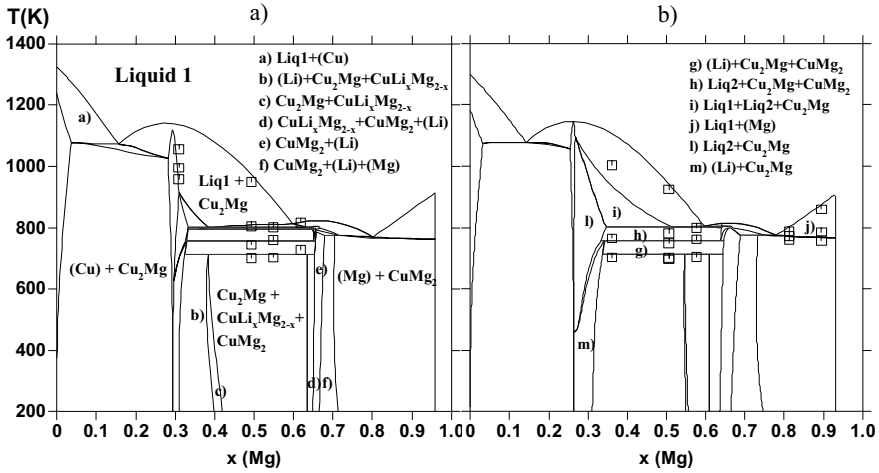

Figure 1. Assessed vertical sections of the ternary system Cu-Li-Mg [3]: a) x(Li) = 0.04 and b) x(Li) = 0.07. Some of the DSC/DTA experimental data are represented by squares.

The samples were polished and cleaned in pure ethanol in order to remove the oxide layer and to ensure a flat surface for a better thermal contact between sample and crucible. Experiments took place in a DSC of continuous flux (indeed a DTA) *Shimadzu 50* that operates between room temperature and 1003 K, using stainless steel crucibles especially conceived for this propose. Crucibles were quasi-hermetic and the volume of the samples and the inner

volume of the crucibles were very close. For each composition, at least four cycles of heating /cooling were made, always with four different samples. The heating/cooling rates used were 5, 10 and 20 K/min. Transformation temperatures in figure 1 correspond to a "0 K/min." heating rate.

SEM/EDS measurements

SEM/EDS analyses were also performed on each sample, at room temperature and after being annealed for 60 min. at 773 K followed by quenching into liquid N_2. The Li content was found by difference [5]; high quality standards of Cu and Mg were used as patterns. A JEOL, JSM - 35C or JFM 6301 F was used. Figure 2 shows one of the photomicrographs of the samples studied which reveals the presence of a eutectic constituent. In Table 1 it can be seen the obtained EDS results for three of the system's component phases.

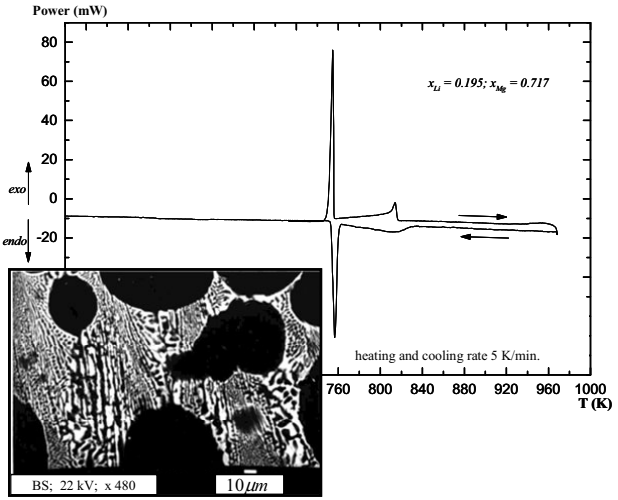

Figure 2. A DSC/DTA heating/cooling curve for a sample with x(Cu) = 0.088, x(Li) = 0.19, x(Mg) = 0.717, for a heating/cooling rate of 5 K/min. SEM backscatter photomicrograph (x 480) of the same sample after being annealed at 773 K for 60 min. followed by quenching into liquid N_2. Two phases can be distinguished: (Mg) and/or (Li) in black and $CuMg_2$ in white. Li content was obtained by difference [5].

Table 1. SEM/EDS results. Average contents were obtained from more than twenty measurements. The error associated with the Li content cannot be precisely determined because Li was found by difference.

Phase	x(Cu) ±0.005	x(Li)	x(Mg) ±0.005	Phase	x(Cu) ±0.006	x(Mg) ±0.006	Phase	x(Cu) ±0.005	x(Mg) ±0.005
$CuLi_xMg_{2-x}$	0.334	0.040	0.626	$CuMg_2$	0.674	0.326	Cu_2Mg	0.669	0.332

RT and HT - powder XRD

At room temperature, some powder samples were measured on a Philips X´Pert Pro MPD using $CuK\alpha_1$ radiation (λ = 0.15406 nm) primary monochromated by a symmetric Ge (111) crystal [1]. When those samples were studied at high temperatures, instead of the primary monochromated radiation $CuK\alpha_1$ and $CuK\alpha_2$ (λ = 0.15443nm) were used, because the inten-

sity of the incident/diffracted beam was already attenuated by the protective graphite foil of the heating chamber. Intensity can become crucial when a sample is being heated because the counting time cannot be very high owing to the sample's reactivity. The heating chamber was an Anton Parr that operates from room temperature to 1473 K. The diffraction pattern in figure 3 was obtained under the same conditions as those for high temperature. Patterns were collected from 5 to 120º (2θ) with steps of 0.01º and a counting time of 10 s.

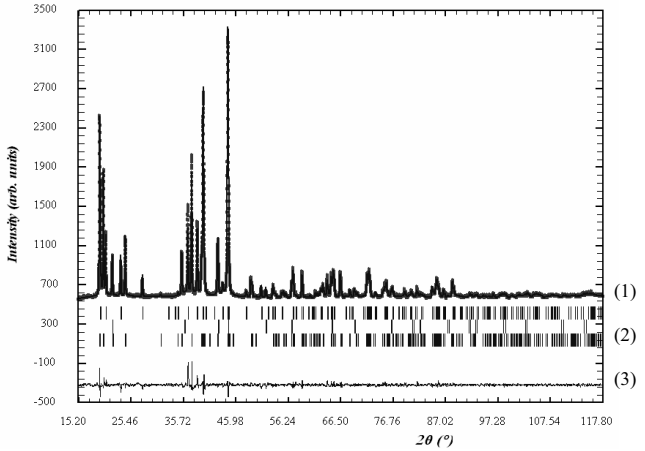

Figure 3. XRD diffraction pattern of $CuLi_xMg_{2-x}$ ($x \sim 0.11$) + Cu_2Mg + $CuMg_2$, at 300 K, after Rietveld refinement, of a sample with x(Cu) = 0.355, x(Li) = 0.067 and x(Mg) = 0.578. (1) observed – points, and calculated - continuous line, (2) Bragg positions for $CuLi_xMg_{2-x}$ ($x \sim 0.11$), Cu_2Mg and $CuMg_2$, respectively, (3) difference between observed and calculated patterns.

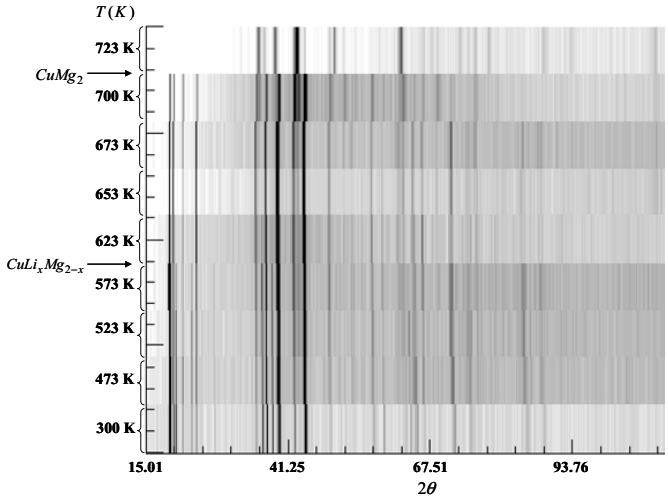

Figure 4. 2D film diffractogram of a sample with x(Cu) = 0.355, x(Li) = 0.067 and x(Mg) = 0.578. Above 573 K $CuLi_xMg_{2-x}$ ($x \sim 0.11$) cannot be distinguished, and above 700 K $CuMg_2$ cannot be distinguished.

Discussion

DSC/DTA results denote the existence of at least three invariant transitions at T = 702 ± 2 K, T = 757 ± 2 K and T = 804 ± 2 K (see figures 1 and 2). It seems that $CuLi_xMg_{2-x}$ (x ~ 0.11) decomposes at T = 702 ± 2 K, although its peaks couldn't be distinguished at temperatures above 623 K in the HT-XRD pattern (see figures 4 and 5). SEM/EDS results assisted us to conclude about the nature of the transitions (see figure 2) and to identify the phases in equilibrium. It was very difficult to determine the Li content due to the difficulties pointed out in [5].

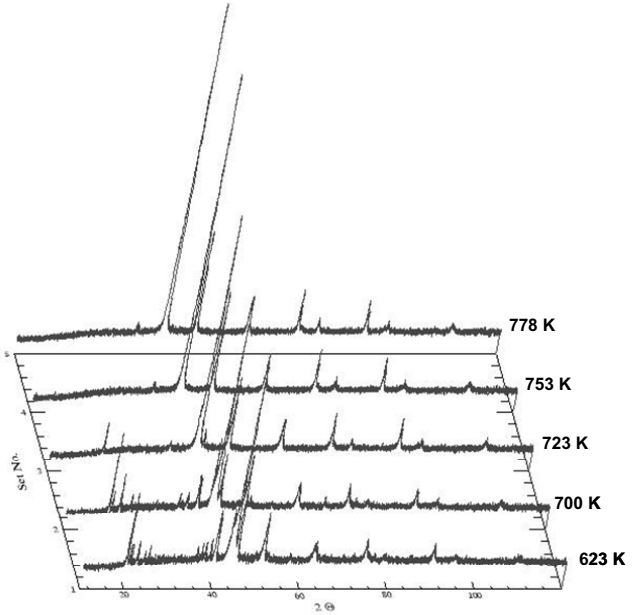

Figure 5. 3D plot diffractogram of sample with x(Cu) = 0.290, x(Li) = 0.096 and x(Mg) = 0.614. Above 623 K it cannot be distinguished $CuLi_xMg_{2-x}$ (x ~ 0.11), and above 700 K it cannot be distinguished $CuMg_2$.

FullProf - WinPLOTR software [6] was used to make a Rietveld refinements of the phase $CuLi_xMg_{2-x}$ (x ~ 0.11) for the sample with x(Cu) = 0.355, x(Li) = 0.067 and x(Mg) = 0.578 at 300 K, 473 K, 523 K, 573 K and 623 K. At 300 K (see figure 3) the lattice parameters obtained were a = b = 0.5262(1) nm and c = 1.3644(1) nm and x ~ 0.08 in $CuLi_xMg_{2-x}$ for an R_p = 13.4% and R_{wp} = 9.71% (conventional Rietveld R-factors), χ^2 = 0.212 and R_B = 5.36% and R_f = 3.91%. These results are in close agreement with those obtained in [1]. However, although the sample has the same composition as that analysed in [1], an extra phase ($CuMg_2$) was detected. A potential explanation for the presence of a third phase in equilibrium relies on the proximity of the sample's composition to the border of the two and three phase domains. The results of the lattice parameters obtained at high temperatures are shown in figure 6. For the other phases in equilibrium, a Le Bail fit was performed.

Even if there is not a straight forward correspondence between the transition' temperatures obtained by DSC/DTA and by HT-XRD, HT-XRD allowed us to know what were the phases

present at different temperatures. The linear thermal expansion parameters were calculated following the obtained lattice parameters (see figure 6) and were found to be, at 300 K, $\alpha_{a=b}$ = 2.89x10^{-5} K^{-1} and α_c = 3.13x10^{-5} K^{-1}. As expected, these results are in good agreement with each other.

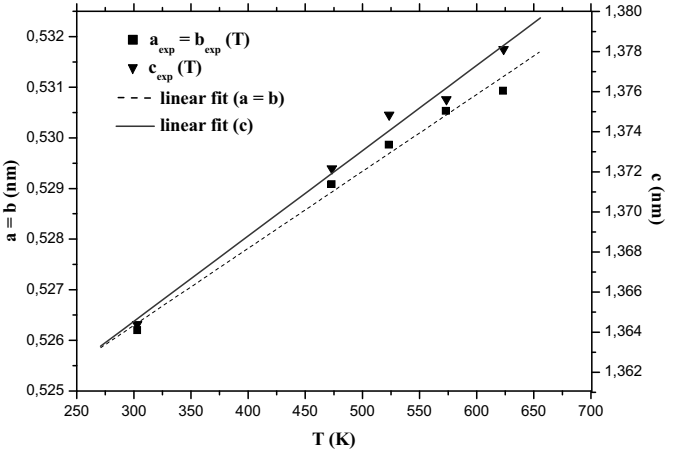

Figure 6. Lattice parameters of the phase $CuLi_xMg_{2-x}$ (x ~ 0.11) obtained by Rietveld refinement of the diffraction patterns of the sample with x(Cu) = 0.355, x(Li) = 0.067 and x(Mg) = 0.578 at different temperatures.

Concluding remarks

The Cu-Li-Mg system was studied by DSC/DTA, SEM/EDS and XRD at room and high temperatures. Results are in good agreement and the techniques complemented each other. The crystal structure and the thermal behaviour of $CuLi_xMg_{2-x}$ (x ~ 0.11) was studied by HT-XRD which seems to be essential for the phase diagram's assessment.

References

1. Braga, M. H., Ferreira, J. & L. Malheiros, *J. Alloys and Comp.*, (in press).
2. Rietveld, H.M., 1969, *J. Appl. Crystallogr.*, **2**, 65.
3. Hämäläinen, M., Braga, H., Bochvar, N., Dobatkina, T., Lyssova, E. & Rokhlin L.L., 1998, *Definition of thermo chemical and thermo physical properties to provide a database for the development of new light alloys (Volume 1)*, pp. 219-227.
4. Mel'nik, E. V., Mitrofanova, M. F., Kripyakevich, P. I., Teslyuk, M. Yu. (decd.) & Malinkovich, A. N. (L'vov), 1976, *Russ. Metall.*, **3**, 152.
5. Braga, M. H., Malheiros, L.F. & Hämäläinen, M., 2000, *Thermochim. Act.*, **344**, 47.
6. Roisnel, T. & Rodríguez-Carvajal, J. (2000). *Proceedings of the Seventh European Powder Diffraction Conference (EPDIC 7)*, Ed. R. Delhez and E.J. Mittenmeijer, pp. 118-123.

Journal of Solid State Chemistry 183 (2010) 10–19

Contents lists available at ScienceDirect

Journal of Solid State Chemistry

journal homepage: www.elsevier.com/locate/jssc

Neutron powder diffraction and first-principles computational studies of $CuLi_xMg_{2-x}$ ($x \cong 0.08$), $CuMg_2$, and Cu_2Mg

M.H. Braga [a,b,*], J.J.A. Ferreira [c], J. Siewenie [a], Th. Proffen [a], S.C. Vogel [a], L.L. Daemen [a]

[a] Manuel Lujan, Jr. Neutron Scattering Center, Los Alamos National Laboratory, Los Alamos, NM 87545, USA
[b] CEMUC and Physics Engineering Department, Engineering Faculty of the University of Porto, R. Dr. Roberto Frias, s/n, 4200-465 Porto, Portugal
[c] LNEG Laboratory, R. da Amieira-P.O. Box 1089, 4466-956 S. Mamede de Infesta, Portugal

ARTICLE INFO

Article history:
Received 18 June 2009
Received in revised form
9 September 2009
Accepted 13 September 2009
Available online 6 October 2009

Keywords:
Cu–Li–Mg
Neutron diffraction
First-principles calculations
X-ray diffraction
Rietveld refinement
Pair distribution function

ABSTRACT

A small addition of Li changes the orthorhombic structure of $CuMg_2$ to hexagonal $CuLi_xMg_{2-x}$ (x=0.08). Determining the Li content of the ternary phase and Li atomic positions was our main objective for this work. For this reason we performed neutron diffraction at several different temperatures below and above room temperature. The results obtained on two neutron powder diffractometers were compared with X-ray diffraction (XRD) data, and with first-principles calculations. The first-principles calculations are in good agreement with Rietveld-refined data from neutron diffraction, but do not show a marked preference for one of several possible Li sites. The pair distribution function (PDF) fitting is consistent with Li substituting only Mg1 (1/2, 0, z). Interstitial spaces in the structure of $CuMg_2$ and of $CuLi_xMg_{2-x}$ were also considered, but are unlikely to be occupied by Li. Neutron diffraction data for binary $CuMg_2$ and Cu_2Mg were also obtained.

Published by Elsevier Inc.

1. Introduction

Recently, we have solved by X-ray diffraction the structure of the only known ternary phase in the Cu–Li–Mg system [1]. Yet, some details about atoms' positions were left to be solved and so was the composition of the alloy.

The main reason for studying this system at the time was its relationship to the quaternary system Al–Cu–Li–Mg—a light alloy with possible applications in the transportation industry.

Another motivation for studying the $CuLi_xMg_{2-x}$ alloy is its possible use to store hydrogen [2–4]. Because the phase diagrams of Cu–Mg and Ni–Mg are similar, and because Cu and Ni have similar electron affinities, it was thought in the sixties that $CuMg_2$ would store hydrogen, too. However this is not the case [5]. $NiMg_2$ has a hexagonal structure ($P6_222$), but $CuMg_2$ has an orthorhombic structure (*Fddd*), and this structural difference is assumed to be the reason that $NiMg_2$ stores H_2 and forms a hydride, but $CuMg_2$ does not. $CuMg_2$ decomposes into Cu_2Mg and MgH_2 [5] upon hydrogen loading. As a result of this reaction and since $CuMg_2$ does not form a hydride, $CuMg_2$ was abandoned as a candidate material for hydrogen storage [5,6]. The hexagonal structure of $CuLi_xMg_{2-x}$, suggested the possibility of using this phase as a hydrogen storage material [2,3] because $CuLi_xMg_{2-x}$ has the same space group ($P6_222$) as $NiMg_2$ and $NiMg_2(H,D)_{0.3}$ (lattice parameters are almost identical: $a=b=5.250$ Å and $c=13.621$ Å (at 300 K) for $CuLi_xMg_{2-x}$ and $a=b=5.256$ Å and $c=13.435$ Å for $NiMg_2(H,D)_{0.3}$ [7]). Therefore, we hypothesized that $CuLi_xMg_{2-x}$ (x=0.08) would be a hydrogen storage material, just like $NiMg_2$—a hypothesis that has been confirmed by now [2–4].

In view of this it became important to determine the structure and composition of $CuLi_xMg_{2-x}$. In our previous work [1], two possibilities were raised for the structure and composition of the ternary disordered alloy, $CuLi_{0.34}Mg_2$ (in which Li occupies some of the Wyckoff 12*k* positions of a $P6_222$ hexagonal structure) and $CuLi_{0.106}Mg_{1.894}$ (in which Li occupies some of the Mg Wyckoff 6*f* positions of a $P6_222$ hexagonal structure). It was not possible to distinguish between these possibilities using X-ray diffraction, owing to the weak scattering of X-rays by Li. While Li is not a strong coherent neutron scatterer, measurements with neutrons coupled to first-principles calculations offer a complementary approach to the determination of the most stable structure and to the most stable composition.

The change of the $CuMg_2$ orthorhombic (*Fddd*) structure to a hexagonal structure ($P6_2222$) upon addition of a small amount of Li has been firmly established [1]. Isostructural phases to $CuLi_xMg_{2-x}$ are the hexagonal phase $NiMg_2$ and $NiMg_2H_{0.24-0.30}$ [7]. For the NiMg-hydrides, several hydrogen positions were

* Corresponding author at: CEMUC and Physics Engineering Department, Engineering Faculty of the University of Porto, R. Dr. Roberto Frias, s/n, 4200-465 Porto, Portugal. Fax: +351 225081447.
E-mail address: mbraga@fe.up.pt (M.H. Braga).

0022-4596/$ - see front matter Published by Elsevier Inc.
doi:10.1016/j.jssc.2009.09.010

reported: In $NiMg_2H_{0.29}$ the hydrogen atoms occupy Wyckoff 6*f* positions [7] and could occupy the interstitial Wyckoff 6*h* position [7]. Other possibilities would be that the H atoms would just occupy interstitial Wyckoff 12*k* position (in $NiMg_2H_{0.26}$) or the Wyckoff 12*k* and 6*j* positions in $NiMg_2H_{0.24}$ [7]. This suggests a number of possible sites for Li in $CuLi_xMg_{2-x}$.

Interestingly Hlukhyy et al. [8] have reported a result closely related to our observations in the Sn-doped Ni–Mg system. These authors show that the synthesis of alloys in the Ni–Mg system is affected by the presence of small amounts of Sn (forming $NiMg_{2-x}Sn_x$ with x=0.22 and 0.40). The replacement of Mg by Sn produces changes in the structure of $NiMg_2$, this time making the alloy change from the $NiMg_2$ type (hexagonal) to the $CuMg_2$ type (orthorhombic). While the structure of $NiMg_{1.85}Sn_{0.15}$ is still of $NiMg_2$ type, the structure of $NiMg_{1.78}Sn_{0.22}$ and $NiMg_{1.60}Sn_{0.40}$ is already of the $CuMg_2$ type. These results represent obviously the converse of our own observations in the $CuMg_2$ structure, and reaffirm our results with respect to $CuLi_xMg_{2-x}$. Again, this suggests possibilities for Li atomic sites.

Table 1
Rietveld refinement's results at 60, 150 and 300 K obtained from NPDF data.

T=60 K (NPDF) wR_p=2.01%; R_p=1.38% Wt. Frac. ($CuLi_{0.069}Mg_{1.931}$)=0.356 (4); Wt. Frac. ($CuMg_2$)=0.426 (4); Wt. Frac. (Cu_2Mg)=0.218 (3)		
$CuLi_{0.069}Mg_{1.917}$ Hexagonal–$P6_222$ (180) a=b=5.2476 (3) Å; c=13.6193 (9) Å; ρ=3.404 g/cm^3	$CuMg_2$ Orthorhombic–Fddd (70) a=5.2622 (3) Å; b=9.0207 (6) Å; c=18.310 (1) Å; ρ=3.428 g/cm^3	Cu_2Mg Cubic–Fd-3m (227) a=b=c=7.0607 (4) Å; ρ=5.714 g/cm^3
Cu1: x=0; y=0; $z=\frac{1}{2}$; occ.=1; $U_{iso}\times100$=0.49 (2) Å^2 Cu2: $x=\frac{1}{2}$; y=0; $z=\frac{1}{2}$; occ.=1; $U_{iso}\times100$=0.42 (3) Å^2 Mg1: $x=\frac{1}{2}$; y=0; z=0.1124 (1); occ.=0.931 (7); $U_{iso}\times100$=0.50 (3) Å^2 Mg2: x=0.1663 (4); y=0.3326 (9); z=0; occ.=1; $U_{iso}\times100$=0.85 (4) Å^2 Li1: $x=\frac{1}{2}$; y=0; z=0.1124 (1); occ.=0.069 (7); $U_{iso}\times100$=0.50 (3) Å^2	Cu1: $x=\frac{1}{8}$; $y=\frac{1}{8}$; z=0.49851 (5); occ.=1; $U_{iso}\times100$=0.29 (2) Å^2 Mg1: $x=\frac{1}{8}$; $y=\frac{1}{8}$; z=0.04164 (8); occ.=1; $U_{iso}\times100$=0.65 (3) Å^2 Mg2: $x=\frac{1}{8}$; y=0.4591 (2); $z=\frac{1}{8}$; occ.=1; $U_{iso}\times100$=0.55 (3) Å^2	Cu1: x=0; y=0; z=0; occ.=1; $U_{iso}\times100$=0.55 (1) Å^2 Mg1: $x=\frac{3}{8}$; $y=\frac{3}{8}$; $z=\frac{3}{8}$; occ.=1; $U_{iso}\times100$=0.67 (2) Å^2
T=150 K (NPDF) wR_p=2.01%; R_p=1.37% Wt. Frac. ($CuLi_{0.083}Mg_{1.931}$)=0.357 (4); Wt. Frac. ($CuMg_2$)=0.424 (4); Wt. Frac. (Cu_2Mg)=0.219 (3)		
$CuLi_{0.083}Mg_{1.917}$ Hexagonal–$P6_222$ (180) a=b=5.2483 (4) Å c=13.620 (1) Å; ρ=3.395 g/cm^3	$CuMg_2$ Orthorhombic–Fddd (70) a=5.2625 (4) Å; b=9.0233 (7) Å c=18.309 (1) Å; ρ=3.427 g/cm^3	Cu_2Mg Cubic–Fd-3m (227) a=b=c=7.0608 (4) Å ρ=5.713 g/cm^3
Cu1: x=0; y=0; $z=\frac{1}{2}$; occ.=1; $U_{iso}\times100$=0.77 (3) Å^2 Cu2: $x=\frac{1}{2}$; y=0; $z=\frac{1}{2}$; occ.=1; $U_{iso}\times100$=0.65 (4) Å^2 Mg1: $x=\frac{1}{2}$; y=0; z=0.1123 (2); occ.=0.917 (7); $U_{iso}\times100$=0.66 (5) Å^2 Mg2: x=0.1666 (5); y=0.333 (1); z=0; occ.=1; $U_{iso}\times100$=1.11 (5) Å^2 Li1: $x=\frac{1}{2}$; y=0; z=0.1123 (2); occ.=0.083 (7); $U_{iso}\times100$=0.66 (5) Å^2	Cu1: $x=\frac{1}{8}$; $y=\frac{1}{8}$; z=0.49860 (5); occ.=1; $U_{iso}\times100$=0.52 (2) Å^2 Mg1: $x=\frac{1}{8}$; $y=\frac{1}{8}$; z=0.04152 (8); occ.=1; $U_{iso}\times100$=0.86 (3) Å^2 Mg2: $x=\frac{1}{8}$; y=0.4594 (2); $z=\frac{1}{8}$; occ.=1; $U_{iso}\times100$=0.77 (3) Å^2	Cu1: x=0; y=0; z=0; occ.=1; $U_{iso}\times100$=0.81 (2) Å^2 Mg1: $x=\frac{3}{8}$; $y=\frac{3}{8}$; $z=\frac{3}{8}$; occ.=1; $U_{iso}\times100$=0.92 (3) Å^2
T=300 K (NPDF) wR_p=1.93%; R_p=1.29% Wt. Frac. ($CuLi_{0.083}Mg_{1.931}$)=0.351 (5); Wt. Frac. ($CuMg_2$)=0.427 (5); Wt. Frac. (Cu_2Mg)=0.222 (3)		
$CuLi_{0.083}Mg_{1.931}$ Hexagonal–$P6_222$ (180) a=b=5.2495 (5) Å; c=13.621 (1) Å; ρ=3.401 g/cm^3	$CuMg_2$ Orthorhombic–Fddd (70) a=5.2625 (5) Å; b=9.0278 (8) Å c=18.307 (2) Å; ρ=3.426 g/cm^3	Cu_2Mg Cubic–Fd-3m (227) a=b=c=7.0598 (6) Å ρ=5.716 g/cm^3
Cu1: x=0; y=0; $z=\frac{1}{2}$; occ.=1; $U_{iso}\times100$=1.26 (4) Å^2 Cu2: $x=\frac{1}{2}$; y=0; $z=\frac{1}{2}$; occ.=1; $U_{iso}\times100$=1.09 (5) Å^2 Mg1: $x=\frac{1}{2}$; y=0; z=0.1123 (2); occ.=0.917 (8); $U_{iso}\times100$=1.15 (7) Å^2 Mg2: x=0.1669 (6); y=0.334 (1); z=0; occ.=1; $U_{iso}\times100$=1.66 (6) Å^2 Li1: $x=\frac{1}{2}$; y=0; z=0.1123 (2); occ.=0.083 (8); $U_{iso}\times100$=1.15 (7) Å^2	Cu1: $x=\frac{1}{8}$; $y=\frac{1}{8}$; z=0.49860 (6); occ.=1; $U_{iso}\times100$=0.98 (2) Å^2 Mg1: $x=\frac{1}{8}$; $y=\frac{1}{8}$; z=0.0415 (1); occ.=1; $U_{iso}\times100$=1.41 (4) Å^2 Mg2: $x=\frac{1}{8}$; y=0.4598 (3); $z=\frac{1}{8}$; occ.=1; $U_{iso}\times100$=1.35 (4) Å^2	Cu1: x=0; y=0; z=0; occ.=1; $U_{iso}\times100$=1.27 (2) Å^2 Mg1: $x=\frac{3}{8}$; $y=\frac{3}{8}$; $z=\frac{3}{8}$; occ.=1; $U_{iso}\times100$=1.41 (3) Å^2

Note: $R_p=\sum|I_o-I_c|/\sum I_o$ and $wR_p=[\sum w(I_o-I_c)^2/\sum wI_o^2]^{1/2}$, in which I_o is the observed intensity, I_c is the calculated one. The weights, w, are derived from an error propagation scheme.

2. Material and methods

2.1. Synthesis and characterization

The Cu–Li–Mg samples were prepared with a target composition of $CuLi_{0.10}Mg_{1.90}$ and $CuLi_{0.34}Mg_2$. They were prepared by mixing stoichiometric amounts of Cu (electrolytic, 99.99% purity, 325 mesh), Mg (99.8% purity, 200 mesh, Alfa Aesar), and small (less than 3 mm wide) pieces of Li (99% purity, Alfa Aesar). Because of the large vapor pressure of Mg, even below its melting point, the reagents were sealed in a stainless steel crucible in a dry box with He atmosphere. This had the added advantage of minimizing possible reagent loss. The samples were heated in a tube furnace with a stirring device to ensure proper mixing of the heterogeneous starting mixture and complete dispersion of Li in the sample. Different reaction temperatures and times were used. Regardless of reaction conditions, the samples, as investigated by XRD, invariably contained Cu_2Mg, $CuMg_2$, or both (but no pure metals). Nonetheless, we obtained final products containing approximately up to 81.0 wt% (75.6 at%) of $CuLi_xMg_{2-x}$. Since the structures of Cu_2Mg and $CuMg_2$ are known (and they are confirmed in this paper), this complication translated merely in the refinement of two additional phases in the neutron powder diffraction pattern.

We studied two samples with very different compositions, both of them containing $CuLi_xMg_{2-x}$, $CuMg_2$ and Cu_2Mg: 70.4 at% $CuLi_xMg_{2-x}$, 21.0 at% $CuMg_2$, 8.6 at% Cu_2Mg in the first sample and 38.0 at% $CuLi_xMg_{2-x}$, 44.8 at% $CuMg_2$, 17.2 at% Cu_2Mg. By means of XRD, we have studied previously a sample with: 75.6 at% of $CuLi_xMg_{2-x}$ and 24.4 at% of Cu_2Mg [9].

Samples were first characterized by means of XRD using a Rigaku Ultima III powder diffractometer, and their composition was roughly determined by means of the Match software [10], which uses the "reference intensity ratio method" (RiR-method) [11] to obtain phase fractions. Patterns were collected with Cu$K\alpha$ typically from 2θ=15 to 70° with steps of 0.02° and a counting time of 10 s per bin.

2.2. Powder X-ray diffraction measurements

At room temperature, some powder samples were measured on a Philips X'Pert Pro MPD using Cu$K\alpha_1$ radiation (λ=0.15406 nm) monochromated by a symmetric Ge (111) crystal [1]. When those samples were studied at high temperatures, instead of the primary monochromated monochromatic radiation, Cu$K\alpha_1$ and Cu$K\alpha_2$ (λ=0.15443 nm) were used, because the intensity of the incident/diffracted beam was already attenuated by the protective graphite foil of the heating chamber. Intensity can become crucial when a sample is being heated because the counting time cannot be very high owing to the sample's reactivity. The heating chamber was an Anton Parr that operates from room temperature to 1473 K in vacuum ($\lesssim 10^{-5}$ mbar) or in argon atmosphere. Patterns were collected from 5 to 120° (2θ)

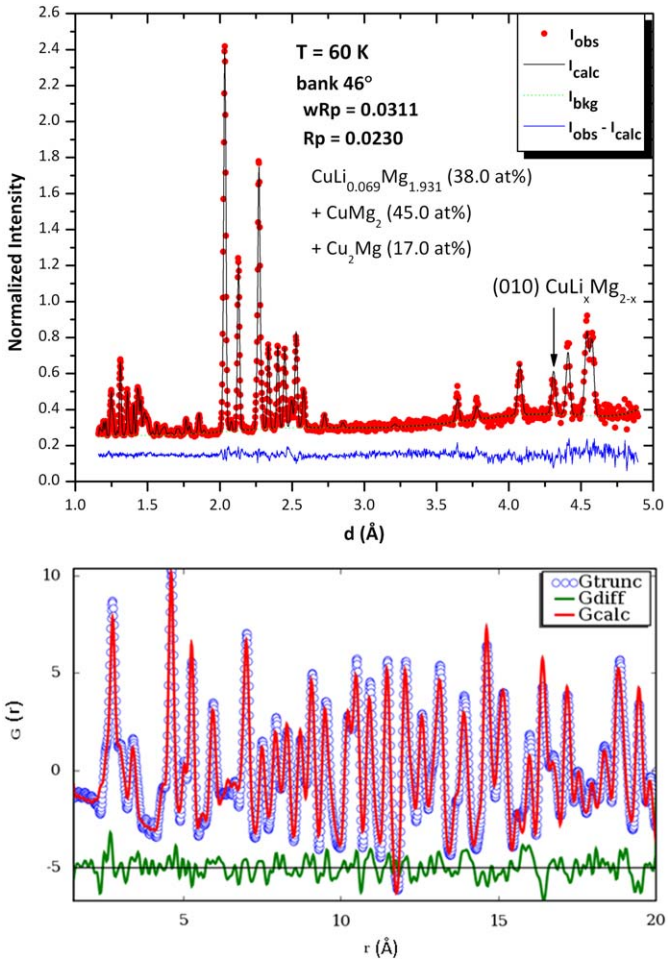

Fig. 1. NPDF after Rietveld refinement diffraction pattern at 60 K for 46° bank (the results at the graph are only due to the 46° bank). PDF experimental and fitted.

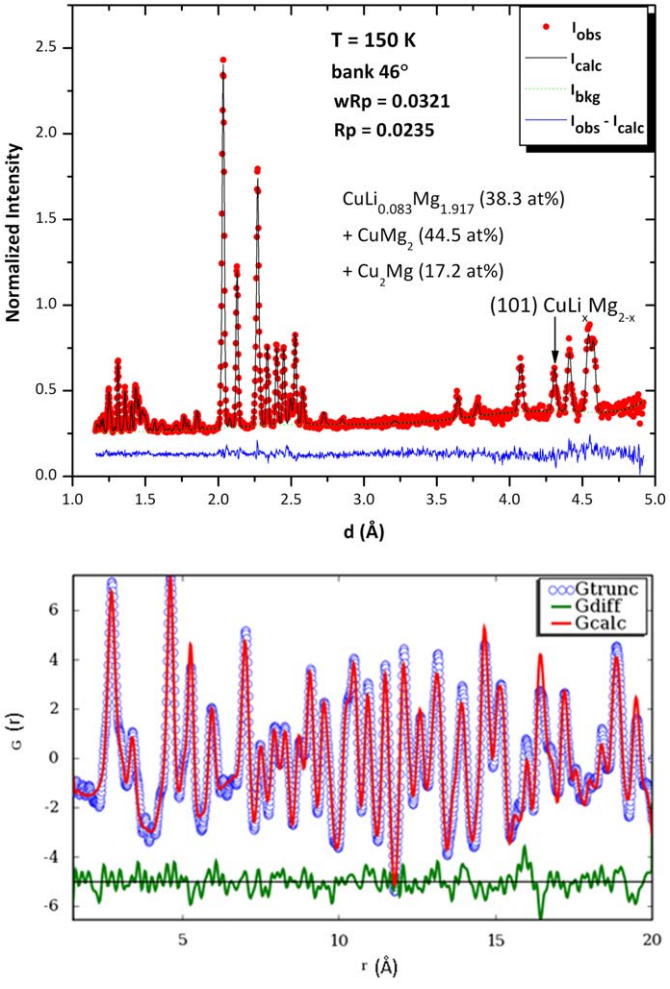

Fig. 2. NPDF after Rietveld refinement diffraction pattern at 150 K for 46° bank (the results at the graph are only due to the 46° bank). PDF experimental and fitted.

with steps of 0.01° and a counting time of 10 s at 303, 473, 523, 573 and 623 K [9]. Results from differential scanning calorimeter (DSC) have shown that $CuLi_xMg_{2-x}$ decomposes at approximately 702 K [9].

2.3. Neutron powder diffraction measurements (below room temperature)

Time-of-flight (TOF) neutron diffraction data were collected on the NPDF neutron diffractometer at the Manuel Lujan Neutron Scattering Center at Los Alamos National Laboratory. This instrument is a high-resolution powder diffractometer located 32 m from the neutron spallation target. The data were collected at 60 K (for 7.7 h), 150 K (for 6.4 h) and 300 K (for 6.2 h), at an average proton beam current of 100 μA, using the 46, 90, 119 and 148° banks, which cover a *d*-spacing range from 0.12 to 7.2 Å. A sample powder with 38.0 at% of $CuLi_xMg_{2-x}$, 44.8 at% of $CuMg_2$ and 17.2 at% of Cu_2Mg was manually grinded to a diameter of less than 37 μm and placed in a vanadium sample holder in a glove box under He. The vanadium sample holder contribution, at each *T*, was subsequently removed from the diffraction pattern. The structure was refined using the general structure analysis system (GSAS), a Rietveld profile analysis program developed by Larson and von Dreele [12]. Background coefficients, scale factors, phase fractions, profile function coefficients (sigma-1), sample absorption, atomic positions, lattice parameters, temperature factors, and occupancies (in the case of the phase $CuLi_xMg_{2-x}$ and for Mg and Li) were refined for the three phases (whenever applicable) making a total of 81 variables.

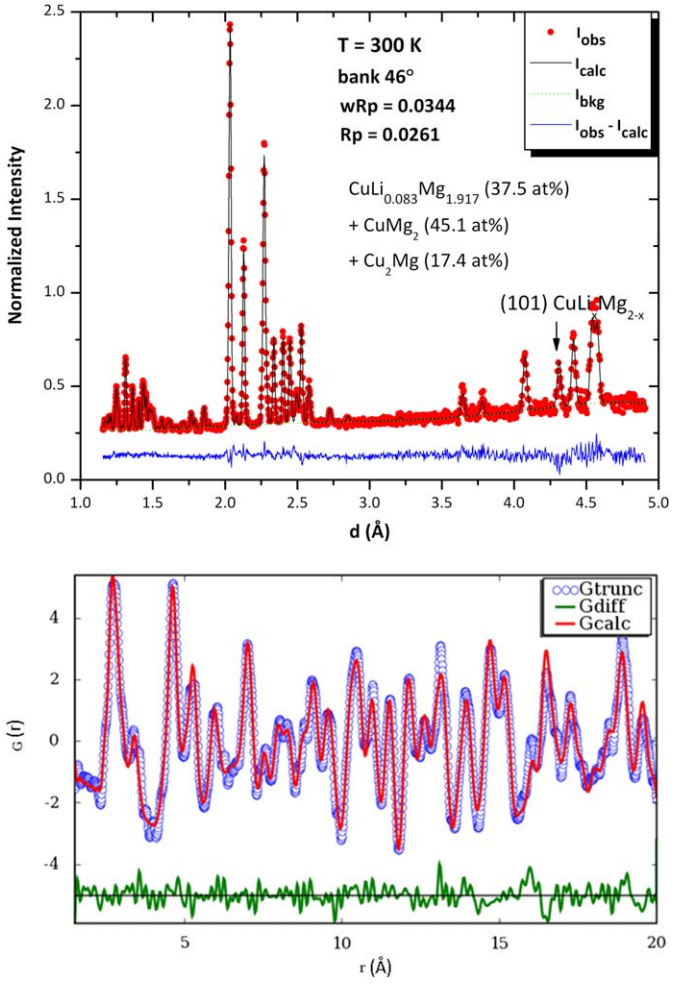

Fig. 3. NPDF after Rietveld refinement diffraction pattern at 300 K for 46° bank (the results at the graph are only due to the 46° bank). PDF experimental and fitted.

For NPDF data, pair distribution function (PDF), $G(r)$, was obtained via the Fourier Transform of the total diffraction pattern as indicated below,

$$G(r) = 4\pi r[\rho(r) - \rho_0] = \frac{2}{r}\int_0^{\infty} Q[S(Q) - 1]\sin(Qr)\,dQ \quad (1)$$

where $\rho(r)$ is the microscopic pair density, ρ_0 is the average atomic number density, and r the radial distance. Q is the momentum transfer ($Q = 4\pi\sin(\theta)/\lambda$). $S(Q)$ is the normalized structure function determined from the experimental diffraction intensity [13]. PDF yields the probability of finding pairs of atoms separated by a distance *r*. PDF fittings were performed using the software PDFgui [14].

2.4. Neutron powder diffraction measurements (above room temperature)

Time-of-flight (TOF) neutron diffraction data were also collected on the neutron powder diffractometer (HIPPO) at the Manuel Lujan Neutron Scattering Center at Los Alamos National Laboratory. This instrument achieves very high neutron count rates by virtue of a short (9 m) flight path and large detector solid angle. The data were collected at approx. 313 K (for 1.6 h), 373 K (for 6.3 h), 453 K (for 2 h) and 523 K (for 0.90 h), at an average proton beam current of 100 μA, using the 90, and 144.45° banks, which cover a *d*-spacing range from 0.12 to 4.80 Å.

A sample powder with 70.4 at% of $CuLi_xMg_{2-x}$, 21.0 at% of $CuMg_2$ and 8.6 at% of Cu_2Mg was enclosed in an aluminum sample holder to which a resistive heater and a thermocouple was attached. A standard laboratory temperature controller maintained the desired temperature during the measurement. A capillary tube attached to the sample holder allowed for pressure measurements and gas loading during the experiments.

The aluminum sample holder contributes to the diffraction pattern. An aluminum phase was refined in all our data sets. The measured sample (including Al) had: 42.1 wt% (14.6 at%) of $CuLi_xMg_{2-x}$+$CuMg_2$+Cu_2Mg and 57.9 wt% (86.4 at%) of Al. The structure was refined using GSAS. Background coefficients, scale factors, phase fractions, profile function coefficients (sigma-1),

Table 2
PDF fittings' results at 60, 150 and 300 K obtained from NPDF data.

T=60 K (NPDF) R_{wp}=18.6%		
$CuLi_xMg_{2-x}$ (x=0.03 ± 0.04)	$CuMg_2$	Cu_2Mg
Hexagonal–$P6_222$ (180)	Orthorhombic–Fddd (70)	Cubic–Fd-3m (227)
a=b=5.250 (2) Å; c=13.666 (7) Å;	a=5.240 (5) Å; b=9.003 (8) Å; c=18.25 (2) Å	a=b=c=7.058 (2) Å;
T=150 K (NPDF) R_{wp}=17.6%		
$CuLi_xMg_{2-x}$ (x=0.10 ± 0.04)	$CuMg_2$	Cu_2Mg
Hexagonal–$P6_222$ (180)	Orthorhombic–Fddd (70)	Cubic–Fd-3m (227)
a=b=5.258 (3) Å; c=13.67 (1) Å	a=5.248 (8) Å; b=9.01 (1) Å; c=18.25 (2) Å	a=b=c=7.066 (2) Å
T=300 K (NPDF) R_{wp}=17.6%		
$CuLi_xMg_{2-x}$ (x=0.08 ± 0.06)	$CuMg_2$	Cu_2Mg
Hexagonal–$P6_222$ (180)	Orthorhombic–Fddd (70)	Cubic–Fd-3m (227)
a=b=5.273 (4) Å; c=13.70 (2) Å	a=5.30 (2) Å; b=9.00 (2) Å c=17.92 (5) Å	a=b=c= 7.082 (4)

sample absorption, atomic positions, lattice parameters, temperature factors, and occupancies (in the case of the phase $CuLi_xMg_{2-x}$ and for Mg and Li) were refined for the four phases (whenever applicable) making a total of 63 variables.

3. First principles data

In a solid, where there are upward of 10^{24} interacting electrons and nuclei per cubic centimeter, the resolution of the many body Schrödinger equation for the electronic wavefunctions and energy eigenvalues is a big challenge. However, based on the periodicity of the structure of pure elements and perfectly ordered compounds, Bloch's theorem shows that it is only necessary to solve the many body Schrödinger equation within one unit cell; in the case of disordered compounds that is not the case and it is necessary to solve it within a supercell. The basic information that one wishes to obtain from quantum mechanical calculations in solids is the total electronic energy for various arrangements of atoms on various lattices.

One of the most sophisticated solutions to the quantum mechanical problem in solids lies within the framework of the density functional theory (DFT) [15] using the local density approximation (LDA) [16] or the Generalized Gradient Approximation (GGA) [17]. The basic notion of these theories is to replace the true interacting many-body-system with a system of one electron in an effective potential due to all of the other electrons and nuclei. From a fundamental point of view, the one-electron functions are a unique tool for calculating the total energy and the electronic density of states; these functions have no particular physical meaning. But this simplification of the problem needs a self-consistent calculation and it is one of the major technical problems in the *ab initio* approach [18].

Density functional theory calculations with projector augmented wave (PAW) pseudopotentials [19], as implemented in the Vienna *Ab Initio* Simulation Package (VASP) code [20], implemented in MedeA [21], were performed. A plane wave cutoff of 355.18 eV, and *k*-spacings of $0.230 \times 0.230 \times 0.230\,\text{Å}^{-1}$ were used. Calculations were done in real space and were performed with *P*1 space group supercells containing 144 atoms (48 atoms of Cu, 96-*n* of Mg, and *n*=0 to 12 of Li). The supercells contained as many atoms as possible to allow better approximations with the real Li concentrations (but such that the time spent on calculations were not completely impractical). Since $CuLi_xMg_{2-x}$ is a disordered structure, it had to be obtained by randomly substituting Mg by Li in several Wyckoff 6*f* positions (1/2, 0, *z*) or Wyckoff 6*i* positions (*x*, 2*x*, 0) or in both positions within the supercells. The generalized gradient approximation (GGA), and the Perdew–Burke–Ernzerhof (PBE) functional [22] were used, and no magnetic moments were included in the model.

The total energy was minimized with respect to the volume (volume relaxation), the shape of the unit cell (cell external relaxation), and the position of the atoms within the cell (cell internal relaxation).

The *ab initio* calculations furnish the total energy (or the cohesive energy) at $T=0$ K, E^{Φ}. The energy of formation is easily

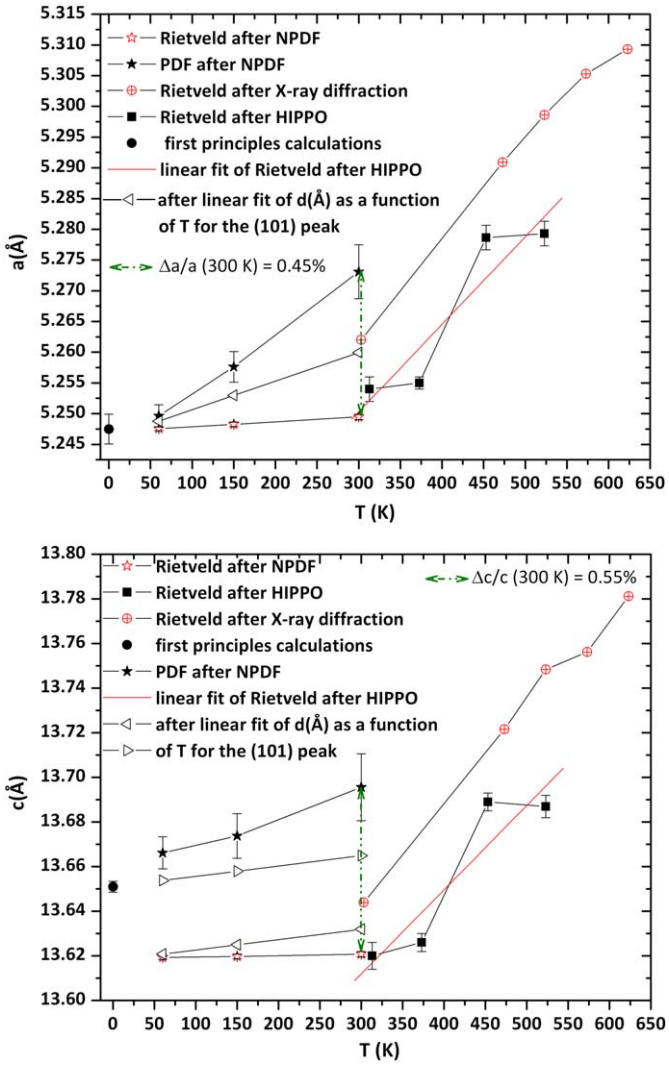

Fig. 4. Lattice parameters of the phase $CuLi_xMg_{2-x}$ as a function of the absolute temperature. It can be observed a linear dependence from the lattice parameters towards the temperature between 60 and 300 K as well as a small difference between lattice parameters obtained by first principles and obtained after refinement of the experimental data. Notice that the slope of the fitting line between 300 and 523 K is very similar to that obtained by X-ray diffraction [9]. It can also be observed that results obtained by PDF fitting differ 0.45% in the case of *a* and 0.55% in the case of *c*, at 300 K. Lattice parameters calculated using the slope obtained after plotting the interatomic distance *d*, as a function of temperature for the (101) peak were also plotted (note that the only peaks that were not overlapped with peaks from another phase, depend on *a* and *c*). As the phase is not isotropic, the use of this value is not completely correct. Nonetheless, it allows us to be more confident about the non-interference of $CuLi_xMg_{2-x}$ and $CuMg_2$ during calculations, since these two phases have several overlapping peaks.

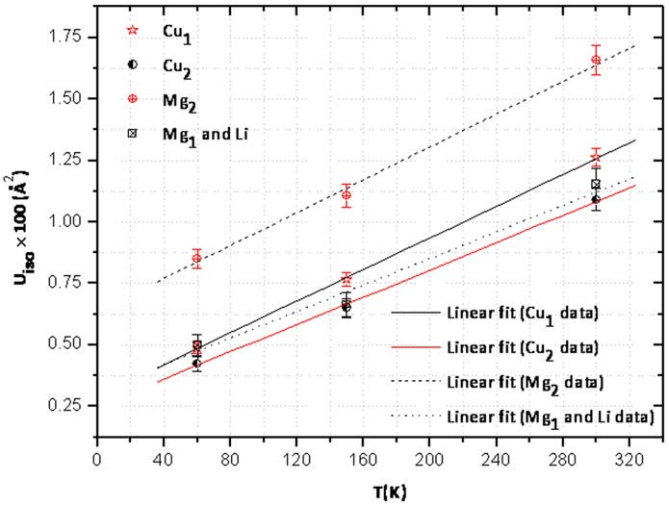

Fig. 5. Isotropic temperature factors for all the atoms of the phase $CuLi_xMg_{2-x}$ as a function of the absolute temperature. It can be seen that between 60 and 300 K all temperature factors behave linearly and increase similarly with temperature. U_{iso} is related with the Debye–Waller factor, B_{iso}, by: $B_{iso}=8\pi^2U_{iso}$.

calculated by the relation

$$\Delta_f E = E^{\Phi} - \sum x_i E_i^O \quad (2)$$

where E_i^O is the total energy (or cohesive energy) of i in its stable state at T=0 K. In the following we will assume that the enthalpy of formation is equal to the energy of formation.

In addition to the total energies, *ab initio* calculations allowed us to obtain the values of the lattice parameters at 0 K. We performed most of the calculations for $CuLi_xMg_{2-x}$ at least twice (from 1 to 5 atoms of Li calculations were performed three or more times) with different random Li positions.

We also calculated the X-ray diffraction pattern from the *ab initio* results. The code is implemented in MedeA and is based on the LAZY-PULVERIX computer program [23] that calculates the position of the diffraction lines from Bragg's law and their d-spacings. The diffraction intensity I_{hkl} is calculated as,

$$I_{hkl} = MLPF_{hkl}^2 \quad (3)$$

where M is the multiplicity factor of a powder line, L is the Lorentz factor and P is the polarization factor. The structure factor F_{hkl} is defined by,

$$F_{hkl} = \sum_{i}^{unit\text{-}cell} f_j O_j \exp[2\pi i(hx_j + kx_j + lz_j)] \exp\left(-B_j \frac{\sin^2\theta}{\lambda^2}\right) \quad (4)$$

where f_j is the atomic scattering factor of atom j, O_j is the occupation factor at site x_j, y_j, z_j, for atom j and B_j the Debye–Waller factor in Å^2 for atom j.

Table 3
Rietveld refinement's results at 313, 373, 453 and 523 K obtained from NPDF data.

~313 K (HIPPO) wR_p=3.79%; R_p=2.89% Wt. Frac. ($CuLi_{0.09}Mg_{1.91}$)=0.280 (8); Wt. Frac. ($CuMg_2$)=0.090 (3); Wt. Frac. (Cu_2Mg)=0.041 (1); Wt. Frac. (Al)=0.589 (7); $CuLi_{0.09}Mg_{1.91}$: hexagonal–$P6_222$ (180) a=b=5.254 (2) Å; c=13.620 (6) Å; ρ=3.384 g/cm^3	$CuMg_2$: orthorhombic–Fddd (70) a=5.264 (4) Å; b=9.026 (5) Å ; c=18.33 (1) Å; ρ=3.422 g/cm^3
Cu1: x=0; y=0; $z=\frac{1}{2}$; occ.=1; $U_{iso}\times100$=1.3 (1) Å^2 Cu2: $x=\frac{1}{2}$; y=0; $z=\frac{1}{2}$; occ.=1; $U_{iso}\times100$=1.4 (1) Å^2 Mg1: $x=\frac{1}{2}$; y=0; z=0.1092 (4); occ.=0.91 (2); $U_{iso}\times100$=1.4 (2) Å^2 Mg2: x=0.164 (1); y=0.328 (2); z=0; occ.=1; $U_{iso}\times100$=2.1 (2) Å^2 Li1: $x=\frac{1}{2}$; y=0; z=0.1092 (4); occ.=0.09 (2); $U_{iso}\times100$=1.4 (2) Å^2	
~373 K (HIPPO) wR_p=3.52%; R_p=2.36% Wt. Frac. ($CuLi_{0.08}Mg_{1.92}$)=0.297 (5); Wt. Frac. ($CuMg_2$)=0.083 (3); Wt. Frac. (Cu_2Mg)=0.051 (2); Wt. Frac. (Al)=0.569 (5); $CuLi_{0.08}Mg_{1.92}$: hexagonal–$P6_222$ (180) a=b=5.255 (1) Å; c=13.626 (4) Å ρ=3.386 g/cm^3	$CuMg_2$: orthorhombic–Fddd (70) a=5.262 (2) Å; b=9.033 (3) Å c=18.327 (6) Å; ρ=3.420 g/cm^3
Cu1: x=0; y=0; $z=\frac{1}{2}$; occ.=1; $U_{iso}\times100$=1.64 (9) Å^2 Cu2: $x=\frac{1}{2}$; y=0; $z=\frac{1}{2}$; occ.=1; $U_{iso}\times100$=1.04 (1) Å^2 Mg1: $x=\frac{1}{2}$; y=0; z=0.1111 (3); occ.=0.919 (8); $U_{iso}\times100$=1.5 (1) Å^2 Mg2: x=0.1719 (7); y=0.344 (1); z=0; occ.=1; $U_{iso}\times100$=2.0 (1) Å^2 Li1: $x=\frac{1}{2}$; y=0; z=0.1111 (3); occ.=0.081 (8); $U_{iso}\times100$=1.5 (1) Å^2	Cu1: $x=\frac{1}{8}$; $y=\frac{1}{8}$; z=0.4976 (3); occ.=1; $U_{iso}\times100$=1.3 (2) Å^2 Mg1: $x=\frac{1}{8}$; $y=\frac{1}{8}$; z=0.0416 (6); occ.=1; $U_{iso}\times100$=1.1 (3) Å^2 Mg2: $x=\frac{1}{8}$; y=0.4708 (1); $z=\frac{1}{8}$; occ.=1; $U_{iso}\times100$=1.37 (3) Å^2
~453 K (HIPPO) wR_p=3.38%; R_p=2.28% Wt. Frac. ($CuLi_{0.09}Mg_{1.91}$)=0.300 (6); Wt. Frac. ($CuMg_2$)=0.088 (3); Wt. Frac. (Cu_2Mg)=0.053 (2); Wt. Frac. (Al)=0.559 (6); $CuLi_{0.09}Mg_{1.91}$: hexagonal–$P6_222$ (180) a=b=5.279 (2) Å; c=13.689 (4) Å ρ=3.337 g/cm^3	$CuMg_2$: orthorhombic–Fddd (70) a=5.286 (2) Å; b=9.072 (3) Å c=18.406 (7) Å; ρ=3.376 g/cm^3
Cu1: x=0; y=0; $z=\frac{1}{2}$; occ.=1; $U_{iso}\times100$=1.9 (1) Å^2 Cu2: $x=\frac{1}{2}$; y=0; $z=\frac{1}{2}$; occ.=1; $U_{iso}\times100$=1.51 (9) Å^2 Mg1: $x=\frac{1}{2}$; y=0; z=0.1106 (3); occ.=0.91 (1); $U_{iso}\times100$=2.0 (1) Å^2 Mg2: x=0.1712 (8); y=0.342 (2); z=0; occ.=1; $U_{iso}\times100$=2.4 (1) Å^2 Li1: $x=\frac{1}{2}$; y=0; z=0.1106 (3); occ.=0.09 (1); $U_{iso}\times100$=2.0 (1) Å^2	Cu1: $x=\frac{1}{8}$; $y=\frac{1}{8}$; z=0.4984 (4); occ.=1; $U_{iso}\times100$=1.6 (3) Å^2 Mg1: $x=\frac{1}{8}$; $y=\frac{1}{8}$; z=0.0411 (6); occ.=1; $U_{iso}\times100$=1.3 (3) Å^2 Mg2: $x=\frac{1}{8}$; y=0.4741 (2); $z=\frac{1}{8}$; occ.=1; $U_{iso}\times100$=2.63 (3) Å^2
~523 K (HIPPO) wR_p=2.71%; R_p=1.91% Wt. Frac. ($CuLi_{0.09}Mg_{1.91}$)=0.282 (6); Wt. Frac. ($CuMg_2$)=0.089 (4); Wt. Frac. (Cu_2Mg)=0.050 (2); Wt. Frac. (Al)=0.579 (6); $CuLi_{0.09}Mg_{1.91}$: hexagonal–$P6_222$ (180) a=b=5.279 (2) Å; c=13.687 (5) Å ρ=3.334 g/cm^3	$CuMg_2$: orthorhombic–Fddd (70) a=5.285 (2) Å; b=9.076 (4) Å c=18.406 (8) Å; ρ=3.374 g/cm^3
Cu1: x=0; y=0; $z=\frac{1}{2}$; occ.=1; $U_{iso}\times100$=1.9 (1) Å^2 Cu2: $x=\frac{1}{2}$; y=0; $z=\frac{1}{2}$; occ.=1; $U_{iso}\times100$=1.55 (1) Å^2 Mg1: $x=\frac{1}{2}$; y=0; z=0.1093 (4); occ.=0.91 (1); $U_{iso}\times100$=2.0 (2) Å^2 Mg2: x=0.1692 (9); y=0.338 (2); z=0; occ.=1; $U_{iso}\times100$=2.3 (2) Å^2 Li1: $x=\frac{1}{2}$; y=0; z=0.1093 (4); occ.=0.09 (1); $U_{iso}\times100$=2.0 (2) Å^2	Cu1: $x=\frac{1}{8}$; $y=\frac{1}{8}$; z=0.4978 (4); occ.=1; $U_{iso}\times100$=1.5 (3) Å^2 Mg1: $x=\frac{1}{8}$; $y=\frac{1}{8}$; z=0.0442 (6); occ.=1; $U_{iso}\times100$=1.3 (3) Å^2 Mg2: $x=\frac{1}{8}$; y=0.4726 (2); $z=\frac{1}{8}$; occ.=1; $U_{iso}\times100$=2.5 (4) Å^2

We used the MedeA empty space finder (ESF) [21] to analyze the empty spaces of the $CuLi_xMg_{2-x}$ supercell. The ESF algorithm divides the supercell into so-called Voronoi cells around each atom [24]. (A Voronoi cell is defined to be the volume enclosing all points that are closer to the center atom than to all other atoms). The ESF module positions non-overlapping spheres at the vertices of the resulting polyhedral grid and maximizes their radii. In doing so the physical size of different atomic species is taken into account through a set of covalent radii.

4. Results and discussion

4.1. Analysis of the diffraction data

The results from the refined data from NPDF at 60, 150 and 300 K can be found in Table 1 and indicate very good agreement between the experimental and model powder patterns. Phase fractions were varied for each pattern; the difference between the results is less than the refinement error, indicating phase stability over the investigated range of temperatures. The same statement is valid for the Li occupation and atomic parameters for both the Cu_xLiMg_{2-x} and $CuMg_2$ phases. Figs. 1–3 show the diffraction patterns at 60, 150 and 300 K and the Rietveld fits.

Results from PDF fittings at 60, 150 and 300 K can be found in Table 2 and Figs. 1–3. They indicate good agreement between the experimental and fitted curves. The error associated with each parameter obtained by PDF fitting is always higher than obtained with Rietveld, still, for 300 K where this difference is more valuable, the associated errors are $\Delta a/a$=0.45% and $\Delta c/c$=0.55% (Fig. 4).

In Fig. 4 it can be observed the result of the calculation of the lattice parameters after obtaining the slop of the interplanar distance d(Å) of the peak corresponding to the reflection (101) for Cu_xLiMg_{2-x} as a function of temperature using different values for

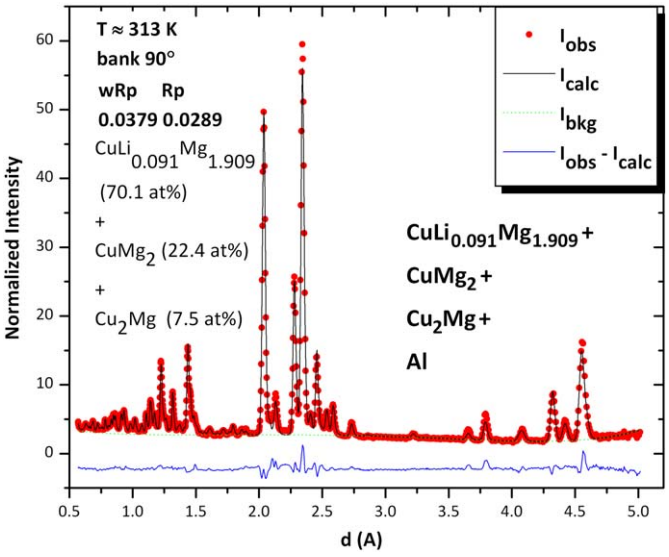

Fig. 6. HIPPO diffraction pattern at 313 K for bank 90° (the results at the graph are only due to the 90° bank).

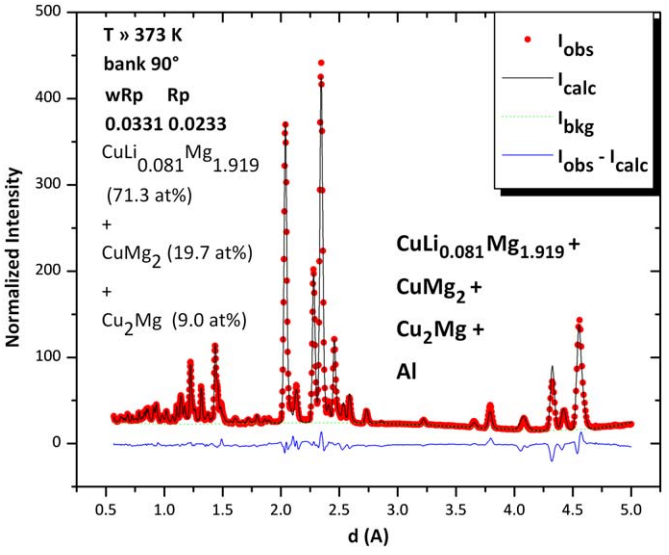

Fig. 7. HIPPO diffraction pattern at 373 K for bank 90° (the results at the graph are only due to the 90° bank).

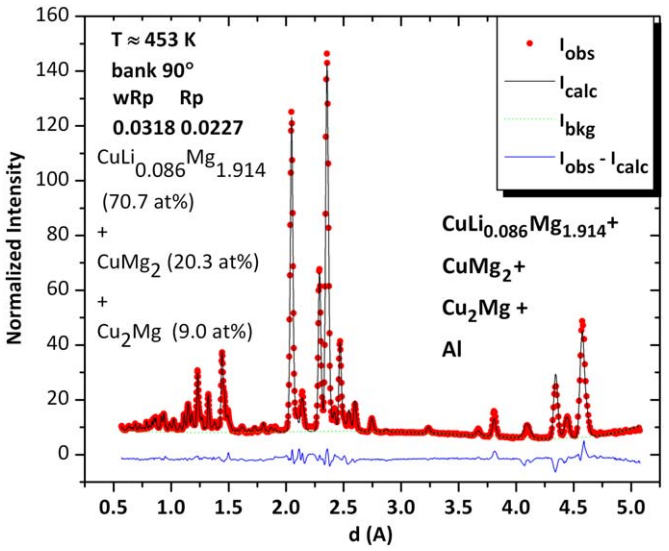

Fig. 8. HIPPO diffraction pattern at 453 K for bank 90° (the results at the graph are only due to the 90° bank).

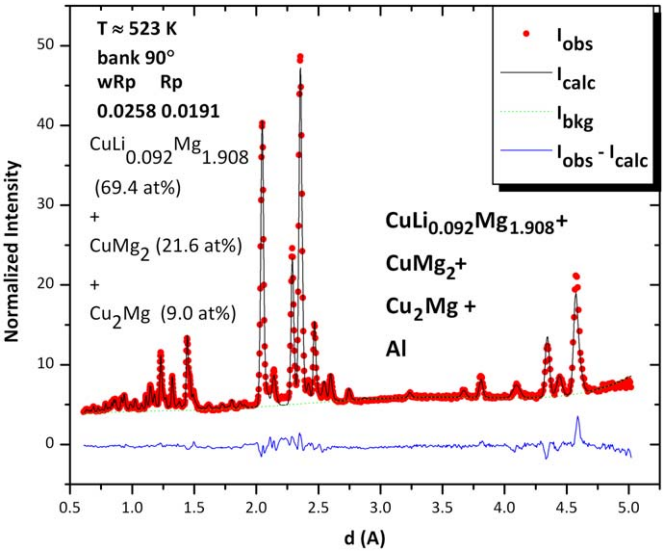

Fig. 9. HIPPO diffraction pattern at 523 K for bank 90° (the results at the graph are only due to the 90° bank).

a and c at T=0 K. Although this peak, as the other more intense non-overlapping ones, depends on both a and c lattice parameters and thus the extrapolation for a and c temperature dependence is not straight forward, we wanted to ensure that the calculations of the parameters of Cu_xLiMg_{2-x} were not interfering too much with those of $CuMg_2$ since these two phases have many overlapping peaks.

The lattice parameters of the phase Cu_xLiMg_{2-x} and the isotropic thermal parameters seem to depend linearly on temperature (Figs. 4 and 5) between 60 and 300 K.

A harmonic crystal does not undergo thermal expansion since its equilibrium size does not depend on temperature. The thermal expansion of solids is a consequence of the anharmonicity of the lattice vibrations. The earliest approach to lattice vibrations was Einstein's [25]. He proposed that all the N atoms of the crystal vibrate with $3N$ equal frequencies as harmonic oscillators. Beyond Einstein's approach, the Debye–Grüneisen approximation [26] is a good starting point for describing the contribution of lattice vibrations to the thermal expansion of solid crystals [27]. The theory is only directly applicable to crystals containing a single kind of atom; however, it has been used with success with simple compounds and with elements which do not have cubic symmetry [28]. Krishnan et al. [29] proposed an extension of Grüneisen's law for an anisotropic crystal that would depend on two different thermal expansion coefficients (with respect to a=b and to c). Thus, we are expecting to find the expression of Grüneisen's law for a=b and for c, independently (Fig. 4).

For metals, on the other hand, the excitation of electrons is as important as that of phonons; when included, it gives different behavior for the thermal expansion coefficient at low temperature.

We have obtained for Cu_xLiMg_{2-x} the expansion coefficient with respect to a, $\alpha_a=(1/a_{340\,K})da/dT$ (at constant pressure), approx. equal to $2.4\times10^{-5}\,K^{-1}$. The expansion coefficient with respect to c, $\alpha_c=(1/c_{340\,K})dc/dT$ (at constant pressure), is approx. equal to $0.8\times10^{-5}\,K^{-1}$. The expansion coefficient of Cu is $1.7\times10^{-5}\,K^{-1}$ and of Mg is $0.8\times10^{-5}\,K^{-1}$ at 273 K [30]. We have chosen 340 K to calculate the thermal expansion coefficient because, at this temperature, we are already in the high temperature range of our measurements.

The Debye–Waller factors, B_{iso}, that can be obtained from U_{iso} (Fig. 5), by making $B_{iso}=8\pi^2U_{iso}$ were also found to vary linearly between 60 and 300 K; additionally, all atoms seem to behave in a similar way with increasing temperature since the slope of the straight lines in Fig. 5 is very similar.

The results from the refined data from HIPPO at approximately, 313, 373, 453 and 523 K can be found in Table 3 and show good agreement between experimental and model powder patterns. On HIPPO the aluminum sample holder diffracts strongly, and the weight fraction of Cu_2Mg becomes relatively low (4–5 wt%). Refinement results for this phase were not included in Table 3 because the isotropic temperature factors became unstable and we were forced to constrain them. Still, the results seem to be very consistent *vide*, for example, Li occupancy and the atomic parameters for both the Cu_xLiMg_{2-x} and $CuMg_2$ phases. Figs. 6–9 show the diffraction patterns at 313, 373, 453 and 523 K together with the Rietveld fits.

Fig. 4 shows the difference between the XRD data and the neutron diffraction data obtained on HIPPO. Notice that the relative difference between results obtained with X-ray and obtained with neutrons never exceeds 0.4% in the case of a and 0.5% in the case of c. Additionally, the slope of the fitting line between 300 and 523 K seems to be similar in both cases. Small differences between neutron diffraction and X-ray diffraction are expected since these two techniques "see" different constituents of the atom.

The NPDF 300 K results are very similar to the 313 K HIPPO results, which is one more indicator of the results' coherence.

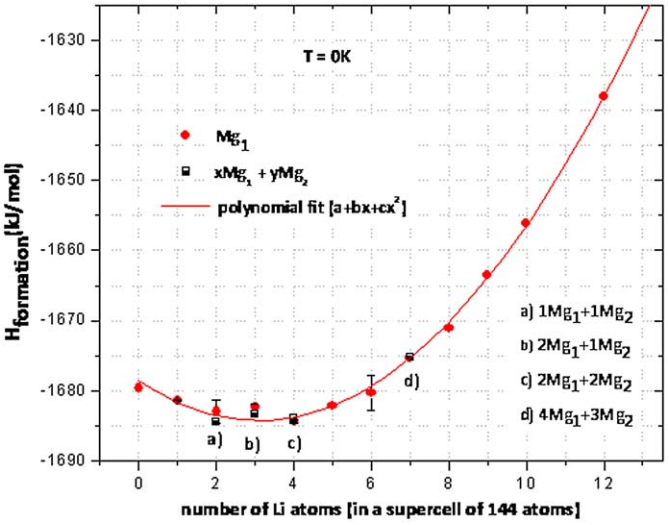

Fig. 10. First principles (*ab initio*) calculated enthalpies of formation for a mole with 144 atoms of the phase $CuLi_xMg_{2-x}$ in which 48 atoms are of Cu, $96-n$ are of Mg and n of Li (x=n/48). It can be observed that the most stable composition corresponds to n between 3 and 4 ($x\in$ [0.0625,0.0833]).

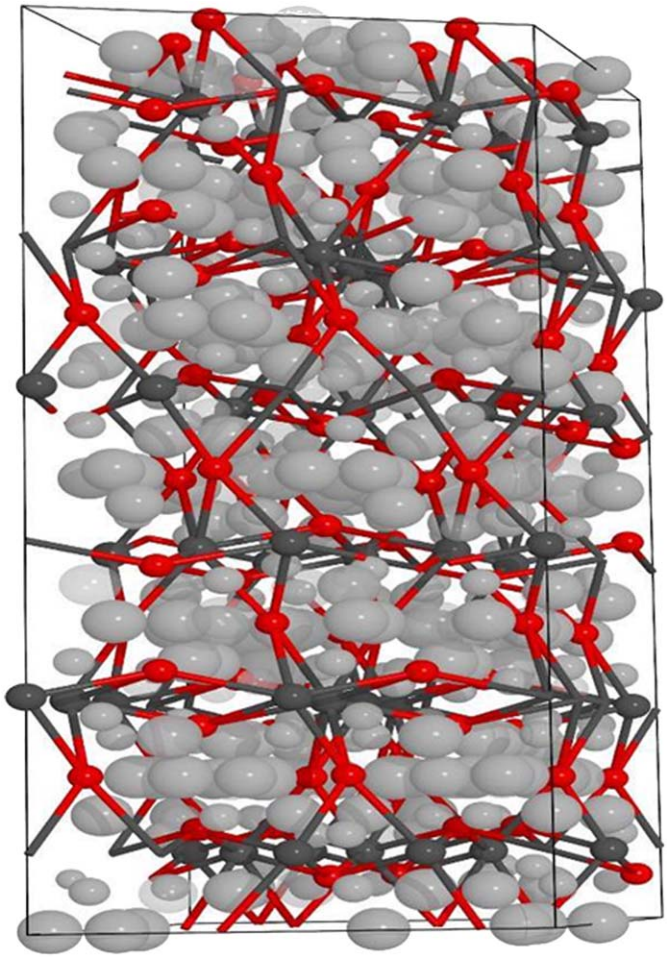

Fig. 11. Supercell of the phase $CuLi_xMg_{2-x}$ (x=0) with calculated empty spaces (in light grey: empty spaces, in dark grey: Cu atoms, in red: Mg atoms). (For interpretation of the references to the color in this figure legend, the reader is referred to the web version of this article.)

4.2. Analysis of the first-principles data

We studied the enthalpy of formation of the alloy $CuLi_xMg_{2-x}$ as a function of the number of Li atoms in a supercell with 144 atoms in which 48 atoms are of Cu, 96-n are of Mg and n of Li ($x=n/48$). The most stable composition (that has the lowest enthalpy of formation) corresponds to n between 3 and 4 ($x\in[0.0625,0.0833]$) (Fig. 10).

One of the purposes of this work was to determine which structure was more stable: $CuLi_{0.34}Mg_2$ (where Li occupies some of the Wyckoff 12k position of a $P6_222$ hexagonal structure) or $CuLi_xMg_{2-x}$ (with $x\cong 0.1$, in which Li occupies some of the Mg Wyckoff 6f position of a $P6_222$ hexagonal structure). For that, we have used the minimized structure of a supercell (Fig. 11) with $n=0$ ($x=0$; $CuMg_2$ with $P6_222$ hexagonal structure) and with $n=4$ ($x=0.0833$; $CuLi_{0.0833}Mg_{1.9167}$ with $P6_222$ hexagonal structure) and calculated the empty space using the ESF MedeA module (Fig. 11). Results show that in the first case the radii of the empty spaces found are $0.410\,\text{Å}\le r\le 0.650\,\text{Å}$ and in the second case $0.397\,\text{Å}\le r\le 0.666\,\text{Å}$. As the covalent radius of Li is 0.68 Å [31], we do not expect to have Li occupy interstitial sites, even if some atoms of Li substitute the Mg atoms. Still, we have tried to refine the NPDF data at 60 and 150 K for several possibilities that always contained Li atoms in interstitial sites (just in interstitial and both substituting Mg and in an interstitial site) and we have always obtained negative occupancies for these atoms.

Upon using first-principles calculations, it was not possible to determine which Mg sites are occupied with Li (Fig. 10).

In a 2007 article, Zhou et al. [32] calculated the enthalpy of formation of a mole of $CuMg_2$: $\Delta H=-13.20$ KJ/mol within the *Fddd* space group. In the present work we have obtained for $CuMg_2$ with hexagonal structure belonging to the $P6_222$ space group $\Delta H=-11.66$ KJ/mol, which is consistent with the results of Zhou et al. [32] since the orthorhombic *Fddd* structure is the stable structure for pure $CuMg_2$. What we expected is that the substitution of Mg by Li would make the *Fddd* structure of the solid solution of $CuMg_2$ less stable until $CuLi_xMg_{2-x}$ ($x=0.08$) in the hexagonal $P6_222$ structure became more stable (note that the difference between the enthalpies of formation is small, of 1.5 KJ/mol of atoms).

In the same article [32] the enthalpy of formation of $CuMg_2$ at 298 K was also determined using the CALPHAD method [33]: $\Delta H=-9.6$ KJ/mol (CALPHAD uses experimental results and theoretical models for the structure of the phases and for its Gibbs energies). The experimental value from [34] is $\Delta H=-9.55$ KJ/mol. As the enthalpy of formation of $CuMg_2$ will vary from -13.20 KJ/mol ($T=0$ K) to -9.6 KJ/mol ($T=298$ K), it still seems possible that at room temperature $CuLi_xMg_{2-x}$ ($x=0.08$) in the hexagonal $P6_222$ structure will be more stable than the orthorhombic solid solution of $CuMg_2$ for the same composition of Li. In Fig. 12, the XRD calculated pattern of $CuLi_{0.08}Mg_{1.92}$ is compared with an experimental one for a sample containing both $CuLi_{0.08}Mg_{1.92}$ and Cu_2Mg.

5. Summary

Prepared samples were invariably contaminated with Cu_2Mg, $CuMg_2$, or both. Nonetheless, the final product contained approximately 81.0 wt% (75.6 at%) of Cu_xLiMg_{2-x}, the phase we wanted to study. Thermodynamics is probably responsible for this limitation on sample composition. Indeed, preliminary tests indicate that the final amount of $CuLi_xMg_{2-x}$ material recovered depends (at the very least) on the reaction temperature and (to a lesser extent) on reaction time. We have taken advantage of this fact to extract refined parameters of $CuMg_2$ between 60 and 523 K, and of Cu_2Mg between 60 and 300 K as well as of $CuLi_xMg_{2-x}$ between 60 and 523 K.

Both neutron diffraction and first-principles calculations indicate that the composition of the ternary compound should be $CuLi_xMg_{2-x}$ ($x=0.08$).

Neither with first-principles calculations, nor with neutron diffraction, was it possible to distinguish between structures where Li substituted Mg at each of its sites individually or at both

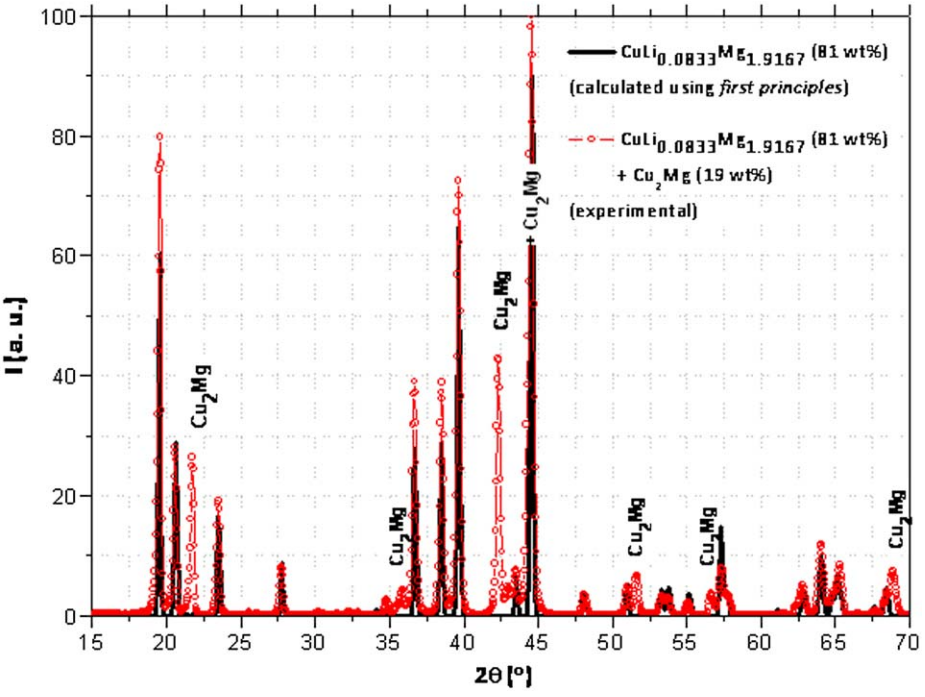

Fig. 12. Comparison between the diffraction pattern obtained using first principles and the LAZY PULVERIX code implanted in MedeA and XRD obtained at room temperature with a sample powder containing 81.0 wt% (75.6 at%) of $CuLi_xMg_{2-x}$ and 19.0 wt% (24.4 at%) of Cu_2Mg. The calculated pattern was obtained for a $B_{iso}=1.00\,\text{Å}^2$ for all the atoms.

sites. The refinement of the diffraction data revealed that the reliability factors did not change much for the three different structures, and nothing unusual happened with the other parameters (such as, for example, the Li occupancy). The calculated enthalpy of formation curve also shows differences for different occupancies of Li for the same number of Li atoms that are within the error bar. Thus we cannot draw any conclusions regarding the substituted Mg sites based on Rietveld refinement and first-principles calculations. The neutron data agrees best with the results of first-principles calculations when Li occupies Mg1 sites (1/2, 0, z). In this case, the Li occupancy corresponds to x=0.08 (in $CuLi_xMg_{2-x}$) when this value is calculated by means of Rietveld refinement and using first-principles methods. This agreement does not happen for the other possibilities. With PDF fittings we were allowed to go further. PDF does not see the average but the local structure and with PDF all results but those in which Li would substitute Mg1 sites, gave negative occupancies for Li. For Li substituting Mg1 we have obtained an average composition for $CuLi_xMg_{2-x}$ (x=0.07) which is in agreement with the other obtained results.

By calculating empty space in our structures, we found that it was unlikely that Li can occupy interstitial sites, but we note that it is possible for H to occupy these empty spaces.

Acknowledgments

M.H. Braga would like to acknowledge Portuguese Science Foundation, FCT, for the sabbatical grant (SFRH/BSAB/791/2008). This work has benefited from the use of NPDF and HIPPO at the Lujan Center at Los Alamos Neutron Science Center, funded by DOE Office of Basic Energy Sciences. Los Alamos National Laboratory is operated by Los Alamos National Security LLC under DOE Contract DE-AC52-06NA25396. The upgrade of NPDF has been funded by NSF through grant DMR 00-76488.

Appendix A. Supplementary material

Supplementary data associated with this article can be found in the online version at doi:10.1016/j.jssc.2009.09.010.

References

[1] M.H. Braga, J. Ferreira, L. Malheiros, J. Alloys Compds. 436 (2007) 278–284.
[2] M.H. Braga, L.F. Malheiros, International patent, WO2007046017.
[3] M.H. Braga, L.F. Malheiros, National patent, PT103368.
[4] M.H. Braga, A. Acatrinei, M. Hartl, S. Vogel, Th. Proffen, L. Daemen, ICNS, Knoxville, 2009.
[5] J.J. Reilly, R.H. Wiswall, Inorg. Chem. 6 (12) (1967) 2220–2223.
[6] L. Schlapbach, A. Zuttel, Nature 414 (2001) 353–358.
[7] J. Senegas, A. Mikou, M. Pezat, B. Darriet, J. Solid State Chem. 52 (1984) 1–11.
[8] V. Hlukhyy, U.Ch. Rodewald, R. Pöttgen, Z. Anorg. Allg. Chem. 631 (2005) 2997–3001.
[9] M.H. Braga, J. Ferreira, L.F. Malheiros, M. Hamaläinen, Z. Kristallogr. 26 (Suppl.) (2007) 299–304.
[10] Match, 〈http://www.crystalimpact.com/〉, 2009.
[11] P.M. de Wolff, J.W. Visser, Absolute Intensities, Report 641.109, Technisch Physische Dienst, Delft, The Netherlands. Reprinted Powder Diffract 3 (1988) 202–204.
[12] A.C. Larson, R.B. von Dreele, GSAS Generalized Structure Analysis System, LANSCE, Los Alamos, 2004.
[13] T. Egami, S.J.L. Billinge, Underneath the Bragg-Peaks: Structural Analysis of Complex Materials, Elsevier Science B.V., Amsterdam, 2003.
[14] C.L. Farrow, P. Juhas, J.W. Liu, D. Bryndin, E.S. Bozin, J. Bloch, Th. Proffen, S.J.L. Billinge, J. Phys. Condens. Matter 19 (2007) 335219.
[15] P. Hohenberg, W. Kohn, Phys. Rev. 136 (1964) B864.
[16] W. Kohn, L.J. Sham, Phys. Rev. 140A (1965) 1133.
[17] J.P. Perdew, Y. Wang, Phys. Rev. B 45 (1992) 13244.
[18] C. Colinet, Intermetallics 11 (2003) 1095–1102.
[19] P.E. Blochl, Phys. Rev. B 50 (1994) 17953.
[20] G. Kresse, J. Furthmüller, Phys. Rev. B 54 (1996) 11169;
G. Kresse, J. Furthmüller, Comp. Mater. Sci. 6 (1996) 1;
G. Kresse, D. Joubert, Phys. Rev. B 59 (1999) 1758.
[21] MedeA, Materials Design, Inc., 〈http://www.MaterialsDesign.com〉, 2009.
[22] J.P. Perdew, K. Burke, M. Ernzerhof, Phys. Rev. Lett. 77 (1996) 3865;
J.P. Perdew, K. Burke, M. Ernzerhof, Phys. Rev. Lett. 78 (E) (1997) 1396.
[24] G. Voronoi, J. für die Reine und Angew. Math. 133 (1907) 97–178.
[23] K. Yvon, W. Jeitschko, E. Parthe, J. Appl. Cryst. 10 (1977) 73–74.
[25] A. Einstein, Ann. Phys. (Leipzig) 22 (1907) 180–800;
A. Einstein, Ann. Phys. (Leipzig) 34 (1911) 170 590.
[26] P. Debye, Ann. Phys. (Leipzig) 33 (1910) 442–489.
[27] T.H.K. Barron, M.L. Klein (1962) reedited in Phys. Rev. 127 (1997) 77.
[28] F. Sayetat, P. Fertey, M. Kessler, J. Appl. Cryst. 31 (1998) 121–127.
[29] R. Krishnan, R. Srinivasan, S. Devanarayan, Thermal Expansion of Crystals, Pergamon Press, London, 1979.
[30] Web Elements periodic table, 〈http://www.webelements.com/periodicity/coeff_thermal_expansion/〉, 2009.
[31] Cambridge Crystallographic Data Centre, 〈http://www.ccdc.cam.ac.uk/products/csd/radii/〉, 2008.
[32] S. Zhou, Y. Wang, F.G. Shi, F. Sommer, L.-Q. Chen, Z.-K. Liu, R.E. Napolitano, JPEDAV 28 (2007) 158–166.
[33] H.L. Lukas, S.G. Fries, B. Sundman, Computational Thermodynamics The Calphad Method, Cambridge, 2007.
[34] R.C. King, O.J. Kleppa, Acta Metall. 12 (1964) 87–97.

J Therm Anal Calorim (2012) 108:733–739
DOI 10.1007/s10973-011-2126-0

Study of the Cu–Li–Mg–H system by thermal analysis

M. H. Braga · J. A. Ferreira · M. J. Wolverton

MEDICTA2011 Conference Special Chapter

Abstract Finite fossil-fuel supplies, nuclear waste and global warming linked to CO_2 emissions have made the development of alternative/'green' methods of energy production, conversion and storage popular topics in today's energy-conscious society. These crucial environmental issues, together with the rapid advance and eagerness from the electric automotive industry have combined to make the development of radically improved energy storage systems a worldwide imperative. $CuMg_2$ has an orthorhombic crystal structure and does not form a hydride: it reacts reversibly with hydrogen to produce Cu_2Mg and MgH_2. However, $CuLi_xMg_{2-x}$ ($x = 0.08$) has a hexagonal crystal structure, just like $NiMg_2$, a compound known for its hydrogen storage properties. $NiMg_2$ absorbs up to 3.6 wt% of H. Our studies showed that not only $CuLi_xMg_{2-x}$ absorbs a considerable amount of hydrogen, but also starts releasing it at a temperature in the range of 40–130 °C. In order to determine the properties of the hydrogenated $CuLi_xMg_{2-x}$, absorption–desorption, Differential scanning calorimeter and thermogravimetric experiments were performed. Neutron spectra were collected to elucidate the behavior of hydrogen in the Li-doped $CuMg_2$ intermetallic. Using DFT calculations we were able to determine the best value for x in $CuLi_xMg_{2-x}$ and compare different possible structures for the $CuLi_xMg_{2-x}$ hydride.

M. H. Braga (✉)
CEMUC, Engineering Physics Department, Engineering Faculty, Porto University, R. Dr. Roberto Frias s/n, 4200-465 Porto, Portugal
e-mail: mbraga@fe.up.pt

M. H. Braga · M. J. Wolverton
Los Alamos National Laboratory (LANSCE), Los Alamos, NM 87545, USA

J. A. Ferreira
Laboratorio Nacional de Energia e Geologia, Rua da Amieira, Apartado 1089, 466-901 S. Mamede de Infesta, Portugal

Keywords DSC/TG · INS · Mg based alloys · Energy storage · Hydrides

Introduction

Efficient hydrogen storage remains a major technological obstacle toward the development of a hydrogen-based energy economy. Electric and hybrid vehicles use metal hydrides as the negative electrode (instead of cadmium) in their batteries [1, 2]. In fact, metal hydrides are widely used in consumer electronics rechargeable batteries. In Ni–MH, M is an intermetallic compound. The most common one has the AB_5 type, where A is a rare-earth mixture (e.g., La, Ce, Nd, Pr) and B is Ni, Co, Mn, and/or Al. Note that $LaNi_5H_6$, which is commonly used in batteries, stores only a maximum of 1.4 wt% of H. Another disadvantage of these materials for hydrogen storage is that lanthanides tend to be expensive and heavy.

We are currently investigating the Cu–Li–Mg–H system. The lighter and cheaper metals and our recent discovery that hydrogen can be reversibly stored in these compounds make them a very attractive alternative to lanthanide-based systems.

$CuMg_2$ has an orthorhombic crystal structure and does not form a hydride: it reacts reversibly with hydrogen to produce Cu_2Mg and MgH_2 [3]. However, $CuLi_xMg_{2-x}$ ($x = 0.08$) has a hexagonal crystal structure [4] (ICSD database [5]), just like $NiMg_2$, a compound known for its hydrogen storage properties. $NiMg_2$ absorbs up to 3.6 wt% H (of the hydride's weight) [6]. In spite of the fact that the percentage of hydrogen absorbed by $NiMg_2$ is enough to propitiate practical applications, the temperature at which the alloy desorbs hydrogen (282 °C (555 K) at 1 bar) is much too high for practical applications.

A comparison between the phase diagrams of the systems Cu–Mg and Ni–Mg shows that these binary systems form compounds with similar stoichiometry. $NiMg_2$ is formed by peritectic reaction of the elements at 759 °C (1,032 K) and $CuMg_2$ by congruent melting at 568 °C (841 K). The presence of Li lowers even further the melting point of $CuMg_2$ [7].

Since the enthalpy of formation of the hydride is related to that of the primary alloy [8], it was hypothesized that $CuLi_xMg_{2-x}$ might also be a hydrogen storage material similar to $NiMg_2$ [9]. Presumably, its advantage would be that it would release hydrogen at a lower temperature (possibly close to room temperature) [10].

Preliminary studies at the Los Alamos Neutron Scattering Center (LANSCE) showed that hydrogen unsaturated samples could desorb up to 4.4–5.3 wt% of hydrogen. Experiments furthermore shown that samples containing $CuLi_xMg_{2-x}$ will start desorbing hydrogen at a temperature from 40–130 °C where applications are easier to develop. Hence it should be possible to use this alloy with fuel cells or in batteries and hydrogen storage devices.

Sample preparation

The Cu–Li–Mg samples were prepared from the pure elements with a target composition of $CuLi_{0.1}Mg_{1.9}$. They were prepared by mixing stoichiometric amounts of Cu (electrolytic, 99.99% purity, 325 mesh), Mg (99.8% purity, 200 mesh, Alfa Aesar), and granules (approx. 2 × 2 × 3 mm) of Li (99% purity, Alfa Aesar). Because of the large vapour pressure of Mg, even below its melting point, the reagents were sealed in a stainless steel crucible in a dry box (He atmosphere). This eliminated possible reagent loss. The samples were heated in a tube furnace with a stirring device to ensure proper mixing of the heterogeneous starting mixture and complete dispersion of Li in the sample. Different reaction temperatures and times were used (from 450 °C for 24 h to 1,200 °C for 1–2 h). Regardless of reaction conditions, the samples invariably contained Cu_2Mg, $CuMg_2$, or both. Nonetheless, we obtained final products containing up to 82.5 at% (77.5 wt%) of $CuLi_xMg_{2-x}$. Since the structure of Cu_2Mg and $CuMg_2$ is known as well as their hydrogen storage behaviour; this complication translated merely in the refinement of additional phases in the neutron/X-ray powder diffraction patterns.

Samples were firstly characterized by means of X-ray diffraction (XRD) using a Rigaku Ultima III powder diffractometer, and their composition was roughly determined by means of the Match software, [11] which uses the "Reference Intensity Ratio method" RiR method) [12] to obtain phase fractions. Patterns were collected with CuK-alpha radiation with 2θ typically from 15° to 70° with steps of 0.02° and a counting time of 10 s per bin.

Hydrogen absorption experiments

A sample with approx. 74 at% of $CuLi_{0.08}Mg_{2-0.08}$, 20 at% of $CuMg_2$ and 6 at% of Cu_2Mg was grinded to obtain a powder with particle size of the order of 37 μm. The sample was then studied in a HPVA high pressure absorption analyser [13]. The latter gas adsorption analysers are designed to obtain high pressure adsorption isotherms of gases, such as hydrogen, using the static volumetric method. Two additional samples with –79 at% of $CuLi_{0.08}Mg_{1.92}$ and 21 at% of Cu_2Mg and –57 at% of $CuLi_{0.08}Mg_{1.92}$, 34 at% of $CuMg_2$ and 9 at% of Cu_2Mg– were measured too, to determine H_2 equilibrium pressure at different temperatures during the absorption process (Fig. 1).

The plot of the natural logarithm of the equilibrium pressure of hydrogen versus 1,000/T in which T is the absolute temperature in Kelvin allows us to understand that to equal equilibrium pressures will correspond very different temperatures when Cu–Li–Mg–H samples (with high initial content of $CuLi_{0.08}Mg_{1.92}$) are compared with MgH_2, $NiMg_2H_4$, or even with $Cu_2Mg + 3MgH_2$ [13]. Additionally, when the equilibrium pressure, at 200 °C, for a sample containing $CuLi_{0.08}Mg_{1.92}$–H is compared with

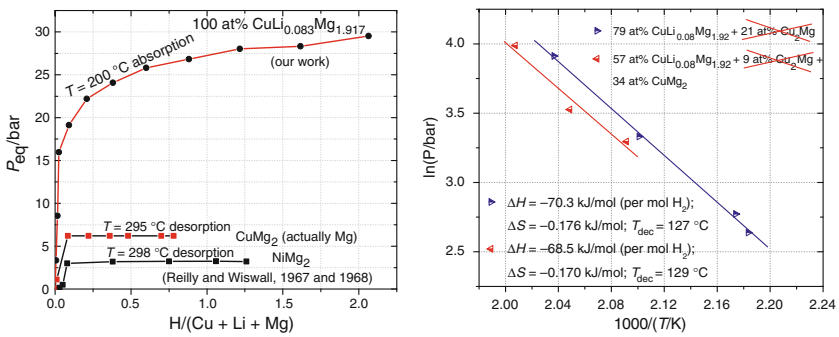

Fig. 1 *left* Absorption curve for a sample containing $CuLi_{0.08}Mg_{1.92}$ (considering that Cu_2Mg does not absorb hydrogen at 200 °C and at the referred pressures). *right* Natural logarithm of the equilibrium pressure versus 1,000/T for two samples with initial compositions (prior to hydrogen absorption) referred in the plot's legend

the equilibrium pressure of a sample containing $CuMg_2$, at 295 °C, the difference between plateau pressures can be higher than 21 bar [13] (Fig. 1). The latter means that $CuLi_{0.08}Mg_{1.92}$–H will release hydrogen at a much lower temperature.

Calculations of the decomposition temperature can be done, using:

$$G_{MH} - G_{H_2} = \Delta G = 0 \Leftrightarrow G^0_{MH} - G^0_{H_2} - R \cdot T \cdot \ln\left(\frac{P_{eq}}{P_0}\right) = 0 \quad (1)$$

$$\Delta G^0 = R \cdot T \cdot \ln\left(\frac{P_{eq}}{P_0}\right) = \Delta H^0 - T \cdot \Delta S^0 \quad (2)$$

$$\ln\left(\frac{P_{eq}}{P_0}\right) = \frac{\Delta H^0}{R} \cdot \frac{1}{T} - \frac{\Delta S^0}{R} \quad (3)$$

For

$$P_{eq} = P_0 \Rightarrow T_{dec} = \frac{\Delta H^0}{\Delta S^0} \quad \text{(per mol of } H_2\text{)} \quad (4)$$

in which G is the Gibbs energy, MH (metal-hydride), R the ideal gas constant, P_{eq} and P_0 is the equilibrium and atmospheric pressure, respectively, H^0 the enthalpy and S^0 the entropy when $P_{eq} = P_0$.

The previous calculations for the Cu–Li–Mg–H system lead to decomposition temperatures of 400 K (127 °C) for a sample containing – 79 at% of $CuLi_{0.08}Mg_{1.92}$ and 21 at% of Cu_2Mg– and of 402 K (129 °C) for a sample containing – 57 at% of $CuLi_{0.08}Mg_{1.92}$, 34 at% of $CuMg_2$ and 9 at% of Cu_2Mg. Cu_2Mg does not absorb hydrogen at the temperatures shown in Fig. 1.

Hydrides stability depends mostly on the enthalpy term (ΔH^0) as ΔS^0 is usually around -130 J (mol H_2)$^{-1}$ K^{-1}, which roughly corresponds to the H_2 molecule losing its translational degrees of freedom upon transformation from the gas phase into the solid state of the hydride. Nevertheless, in this system, ΔS^0 is higher than usually but still into the boundaries of the entropy of formation of the hydrides studied in the literature ($\Delta S(FeTi) \approx -0.104$ kJ/mol H_2 [14]; $\Delta S(LaNi_5) \approx -0.105$ kJ/mol H_2 [14]; $\Delta S(VH_2) \approx 0.141$ kJ/mol H_2 [14]; $\Delta S(PdH_{0.7}) \approx -0.098$ kJ/mol H_2 [14]; ΔS(CuLiMg–H) ≈ -0.170 kJ/mol H_2; $\Delta S(CuMg_2) \approx 0.138$ kJ/mol H_2 [15]; $\Delta S(NiMg_2) \approx -0.123$ kJ/mol H_2 [14]; $\Delta S(MgH_2) \approx -0.135$ kJ/mol H_2 [16]; $\Delta S(NaH) \approx -0.164$ kJ/mol H_2 [16]; $\Delta S(KH) \approx -0.169$ kJ/mol H_2 [16]; $\Delta S(UH_3) \approx -0.179$ kJ/mol H_2 [14]; $\Delta S(TiH_2) \approx -0.178$ kJ/mol H_2 [14]; $\Delta S(LiH) \approx -0.126$ kJ/mol H_2 [14]; $\Delta S(SrH_2) \approx -0.141$ kJ/mol H_2 [16]). ΔS^0 is mostly the responsible by the difference between the $Cu_2Mg + MgH_2$ and the $CuLi_{0.08}Mg_{1.92}$–H desorption temperatures.

For all of the hydrides to be discussed, ΔH^0 and ΔS^0 are negative, i.e., the hydrogenation reaction is exothermic and the dehydrogenation reaction is endothermic.

Inelastic neutron scattering

Time-of-flight (TOF) inelastic incoherent neutron scattering was collected at low temperatures at LANSCE, in FDS.

A sample with approximately –76 at% of $CuLi_{0.08}Mg_{1.92}$ and 24 at% of Cu_2Mg– was loaded with H_2 at 200 °C, at different pressures and loading times, before collecting a neutron vibrational spectrum (cycling treatments were performed over the same sample after each measurement. Between loadings, H_2 pressure was $\sim$1 bar and temperature dropped to room temperature). The sample was loaded: once for 1 h under 36 bar of H_2; twice for 6 h under 100 bar of H_2 and once for 21 h; once for 17 h and 25 min. and twice for 3 h (100 bar).

All data were collected at 10 K. Figure 2 shows the first Inelastic Neutron Scattering (INS) experiment in comparison with measurements of other samples of the same system – 33 at% of $CuLi_{0.08}Mg_{1.92}$, 35 at% of $CuMg_2$ and 32 at% of Cu_2Mg- and – 42 at% of $CuLi_{0.08}Mg_{1.92}$, 32 at% of $CuMg_2$ and 26 at% of Cu_2Mg- after being submitted to one hydrogenation cycle and of $NiMg_2H_4$. The latter hydride exhibits the same spectra whatever the hydrogenation treatment used or number of cycles. It seems that the lattice vibrations happen at similar wavenumbers possibly indicating a similar monoclinic structure comprising a $[CuH_4]^{3-}$ anion complex.

INS spectra show that cycling has a strong effect on structure and ion distribution. On the other hand, this effect on the structure can moreover be due to the loading time or to the waiting time (time the sample waited, at ambient pressure, before being measured). In other words, there

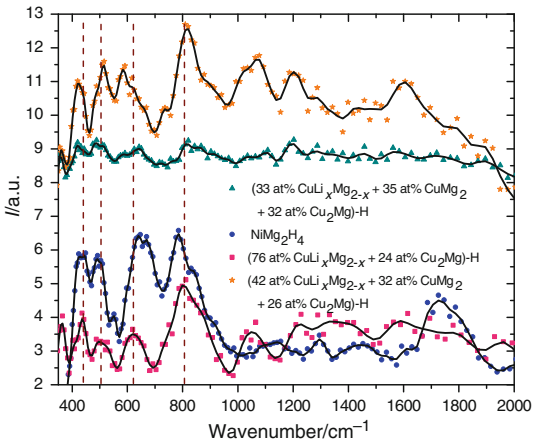

Fig. 2 INS results show similar spectra for different Cu–Li–Mg–H samples after one hydrogenation cycle. INS for $NiMg_2H_4$ is similar to the others spectra shown and does not depend of the hydrogenation process

might be a phase transition during hydrogen loading/releasing. These results show that during the first loading the structure was monoclinic with the Cu (bonded to H) ion probably occupying C_1 sites like in $[NiH_4]^{4-}$ in $NiMg_2H_4$ (monoclinic) [17], and that after 3 and 6 cycles the sample is likely to present a tetragonal structure similar to $CoMg_2H_5$ in which $[CoH_5]^{4-}$ occupies square-based pyramidal C_{4v} sites [18] or to present an extra phase with a tetragonal structure that can actually be MgH_2 [19] (Fig. 3).

Differential scanning calorimetry (DSC) and Thermogravimetry (TG)

Several samples were analysed by DSC/TG using a Netzsch instrument. Samples were heated from room temperature to 450 °C, at 5 and 10 °C/min. Alumina crucibles with lids were used at all times under high-purity argon gas flowing at 27 mL/min. Samples in the form of powder were hydrogenised before measured.

A literature search shows that MgH_2 in form of powder releases hydrogen in DSC instruments at temperatures that vary from the minimum of 325 °C [20] to a maximum of 433 °C [21] (Table 1). Although for MgH_2 the equilibrium desorption temperature (1–4) should be approximately 280 °C (553 K), in DSC the effect of kinetics counts as well, and therefore the lowest temperature found in the literature was 325 °C. Several DSC studies, that aimed to determine at which temperature MgH_2 releases hydrogen, were reported in the literature [20–28] (Table 1). Most of them focus on the effect of a catalyst on the desorption temperature of MgH_2.

One of the studies refers to nanoparticles of $CuMg_2$ [28]. $CuMg_2$ is hydrogenised to form MgH_2 and Cu_2Mg (5).

$$2CuMg_2 + 3H_2 \leftrightarrow Cu_2Mg + 3MgH_2 \quad (5)$$

According to Shao et al. [28] nanoparticles of $MgH_2 + Cu_2Mg$ will start releasing H_2 at 409 °C when the sample is at 4 MPa (40 bar) of H_2, while the equilibrium desorption temperature is 385 °C. The same study reports that Mg nanoparticles under the previous conditions desorb hydrogen at 472 °C (Table 1), while the equilibrium desorption temperature is 442 °C [28].

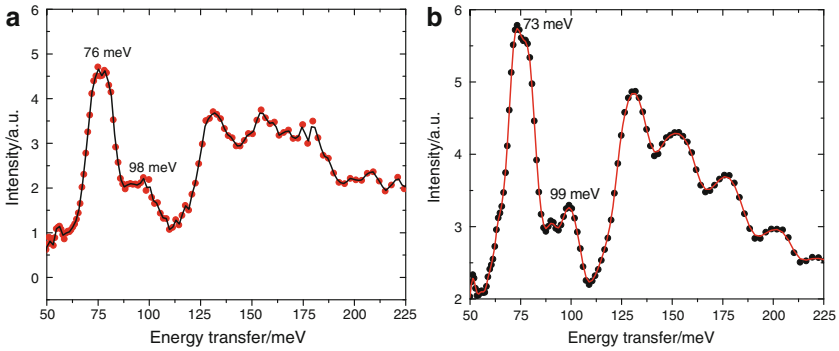

Fig. 3 **a** INS results show similar spectra for the third hydrogenation cycle for a Cu–Li–Mg–H sample (76 at% of $CuLi_{0.08}Mg_{1.92}$ and 24 at% of Cu_2Mg-loaded at 200 °C, twice for 6 h and once for 21 h under 100 bar of H_2). **b** INS spectra for MgH_2. After the first hydrogenation cycle results seem to indicate that MgH_2 is formed even in samples that do not contain $CuMg_2$

Table 1 Desorption temperature of MgH_2 (with tetragonal structure), obtained by means of DSC

Reference	Atmos.	Average particle size/milling conditions	Heating rate/°C min^{-1}	Desorption temperature/°C
[20]	Ar	Nano (20 h, Fritsch P7 planetary, 400 rpm, ball to powder weight ratio 40:1)	5	325
[21]	He	Nano (48 h, Fritsch P0 vibratory)	10	433
[21]	He	Nano (48 h, Fritsch P7 planetary, b–p–w–r 10:1)	10	372
[22]	Ar	7.9 nm	5	380
[23] (with 2% Co)	Ar	Order of μm (10 h, Spex planetary, b–p–w–r 3:1)	20	375
[24]	Ar	(15 h, Fritsch P5 planetary, b–p–w–r 15:1, 300 rpm)	5	330
[25]	Ar	(40 h, Kurimoto planetary, 885 rpm)	–	427
[26]	Ar	30 μm (10 h, Turbula planetary, b–p–w–r 10:1)	15	379
[27]	He	<100 nm (48 h, Fritsch P0 vibratory, b–p–w–r 20:1)	10	357
[28]	H_2 40 bar	300 nm	20	472 (Equilibrium temp. ~442 °C [28])
[28] (with Cu_2Mg)	H_2 40 bar	100 nm	20	409 (Equilibrium temp. ~385 °C [28])

In addition, the amount of desorbed hydrogen is not only related with the capacity of the hydride, its kinetics, grain size, possible catalysts added, but also with the way powders are milled [21]. Moreover, if the samples are not saturated, the amounts of released hydrogen cannot be compared or controlled.

Results show that hydrogenated samples containing $CuLi_{0.08}Mg_{1.92}$, start releasing hydrogen at $T < 50$ °C/323 K, then have a second release rate at around ~200 °C/473 K and finally a third release rate at about ~280 °C/553 K (Figs. 4 and 5). The first and second releases seem to be related with $CuLi_{0.08}Mg_{1.92}$–H and the third could be due to MgH_2 desorption. If this assumption is correct, this means that $CuLi_{0.08}Mg_{1.92}$–H will disproportionate into other hydrides.

Furthermore, if only $CuMg_2$ had contributed for the formation of MgH_2 (Fig. 4 mass losses and peaks at 282 and 287 °C), the maximum loss in weight percentage of the sample should be ~0.6 wt% since $CuMg_2$ is not present with more than ~23 wt%. The theoretical amount of hydrogen that can be released by $Cu_2Mg + 3MgH_2$ (5) is 2.6 wt% in a sample containing 100% of the mixture.

Likewise, if MgH_2 desorbs hydrogen at 282 °C, then the catalytic effect of $CuMg_2/Cu_2Mg$ is likely present and in addition a catalytic effect of $CuLi_{0.08}Mg_{1.92}$–H, since MgH_2 desorption temperature is 43 °C lower than the minimum temperature found in the literature for DSC experiments.

Hydrogen absorption experiments with nanostructured $CuMg_2$ samples, without activation process as in the case of this study, reveal that this compound will start absorbing hydrogen at ~250 °C [28]. All our samples absorbed hydrogen at 200 °C.

Using the total amount of hydrogen released by the sample during heating in Fig. 4 (left), the stoichiometry of $CuLi_{0.08}Mg_{1.92}$–H can be determined. Nonetheless, the absorption of hydrogen by $CuMg_2$ has to be taken into account, as well as the fact that Cu_2Mg will not absorb

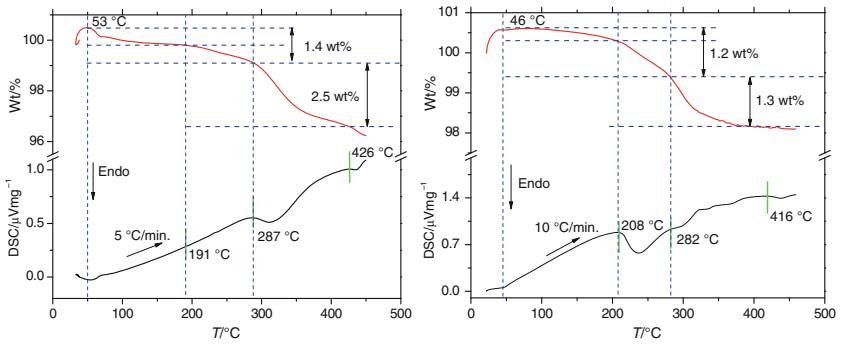

Fig. 4 DSC/TG curve of a sample containing 60 wt% of $CuLi_{0.08}Mg_{1.92}$, 28 wt% of $CuMg_2$ and 12 wt% of Cu_2Mg (62 at% of $CuLi_{0.08}Mg_{1.92}$, 28 at% of $CuMg_2$ and 10 at% of Cu_2Mg) that was hydrogenated at 200 °C and of a sample containing 69 wt% of $CuLi_{0.08}Mg_{1.92}$, 18 wt% of $CuMg_2$ and 13 wt% of Cu_2Mg (72 at% of $CuLi_{0.08}Mg_{1.92}$, 18 at% of $CuMg_2$ and 10 at% of Cu_2Mg) that was also hydrogenated at 200 °C. Samples do not seem to be saturated with hydrogen since they still present a peak corresponding to the parent's phase melting point (426 and 416 °C). Nonetheless, XRD patterns of the sample corresponding to the left curve have showed saturation

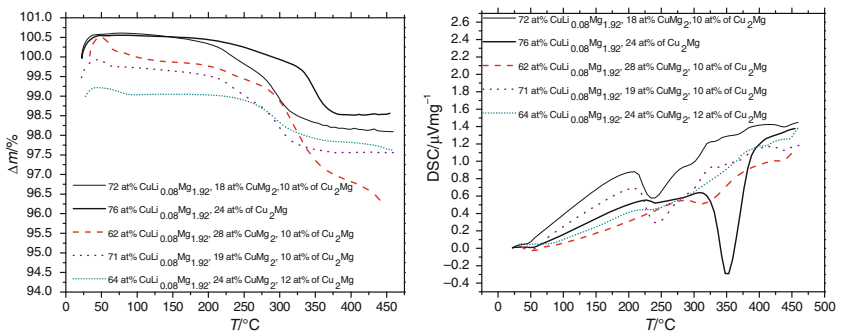

Fig. 5 DSC/TG curves of different samples from the Cu–Li–Mg–H system that prior from hydrogenation contained the phases and compositions signalized in the figures' captions. Samples were not saturated with hydrogen and suffered different hydrogenation cycles, at different pressures of H_2 and all at 200 °C. It can be observed a peak at low temperature ($T < 50$ °C), at approximately 208–220 °C, at 280–300 °C and finally the melting point of the parent $CuLi_{0.08}Mg_{1.92}$ at 420–426 °C

hydrogen at 200 °C. We have obtained a value of ~5.3 wt% that corresponds to $CuLi_{0.08}Mg_{1.92}H_6$ ($wt_H\% = 5.2\%$).

Ab initio calculations

Parent phase, $CuLi_{0.08}Mg_{1.92}$

Density Functional Theory (DFT) calculations with Projector Augmented Wave (PAW) pseudopotentials [29], as implemented in the Vienna Ab Initio Simulation Package code (VASP) [30–32], were performed. A plane wave cutoff of 355.18 eV, and k-spacings of 0.230 × 0.230 × 0.230 $Å^{-1}$ were used. Calculations were done in real space and were performed with P1 space group supercells containing 144 atoms (48 atoms of Cu, 96-n of Mg, and $n = 0$–12 of Li). The supercells contained as many atoms as possible to allow better approximations with the real Li concentrations (but such that the time spent on calculations were not completely impractical). Since $CuLi_xMg_{2-x}$ is a disordered structure, it had to be obtained by randomly substituting Mg by Li in several 6f Wyckoff positions (1/2, 0, z) or 6i Wyckoff positions (x, 2x, 0) or in both positions within the supercells. The Generalized Gradient Approximation (GGA), and the Perdew–Burke–Ernzerhof (PBE) functional [33] were used, and no magnetic moments were included in the model. We have concluded that the stoichiometry that minimizes the energy of formation is $CuLi_{0.08}Mg_{1.92}$, which is in agreement with the experimental results [34]. Phonon calculations were also implemented and results of the phonon Density of States (DOS) are in agreement with the INS experimental results for the parent phase (Fig. 6).

Hydride phase, $CuLi_{0.08}Mg_{1.92}H_x$

Using DFT and the same conditions described for the parent phase (with one exception: we did not use supercells), several possible structures of $CuMg_2H_x$ were optimized. We did not replace Mg with Li because that would mean building a supercell and spend a large computational time. The goal was to obtain a starting point for further studies.

Therefore, since most of the hydrides are cubic structures or structures that can be considered as distortions of a cubic structure [17], we have started calculations with tetragonal and monoclinic structures, similar to that of the hydrides formed by the nearest neighbours of copper in the periodic table and Mg: $NiMg_2H_4$ and $CoMg_2H_5$ (e.g., $CuMg_2H_4$, as monoclinic C 2/c similar to $NiMg_2H_4$ structure—low temperature; $CuMg_2H_5$ as tetragonal P 4/nmm similar to $CoMg_2H_5$ structure). In Fig. 7 it can be observed that the most stable configuration corresponds to $CuMg_2H_5$ with a monoclinic C 2/c structure. Using this structure, we have built a supercell and replaced Mg atoms by Li atoms in three different sites of the initial configuration. The new optimized structure is even more stable ($\Delta E_f = -4$ kJ/mol of H_2).

Knowing what the most stable structure of the hydride is, is necessary, but not sufficient. To make a statement about what will be the reaction occurring upon hydrogen absorption more information is needed since the compound may disproportionate into other compounds/hydrides like in the case of $CuMg_2$. Nonetheless, when we compare these results with neutron diffraction [12] and inelastic neutron spectroscopy, we observe that it is highly possible that the first structure formed upon hydrogenation is a monoclinic one.

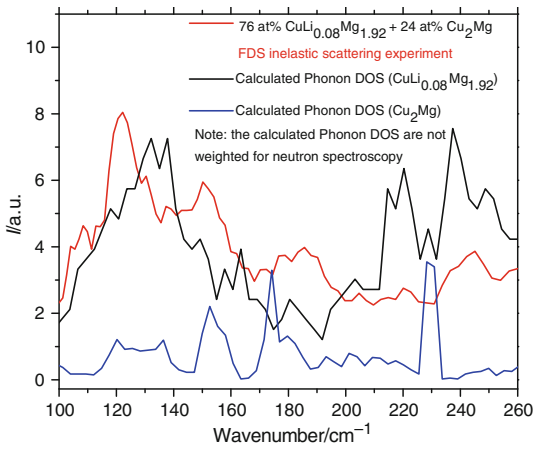

Fig. 6 Unweighted phonon DOS spectra, after ab initio, for the $CuLi_{0.08}Mg_{1.92}$ and Cu_2Mg crystal structures in comparison with the experimental INS spectrum of a sample containing both phases (without hydrogenation treatments)

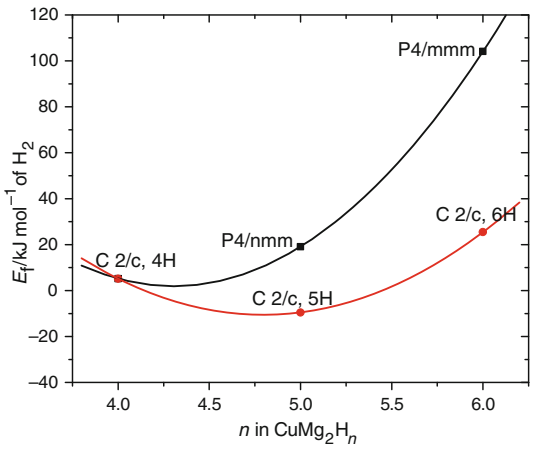

Fig. 7 Energy of formation of the hydride $CuMg_2H_n$ as a function of n (zero point energy was not included), for different types of crystal structures

Conclusions

After analysing the data obtained by hydrogen absorption, inelastic neutron spectroscopy, DSC/TG and first principles calculations we conclude that it is very likely that $CuLi_{0.08}Mg_{1.92}$ will react with hydrogen to form $CuLi_{0.08}Mg_{1.92}H_5$. Nonetheless, according to DSC's results, it is also possible that the stoichiometry of the product is $CuLi_{0.08}Mg_{1.92}H_6$.

The monoclinic C 2/c structure for the $CuLi_{0.08}Mg_{1.92}$ hydride (or a nearly derived structure) is in agreement with the results obtained both using neutron scattering techniques and first principles calculations.

Additionally, it can be concluded that even in samples that did not initially contain $CuMg_2$, it is clear the presence of MgH_2 formed after hydrogen uptake.

In this work it is also clear the roll of the Cu–Li–Mg–(H) as a catalyst for both $CuMg_2$ and MgH_2 during absorption and desorption.

Acknowledgements The authors would like to acknowledge Portuguese Science Foundation, FCT, for the project (PTDC/CTM/099461/2008 and FCOMP-01-0124-FEDER-009369). This work has benefited from the use of neutron scattering instrument FDS at the Lujan Center at Los Alamos Neutron Science Center, funded by DOE Office of Basic Energy Sciences. Los Alamos National Laboratory is operated by Los Alamos National Security LLC under DOE Contract DE-AC52-06NA25396.

References

1. Yang K, An JJ, Chen S. Influence of additives on the thermal behavior of nickel/metal hydride battery. J Therm Anal Calorim. 2010;102:953–9.
2. Fang KZ, Mu DB, Chen S, Wu F, Zeng XJ. Thermal behavior of nickel–metal hydride battery during charging at a wide range of ambient temperatures. Therm Anal Calorim. 2011;105:383–8.
3. Reilly JJ, Wiswall RW. The reaction of hydrogen with alloys of magnesium and copper. Inorg Chem. 1969;6(12):2220–3.
4. Braga MH, Ferreira J, Malheiros LF. A ternary phase in Cu–Li–Mg system. J Alloy Comp. 2007;436:278–84.
5. Hewat P. (2007) Inorganic Crystal Structure Database. 156880.
6. Schlapbach L, Zuttel A. Hydrogen-storage materials for mobile applications. Nature. 2001;414:353–8.
7. Braga MH, Ferreira J, Malheiros LF, Hamalainen M. HT-XRD on the study of Cu–Li–Mg Z. Kristallog suppl. 2007;26:299–304.
8. Orimo S, Nakamori Y, Eliseo JR, Zuttel A, Jensen CM. Complex hydrides for hydrogen storage. Chem Rev. 2007;107:4111–32.
9. Reilly J, Wiswall R. The reaction of hydrogen with alloys of magnesium and nickel and the formation of Mg_2NiH_4. Inorg Chem. 1968;7(11):2254–6.
10. Braga MH, Malheiros LF. WO2007046017.dp.
11. Match software, http://www.crystalimpact.com/match/Default.htm, Accessed 31 Aug 2011.
12. de Wolff PM, Visser JW. Absolute Intensities. Report 641.109. Technisch Physische Dienst, Delft, Netherlands. Reprinted Powder Diffract. 1988;3:202.
13. Braga MH, Acatrinei A, Hartl M, Vogel S, Proffen Th, Daemen L. New promising hydride based on the Cu–Li–Mg system. J Phys Conf Ser. 2010;251:012040.
14. Sandrock GD, Thomas G. IEA DOE SNL On-line Hydride Database. http://hydepark.ca.sandia.gov. Accessed 2009.
15. Andreasen A. Hydrogen storage materials with focus on main group I-II elements. PhD thesis. ISBN 87-550-3498-5; 2005.
16. Mueller WM, Blackledge JP, Libowitz GG, editors. Metal hydrides. London: Academic Press Inc; 1968.
17. Yvon K, Renaudin G. Hydrides: solid state transition metal complexes. Encyclopaedia of Inorganic Chemistry, 2006.
18. Parker SF, Jayasooriya UA, Sprunt JC, Bortz M, Yvon K. Inelastic neutron scattering, IR and Raman spectroscopic studies of Mg_2CoH_5 and Mg_2CoD_5. J Chem Soc Farad Trans. 1998;94(17):2595–9.
19. Schimmel HG, Johnson MR, Kearley GJ, Ramirez-Cuesta AJ, Huot J, Mulder FM. The vibrational spectrum of magnesium hydride from inelastic neutron scattering and density functional theory. Mater Sci Eng B. 2004;108:38–41.
20. Patah A, Takasaki A, Szmyd JS. The Effect of Cr_2O_3/ZnO on hydrogen desorption properties of MgH_2. Mater Res Soc Symp Proc. 2009:1148-PP03-38.
21. Balasooriya NWB. Poinsignon Ch. Preparation and characteristics of ball milled $MgH_2 + M$ (M = Fe, FeF_3 and VF_3) nanocomposites for hydrogen storage. Solid state ionics advanced materials for emerging technologies. Singapore: World scientific publishing Co. Pte. Ltd 2006. p 220–7.
22. Wu CZ, Wang P, Yao X, Liu C, Chen DM, Lu GQ, Cheng HM. Hydrogen storage properties of MgH_2/SWNT composite prepared by ball milling. J Alloys Comp. 2006;420(1–2):278–82.
23. Montone A, Grbovic J, Stamenkovic Lj, Fiorini AL, Pasquini L, Bonetti E, Antisari MV. Desorption Behaviour in Nanostructured MgH_2-Co. Mat Sci Forum. 2008;518:79–84.
24. Lillo-Rodenas MA, Aguey-Zinsou KF, Cazorla-Amoros D, Linares-Solano A, Guo ZX. Effects of carbon-supported nickel catalysts on MgH_2 decomposition. J Phys Chem C. 2008;112:5984–92.
25. Tessier P, Akiba E. Decomposition of nickel-doped magnesium hydride prepared by reactive mechanical alloying. J Alloys Comp. 2000;302:215–7.
26. Milovanovic S, Matovic L, Drvendzija M, Novakovic JG. Hydrogen storage properties of MgH_2-diatomite composites obtained by high-energy ball milling. J Micros. 2008;232(3):522–5.
27. Deledda S, Borissova A, Poinsignon C, Botta WJ, Dornheim M, Klassen T. H-sorption in MgH_2 nanocomposites containing Fe or Ni with fluorine. J Alloys Comp. 2005;404–406:409–12.
28. Shao H, Wang Y, Xu H, Li X. Preparation and hydrogen storage properties of nanostructured Mg_2Cu alloy. J Solid State Chem. 2005;178:2211–7.
29. Blochl PE. Projector augmented-wave method. Phys Rev B. 1994;50:17953–79.
30. Kresse G, Furthmüller J. Efficient iterative schemes for ab initio total-energy calculations using a plane-wave basis set. J. Phys Rev B. 1996;54:11169–86.
31. Kresse G, Furthmüller J. Efficient iterative schemes for ab initio total-energy calculations using a plane-wave basis set. Comp Mat Sci. 1996;6:1.
32. Kresse G, Joubert D. From ultrasoft pseudopotentials to the projector augmented-wave method. Phys Rev B. 1999;59:1758–75.
33. Perdew JP, Burke K, Ernzerhof M. Generalized Gradient Approximation Made Simple. Phys Rev Lett. 1996;77(18):3865–8.
34. Braga MH, Ferreira JJA, Siewenie J, Proffen Th, Vogel SC, Daemen LL. Neutron powder diffraction and first-principles computational studies of $CuLi_xMg_{2-x}$ ($x \cong 0.08$), $CuMg_2$, and Cu_2Mg. J Sol. Stat Chem. 2010;183:10–9.

Materials Science Forum Vols. 730-732 (2013) pp 799-804

doi:10.4028/www.scientific.net/MSF.730-732.799

First Principles Calculations and Experiments to Determine the Hydrogenation Process of Cu-Li-Mg

M.H. Braga[1,2,a], M.H. Sá[2,b], J.A. Ferreira[3,c], L.L. Daemen[1,d]

[1]Los Alamos Neutron Scattering Center, Los Alamos National Laboratory, NM, USA

[2]CEMUC, Engineering Physics Dep., Engineering Faculty, Porto University, Portugal

[3] LNEG, Laboratório Nacional de Energia e Geologia, S. Mamede Infesta, Portugal

[a]mbraga@fe.up.pt (corresponding author), [b]mhsa@fe.up.pt, [c]jorge.ferreira@lneg.pt, [d]lld@lanl.gov

Keywords: Cu-Li-Mg-H, Density Functional Theory (DFT), Phonons, Neutron Scattering

Abstract. Density Functional Theory (DFT) calculations were performed. They were firstly implemented to optimize the structure and refine the stoichiometry of the only ternary compound, $CuLi_{0.08}Mg_{1.92}$ of the Cu-Li-Mg system. Furthermore using DFT, several possible structures of $CuMg_2H_x$ were optimized. Since most of the hydrides are cubic structures or can be considered as distortions of a cubic structure, we have started calculations for $CuMg_2H_x$ (x = 4 - 6) with tetragonal and monoclinic structures, similar to those of the hydrides formed by the nearest neighbors of Cu and Mg in the periodic table: $NiMg_2H_4$ and $CoMg_2H_5$ (e.g. monoclinic C2/c and tetragonal P4/nmm, respectively). It can be concluded that the most stable configuration corresponds to $CuMg_2H_5$ with C2/c structure. We have performed several neutron scattering experiments that are in agreement with the first principles calculations.

Introduction

Efficient hydrogen storage remains a major technological obstacle toward the development of a hydrogen-based energy economy. We are currently investigating the Cu-Li-Mg-H system. The lighter and cheaper metals and our recent discovery that hydrogen can be reversibly stored in these compounds make them a very attractive alternative to lanthanide-based systems that still constitute Ni-MH batteries nowadays. Preliminary studies at the Los Alamos Neutron Scattering Center (LANSCE) showed that hydrogen unsaturated samples could desorb up to 4.4-5.3 wt% of hydrogen. Experiments furthermore shown that samples containing $CuLi_xMg_{2-x}$ (x = 0.08) will start desorbing hydrogen at a temperature from 50 – 130 ºC where applications are easier to develop. Hence it should be possible to use this alloy as a hydrogen storage material for fuel cells, batteries and other hydrogen storage devices.

Experimental Methods

Sample Preparation. The Cu-Li-Mg samples were prepared from the pure elements with a target composition of $CuLi_{0.08}Mg_{1.92}$. They were prepared by mixing stoichiometric amounts of Cu (electrolytic, 99.99% purity, 325 mesh), Mg (99.8% purity, 200 mesh, Alfa Aesar), and small granules (approx. 2 x 2 x 3 mm) of Li (99% purity, Alfa Aesar). Because of the large vapor pressure of Mg, even below its melting point, the reagents were sealed in a stainless steel crucible in a dry box (He atmosphere). This eliminated possible reagent loss. The samples were heated in a tube furnace with a stirring device to ensure proper mixing of the heterogeneous starting mixture and complete dispersion of Li in the sample. Different reaction temperatures and times were used (from 450 ºC for 24h to 1200 ºC for 1-2 h). Regardless of reaction conditions, the samples invariably contained Cu_2Mg, $CuMg_2$, or both. Nonetheless, we obtained final products containing up to 82.5 at% (77.5 wt%) of $CuLi_xMg_{2-x}$. Since the structure of Cu_2Mg and $CuMg_2$ is known as well as their hydrogen storage behaviour; this complication translated merely in the refinement of additional phases in the neutron/x-ray powder diffraction patterns. Samples were firstly

characterized by means of x-ray diffraction (XRD) using a Rigaku Ultima III powder diffractometer, and their composition was roughly determined by means of the Match software, [1] which uses the "Reference Intensity Ratio method" RiR) [2] to obtain phase fractions. Patterns were collected with CuKalpha typically from 2θ = 15 to 70º with steps of 0.02º and a counting time of 10 s per bin.

Neutron scattering in deuteride and hydride samples. Time-of-flight (TOF) neutron diffraction data were collected at low and room temperatures on NPDF and HIPD neutron diffractometers at LANSCE.

Neutron diffraction. Neutron diffraction was firstly performed in order to characterize the phase $CuLi_xMg_{2-x}$. Rietveld refinements using GSAS [3] and Pair Distribution Function (PDF) refinements using PDFgui [4] were carried out to characterize the phases present in the samples. Results obtained show that Li will substitute Mg in (1/2,0,z) forming a hexagonal $P6_222$ compound $CuLi_{0.08}Mg_{1.92}$ with lattice parameters, a = b = 5.250 (1) Å and c = 13.621(1) Å (at T = 300 K). A detailed study of the $CuLi_{0.08}Mg_{1.92}$, $CuMg_2$ and Cu_2Mg phases of the Cu-Li-Mg system can be found in [5]. Samples of the Cu-Li-Mg-D system were also studied in NPDF and HIPD Fig. 1. Samples were always deuterized at 200 ºC. The sample correspondent to Fig. 1 (left) was deuterized for 55h30min. under 69 bar (D_2). Before being deuterized, it had around 38 at% of $CuLi_{0.08}Mg_{1.92}$, 45 at% of $CuMg_2$ and 17 at% of Cu_2Mg. The sample correspondent to Fig. 1 (right) suffered different hydrogen sorption/desorption cycles before being measured in HIPD; however before being cycled it had around 76 at% of $CuLi_{0.08}Mg_{1.92}$, and 24 at% of Cu_2Mg. During cycling, the gas pressure was never higher than 100 bar H_2/D_2. When measured in HIPD, the sample correspondent to Fig. 1 (right) was not fully saturated (parent phases were still present). In the case of this last sample the presence of $CuLi_{0.08}Mg_{1.92}D_5$ is clear although the compound contributes in a small percentage for the final weight of the sample.

Inelastic Neutron Scattering. A sample with 76 at% of $CuLi_{0.08}Mg_{1.92}$ and 24 at% of Cu_2Mg was loaded with H_2 at 200 ^oC, at different pressures and with different loading times, before collecting a neutron vibrational spectrum (cycling treatments were performed over the same sample after each measurement. Between loadings, H_2 pressure was ~ 1 bar and temperature dropped to room temperature). The sample was loaded:

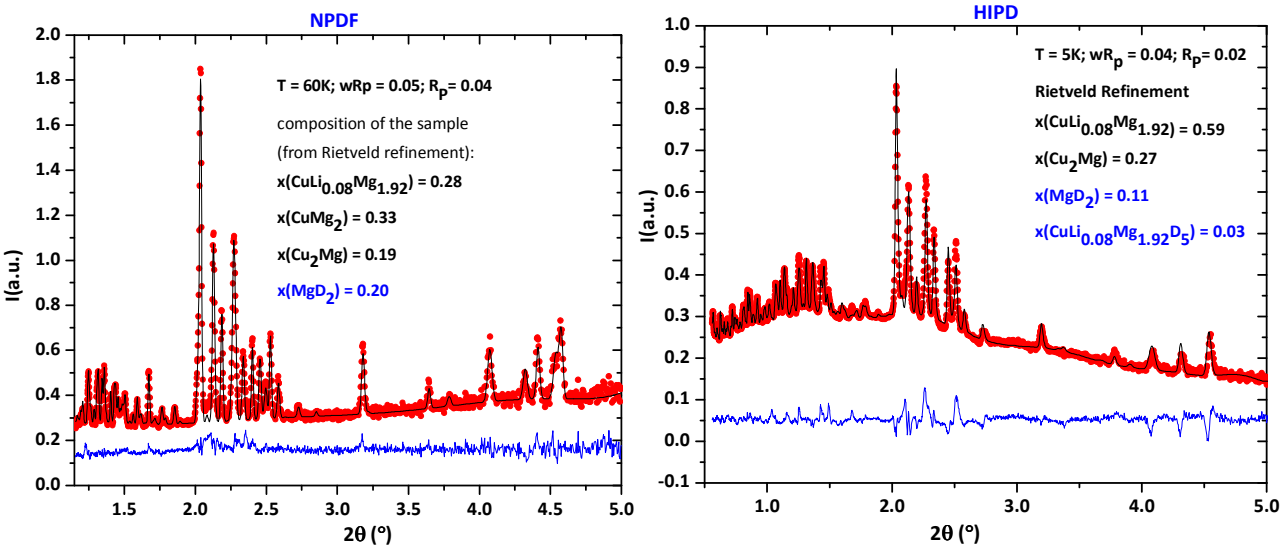

Fig. 1(left) Sample containing around 28 at% of $CuLi_{0.08}Mg_{1.92}$, 33 at% of $CuMg_2$, 19 at% of Cu_2Mg and 20 at% of MgD_2. This sample was not refined with $CuLi_{0.08}Mg_{1.92}D_5$ since the presence of this phase was too small to make a difference in the refinement. (right) Sample containing around 59 at% of $CuLi_{0.08}Mg_{1.92}$, 27 at% of Cu_2Mg, 11 at% of MgD_2 and 3 at% of $CuLiMg_{0.08}Mg_{1.92}D_5$. All phases had to be present to allow a reliable Rietveld refinement.

- under 36 bar of H_2 for 1 hour once;
- twice under 100 bar of H_2 for 6 hours and once for 21 h;
- once for 17 h and 25 min. and twice for 3 hours (100 bar).

All data were collected at 10 K. Fig. 2 shows the first and third experiment.

Inelastic neutron scattering (INS) spectra show that cycling has a strong effect on structure and ion distribution. On the other hand, this effect on the structure can moreover be due to the loading time or to the waiting time (time the sample waited, at ambient pressure, before being measured). In other words there might be a phase transition during hydrogen loading / unloading. These results show that during the first loading the structure was monoclinic with the Cu-H, eventually forming $[CuH_4]^{3-}$ and probably occupying C_1 sites like $[NiH_4]^{4-}$ in $NiMg_2H_4$ (monoclinic) [6], and that after 3 and 6 cycles the sample is likely to present a tetragonal structure similar to $CoMg_2H_5$ in which $[CoH_5]^{4-}$ occupies square-based pyramidal C_{4v} sites [7] or a tetragonal structure that can actually be MgH_2 [8].

Differential scanning calorimetry (DSC) and Thermogravimetry (TG). Several samples were analyzed by DSC/TG using a Netzsch instrument. Samples were heated from room temperature to 450 °C, at 5 and 10 °C/min. Alumina crucibles and lids were used at all times under high-purity argon gas flowing at 27 ml/min. Samples in the form of powder were hydrogenised before measured.

A literature search shows that MgH_2 in form of powder releases hydrogen in DSC instruments at temperatures that vary from the minimum of 325 °C [9] to a maximum of 433 °C [10]. Although for MgH_2 the equilibrium desorption temperature should be approximately 280 °C (553 K), in DSC the effect of kinetics counts as well, and therefore the lowest temperature found in the literature was 325 °C. Several DSC studies, that aimed to determine at which temperature MgH_2 releases hydrogen, were reported in the literature [9-17]. Most of them focus on the effect of a catalyst on the desorption temperature of MgH_2.

One of the studies refers to nanoparticles of $CuMg_2$ [17]. $CuMg_2$ is hydrogenised to form MgH_2 and Cu_2Mg ($2CuMg_2 + 3H_2 \leftrightarrow Cu_2Mg + 3MgH_2$). According to Shao *et al.*, nanoparticles of MgH_2 + Cu_2Mg will start releasing H_2 at 409°C when the sample is under 4MPa (40 bar) of H_2 [17], while the equilibrium desorption temperature is 385 °C. The same study reports that Mg nanoparticles under the same previous conditions absorb hydrogen at 472°C, while the equilibrium desorption temperature is 442 °C [17].

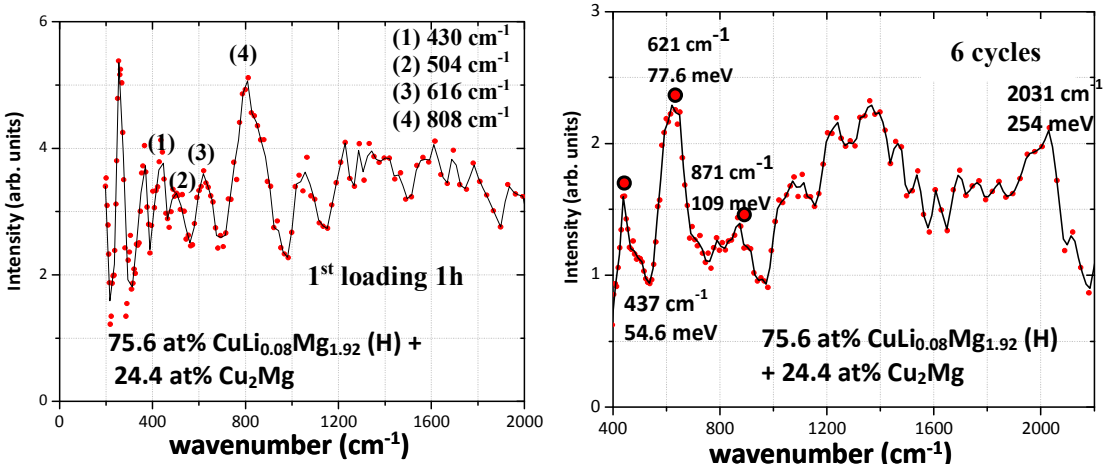

Fig. 2 INS results for two different structures of the $CuLi_{0.08}Mg_{1.92}H_x$ hydride. Results show different structures depending on the number of cycles / hydrogenation stage.

In addition, the amount of desorbed hydrogen is not only related with the capacity of the hydride; it has moreover to do with kinetics, grain size, possible catalysts added, and also with the way powders are grinded [10]. Furthermore, if the samples are not saturated, the amounts of released hydrogen cannot be compared or controlled.

Results show that hydrogenised samples containing $CuLi_{0.08}Mg_{1.92}$, start releasing hydrogen at T < 55 °C / 328 K, and have a second release rate at around ~200 °C / 473 K and finally a third release rate at about ~280 °C/553 K. The first and second releases seem to be related with $CuLi_{0.08}Mg_{1.92}$-H and the third could be due to MgH_2 desorption. If this assumption is correct, this means that $CuLi_{0.08}Mg_{1.92}$-H will disproportionate into other hydrides.
Furthermore, if only $CuMg_2$ had contributed to the formation of MgH_2 (mass losses and peaks at 282 °C in Fig. 3), the maximum loss in weight percentage of the sample should be ~0.6 wt% since $CuMg_2$ is not present with more than ~23 wt% (the theoretical amount of hydrogen that can be released by $Cu_2Mg + 3MgH_2$ is 2.6 wt% in a sample containing 100 % of the mixture).
Likewise, if MgH_2 desorbs hydrogen at 282 °C, then the catalytic effect of Cu_2Mg is likely present and in addition a catalytic effect of $CuLi_{0.08}Mg_{1.92}$-H, since MgH_2 desorption temperature is 43 °C lower than the minimum temperature found in the literature for DSC experiments [9-17] of samples containing 100% of MgH_2.

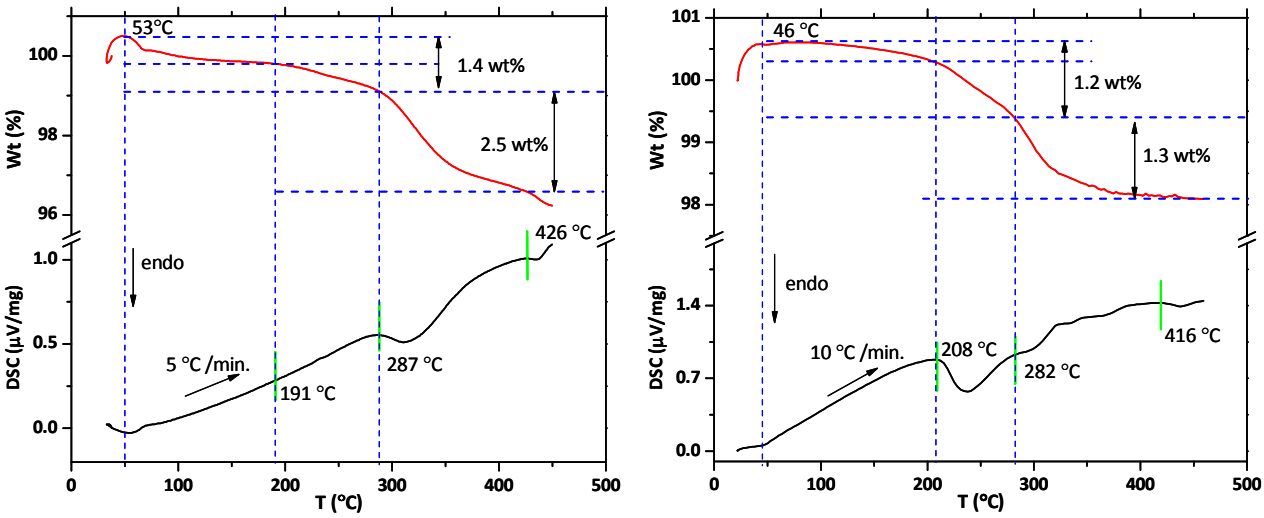

Fig. 3 DSC/TG curve of a sample containing 60.0 wt% of $CuLi_{0.08}Mg_{1.92}$, 27.6 wt% of $CuMg_2$ and 12.4 wt% of Cu_2Mg (62.4 at% of $CuLi_{0.08}Mg_{1.92}$, 28.2 at% of $CuMg_2$ and 9.4 at% of Cu_2Mg) and of a sample containing 68.6 wt% of $CuLi_{0.08}Mg_{1.92}$, 18.0 wt% of $CuMg_2$ and 13.4 wt% of Cu_2Mg (71.4 at% of $CuLi_{0.08}Mg_{1.92}$, 18.4 at% of $CuMg_2$ and 10.2 at% of Cu_2Mg) that were hydrogenated at 200 °C beforehand. Samples do not seem to be saturated with hydrogen since they still present a peak corresponding to the parent's phase melting point (426 °C and 416 °C). Nonetheless, XRD patterns of the sample corresponding to the left curve showed saturation.

On the other hand, the catalytic effects of $CuLi_{0.08}Mg_{1.92}$(-H) over $CuMg_2$ were also present during hydrogen absorption. Hydrogen absorption experiments with nanostructured $CuMg_2$ samples, without prior activation process as in the case of this study, reveal that this compound will start absorbing hydrogen at ~ 250 °C (5) [17]. All our samples absorbed hydrogen at 200 °C.
Using the total amount of hydrogen released by the sample during heating in Fig. 3 (left), the stoichiometry of $CuLi_{0.08}Mg_{1.92}$-H can be determined. Nonetheless, the absorption of hydrogen by $CuMg_2$ has to be taken into account; conversely, Cu_2Mg will not absorb hydrogen at 200 °C. We have obtained a value of ~ 5.3 wt% that corresponds to $CuLi_{0.08}Mg_{1.92}H_6$ ($Wt_H\%$ = 5.2 %).

Ab Initio Calculations

Parent phase, $CuLi_{0.08}Mg_{1.92}$. Density Functional Theory (DFT) calculations with Projector Augmented Wave (PAW) pseudopotentials [18], as implemented in the Vienna *Ab Initio* Simulation Package code (VASP) [19], were performed. A plane wave cutoff of 355.18 eV, and k-spacings of 0.230 x 0.230 x 0.230 $Å^{-1}$ were used. Calculations were done in real space and were performed with P1 space group supercells containing 144 atoms (48 atoms of Cu, 96 - n of Mg, and n = 0 to 12 of

Li). The supercells contained as many atoms as possible to allow better approximations with the real Li concentrations (but such that the time spent on calculations were not completely impractical). Since $CuLi_xMg_{2-x}$ is a disordered structure, it was obtained by randomly substituting Mg by Li in several 6f Wyckoff positions (1/2,0,z) of the initial hexagonal structure that conducted to the P1 supercells. The Generalized Gradient Approximation (GGA), and the Perdew–Burke–Ernzerhof (PBE) functional [20] were used, and no magnetic moments were included in the model. We have concluded that the stoichiometry that minimizes the energy of formation is $CuLi_{0.08}Mg_{1.92}$, which is in agreement with the experimental results [5].

Hydride phase, $CuLi_{0.08}Mg_{1.92}H_x$. Using DFT and the same conditions described for the parent phase (with one exception: we did not initially use supercells), several possible structures of $CuMg_2H_x$ were optimized. We did not replace Mg with Li because that would mean building a supercell and spend a large computational time. The goal was to obtain a starting point for further studies.

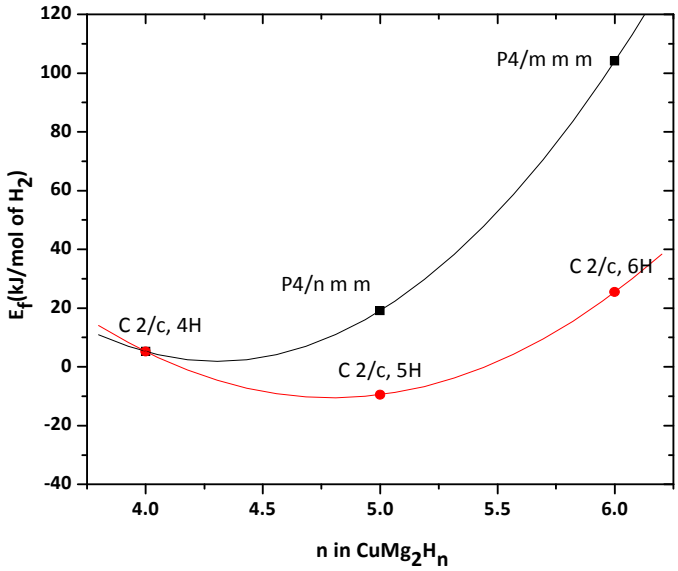

Fig. 4 Energy of formation of the hydride $CuMg_2H_n$ as a function of n, for different types of crystal structures.

Therefore, since most of the hydrides are cubic structures or structures that can be considered as distortions of a cubic structure [6], we have started calculations with tetragonal and monoclinic structures, similar to those of the hydrides formed by the nearest neighbours of Cu and Mg in the periodic table: $NiMg_2H_4$ and $CoMg_2H_5$ (e.g. $CuMg_2H_4$ was optimized as monoclinic C 2/c; $CuMg_2H_5$ tetragonal P 4/nmm, respectively). In Fig. 4 it can be observed that the most stable configuration corresponds to $CuMg_2H_5$ with a monoclinic C2/c structure. Using this structure, we have built a supercell and replaced Mg atoms by Li atoms in three different sites of the initial configuration. The new optimized structure is even more stable (the difference is: ΔE_f = - 4 kJ/mol of H_2).

Knowing what the most stable structure of the hydride is, is necessary, but not sufficient to make a statement about the reaction occurring upon hydrogen absorption. More information is needed since the compound may disproportionate into other compounds/hydrides like in the case of $CuMg_2$. Nonetheless, when we compare these results with neutron diffraction and inelastic neutron spectroscopy, we conclude that it is highly possible that the first structure formed upon hydrogenation is a monoclinic C2/c.

Summary

After analysing the data obtained by neutron diffraction and neutron spectroscopy, DSC and first principles calculations we conclude that it is very likely that $CuLi_{0.08}Mg_{1.92}$ will react with hydrogen to form $CuLi_{0.08}Mg_{1.92}H_5$. Nonetheless, according to DSC's results, it is also possible that the stoichiometry of the product is $CuLi_{0.08}Mg_{1.92}H_6$.

The monoclinic C2/c structure for the $CuLi_{0.08}Mg_{1.92}$ hydride is in agreement with the results obtained both using neutron scattering techniques and first principles calculations.
Additionally, it can be determined the presence of MgH_2, formed after hydrogen uptake, even for those samples that did not initially contain $CuMg_2$. In this work it is also clear the roll of the Cu-Li-Mg-(H) as a catalyst for both $CuMg_2$ and MgH_2 during absorption and desorption.

Acknowledgements
The authors would like to acknowledge Portuguese Science Foundation, FCT, for the project (PTDC/CTM/099461/2008 and and FCOMP-01-0124-FEDER-009369). This work has benefited from the use of neutron scattering instruments NPDF, HIPD and FDS at the Lujan Center at Los Alamos Neutron Science Center, funded by DOE Office of Basic Energy Sciences, USA. This work has benefited from the use of 11-beamline at the Advanced Photon Source at Argonne National Laboratory, USA.

References

[1] Match, http://www.crystalimpact.com/, 2009.
[2] P.M. de Wolff, J.W. Visser, Absolute Intensities. Report 641.109. Technisch Physische Dienst, Delft, Netherlands. Reprinted Powder Diffract 3 (1988) 202.
[3] A.C. Larson, R.B. von Dreele, GSAS Generalized Structure Analysis System, LANSCE, Los Alamos, 2004.
[4] C.L. Farrow, P. Juhas, J.W. Liu, D. Bryndin, E.S. Bozin, J. Bloch, Th. Proffen, S.J.L. Billinge J. Phys.: Cond.. Matter. 19 (2007) 335219.
[5] M.H. Braga, J.J.A. Ferreira, J. Siewenie, Th. Proffen, S.C. Vogel, L.L. Daemen, J. of Sol. State Chem. 183(1) (2010) 10.
[6] K. Yvon, G. Renaudin Hydrides: Solid State Transition Metal Complexes. Encyclopedia of Inorganic Chemistry, 2006.
[7] S.F. Parker, U.A. Jayasooriya, J. C. Sprunt, M. Bortz, K. Yvon J. Chem. Soc. Faraday Trans. 94(17) (1998) 2595.
[8] H.G. Schimmel, M.R. Johnson, G.J. Kearley, A.J. Ramirez-Cuesta, J. Huot, F.M. Mulder, Mat. Sci. Eng. B 108 (2004) 38.
[9] A. Patah, A. Takasaki, J.S. Szmyd, Mater. Res. Soc. Symp. Proc. 1148-PP03-38, 2009.
[10] N.W.B. Balasooriya, Ch. Poinsignon, IEEE Inter. Nanoelect. Conf. 2008, 894.
[11] C. Z. Wu, P. Wang, X. Yao, C. Liu, D.M. Chen, G.Q. Lu, H.M. Cheng, J. Alloys Comp. 420 (2006) 278.
[12] A. Montone, J. Grbovic, Lj. Stamenkovic, A.L. Fiorini, L. Pasquini, E. Bonetti, M.V. Antisari Mat. Sci. For. 518 (2006) 79.
[13] M.A. Lillo-Rodenas, K.F. Aguey-Zinsou, D. Cazorla-Amoros, A. Linares-Solano, Z.X. Guo, J. Phys. Chem. C 112 (2008) 5984.
[14] P. Tessier, E. Akiba, J. Alloys Comp. 302 (2000) 215.
[15] S. Milovanovic, L. Matovic, M. Drvendzija, J.G. Novakovic, J. Micros., 232 (3) (2008) 522.
[16] S. Deledda, A. Borissova, C. Poinsignon, W.J. Botta, M. Dornheim, T. Klassen, J. Alloys Comp. 404-406 (2005) 409.
[17] H. Shao, Y. Wang, H. Xu, X. Li, J. Sol. State Chem. 178 (2005) 2211.
[18] P.E. Blochl, Phys. Rev. B 50 (1994) 17953.
[19] G. Kresse, J. Furthmüller, Phys. Rev. B 54 (1996) 11169; Comp. Mat. Sci. 6 (1996) 1; G. Kresse, D. Joubert, Phys. Rev. B 59 (1999) 1758.
[20] J.P. Perdew, K. Burke, M. Ernzerhof, Phys. Rev. Lett. 77 (1996) 3865; 78 (E) (1997) 1396.

Chapter 4- Bi-Sn-Zn System

Chapter 4.

Bi-Sn-Zn SYSTEM

4.1. Introduction

Lead and lead-containing compounds are considered toxic substances due to their detrimental effect to the well-being of humans and the environment. Suitable development policy has been implemented by many countries around the world and, in order to protect the environment, the restriction of lead used in industry has been strongly promoted.

In this context, since July 1st, 2006, both the European Union (RoHS — Restriction of Certain Hazardous Substances and WEEE — Waste Electrical and Electronic Equipment Legislations) and the U.S. Environmental Protection Agency have banned the lead-containing electronic products (Islam et al., 2006; Yu et al., 2000).

In order to replace the traditional Sn–Pb eutectic solder alloy by lead-free alternatives great efforts were developed. The Sn–Zn eutectic alloy is the nontoxic Pb-free solder alloy alternative having a melting temperature which is closest to that of the eutectic Sn–Pb alloy (471 K and 456 K, respectively). However, new solder alloys must fulfill a number of other requirements in both economic and physical/chemical points of view. In this context, the melting temperature should be in the same range as that of the traditional Sn–Pb eutectic alloy, strength and integrity should also be similar or superior, and manufacturing costs must be competitive (Garcia et al., 2010). Poor oxidation resistance and embrittlement behavior are the major problems with the Sn-Zn alloys.

In order to overcome these drawbacks, and further enhance the properties of Sn–Zn lead-free solder alloys, a small amount of alloying elements (rare earths, Bi, Ag, Al, Ga, In, Cr, Cu, Sb, Ni, Ge) added into Sn–Zn alloys were selected by many researchers. For example, a small amount of Al, P, Bi, Ga can improve the high-temperature oxidation resistance of Sn–Zn solders remarkably as well as Cr (Zhang et al., 2010).

We have studied the Bi-Sn-Zn as well as the Sn-Zn and Bi-Zn systems, on ambit of the COST 531 and COST MP0602, EU actions, on lead free solders. Our studies contemplated both

experimental (using DSC- Differential Scanning Calorimetry , HT-XRD - High Temperatures X-ray Diffraction, RT-XRD - Room Temperatures X-ray Diffraction, SEM – Scanning Electron Microscopy), and assessments (using Thermo-Calc software).

The need for new, improved solder alloys and a better understanding of reactions during the soldering process grows steadily as the need for smaller and more reliable electronic products increases. Information obtained from phase equilibria data and thermodynamic calculations has proven to be an important tool in the design and understanding of new lead-free solder alloys.

A wide range of candidate alloys can be rapidly evaluated for proper freezing ranges, susceptibility to contamination effects, and reactions with substrate materials before the expensive process of preparing and testing candidate alloys is initiated (Kattner, 2002). Therefore, the latter was the objective of the above mentioned COST actions that joined researchers from many European countries around the same goal.

4.2. References

Garcia,L., Osório, W., Peixoto, L., & Garcia, A., (2010). Mechanical properties of Sn–Zn lead-free solder alloys based on the microstructure array, Materials Characterization, Vol. 61, No. 2, pp. 212–220, ISSN 1044-5803

Kattner, U., (2002). Phase diagrams for lead-free solder alloys, JOM, Vol. 54, No. 12, pp. 45-51, ISSN 1047-4838

Islam, R., Chan Y., Jillek W., & Islam S., (2006). Comparative study of wetting behavior and mechanical properties (microhardness) of Sn–Zn and Sn–Pb solders, Microelectronics Journal, Vol. 37, No. 8, pp. 705–713, ISSN 0026-2692

Yu, S., Lin, H., Hon, M., &Wang, M-C., (2000). Effects of process parameters on the soldering behavior of the eutectic Sn–Zn solder on Cu substrate. Journal of Materials Science: Materials in Electronics, Vol. 11, No. 6, pp. 461-471, ISSN 1573-482X

Zhang, L., Xue, S., Gao, L., Sheng, Z., Ye, H., Xiao, Z., Zeng, G., Chen, Y., Yu, S., (2010). Development of Sn–Zn lead-free solders bearing alloying elements, Journal of Materials Science: Materials in Electronics, Vol. 21, No. 1, pp. 1-15, ISSN 1573-482X.

Papers on the Bi-Sn-Zn system

4.3 Experimental Phase Diagram of the Ternary Bi-Sn-Zn

4.4 The experimental study of the Bi-Sn, Bi-Zn, and Bi-Sn-Zn System

4.5 Thermodynamic assessment of the Bi–Sn–Zn System

4.6 The Behaviour of the Lattice Parameters in the Bi-Sn-Zn System

4.7 Phase field simulations in miscibility gaps

Materials Science Forum Vols. 514-516 (2006) pp 1682-1688
online at http://www.scientific.net

Online available since 2006/May/15

Experimental Phase Diagram of the Ternary Bi-Sn-Zn

M. H. Braga[1,a], L. F. Malheiros[2,b], D. Soares[3,c], J. Ferreira[4,d] and F. Castro[5,e]

[1]GMM-IMAT, Dep. of Physics, R. Dr. Roberto Frias s/n, 4200-465 Porto, Portugal

[2]GMM-IMAT, Dep. of Metallurgical and Materials Engineering, FEUP, R. Dr. Roberto Frias s/n, 4200-465 Porto, Portugal

[3]Dep. of Mechanical Engineering, School of Engineering of UM, Campus de Azurém 4800-058 Guimarães, Portugal

[4]INETI Laboratory, R. da Amieira - Apartado 1089, 4466-956 S. Mamede de Infesta, Portugal

[5]Dep. of Mechanical Engineering, School of Engineering of UM, Campus de Azurém 4800-058 Guimarães, Portugal

[a]mbraga@fe.up.pt, [b]lfmf@fe.up.pt, [c]dsoares@dem.uminho.pt, [d]jorge.ferreira@ineti.pt, [e]fcastro@ dem.uminho.pt

Keywords: Lead-free solders, Bi-Sn-Zn, DTA/DSC, SEM/EDS, XRD room / high temperature, phase diagram.

Abstract. Bi-Sn-Zn is one of the systems being used as substitute of the traditional lead solders. Therefore a deeper knowledge of its phase diagram is a priority. Due to the lack of data about the thermodynamic properties of terminal solid solutions as well as on their phase boundaries, only binary contributions were utilized and the ternary terms were ignored on the published assessments [1, 2]. Samples corresponding to several vertical sections were prepared and DTA, SEM/EDS and XRD at room and high temperatures were performed. It was concluded that ternary terms should be held in consideration in a future assessment of the system.

Introduction

The known health problem that may arise from the excess of lead in the organism (especially neurological and born malformations) brought the water contamination, with lead, to the list of apprehensions with the ambient [3].

COST – 531 action: *"Lead-free Solder Materials"* [4] (from EU) has, as main objective, to study some systems (out of lead) that may be used as solders. There are some criteria for the selection of these systems. To select a solder alloy some properties should be measured, namely: melting temperature, wettability, surface tension, viscosity of the liquid alloys at different temperatures, oxidation behavior, thermomechanical fatigue, etc.

Experimental phase diagrams, thermodynamic properties and optimisation of the corresponding phase diagrams (using CALPHAD method) are some of the aims of COST – 531 in which this work is included.

Table 1. References of the parameters, for the binaries, used by [1] and [2] in the assessment of Bi-Sn-Zn.

Bi-Sn-Zn assessed by [1]	
Zn	[5]
Bi-Sn	[6]
Bi-Zn	[7]
Sn-Zn	[8]
Bi-Sn-Zn (liquid)	[1]
Bi-Sn-Zn assessed by [2]	
Zn	[5]
Bi-Sn	[9]
Bi-Zn	[7]
Sn-Zn	[10] – except for the excess Gibbs energy for (Zn) which is from [2]
Bi-Sn-Zn (liquid)	[2]

Two references with the optimisation and assessment of the Bi-Sn-Zn system were found in the literature: one from D. V. Malakhov *et al.* (2000) [1] and another from N. Moelans *et al.* (2003) [2]. In both references, it was taken into account different parameters for the binaries (Table 2).

The experimental data for the ternary Bi-Sn-Zn are not up-to-date, especially those for the phase diagram. For instance, in the references [11, 12], from Wright (1891 and 1892), experimental data aren't very reliable. The work of Muzzaffar (1923) [13] (measurements of thermal arrests) is the most used (in spite of the lack of information about the liquid miscibility gap, since thermal arrests corresponding to liquid-liquid separation were not observed under the experimental conditions employed). Jänecke's data from 1937 [14] are also not very reliable since they are not in agreement with the data from the binaries Bi-Sn and Sn-Zn.

Experimental

Vertical sections for 5 wt% (Sn), 13 wt% (Sn), 21 wt% (Sn), 40 wt% (Sn) and 60 wt% (Sn) were chosen for this study. The samples were melted in a resistance furnace, under an inert atmosphere, from Bi > 99.8%, Sn > 99.5% and Zn > 99.9% pure elements; their compositions were confirmed by XRF (X-ray fluorescence) and atomic absorption spectroscopy. Samples with ~ 20 mm of diameter, ~ 3 mm high and ~ 2 g were homogenised at 120 ºC for 60 minutes. DTA (differential thermal analysis) / DSC (differential scanning calorimeter) measurements were performed on a TA Instruments SDT 2960 in order to determine the temperatures for the phase transitions. Table 2 presents the composition of the samples and DTA/DSC results. Samples were observed by optical microscopy, as so as by SEM (scanning electron microscopy) / EDS (energy dispersive spectroscopy) on a JEOL JFM 6301 F. Finally, powder XRD (X-ray diffraction) measurements at room and high temperatures were also performed, on a Philips X´Pert Pro MPD, in order to characterize the phases involved on some equilibria.

Table 2. Samples' composition (from FRX and atomic absorption spectroscopy) and DTA/DSC results.

	wt%(Bi)	*wt%(Sn)*	*wt%(Zn)*	*Phase diagram's invariant and liquidus points (ºC)*			
1.	10.1	57.8	32.1	134.0	187.2	330.0	
2.	18.3	58.8	22.9	134.9	177.5	301.3	
3.	29.6	58.2	12.2	134.8	165.6	254.7	
4.	10.1	40.1	49.8	134.0	182.6	367.7	
5.	23.3	38.3	38.4	135.1	161.4	367.0	
6.	47.6	39.8	12.6	134.1	295.4		
7.	19.5	4.0	76.5	134.2	187.2	399.2	408.0
8.	53.7	5.0	41.3	134.3	232.4	406.9	
9.	68.4	6.0	25.6	134.6	232.8	410.6	
10.	74.0	11.9	14.1	133.9	223.0	407.8	
11.	55.6	13.7	30.7	134.2	212.6	407.8	
12.	37.9	19.8	42.3	134.4	144.2	397.3	
13.	56.7	12.6	30.7	134.2	159.9	217.9	400.3
14.	51.1	21.4	27.5	134.6	177.6	386.7	
15.	32.3	47.1	20.6	133.5	147.1	344.9	

Results and discussion

Phase diagram. A database with the assessed Gibbs energy parameters in [1, 2], the Gibbs energy parameters from the binaries (Table 1) and the unary Gibbs energies actualized from [5] was established for the ternary system to be used with the optimisation and assessment software - Thermo-Calc [15] - which was used to compare the new and the available experimental data with the assessed ones (Figs. 1, 2, 3 and 4).

DTA/DSC measurements. All samples were measured by means of DTA/DSC with heating rates of 10ºC/min and 5ºC/min. Values on Table 2 were obtained, on heating, at 5ºC/min. Figs.1 a), 2 a) and 3 present some of the results obtained plotted against the calculated phase diagram obtained after [1].

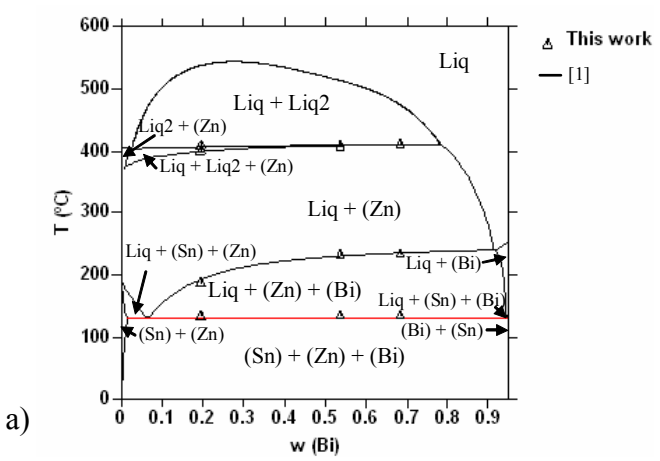

Fig. 1 a) Vertical section of the ternary phase diagram for w(Sn) = 5 %. DTA/DSC data for samples 7, 8 and 9. b) Photomicrograph of sample 7 (magnification ×500) at room temperature. Light grey – (Bi), medium grey – (Sn), dark grey – (Zn).

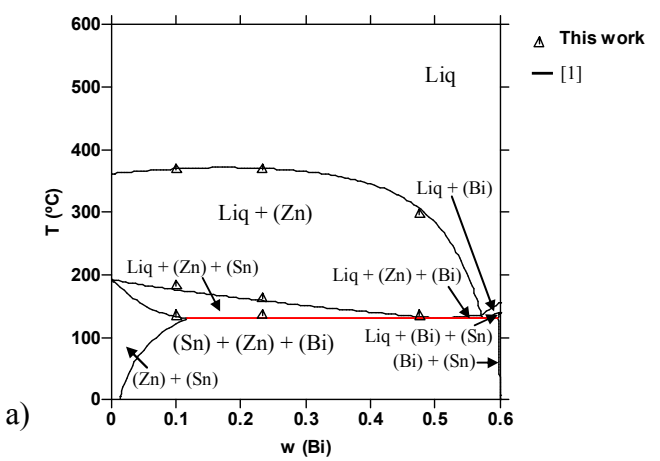

Fig. 2 a) Vertical section of the ternary phase diagram for w(Sn) = 40 %. DTA/DSC data for samples 4, 5 and 6. b) Photomicrograph of sample 5 (magnification ×500) at room temperature. Light grey – (Bi), medium grey – (Sn), dark grey – (Zn).

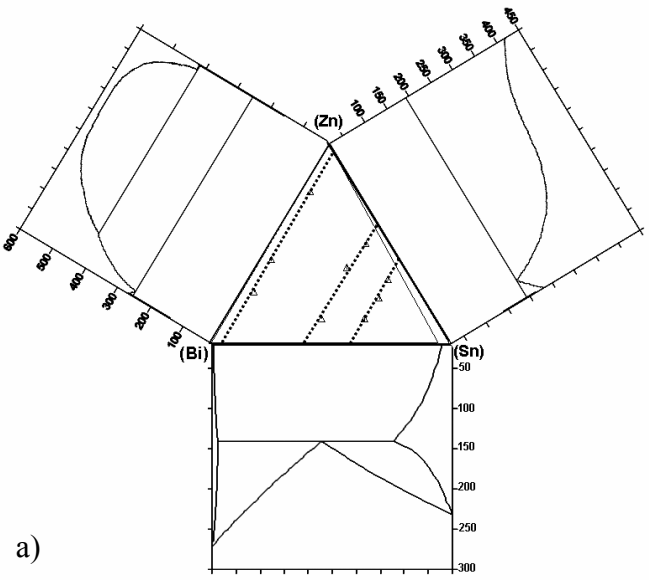

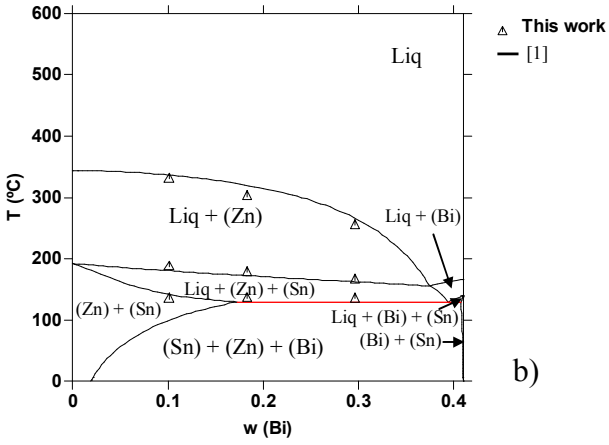

Fig. 3 a) Bi-Sn-Zn at room temperature and its correspondent binaries. Samples from vertical sections in Figs. 1, 2, 3 b)
b) Vertical section of the ternary phase diagram for w(Sn) = 59 %

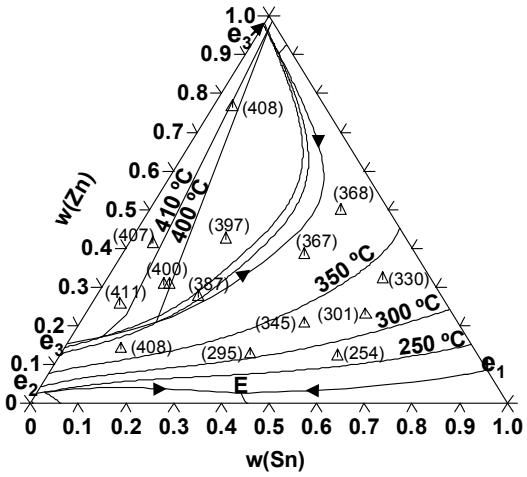

Fig. 4 Projection of the liquidus surface for Bi-Sn-Zn. It can be seen inside of the miscibility gap the surface corresponding to the phase boundary Liq + Liq2 / Liq + (Zn). The triangles corresponding to the sample's composition indicate, in brackets, the temperature in (ºC) of the correspondent liquidus curve, except for those samples which are inside the miscibility gap for which the temperatures in brackets correspond to the phase boundary Liq + Liq2 / Liq + (Zn).

SEM/EDS measurements. All samples were analysed on SEM and the composition of each phase determined by EDS. No external standards for the elements were used; the uncertainty associated with each measurement depends on the element but it is lower than 0.5 wt%. In Figs. 1 and 2 it can be seen two of the photomicrographs taken. It was observed that each sample belongs, at room temperature, to the three phase region (Bi) + (Sn) + (Zn), as it could be expected from the observation of the phase diagram (Fig. 3 a). It was also observed that, in spite of what could be expected from the calculated phase diagrams in [1, 2], (Sn) and (Bi) dissolve, in average and at room temperature, w(Bi) = 4.6 % and w(Zn) = 1.5 %, and w(Sn) = 2.0 % and w(Zn) = 1.6 %, respectively.

XRD at room temperature. All bulk samples were analysed by XRD at room temperature and all peaks were indexed using PDF–2 database [16]. As expected from the SEM/EDS observations, it could be detected for each phase the presence of (Bi) + (Sn) + (Zn) (Fig. 5).

XRD at high temperatures. Samples 8, 9 and 12 were analysed on XRD from 50 – 150º C, 30 – 180 ºC and 120 – 240º, respectively, with temperature increments of 10 ºC. The (Sn)'s peaks couldn't be detected at temperatures higher than 120ºC (Fig. 6) since, at this temperature, the peaks were too small due to the eutectic reaction that occurs at 134 ºC. For higher temperatures, it can be detected on the baseline a curve corresponding to the liquid phase; its concavity grows with temperature as the quantity of liquid increases.

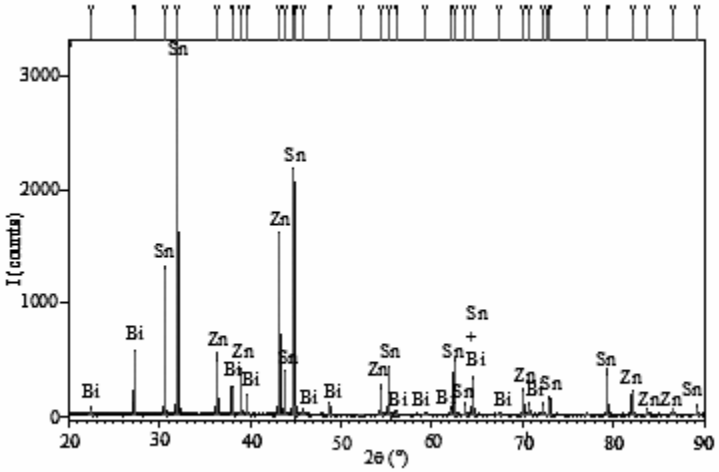

Fig. 5 Diffraction pattern from sample 1, at room temperature.

It can be clearly seen the displacement of the (Zn)'s peak (d = 2.9063 Å), corresponding to the reflection [002], with the temperature increase; this will be a consequence of the enlargement of the distances *a* and *b* (*a* = *b*) at the hexagonal cell.

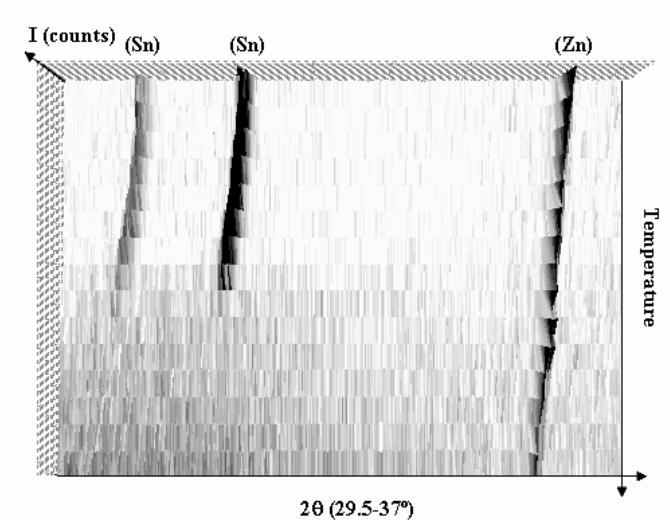

Fig. 6 Zoom of the XRD diffraction patterns as a function of the temperature obtained for sample 9. At T > 120 ºC, Sn peaks cannot be distinguished anymore. For (Zn) the reflection corresponding to [002] suffers a deflection with the increase of temperature.

Conclusions

Experimental results obtained are in better agreement with [1] than with [2].
Results from DTA/DSC are in agreement, not only with the assessed phase diagram from [1], but also with the experimental data from Muzzaffar (1923) [13] (measurements of thermal arrests) that were on the basis of that assessment.
Nevertheless, the eutectic $L \leftrightarrow (Bi) + (Sn) + (Zn)$ was found at 134 ºC, i. e. 4 ºC higher than in the assessed phase diagram in [1].
Results from SEM/EDS show that solvus surfaces, at room temperature, aren't in complete agreement with calculated phase diagrams. (Bi) dissolves Sn and Zn and (Sn) dissolves Bi and Zn. Thus (Bi) and (Sn) should be assessed with ternary terms unlike it was done on [1] and [2].
XRD results, at room and high temperatures, are in agreement with what was expected from the phase diagrams. Nevertheless, the search-match for (Sn) indicated that its reflections are slightly shifted from the pure phase. It's maybe due to a distortion of the cell parameters, probably due to the occupation of some Sn sites by Zn and Bi. The same effect was not so visible on (Bi).
A special attention will be paid, in the future, to the behaviour of the plane [002] in (Zn) with temperature increase, namely, near the eutectic ternary reaction where the interatomic distance, d, has a slight decrease contradicting its tendency to increase with temperature.

References

[1] D. V. Malakhov, X. J. Liu and I. Ohn, J. Phase Equil. 21(6) (2000), p. 514.
[2] N. Moelans K. C. Hari Kumar, P. Wollants, J. Alloys and Comp. 360 (2003), p. 98.
[3] G. Poupon, http://www.sansplomb.org/doc_presentation/pbissue.pdf, 2004
[4] Cost 531 – site, http://www.ap.univie.ac.at/users/www.cost531/, 2005.
[5] A. T. Dinsdale, unpublished data, 1991-1999.
[6] H. Ohtani and K. Ishida, J. Electr. Mater. 23 (1994), p.747.
[7] D. V. Malakhov, CALPHAD, 24 (2000), p. 1.
[8] H. Ohtani, M. Miyashita and K. Ishida, J. Jpn. Inst. Met. 63 (1999), p. 685.
[9] B.-J. Lee, C.-S. Oh, J.-H. Shim, J. Electr. Mater. 25 (1996) 983.
[10] S. Fries, H. L. Lukas, COST507 database, 2 (1998), p. 288.
[11] C. R. Alder-Wright and C. Thomsom, Proc. R. Soc. London, 49 (1891) p. 156.
[12] C. R. Alder-Wright and C. Thomsom, Proc. R. Soc. London, 50 (1892) p. 372.
[13] S. D. Muzaffar, J. Chem. Soc., (123) 1923, p. 2341.
[14] E. Janecke, Z. Metallkd., (29) 1937, p. 367.
[15] B. Sundman, B. Jasson, J. O. Andersson, CALPHAD 9 (2) (1985), p. 153.
[16] 01-085-1329 (Bi), 03-065-0296 (Sn), 01-087-0713 (Zn), ICDD PDF-2 2003.

Available online at www.sciencedirect.com
ScienceDirect
Computer Coupling of Phase Diagrams and Thermochemistry 31 (2007) 468–478
www.elsevier.com/locate/calphad

The experimental study of the Bi–Sn, Bi–Zn and Bi–Sn–Zn systems

M.H. Braga[a,*], J. Vizdal[b,c], A. Kroupa[c], J. Ferreira[d], D. Soares[e], L.F. Malheiros[f]

[a] *GMM-IMAT, Department of Physics, FEUP, R. Dr. Roberto Frias s/n, 4200-465 Porto, Portugal*
[b] *Institute of Mat. Sci. and Eng., Faculty of Mechanical Engineering, Brno University of Technology, Technicka 2896/2, 616 69 Brno, Czech Republic*
[c] *Institute of Physics of Materials AS CR. Zizkova 22, 616 62 Brno, Czech Republic*
[d] *INETI Laboratory, R. da Amieira – P.O. Box 1089, 4466-956 S. Mamede de Infesta, Portugal*
[e] *Department of Mechanical Engineering, School of Engineering of UM, Campus de Azurém, 4800-058 Guimarães, Portugal*
[f] *GMM-IMAT, Department of Metallurgical and Materials Engineering, FEUP, R. Dr. Roberto Frias s/n, 4200-465 Porto, Portugal*

Received 19 April 2006; received in revised form 10 April 2007; accepted 12 April 2007
Available online 22 May 2007

Abstract

The binary Bi–Sn was studied by means of SEM (Scanning Electron Microscopy)/EDS (Energy-Dispersive solid state Spectrometry), DTA (Differential Thermal Analysis)/DSC (Differential Scanning Calorimetry) and RT-XRD (Room Temperature X-Ray Diffraction) in order to clarify discrepancies concerning the Bi reported solubility in (Sn). It was found that (Sn) dissolves approximately 10 wt% of Bi at the eutectic temperature.

The experimental effort for the Bi–Zn system was limited to the investigation of the discrepancies concerning the solubility limit of Zn in (Bi) and the solubility of Bi in (Zn). Results indicate that the solubility of both elements in the respective solid solution is approximately 0.3 wt% at 200 °C.

Three different features were studied within the Bi–Sn–Zn system. Although there are enough data to establish the liquid miscibility gap occurring in the phase diagram of binary Bi–Zn, no data could be found for the ternary. Samples belonging to the isopleths with w(Bi) ∼ 10% and w(Sn) ∼ 5%, 13% and 19% were measured by DTA/DSC. The aim was to characterize the miscibility gap in the liquid phase. Samples belonging to the isopleths with w(Sn) ∼ 40%, 58%, 77/81% and w(Zn) ∼ 12% were also measured by DTA/DSC to complement the study of Bi–Sn–Zn. Solubilities in the solid terminal solutions were determined by SEM/EDS. Samples were also analyzed by RT-XRD and HT-XRD (High Temperature X-Ray Diffraction) confirming the DTA/DSC results for solid state phase *equilibria*.

Keywords: Bi–Sn–Zn; Bi–Sn; DTA/DSC; SEM/EDS; (RT/HT)-XRD

1. Introduction

Health problems (especially neurological and birth malformations) may arise from an excess of lead in human bodies. The excess of lead is due to water contamination. Hence, lead was added to the list of apprehensions with the environment [1].

The objective of COST 531 action "*Lead-free Solder Materials*" [2] (European Cooperation in the field of Scientific and Technical Research) is the study of systems that may be used as lead-free solders. The selection of these systems is based on technical and health considerations. The crucial technical properties to be analyzed should be: melting point, wettability, surface tension, viscosity of the liquid alloys at different temperatures, oxidation behavior, thermomechanical fatigue, etc.

The evaluation of experimental phase diagrams, measurement of the thermodynamic properties and consequent optimization of the corresponding phase diagrams (using the CALPHAD method) are some of the aims of the COST 531 action. The work presented here is a part of this effort.

Bi–Sn–Zn is one of the important systems studied in scope of the above mentioned program. For this system there were no data concerning the liquidus surface in the miscibility gap region (corresponding to the phase boundary Liquid/L1 + L2). A work from Muzaffar [3], concluded in 1923, includes only temperature data for the surface corresponding to the phase boundary Liquid + L1/Liquid + (Zn).

The solvus surfaces for (Bi) and (Sn) were also uncertain. These doubts concern mainly the Sn-rich region within the

* Corresponding author.
E-mail address: mbraga@fe.up.pt (M.H. Braga).

0364-5916/$ - see front matter © 2007 Elsevier Ltd. All rights reserved.
doi:10.1016/j.calphad.2007.04.004

Bi–Sn binary system. Nagasaki and Fujita [4] experimentally defined a (Sn) solvus curve that was not in good agreement with that from Oelsen and Golücke [5]. Experimental results from Ohtani and Ishida [6] were also in contradiction with those from [4]. Nevertheless, Ohtani and Ishida [6] (contradicting their own experimental results) and Lee et al. [7] used only the experimental data from Nagasaki and Fujita [4] in their thermodynamic assessment.

Concerning Bi–Zn, there was a significant discrepancy between the (Bi) solvus estimated by Massalski [8] and that calculated by Malakhov [9] (few wt% of Zn). Thus, targeted experimental alloys were prepared to determine the solubility of Zn in (Bi).

With the aim of clarifying the above indicated aspects of the binaries and ternary, almost all of the samples were studied by SEM/EDS/WDS (Wavelength-Dispersive crystal Spectrometer), RT-XRD/HT-XRD and by DTA/DSC.

2. Experimental

The Bi–Sn and Bi–Sn–Zn systems were objects of two different studies. One more devoted to phase transitions as well as to temperature measurements and the other to the equilibrium study. Hence, the experimental details were different according to the objective of the study and therefore will be presented in two different sections.

2.1. Phase transitions study of the Bi–Sn system

Eight samples of ∼20 mm diameter, ∼3 mm height and weighing ∼2 g were prepared by mixing pure Bi (>99.8%) and Sn (>99.5%). The samples were then put in alumina crucibles and melted in a resistance furnace under an argon atmosphere. The nominal compositions of the samples were Bi$(1-x)$Snx (x = 12.5, 23.5, 36.5, 74.5, 80.1, 84.9, 89.9 and 95.6, wt%). These were confirmed by X-ray Fluorescence (XRF) and Atomic Absorption Spectroscopy (AAS). All samples were homogenized at 120 °C for 60 min and slowly cooled down to the room temperature at a rate less than 2 °C/min.

Samples were studied by Light Optical Microscopy (LOM) and by SEM in a JEOL JSM 6301 F. The SEM is equipped with an INCA Energy 350 EDS analyzer from Oxford Instruments. A backscattered beam with 15 keV is employed. Internal standards are used for the EDS analysis. The experimental uncertainties of the chemical analysis done by EDS are: Bi ±1.2 wt% and Sn ±0.9 wt%.

The Panalytical X'Pert Pro MPD was used for RT-XRD experiments with bulk samples. CuKα or primary monochromated CuKα_1 radiations were used to collect patterns from 5° to 120° (2θ) with steps of 0.01° and counting time of 10 s. The powder HT-XRD was not performed due to problems related with the samples' grinding (the apparatus used only allows powder HT-XRD).

The DTA/DSC measurements were performed on a SETARAM Labsys TG/DTA/DSC in order to establish the transition temperatures. Alumina crucibles were used and measurements were performed under flowing argon atmosphere (approximately 40 cm^3 min^{-1}). Alumina also served as the reference material. Samples weighing between 0.1 and 0.2 g were measured at the heating rates of (in °C/min) 10.0, 5.0 and 2.0–2.5. Transition temperatures were found for "0 °C/min". The temperatures of the invariant phase reactions were taken from the extrapolated temperatures on the onset of heating. The *liquidus* curve temperatures were taken from the peaks on heating.

The global composition and homogeneity of the samples was checked by SEM/EDS, before and after the DTA/DSC experiments.

2.2. Equilibrium study of the Bi–Sn system

Five alloys have been prepared for the equilibrium study. The samples were prepared by mixing pure Bi (>99.9%) and Sn (>99.9%). The nominal compositions of the samples are Bi$(1-x)$Snx (x = 50, 80, 85, 90 and 95, wt%). Samples were analyzed in a SEM from JEOL JSM 6460. The EDS is from Oxford Instruments and it is equipped with an INCA Energy and Wave. The studies were performed in the back-scattered electron mode with 20 keV. Four of the five samples were also studied by DTA/DSC in a Netzsch DTA/DSC 404. For the latter, samples weighing between 0.1 and 0.2 g were introduced into graphite crucibles. Silver was used as a reference material. The measurements were carried out under flowing argon atmosphere (approximately 40 cm^3 min^{-1}).

2.3. Equilibrium study of the Bi–Zn system

The experimental effort was limited to the investigation of the discrepancies concerning the solubility limit of Zn in (Bi) between the theoretical and experimental assessments.

Two alloys were prepared, one with approximately 0.3 wt% Zn and another one with 76.2 wt% Zn. The low Zn content alloy was expected to lie in the single-phase region of the phase diagram, according to the experimental assessment. Nevertheless, according to calculations, it was expected to lie in the two-phase area.

The experimental alloys were melted under an Argon atmosphere in an ERSCEM PV 8920 spill furnace. Samples of approximately 40 g were injected into a copper mould after 20–30 s of stirring.

The low Zn content (approximately 0.3 wt%) alloy was annealed for 336 h at a temperature of 245 °C, just below the eutectic temperature of 254.5 °C. After annealing, the sample was quenched in water and observed by SEM/EDS. The morphology of the sample did not allow the measurement of the composition of the Zn-rich phase. A second alloy was prepared with composition of 23.8 wt% Bi and 76.2 wt% Zn and was therefore cast and annealed at 200 °C for 864 h. This sample was analyzed by SEM/WDS using pure Bi and Zn as standards.

2.4. Phase transitions study of the Bi–Sn–Zn system

Vertical sections for w(Bi) ∼ 10%, w(Zn) ∼ 12%, and w(Sn) ∼ 5%, 13%, 19%, 40%, 59% and 79% were chosen for

this study. The corresponding 29 samples were prepared and annealed like those in Section 2.1. The samples with w(Sn) ∼ 77/81% were re-annealed for more than 180 min at 120 °C, and cooled down at a rate of 0.5 °C/min or quenched into water from 120 °C.

Samples were studied by LOM and by SEM/EDS in the same conditions as those mentioned in Section 2.1. The experimental uncertainties for the chemical analysis obtained by EDS are: Bi ±1.2 wt%, Sn ±0.9 wt% and Zn ±1.1 wt%.

Bulk RT-XRD measurements were performed to identify the present phases. For some samples, powder HT-XRD measurements were also performed, under a vacuum of 10^{-5} mbar or an argon atmosphere. The furnace used is an Anton Parr Chamber applied to the Panalytical X'Pert Pro MPD (details for the XRD data collection are given in Section 2.1).

DTA/DSC measurements were performed on two heat flux instruments with the possibility of determining the latent heat: a TA Instruments SDT 2960 and a SETARAM Labsys TG/DTA/DSC (mentioned in Section 2.1). Alumina crucibles were used and the measurements were performed under flowing argon atmosphere. A graphite plate was sometimes used at the bottom of the crucible in order to improve the removal of the analyzed sample (especially in the case of those samples whose composition fell over the miscibility gap). Alumina (with a similar shape and weight as the measured samples) was used as reference. The samples were polished and cleaned just before being measured in order to improve thermal contact and to avoid spurious or shifted transition peaks due to oxidation. The heating rates mainly used were 20, 10, 5, 2.5 and/or 2.0 °C/min. Unfortunately, the lower heating rates did not allow the detection of transition temperatures (for example, in the case of liquidus surface of the miscibility gap). Consequently, it was impossible to find the transition temperatures at "0 °C/min" by a linear regression. A calibration factor: $C = b_0 + b_1^* T + b_2^* R + b_3^* R^2$ (T — temperature in °C, R – heating rate in °C/min) was evaluated after performing ten calibrations with five different elements (including pure Sn and Zn). Different heating rates (from 2 to 20 °C/min) were also used for determining the coefficients b_0, b_1, b_2 and b_3. The accuracy of all of the given temperatures is ±1 °C. The temperatures of the invariant phase reactions were taken from the extrapolated onset temperatures on heating. The liquidus surface temperatures were taken from the peaks on heating.

After the DTA/DSC measurements, some Bi–Sn–Zn samples were also investigated by SEM/EDS in order to check their compositions.

2.5. Equilibrium study of the Bi–Sn–Zn system

A second set of experiments were carried out in the scope of this study with the aim of reaching states close to the thermodynamic equilibrium and confirming the previous results. Seven samples with nominal compositions (A – Bi35Sn35Zn30, B – Bi20Sn50Zn30, C – Bi10Sn70Zn20, D – Bi18.5Sn45Zn36.5, E – Bi10Sn70Zn20, F – Bi60Sn30Zn10, G – Bi25Sn37.5Zn37.4 and H – Bi25Sn47.6Zn27.4, wt%) were prepared from pure Bi, Sn and Zn (Bi, Sn, Zn > 99.9%, all supplied by Alfa Aesar). The homogeneity of all samples was checked by SEM/EDS (in a JEOL JSM 6460) in the back-scattered electron mode. The microstructure of the samples was, in all cases, found to be reasonably homogeneous in the whole sample volume. Slices of the samples were annealed at two selected temperatures during different intervals of time, before being quenched into cold water. The first set of alloys (A, B and C) was annealed at 100 °C. For a more detailed study and verification of the previously obtained results, a second set of alloys (D, E, F, G and H) was prepared. The annealing temperature for the second set of samples was 120 °C.

SEM/EDS analysis was used to identify the coexisting phases and to measure their compositions (both overall and phase compositions).

Some of the annealed samples were also studied by DTA/DSC (in a Netzsch DTA/DSC 404). The studied samples correspond to compositions that lay in phase regions where the phase *equilibria* were uncertain. The latter measurements were conducted on samples weighing approximately 0.3–0.4 g, which had been sealed under vacuum in quartz crucibles. Gold was used as the reference material. A heating rate of 2.0 °C/min was employed both for calibration and measurement of the prepared samples. The temperatures of the invariant phase reactions were usually taken from the extrapolated onset on heating. The accuracy of all of the given temperatures is ±2 °C.

Table 1
Bi–Sn experimental data from DTA/DSC

w(Sn) (%)	Transition temperatures (°C)	
12.5	138.9[a]	230.1[c]
23.5	138.9[a]	200.9[c]
36.5	139.0[a]	160.5[c]
74.5	138.7[a]	195.7[c]
80.1	138.2[a]	202.8[c]
84.8	138.4[a]	210.5[c]
89.9	138.0[a]	219.3[c]
95.6	188.9[b]	227.0[c]

Final composition was found after AAS and/or XRF and SEM/EDS.
[a] Eutectic temperatures.
[b] *Solidus* temperatures.
[c] *Liquidus* temperatures.

3. Results and discussion

3.1. Bi–Sn system

The DSC/DTA results obtained for the first eight samples can be seen in Table 1. Their comparisons can be made by studying Fig. 1. The invariant temperature measured for the binary eutectic L ↔ (Bi) + (Sn) is 138.6 ± 0.6 °C, which is in agreement with that proposed in [4,6].

For the equilibrium study, the results of five samples studied are summarized in Table 2, along with the experimental uncertainties associated with the EDS work. It has been found that there are no major differences between equilibrated samples annealed at 190, 430, 600, 770, 890 and 950 h (Table 2). Therefore, an annealing time of around 400 h is

Table 2
Bi–Sn experimental data from DTA/DSC and SEM/EDS for samples in equilibrium

Sample	BS 1	BS 2	BS 3	BS 4	BS 5
w(Sn)	50	80	85	90	95
Annealing at 130 °C					
Time (h)	kin. st.[a]	770	600	890	770
SEM/EDS results – composition measurements (wt%)					
w(Sn)	49.4 ± 0.9	78.4 ± 0.5	83.8 ± 1.1	88.0 ± 0.4	93.2 ± 0.2
Sn in (Bi)	0.5 ± 0.2	N/A	N/A	N/A	N/A
Bi in (Sn)	5.8 ± 0.1	N/A	N/A	N/A	5.4 ± 0.3
DSC results (°C)					
Invariant reactions	[b]	138	138	–	–
Solidus	[b]	–	–	186	201
Liquidus	[b]	205	222	220	229

[a] Kinetic study: three samples were annealed for different times (190, 430 and 950 h). Bi content of BCT_A5 (Sn) analyzed by SEM + EDS (5, 6.2 and 5.8 wt%).
[b] Not measured.

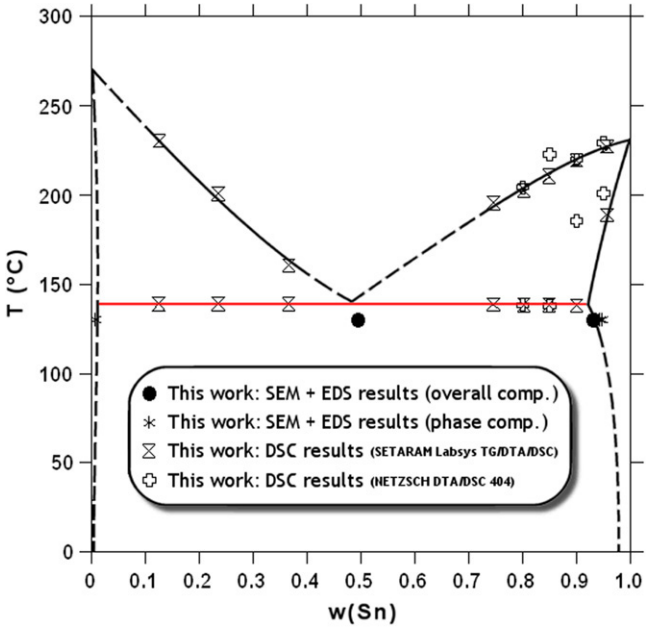

Fig. 1. Bi–Sn experimental phase diagram after results from DTA/DSC and SEM/EDS obtained in the present work. Dashed lines were drawn according to what was expected from our results and having in consideration the literature [6].

sufficient to get close to the equilibrium state. Also, no major discrepancies are found between samples heat treated with annealing times as short as 60 min at 120 °C.

The annealed structures of the samples are elucidated in Fig. 2(a)–(c). They may be viewed as two-phase structures consisting of (Bi) and (Sn), in all of the five alloys annealed at 130 °C. These results are thus consistent with the DTA/DSC results for alloys BS 2 and BS 3 (Table 2).

In disagreement with what was proposed by the authors [6,7], results of this work point to a much lower solubility of Bi in (Sn) (approximately 10 wt% as against approximately 25 wt% [6,7]). On the other hand, the results presented in this paper are apparently in agreement with those proposed by Oelsen and Golücke [5].

The DSC/DTA data obtained with the equilibrated samples, using the Netzsch DTA/DSC 404, point to slightly different solubility of Bi in (Sn) (15 wt%). There are also some discrepancies concerning the Liquid + (Sn) ↔ (Sn). This could be because of the possibility of a slight shift in the corresponding samples' composition.

The authors of the present paper gave more gravity to the data from the set of eight samples (Section 2.1), while assembling the experimental phase diagram. The DTA/DSC data for these eight samples were in agreement with the SEM/EDS and XRD results and also with the results from the ternary Bi–Sn–Zn (Section 3.3).

The microstructure of samples with w(Bi) = 74.5% and w(Sn) = 25.5%, were analyzed by SEM/EDS after being measured by DTA/DSC (and cooled down to room temperature with a rate of 5 °C/min), (Fig. 3). As expected, it confirms the existence of a pro-eutectic and eutectic structure.

The XRD pattern from a bulk sample with w(Bi) = 4.4% and w(Sn) = 95.6%, exhibiting one-phase structure (Sn), is shown in Fig. 4. All other samples from the binary Bi–Sn, detailed in Section 2.1, have been analyzed by RT-XRD. The presence of (Bi) confirms the results of DTA/DSC experiments (Table 1).

3.2. Bi–Zn system

The assessment of Massalski [8] is based on existing experimental results. It indicates a significant solubility of Zn in (Bi) (few wt% of Zn). Nevertheless, the calculations carried out by [9] indicated a much lower solubility (significantly less than 1 wt%). Therefore, the experimental program is focused on the discrepancies of the solubility of the alloying elements in the relevant terminal solid solutions.

The experimental results at 245 °C confirmed the low solubility of Zn in (Bi), as the sample with low Zn content clearly exhibits a two-phase structure (Fig. 5). The results of solubility of both the elements in the respective solid solutions, is shown in Table 3.

3.3. Bi–Sn–Zn system

Muzaffar [3], who thoroughly studied the system by means of thermal arrests, did not measure any point for the *liquidus* surface in the region of the miscibility gap (L1 + L2/Liquid).

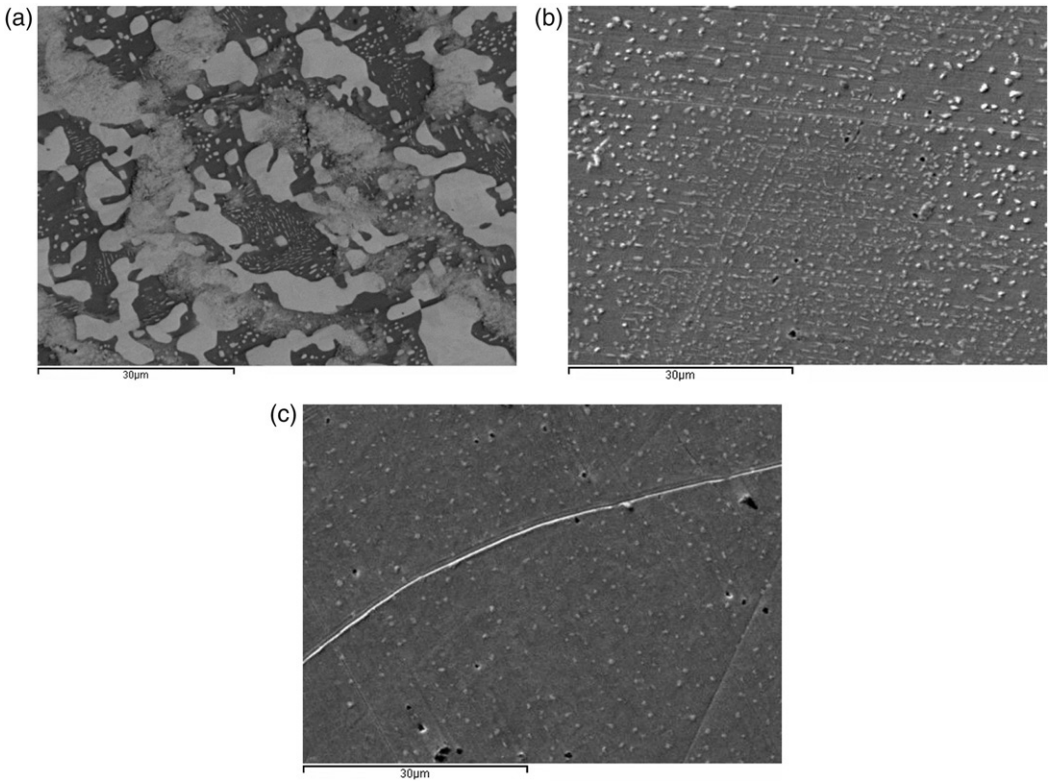

Fig. 2. Microstructure (2000×) of the annealed samples – mixture of light (Bi) and dark (Sn) phases: (a) "BS 1"; (b) "BS 3" and (c) "BS 5".

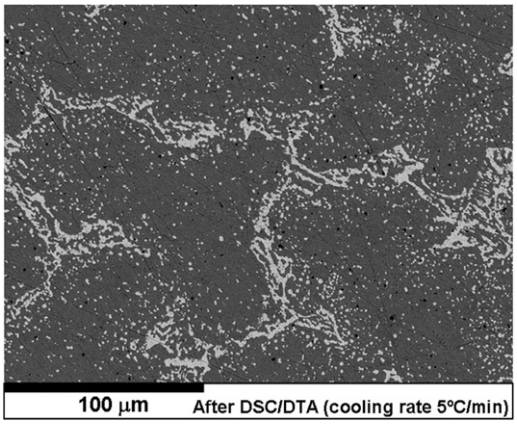

Fig. 3. Microstructure (500×) of the sample with w(Bi) = 74.5% and w(Sn) = 25.5%, after the DTA/DSC experiment with a cooling rate of 5 °C/min: (Bi) – light grey, (Sn) – medium grey.

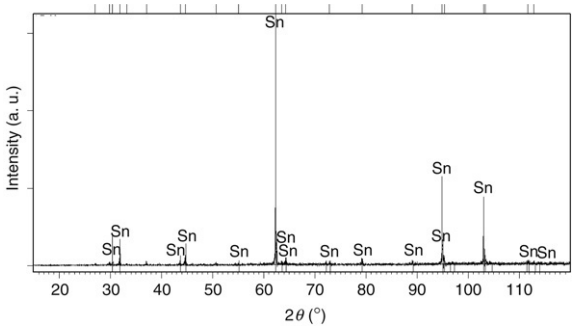

Fig. 4. The XRD pattern at room temperature for a bulk sample with composition: w(Bi) = 4.4% and w(Sn) = 95.6%. This sample was the only one, studied in the Bi–Sn system, which was monophasic (Sn), at room temperature.

Table 3
Composition of the phases present in the Bi–Zn alloy with w(Zn) = 76.2% after the annealing at 200 °C

Phase		Composition of phases (wt%)
(Bi)	Bi	99.7 ± 0.2
	Zn	0.3 ± 0.1
(Zn)	Bi	0.3 ± 0.2
	Zn	99.7 ± 0.2

Fig. 5. Microstructure (1000×) after 336 h of annealing (overall composition: w(Zn) ∼ 0.3 and w(Bi) ∼ 99.7%). The matrix comprises a solid solution of Zn in (Bi) phase and dark particles formed by a solid solution of Bi in (Zn).

In this work, we measured the miscibility gap in the liquid phase by using DTA/DSC at heating rates of 10–20 °C/min.

Table 4
Bi–Sn–Zn experimental data from DTA/DSC and SEM/EDS

Results for Bi–Sn–Zn from DTA/DSC							
w(Bi)	w(Sn) (%)	w(Zn)	Transition temperatures (°C)				
10.0	4.1	85.9	133.7[a]	182.9	394.3	402.5	502.6
20.1	5.0	74.9	133.1[a]	200.6	394.4	406.1	518.2
30.4	5.0	64.6	134.4[a]	217.0	398.7	410.3	524.8
32.8	5.1	62.1	133.7[a]	223.3	405.5	407.5	528.1
43.8	4.7	51.5	133.6[a]	229.4	407.3	413.2	519.8
53.3	4.9	41.8	134.4[a]	230.7	407.1	414.4	509.5
55.4	5.5	39.1	134.2[a]	236.4	409.1	414.0	510.9
68.5	5.7	25.8	133.4[a]	232.9	–	412.1	460.3
31.7	14.3	54.0	133.5[a]	186.0	399.9	401.9	463.0
55.6	13.7	30.7	134.2[a]	212.6	–	403.0	
56.7	12.6	30.7	133.9[a]	217.9	–	404.3	
74.0	11.9	14.1	133.9[a]	223.0	360.3		
11.7	18.0	70.3	134.3[a]	153.7	384.5	393.7	439.4
26.5	18.2	55.3	135.1[a]	138.0	390.7	399.2	443.9
28.0	17.8	54.2	133.5[a]	148.0	394.6	399.0	447.0
37.9	19.8	42.3	134.4[a]	171.4	395.4	404.9	
51.1	21.4	27.5	134.6[a]	177.6	386.7		
55.0	28.9	16.1	134.8[a]	170.4	343.7		
10.1	40.1	49.8	134.0[a]	182.6	367.7		
23.7	38.5	37.8	135.1[a]	161.4	367.0		
47.2	40.4	12.4	134.1[a]	137.7	295.4		
30.6	45.8	23.6	133.4[a]	143.2	341.7		
37.2	44.1	18.7	133.5[a]	147.1	344.9		
10.1	57.8	32.1	134.0[a]	187.2	330.0		
18.2	59.5	22.3	134.2[a]	181.5	299.5		
29.3	58.5	12.2	134.8[a]	165.6	254.7		
4.7	76.5	18.8	–	168.8	193.3	282.2	
9.2	81.0	9.8	131.0	188.2	231.5		
9.6	81.0	9.4	131.7	182.6	230.1		

Average compositions for the solid phases of Bi–Sn–Zn from SEM/EDS (calculated from 29 samples) (for $T < 120$ °C)

Phase	Composition of phases (wt%)		
	$w(Bi)_{av.} \pm 1.2\%$	$w(Sn)_{av.} \pm 0.9\%$	$w(Zn)_{av.} \pm 1.1\%$
(Bi)	95.5	1.9	2.6
(Sn)	4.4	93.3	2.3
(Zn)	0.2	0.3	99.5

Final composition was found after AAS and/or XRF and SEM/EDS.
[a] Eutectic temperatures.

The results, listed in Table 4, are plotted in Figs. 6 and 7. In some cases, the cooling curve is helpful in identifying the peak corresponding to the *liquidus* temperature. It is difficult to find *liquidus* surface' peaks for samples belonging to the vertical section w(Sn) ∼ 5%, with w(Bi) ∼ 20% and 70%; which may be due to the spinodal effect. The *liquidus* temperatures for these two samples are shown in Table 4 but it has to be taken into account that the experimental uncertainty can be higher for these two samples than for the rest. An example of a DTA/DSC curve obtained for a sample with w(Bi) = 53.3%, w(Sn) = 4.9% and w(Zn) = 41.8% is depicted in Fig. 8.

DTA/DSC results from equilibrated samples are in agreement with the previous ones (Table 5).

The invariant temperature measured for the ternary eutectic L ↔ (Bi) + (Sn) + (Zn) is 134.1 °C ± 1.0 °C which is 4.2 °C higher than that proposed in [3].

All samples in Table 4 have been analyzed by bulk XRD at room temperature after being annealed for 60 min at 120 °C and slowly cooled down to room temperature. All peaks were searched/matched using the ICDD PDF-2 2003 database [10–12]. The results show that all samples are homogeneous and that belong to the three-phase region (Bi) + (Sn) + (Zn) (see Fig. 9). Despite the fact that XRD results are in agreement with what was expected from the phase diagrams, the search/match for (Sn) indicated that its reflections are slightly shifted with respect to their position for pure Sn. This maybe due to a

Table 5
Experimental results obtained from Bi–Sn–Zn alloys, annealed at 100 °C

Sample		A	B	C
Composition (wt%)		Bi35–Sn35–Zn	Bi20–Sn50–Zn	Bi10–Sn70–Zn
Annealing at 100 °C				
Time (h)		744	980	980
SEM/EDS results – composition measurements (wt%)				
Overall	Bi	35.5 ± 0.7	22.4 ± 0.4	11.1 ± 0.3
	Sn	33.6 ± 0.9	54.8 ± 0.5	71.9 ± 0.5
	Zn	30.9 ± 0.9	22.8 ± 0.6	17.0 ± 0.6
(Bi)	Bi	95.9 ± 0.8	96.6 ± 0.7	94.4 ± 1.3
	Sn	0.4[a]	0.7 ± 0.4	3.0 ± 1.0
	Zn	3.7 ± 0.6	2.7 ± 0.7	2.6 ± 1.0
(Sn)	Bi	3.6 ± 0.9	4.3 ± 0.3	3.9 ± 0.4
	Sn	93.3 ± 1.0	94.0 ± 0.6	94.6 ± 0.4
	Zn	3.1 ± 1.0	1.7 ± 0.5	1.5 ± 0.3
(Zn)	Bi	0.7 ± 0.2	0.4[a]	0.4[a]
	Sn	0.7 ± 0.3	0.5 ± 0.2	1.5 ± 0.5
	Zn	98.6 ± 0.3	99.5 ± 0.2	98.2 ± 0.7

Sample	D		E[b]	F[b]	G	H
Comp. (wt%)	Bi18.5–Sn45–Zn		Bi10–Sn70–Zn	Bi60–Sn30–Zn	Bi25–Sn37.6–Zn	Bi25–Sn47.6–Zn
Annealing at 120 °C						
Time (h)	1175		1175	1100	1175	1100
SEM/EDS/WDS results – composition measurements (wt%)						
Overall	Bi	19.6 ± 0.5	14.0 ±0.5	61.2 ± 1.1	30.6 ± 1.2	27.3± 1.6
	Sn	48.2 ± 0.7	68.1 ± 1.0	33.9 ± 1.4	40.8 ± 1.1	52.7 ± 1.3
	Zn	32.2 ± 0.9	17.9 ± 1.0	4.9 ± 0.5	28.6 ± 1.4	20.0 ± 1.7
(Bi)	Bi	97.7 ± 0.7		99.2 ± 0.2	97.6 ± 0.5	99.2± 0.2
	Sn	0.6 ± 0.2	N/A	0.4 ± 0.2	0.6 ± 0.2	0.3 ± 0.2
	Zn	1.7 ±0.5		0.4 ± 0.2	1.8 ± 0.5	0.5 ± 0.3
(Sn)	Bi		4.8 ± 0.6	4.4 ± 0.3		
	Sn	N/A	93.5 ± 0.8	94.8 ± 0.6	N/A	N/A
	Zn		1.7 ± 0.7	0.8 ± 0.6		
(Zn)	Bi	0.1[c]	0.0	0.0	0.4 ± 0.5	0.4 ± 0.4
	Sn	0.6 ± 0.3	0.3 ± 0.2	0.3 ± 0.1	0.4 ± 0.3	0.5 ± 0.1
	Zn	99.3 ± 0.3	99.7 ± 0.2	99.7 ± 0.1	99.2 ± 0.7	99.1 ± 0.4
DTA/DSC results (°C)						
Invariant		135	134	136	136	135
Liquidus		364	297	300	376	340
Others		174	193	168	160	168

[a] These values are not reliable because of the accuracy limitations of EDS and/or very small size of (Bi) or (Sn) particles in the structure.
[b] SEM/WDS was used for the analysis of selected phases: for the "E" sample (Sn) and (Zn), and for the "F" sample (Bi) and (Sn) phases were measured (pure Bi, Sn and Zn standards were used).
[c] The values are not reliable because of the accuracy limitations of EDS and/or very small size of (Bi) or (Sn) particles in the structure. N/A – The values of phase compositions could not be reliably measured because of formation of a mixture of tiny (Bi) particles in (Sn) matrix (see Fig. 11).

distortion of the cell by the partial substitution of Sn by Zn and Bi. We could not detect a similar effect for (Bi); this is probably because the solubility of Sn in (Bi) is significantly smaller than the solubility of Bi in (Sn). In addition, the covalent radius of Bi (0.154 nm) [13] is slightly bigger than that of Sn (0.146 nm) [13] possibly increasing this effect.

HT-XRD measurements were performed from 30 to 180 °C with temperature increments of 10 °C. The HT-XRD diffraction patterns can be observed in Fig. 10. The (Sn) peaks (Fig. 9) could not be detected for temperatures higher than 120 °C because the peaks were too small due to the eutectic reaction occurring at 134 °C. An amorphous phase could be detected for higher temperatures (a halo – a curved baseline – is observed for 2θ between 20° and 40°). It corresponds to the liquid phase. As expected, with the increase in the amount of liquid the concavity also increases. Special attention should be given to the behavior of the [002] plane in (Zn) ($T = 30$ °C, $2\theta = 36.37°$; $d = 0.247$ nm) slightly above the ternary eutectic reaction where the inter-atomic distance, d, slightly decreases. This is in contradiction to the expected tendency to increase with temperature probably due to the rearrangement initiated by the appearance of liquid.

Table 4 lists the solubility of each element in all solid solutions measured by SEM/EDS. The temperature is

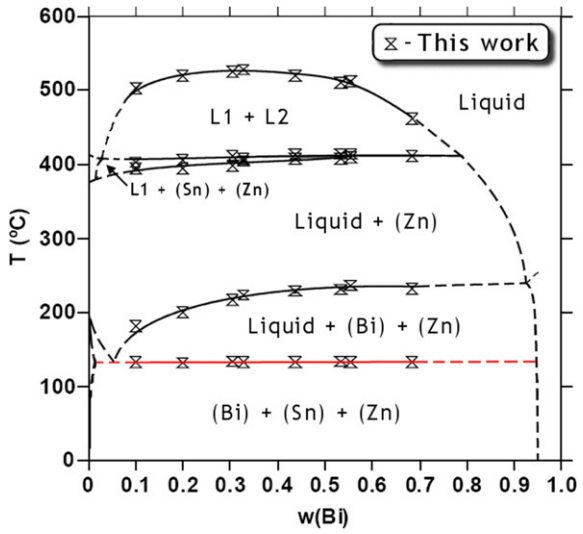

Fig. 6. Experimental vertical section for w(Sn) ∼ 5%. Symbols point for the experimental transition temperatures obtained by DTA/DSC in the present work. Dashed lines were drawn according to what was expected from our results and having in consideration the literature [3].

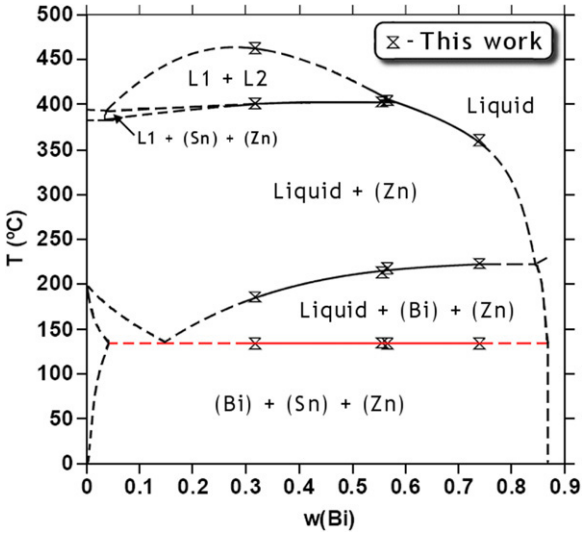

Fig. 7. Experimental vertical section for w(Sn) ∼ 13%. Symbols point for the experimental transition temperatures obtained by DTA/DSC in the present work. Dashed lines were drawn according to what was expected from our results and having in consideration the literature [3].

considered to be less than 120 °C because samples are annealed at 120 °C for 60 min and slowly cooled down to room temperature. Fig. 11 envisages four SEM microstructures of some selected samples showing the three different phases, in accordance with the expectation.

Three samples with w(Sn) ∼ 77/81% have been subjected to two different heat treatments consisting of an annealing at 120 °C for 180 min followed by slow cooling at 0.5 °C/min and an annealing for 180 min at 120 °C, followed by water quenching. Our intention concerning the first heat treatment is to obtain phases' composition near room temperature, comparable with those already referred. For the second heat

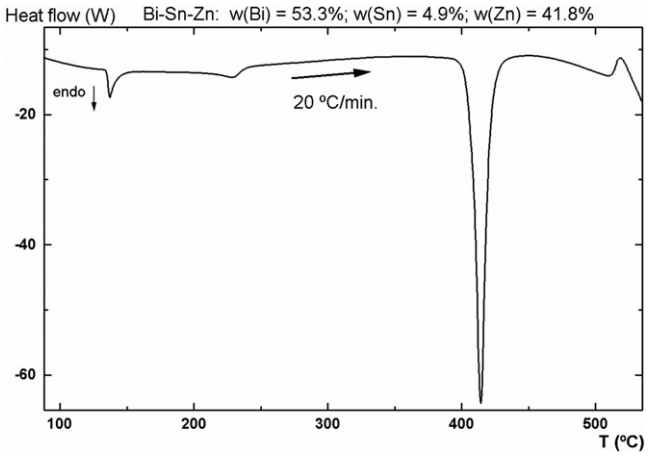

Fig. 8. An example of a DTA/DSC heating curve. The composition of the sample is presented in the figure.

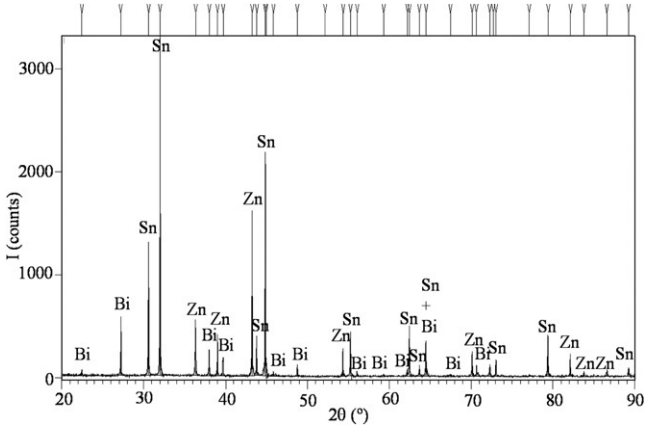

Fig. 9. A XRD pattern at room temperature for a bulk sample with composition: w(Bi) = 10.1%, w(Sn) = 57.8%, w(Zn) = 32.1%.

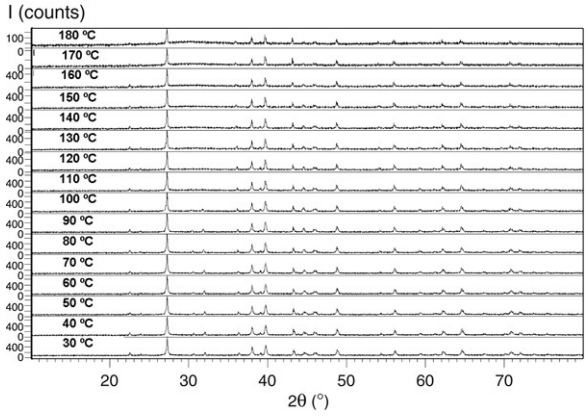

Fig. 10. HT-XRD patterns for a powder sample with composition: w(Bi) = 68.5%, w(Sn) = 5.7%, w(Zn) = 25.8% from room temperature to 180 °C.

treatment, we aim at obtaining the phases' composition at 120 °C. The results show, in both cases, a similarity between phases' composition measured by EDS. This similarity could

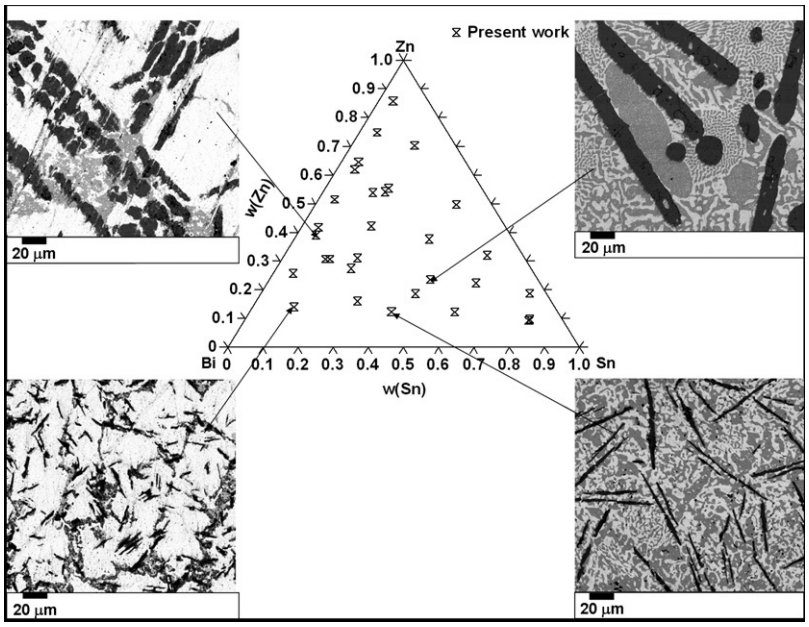

Fig. 11. Microstructures of selected samples (500×): (Bi) – light grey, (Sn) – medium grey, (Zn) – dark grey. The composition of samples is indicated by arrows. All studied Bi–Sn–Zn samples are indicated in the figure.

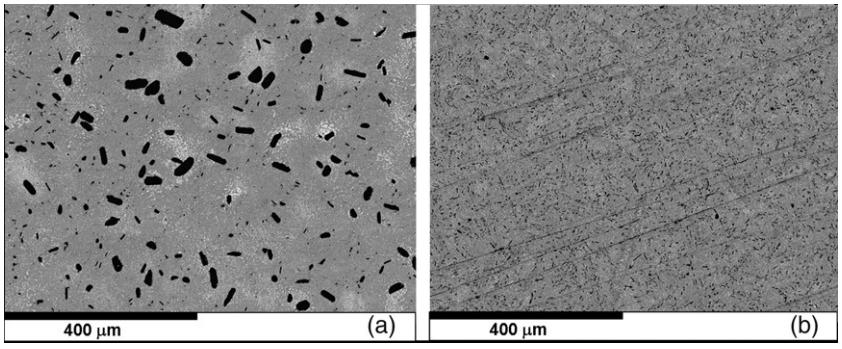

Fig. 12. Microstructures (150×) of a sample with w(Bi) = 9.2%; w(Sn) = 81.0%; w(Zn) = 9.8% after: (a) slow cooling (0.5 °C/min) after 180 min at 120 °C and in (b) water quenched after 180 min at 120 °C: (Bi) – light grey, (Sn) – medium grey, (Zn) – dark grey.

be a result of the short annealing stage, not sufficient to reach the thermodynamic equilibrium. It could also be an effect of the used cooling rate, which is not high enough to "freeze" the "high-temperature" structure. The main difference between samples annealed in different ways reflects in the grain size (Fig. 12).

Concerning the *solvus* of (Bi) and (Sn), SEM/EDS results from samples which previously underwent DTA/DSC experiments, followed by cooling at a rate of 5 °C/min, are also in agreement with the above mentioned results.

As mentioned in Section 2.5, the Bi–Sn–Zn system is also an object of equilibrium study. Examples of the equilibrated samples resulting in microstructures are shown in Figs. 13(a)–(b) and 14(a)–(c).

The results hence obtained agree with the Bi–Sn experimental results (see Section 3.1) and confirm the errors in the predicted phase boundaries. The experimental results also confirmed the observation of Malakhov [9], that the presence of Sn increases the solubility of Zn in (Bi). This increase is significant as the value measured in the ternary alloy is several times higher than the value measured in the binary Bi–Zn system.

Tables 4 and 5 list the results of DTA/DSC measurements (namely the transition temperature found for lower Bi content, corresponding to probable ternary eutectic reaction), which confirmed a much lower Bi solubility in (Sn) than previously anticipated in [6].

4. Conclusions

1. Results from DTA/DSC, SEM/EDS/WDS, RT-XRD and HT-XRD (for some samples) are obtained for the Bi–Sn, Bi–Zn and Bi–Sn–Zn systems and critically compared. New values for the *liquidus* surface of the ternary miscibility gap have also been obtained.
2. Results are generally in agreement with each other. The binaries' results confirm those obtained for the ternary and vice-versa.

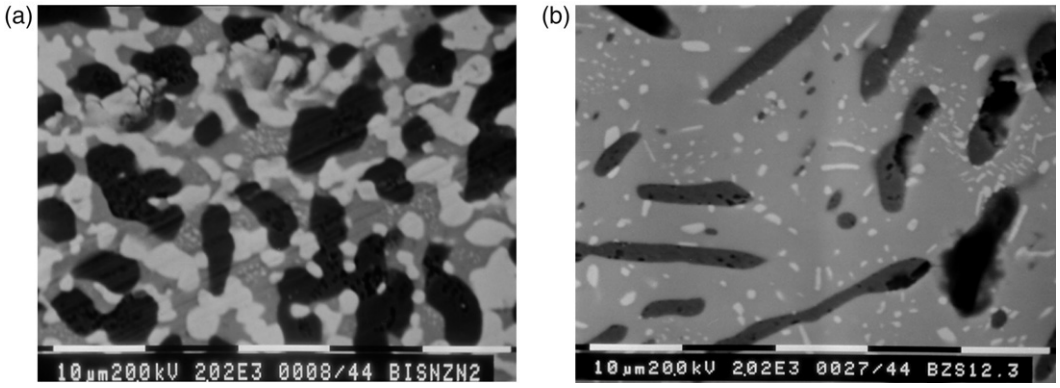

Fig. 13. Microstructure (2000×) of the Bi–Sn–Zn samples (a) "A" (annealed 744 h) and (b) "C" (annealed 980 h), showing a grey matrix of a solid solution of Bi and Zn in (Sn), dark Zn-rich and light Bi-rich phases (both are also solid solutions).

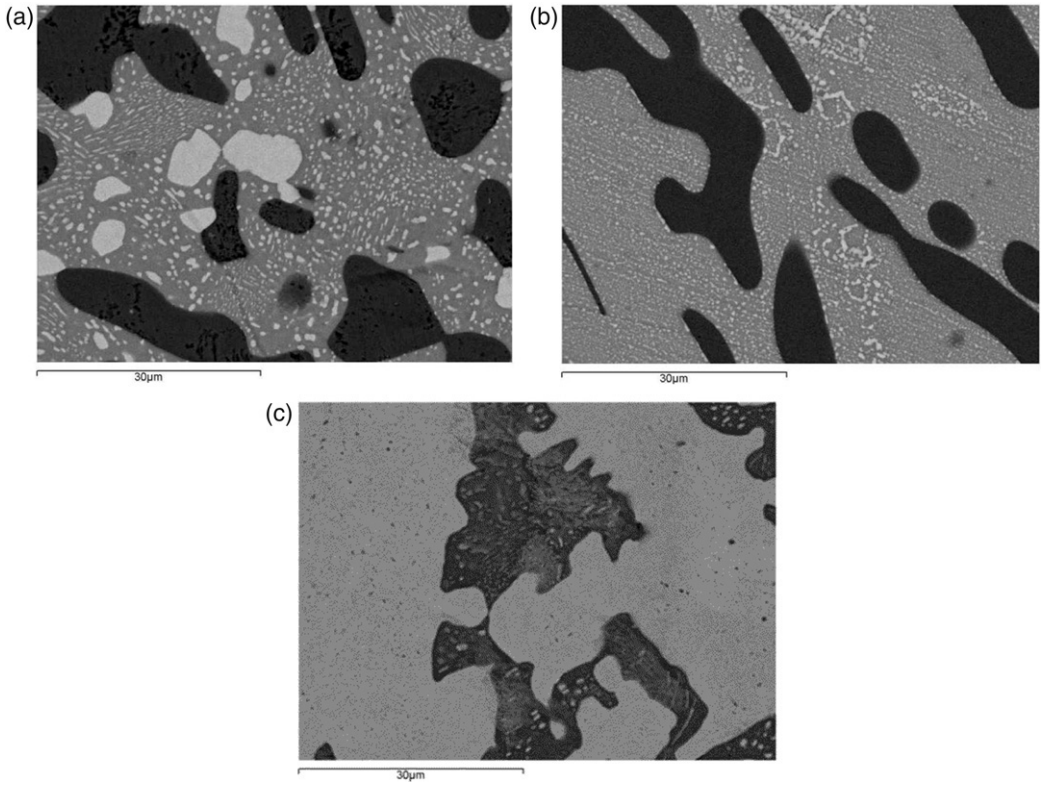

Fig. 14. Microstructure (2000×) of the Bi–Sn–Zn samples (a) "D" (annealed 1175 h), (b) "E" (annealed 1175 h) and (c) "F" (annealed 1100 h), showing the grey matrix of a solid solution of Bi and Zn in BCT_A5 (Sn), dark Zn-rich and light Bi-rich phases (both are also solid solutions).

3. From the ternary and binary results obtained from different techniques, it appears that the solubility of Bi in (Sn) does not surpass w(Bi) ∼ 10%, at the eutectic temperature, which is not in agreement with the assessed phase diagram in [6].
4. Results for Bi–Zn indicate that the solubility of both elements in the respective solid solution is approximately 0.3 wt% at 200 °C as in [9].
5. A reassessment of the Bi–Sn binary and also Bi–Sn–Zn ternary system is desirable. In a recent work of Vizdal et al. [14], the authors of this work reassessed the Bi–Sn and the Bi–Sn–Zn systems based, among others, on the experimental results presented in this study.

Acknowledgments

This work is a contribution to the European COST 531 Action on "Lead-free Solder Materials". J. Vizdal and A. Kroupa would also like to thanks to the Ministry of Education of the Czech Republic and project COST 531.002 for the support.

References

[1] G. Poupon. http://www.sansplomb.org/doc_presentation/pbissue.pdf, 2004.

[2] COST 531 – site. http://www.univie.ac.at/cost531/, 2005.
[3] S.D. Muzaffar, J. Chem. Soc. 123 (1923) 2341–2352.
[4] S. Nagasaki, E. Fujita, J. Japan Inst. Met. 16 (1952) 317–321.
[5] W. Oelsen, K.F. Golücke, Arch. Eisenhüttenwes. 29 (1958) 689–698.
[6] H. Ohtani, K. Ishida, J. Electron. Mater. 23 (1994) 747–755.
[7] B.-J. Lee, C.-S. Oh, J.-H. Shim, J. Electron. Mater. 25 (1996) 983.
[8] T.B. Massalski, Binary Alloy Phase Diagrams, ASM International, Ohio, 1990.
[9] D.V. Malakhov, CALPHAD 24 (2000) 1.
[10] 01-085-1329 ICDD PDF-2 2003; from ICSD using POWD-12++ after P. Cucka, C. S. Barrett, Acta Crystallogr. 15 (1962) 865–872.
[11] 03-065-7657 ICDD PDF-2 2003; from NIST using POWD-12++ after V. T. Deshpande, D. B. Sirdeshmukh, Acta Crystallogr. 14 (1961) 355–356.
[12] 01-087-0713 ICDD PDF-2 2003; from ICSD using POWD-12++ after H. E. Swanson, E. Tatge, Natl. Bur, Stand. (U.S.), circ. 539, 359 (1953) I1.
[13] The Cambridge Crystallographic Data Centre. http://www.ccdc.cam.ac.uk/products/csd/radii/, 2004.
[14] J. Vizdal, M.H. Braga, A. Kroupa, K.W. Richter, D. Soares, L.F. Malheiros, J. Ferreira, The thermodynamic assessment of the Bi–Sn–Zn system, CALPHAD (2007) (in press).

Available online at www.sciencedirect.com
ScienceDirect
Computer Coupling of Phase Diagrams and Thermochemistry 31 (2007) 438–448
www.elsevier.com/locate/calphad

Thermodynamic assessment of the Bi–Sn–Zn System

Jiri Vizdal[a,b,*], Maria Helena Braga[c], Ales Kroupa[a], Klaus W. Richter[d], Delfim Soares[e], Luís Filipe Malheiros[f], Jorge Ferreira[g]

[a] *Institute of Physics of Materials, AS CR, Zizkova 22, Brno, Czech Republic*
[b] *Institute of Materials Science and Engineering, Faculty of Mechanical Engineering, Brno University of Technology, Technicka 2, Brno, Czech Republic*
[c] *GMM-IMAT, Department of Physics, FEUP, R. Dr. Roberto Frias s/n, Porto, Portugal*
[d] *Institut für Anorganische Chemie/Materialchemie, Universität Wien, Währingerstr. 42, Wien, Austria*
[e] *Department of Mechanical Engineering, School of Engineering of University of Minho, Campus de Azurém, Guimarães, Portugal*
[f] *GMM-IMAT, Department of Metallurgical and Materials Engineering, FEUP, R. Dr. Roberto Frias s/n, Porto, Portugal*
[g] *National Institute of Engineering and Industrial Technology Laboratory, R. da Amieira, S. Mamede de Infesta, Portugal*

Received 19 April 2006; received in revised form 4 May 2007; accepted 17 May 2007
Available online 18 June 2007

Abstract

A thermodynamic assessment of the Bi–Sn–Zn ternary system was carried out using the CALPHAD approach along with thermodynamic descriptions from new assessments of the Bi–Sn and Bi–Zn systems. Selected experimental data from the literature and our own work were also used. New sets of optimized thermodynamic parameters were obtained that lead to a very good fit between the calculated and experimental data. The Bi–Sn–Zn system is one of the candidates for lead-free solder materials.

Keywords: Lead-free solders; Bi–Sn assessment; Bi–Sn–Zn assessment; CALPHAD approach; COST531 database

1. Introduction

It is well known that lead and lead-containing materials are toxic and dangerous to the surrounding environment. The EU Directives on Waste Electrical and Electronic Equipment (WEEE) and Restriction of Hazardous Substances (RoHS) prohibited the use of lead in selected electronic equipment sold in the European market. The directives came into force on 13 February 2003, giving 1 July 2006 as the date when the European electronics industry had to be lead-free. Currently, it is generally acknowledged that lead-free soldering is technologically possible (e.g. the Japanese electronics industry is virtually 100% lead-free). Nevertheless, we also have to take into account the adverse properties of possible substituting elements (e.g. toxicity, price, suitability, etc.) in the process of designing new lead-free soldering materials. Selected issues are addressed within the scope of the COST 531 action and the preparation of a self-consistent thermodynamic database for the alloy systems crucial for lead-free soldering is a major aim of this project.

Following new experimental investigations of the Bi–Sn, Bi–Zn and Bi–Sn–Zn systems, and inconsistencies between assessments of these systems already published, we have found it necessary to reassess their thermodynamic descriptions. The latest version of the SGTE unary database [1] was selected as a basis for the calculations. Phase equilibria studies were carried out in regions of the phase diagrams where the most significant differences exist and the relevant results are also reported in this paper.

This work has contributed significantly to the development of the "COST531" database [2].

2. Theoretical part

The *CALPHAD* method is used in this work. This procedure is based on the sequential modeling of phase equilibria and thermodynamic properties of alloy systems, starting from binary systems and leading to higher-order systems. It is

* Corresponding author at: Institute of Physics of Materials, AS CR, Zizkova 22, Brno, Czech Republic. Tel.: +420 532290467; fax: +420 541218657.
E-mail address: jvizdal@centrum.cz (J. Vizdal).

0364-5916/$ - see front matter © 2007 Elsevier Ltd. All rights reserved.
doi:10.1016/j.calphad.2007.05.002

possible to obtain accurate predictions of phase equilibria of multicomponent systems using this approach. The crucial condition for the success of such a method is a good and consistent database for the calculation of the thermodynamic properties of the relevant systems.

The mathematical method for the calculation of thermodynamic equilibrium is based on modeling the Gibbs energies of all phases and minimizing the total Gibbs energy of the system. The total Gibbs energy of the system can be calculated by the formula $G^{\text{tot}} = \sum_f w^p G^p$, where the symbol w^p is the amount of phase p and G^p its Gibbs energy. The Gibbs energy for a particular solution phase is expressed by the general formula $G^p = \sum_i x_i \, {}^\circ G_i^p + G^{\text{id}} + G^E + G^{\text{mag}} + \cdots$, where $x_i \, {}^\circ G_i^p$ is the contribution of the Gibbs energy of the element i in the crystallographic structure, corresponding to the phase p with respect to its reference state (contribution of the pure components), x_i is the molar fraction of element i, and ${}^\circ G_i^p$ is the molar Gibbs energy of pure element i in the structure, corresponding to the phase p. The symbol G^{id} denotes the ideal mixing contribution; G^E is the contribution due to non-ideal interactions between the components (the excess Gibbs energy of mixing) and G^{mag} is the contribution of magnetic Gibbs energy if the phase exhibits magnetic properties. Other excess Gibbs energy terms can be introduced, e.g. pressure dependence $\{G^{\text{press}}\}$, energy of the interface, energy of plastic deformation, energy of defects in the crystal lattice, etc.

Intermediate phases are usually modeled using the sublattice model [3]. This model is based on the distribution of independent lattice positions in the crystal structure into several sublattices, according to their physical properties. The amount of a particular element in the sublattice k is defined by lattice fractions y_i^k, which are defined as

$$y_i^k = \frac{n_i^k}{\sum_{i=1}^{s} n_i^k},$$

where n_i^k is number of moles of component i in sublattice k, and s is number of components occupying sublattice k.

A real crystallographic lattice can be envisaged as a superposition of several sublattices from this point of view [3]. The Thermo-Calc software [4] was used in this work for the optimization of the model parameters and calculation of phase equilibria and thermodynamic properties.

3. The Bi–Sn–Zn system and its subsystems

3.1. Introduction

An extensive experimental investigation of the Bi–Sn–Zn system has been conducted by Braga et al. [5]. The solubilities of the components in the terminal solid solutions were measured and compared with predictions using thermodynamic parameters from [6] and [7]. However, discrepancies between experimental and calculated solubilities were found for Bi in HCP_Zn, and particularly for the solubility of Bi in BCT_A5 (Sn). The results given in [5] indicated a much lower solubility of Bi in the BCT_A5 (Sn) solid solution (around 10 wt% at the eutectic temperature) and confirmed the need for a new thermodynamic description for the Bi–Sn system. This fact is especially important from the point of view of the development of the "COST531" thermodynamic database [2] because other important ternary system descriptions are based on this binary. Therefore, targeted experiments using scanning electron microscopy (SEM) + energy-dispersive solid-state spectrometry (EDS) and differential scanning calorimetry (DSC) were carried out in the Sn-rich part of the Bi–Sn phase diagram as part of the experimental study [5].

Disagreement between the experimental ternary phase equilibria and the solubility limit of bismuth in HCP_Zn calculated using the assessed thermodynamic parameters led to small changes in the description for the Bi–Zn system, too.

Experimental studies and the remodeling of the binary and ternary systems are summarized and discussed in the following sections.

3.2. Bi–Sn system

Many authors have investigated the phase equilibria and thermodynamic properties of this system experimentally, but with a certain amount of disagreement between some of the results. Nagasaki and Fujita [8] measured the specific heat, and Oelsen and Golücke [9] determined heats of mixing. More recently, Ohtani and Ishida [10] reported liquidus data and the eutectic temperature, which they measured using DSC. The agreement among these three sets of data is generally good. Many authors also investigated the enthalpies of mixing of liquid Bi–Sn alloys, e.g. [11–14]. As Ohtani and Ishida [10] pointed out, work carried out before the 1940's (e.g. [11]) show large scatter while there is a rather good agreement amongst later data, e.g. [12–14]. Many authors have measured the activities of Sn in the liquid phase using electromotive force (EMF) methods; one of the most recent works in this field is the contribution of Asryan and Mikula [15]. Yazawa and Koike [16] also measured the activities of Bi in the liquid at 1100 °C, whereas Rickert et al. [17] measured activities at 750–1050 °C. The activities measured by the various authors were in good mutual agreement, showing a slight positive deviation from ideality. However, the calculated enthalpies showed large mutual discrepancies. Only those of Seltz and Dunkerley [18] were in good agreement with directly measured data [12–14]. Enthalpies of formation of solid alloys are also available from the calorimetric measurements made by Oelsen and Golücke [9]. A list of other related references is available in the paper of Lee et al. [19].

Thermodynamic modeling of this system has been carried out by Ohtani and Ishida [10] and Lee et al. [19]. The assessments differ in the unary data used (i.e. the Gibbs energy differences for the pure components in certain crystallographic structure – especially for their metastable states – with respect to Stable Element Reference state of that component). Therefore the phase boundaries calculated using their assessed data disagree. A different solubility of Sn in the Rhombohedral_A7 (Bi) phase can be clearly seen (Fig. 1(a) and

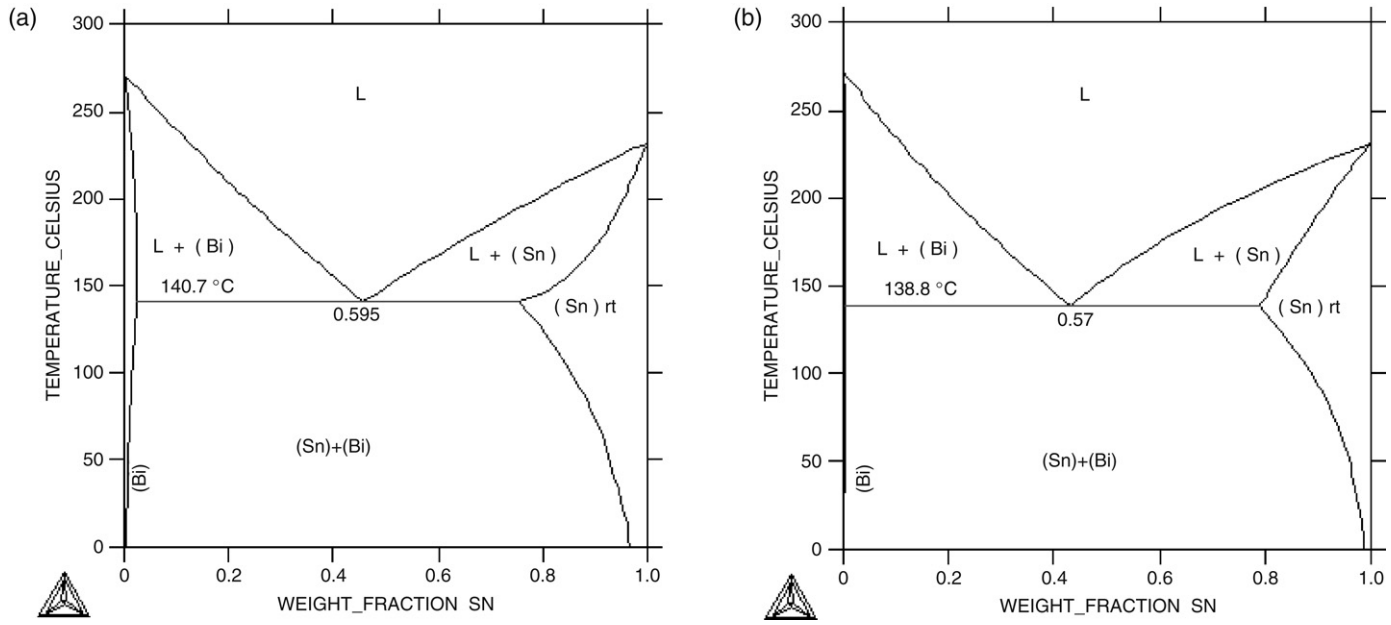

Fig. 1. Optimized phase diagram Bi–Sn according to (a) Ohtani and Ishida [10] and (b) Lee et al. [19].

(b)). Lee et al. [19] did not take into account the solubility of Sn in Rhombohedral_A7 (Bi) reported by Oelsen and Golücke [9] and obtained a much lower solubility in their assessment.

The liquid phase, Rhombohedral_A7 solid solution (Bi-rich) and BCT_A5 solid solution (Sn-rich) are stable in this system. All solid phases were modeled as regular solid solutions with one sublattice.

With respect to the different solubility of Bi in BCT_A5 (Sn-rich) solid solution, we have utilized mainly the newly obtained phase equilibrium data from [5] for the reassessment of the system (Fig. 2 shows these data superimposed on the phase diagram calculated using the thermodynamic parameters from the assessment of Ohtani and Ishida [10]). We have also taken into account new thermodynamic data measured by Asryan and Mikula [15] and the phase equilibrium data published by Oelsen and Golücke [9] concerning the solubility of Sn in the Rhombohedral_A7 (Bi) phase. The selected data of Ohtani and Ishida [10] and Nagasaki and Fujita [8] were used for the comparison with the calculated phase diagram only. We have found that binary thermodynamic parameters published in [10] (using the same unary data for all phases as in our assessment) reproduce reasonable well the phase and thermodynamic data except for the above-mentioned solubility of Bi in BCT_A5 (Sn). Therefore, it seemed reasonable to use the thermodynamic parameters published in their study as starting values in the parametric optimization in this work.

The unary data were taken from v4.4 of the SGTE unary database [1]. The parameters obtained from the present assessment are shown in Table 1. The binary Bi–Sn phase diagram calculated using these newly assessed data is shown in Fig. 3 and is compared with relevant phase equilibrium data taken from our work and those mentioned above. The calculated activity and enthalpy of mixing of liquid Bi–Sn alloys at 450 °C are compared with the calorimetric data of

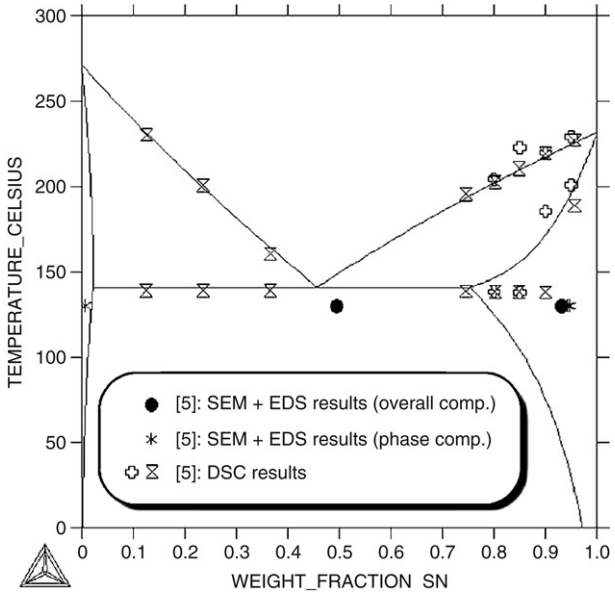

Fig. 2. New experimental data superimposed on the Bi–Sn phase diagram, calculated using the data of Ohtani and Ishida [10].

Sharkey and Pool [14] and Asryan and Mikula [15] in Fig. 4(a) and (b).

3.3. Bi–Zn system

A summary of the experimental data can be found in the papers of Okajima and Sakao [20], Malakhov [21] and Kim and Sanders [22]. Okajima and Sakao [20] studied the equilibria between the two immiscible liquid phases in this system, and the agreement between their experimental data and those of other authors is rather good. Okajima and Sakao [20] also calculated the activities of zinc in the system at 873 K using experimentally determined EMF values and compared them with Kleppa's values [23]. The agreement between the two sets

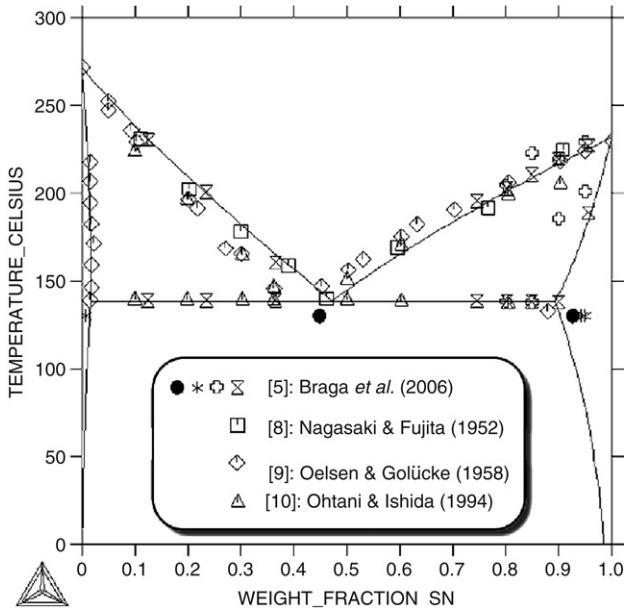

Fig. 3. The assessed Bi–Sn phase diagram in comparison with experimental data used in the assessment.

Table 1
Summary of the thermodynamic parameters of the Bi–Sn system resulting from the present assessment

Phase	Thermodynamic parameters (J mol^{-1})
Liquid	${}^{0}L^{\mathrm{Liq}}_{\mathrm{Bi,Sn}} = +500.0 + 1.5T$
	${}^{1}L^{\mathrm{Liq}}_{\mathrm{Bi,Sn}} = -100.0 - 0.135T$
BCT_A5 (Sn)	${}^{0}L^{\mathrm{BCT\_A5}}_{\mathrm{Bi,Sn}} = +3500.0 - 1.038T$
	${}^{1}L^{\mathrm{BCT\_A5}}_{\mathrm{Bi,Sn}} = -3710.0$
Rhombohedral_A7 (Bi)	${}^{0}L^{\mathrm{Rhom\_A7}}_{\mathrm{Bi,Sn}} = +19\,720.0 - 22.60T$
	${}^{1}L^{\mathrm{Rhom\_A7}}_{\mathrm{Bi,Sn}} = -5760.0 + 13.834T$

of data is good. Kawakami [24] and Wittig et al. [25] measured the enthalpies of mixing for liquid alloys.

A thermodynamic assessment of the Bi–Zn system was carried out by Malakhov [21], Oleari et al. [26], Bale et al. [27], Girard [28] and Wang et al. [29]. Recently, Kim and Sanders [22] assessed miscibility gaps and the metastable liquids in this system and published new interaction parameters for the liquid phases. We used the interaction parameters for liquid phases presented by Malakhov [21] in the current work because of better agreement with experimental data and consistency with other data used.

The liquid phase, Rhombohedral_A7 phase (Bi) and HCP phase (Zn) were used in the modeling. The HCP phase (Zn) is of the A3 type, but with a different c/a ratio. Therefore, we modeled it as a different phase (denoted HCP_Zn instead of the standard HCP_A3) in the database. To keep the consistency with other databases, this phase was modeled with two sublattices. The first sublattice is occupied by the metallic elements and the second by interstitial elements, despite the fact that no interstitial elements exist in these systems. The site-occupancy ratio given by the number of interstitial positions per site on the basic metallic sublattice is 1:0.5.

The currently accepted phase diagrams for the Bi–Zn system are shown in Fig. 5(a) and (b). There is a noticeable difference between the calculated phase diagram according to [21] (Fig. 5(a)) and the assessed experimental phase diagram [30] (Fig. 5(b)).

The assessment published in Massalski's compendium [30], based on existing experimental results, indicates a significant solubility of Zn in Rhombohedral_A7 (Bi) (∼2 wt% of Zn) but the calculations carried out using Malakhov's data [21] indicated a much lower solubility (significantly less than 1 wt%). The calculations for the Zn-rich end of the phase diagram gave a negligible solubility of Bi in HCP_Zn; less than 0.1 wt%. Experimental results [5] at 245 °C confirmed the low solubility of Zn in Rhombohedral_A7 (Bi), as the sample with a Zn content of approximately 0.3 wt% clearly exhibits a two-phase structure. The solubility of both elements in the respective solid solution was found to be approximately 0.3 wt% at 200 °C. This value is in good agreement with the theoretical calculation for the solubility of Zn in Rhombohedral_A7 (Bi), as the calculated solubility at 200 °C is 0.37 wt% of Zn. On the other hand, the calculation according to Malakhov [21] gives much lower solubility of Bi in HCP_Zn than the experiment result (Fig. 5(a)). The difference is not large in absolute numbers, as the solubility is very low, but the calculated value is about 10 times lower than the experimental result. After analysis of the experimental data, the interaction parameter ${}^{0}L^{\mathrm{HCP\_Zn}}_{\mathrm{Bi,Zn:Va}}$ in the Bi–Zn binary system given by Malakhov [21] was changed from +35 000 to +25 000 J mol^{-1}. The resulting difference in the position of the phase boundary calculated using both parameters can be seen by comparing Fig. 6(a) and (b).

3.4. Sn–Zn system

An overview of the experimental data and an estimation of the phase diagram have been published by Moser et al. [31]. The available experimental data for the liquid covered both the enthalpy of mixing and chemical potentials (or activities) of Zn in the liquid state; the data are in very good agreement with each other. The activity measurements were carried using the EMF method, e.g. by Sano et al. [32] and Fiorani and Valenti [33], or by the vapor pressure method, e.g. by Scheil and Müller [34] and Kozuka et al. [35]. Kleppa [36], Oelson [37] and Schürmann and Träger [38] measured the enthalpies of mixing.

Thermodynamic modeling of this system has been carried out by Ohtani et al. [39], Lee [40] and also by Fries et al. [41]. They used the temperature dependence of the enthalpy of mixing for the liquid measured by Kleppa [36] and Bourkba et al. [42] for their assessments. The above authors used different unary data in their assessments and there are also differences in the resulting phase boundaries (Fig. 7(a) and (b)), where a different solubility of Zn in BCT_A5 (Sn) is clearly seen. It is difficult to decide which phase diagram is correct, as the available experimental data are limited in this region. The thermodynamic parameters from Fries et al. [41] were used in

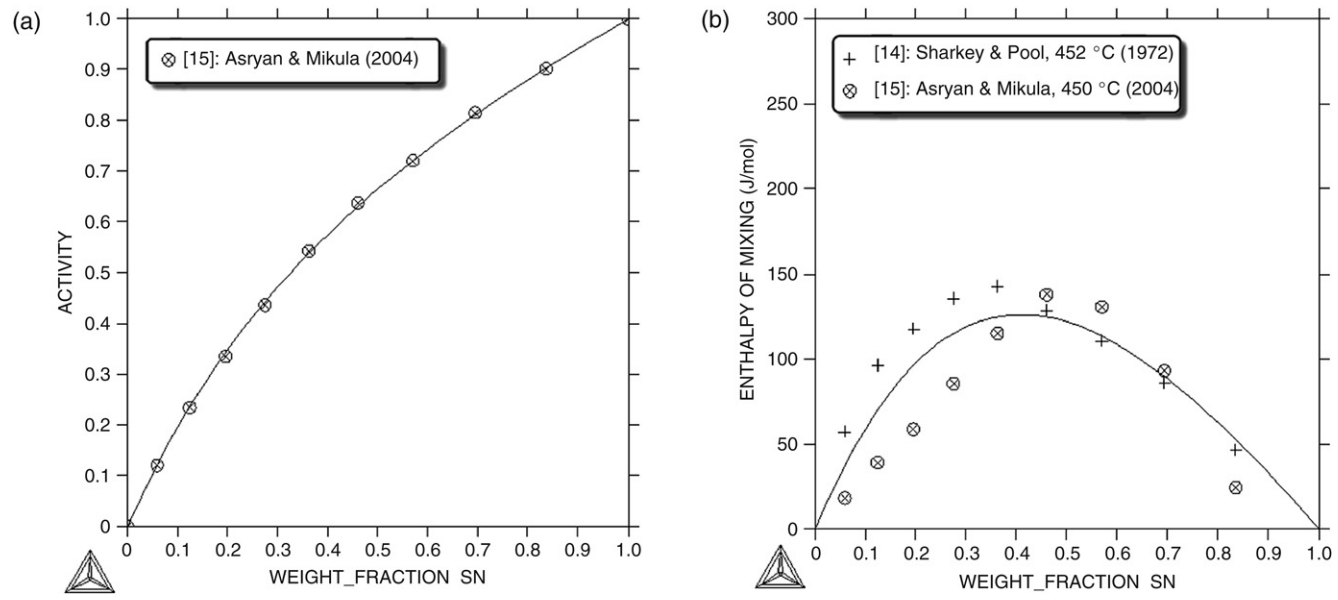

Fig. 4. Calculated (a) activity of Sn and (b) enthalpy of mixing of liquid Bi–Sn alloys at 450 °C in comparison with experimental data used in the assessment.

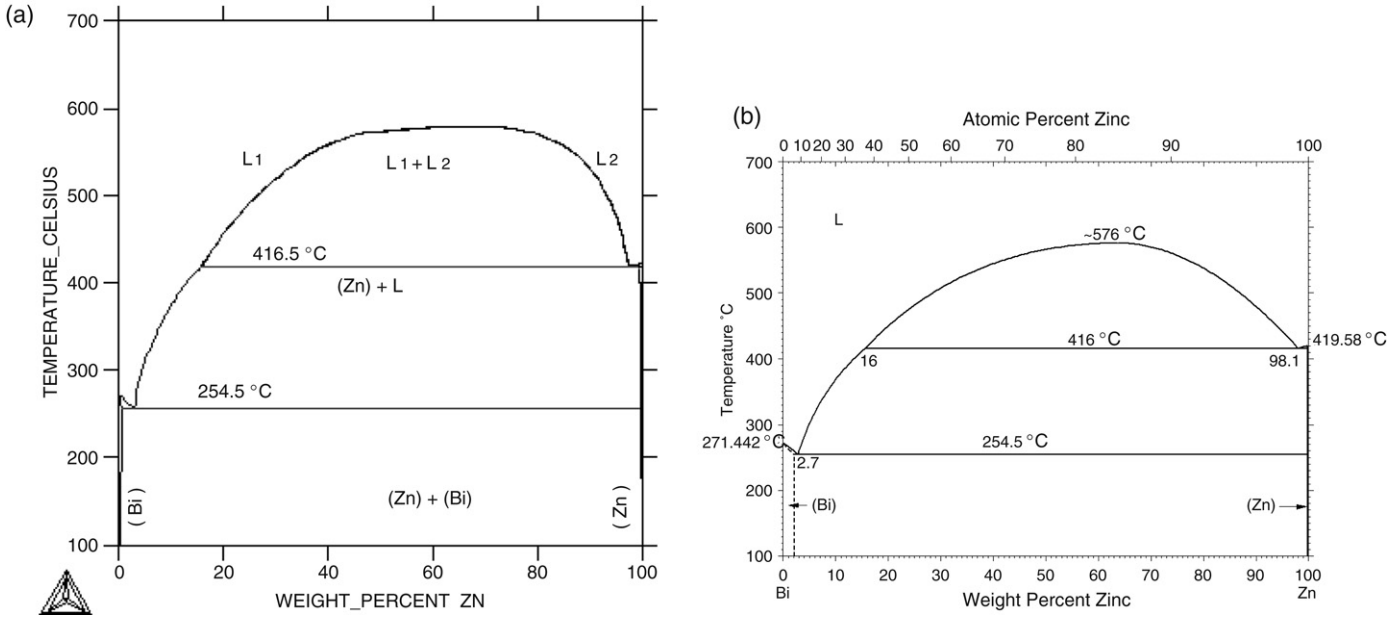

Fig. 5. Calculated Bi–Zn phase diagram using data from Malakhov [21] (a) and assessed experimental Bi–Zn phase diagram from Massalski [30] (b).

the "COST531" database [2] and in our study as they exploited the unary data from the SGTE 4.4 database [1]. The standard state for Sn is BCT_A5; the standard state for Zn is HCP_Zn with the non-standard c/a ratio.

3.5. Bi–Sn–Zn system

The ternary Bi–Sn–Zn system was assessed by Malakhov et al. [6] and Moelans et al. [7]. Both assessments are based on the experimental work of Muzaffar [43], who carried out thermal analysis of a large number of liquid alloys. The experimental information gave a eutectic temperature of $T = 129.87 \pm 0.15$ °C. Malakhov et al. [6] also took into account the results of Ohtani and Ishida [10] and Ohtani et al. [39]. Moelans et al. [7] used thermochemical properties determined from EMF measurements made by a number of authors, e.g. [27, 44–46]. Both Malakhov et al. and Moelans et al. introduced ternary corrections for the liquid only. Unfortunately, the assessments of this system are not mutually consistent as the authors used different unary data (e.g. $G_{\mathrm{Bi}}^{\mathrm{BCT\_A5}} - G_{\mathrm{Bi}}^{\mathrm{Rhom\_A7}} = +4184.07\ \mathrm{J\ mol^{-1}}$ from [10] and $+13\,526.3\ \mathrm{J\ mol^{-1}}$ from [19] in the Bi–Sn system). They either took these values from various versions of the SGTE unary database [10,19] or, in some cases, carried out their own assessment of the unary data [7]. Recently, Luef et al. [47] published an experimental study of this ternary system and determined partial and integral enthalpies of mixing of liquid Bi–Sn–Zn alloys at 500 °C by a drop calorimetric technique. Experiments were

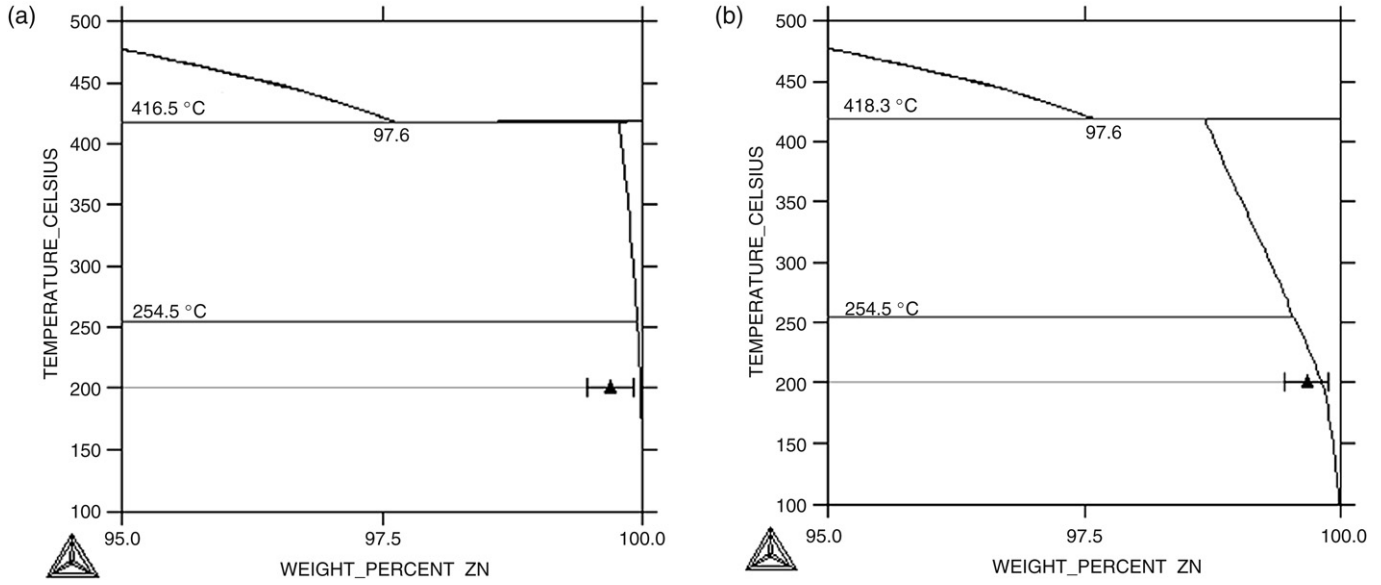

Fig. 6. Calculated Zn-rich part of the Bi–Zn phase diagram, using (a) data from Malakhov [21] (without correction) and (b) data from the "COST531" database [2] (utilizing the interaction parameter correction) in comparison with new experimental results [5].

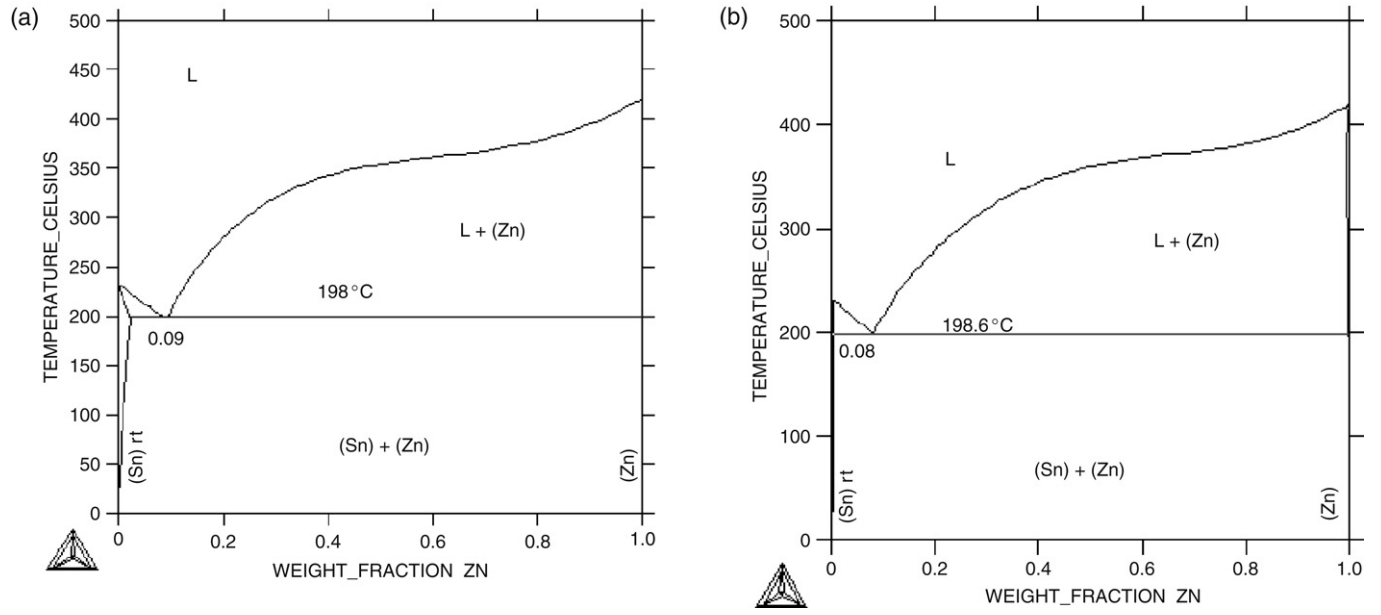

Fig. 7. Optimized Sn–Zn phase diagram according to (a) Ohtani et al. [39] and (b) Fries et al. [41].

conducted using compositions along six sections in the Sn-rich part of the ternary diagram. They also reported DSC data (liquidus temperatures and ternary eutectic reactions) along three sections (3, 5 and 7 at.% of Zn). Braga et al. [5] published new and significant experimental results focusing on the miscibility gap (and also the Sn-rich part of the diagram). DSC, X-ray diffraction (XRD), and SEM in conjunction with EDS were used in the study. For quantitative analysis they used X-ray fluorescence (XRF) and atomic absorption spectrometry (AAS).

Both Malakhov et al. [6] and Moelans et al. [7] have used the older thermodynamic description of the Bi–Sn system for their assessments, and therefore it was necessary to reassess the Bi–Sn–Zn system using the newly assessed Bi–Sn system (Section 3.2) together with the Bi–Sn–Zn experimental results presented in [5,43]. These experimental data were supplemented with new experimentally determined integral enthalpies of mixing of liquid Bi–Sn–Zn alloys [47] and the activities [45].

Ternary interaction parameters were introduced both for the liquid and Rhombohedral_A7 (Bi) phases modifying the ternary system behavior. No ternary interaction parameters were necessary for the BCT_A5 (Sn) phase, as the predicted solubility of Bi and Zn in this phase agreed well with the experimental results. Using the Parrot module [4] of the Thermo-Calc thermodynamic calculation software, a new set of thermodynamic parameters was optimized for the ternary system, which is summarized in Table 2.

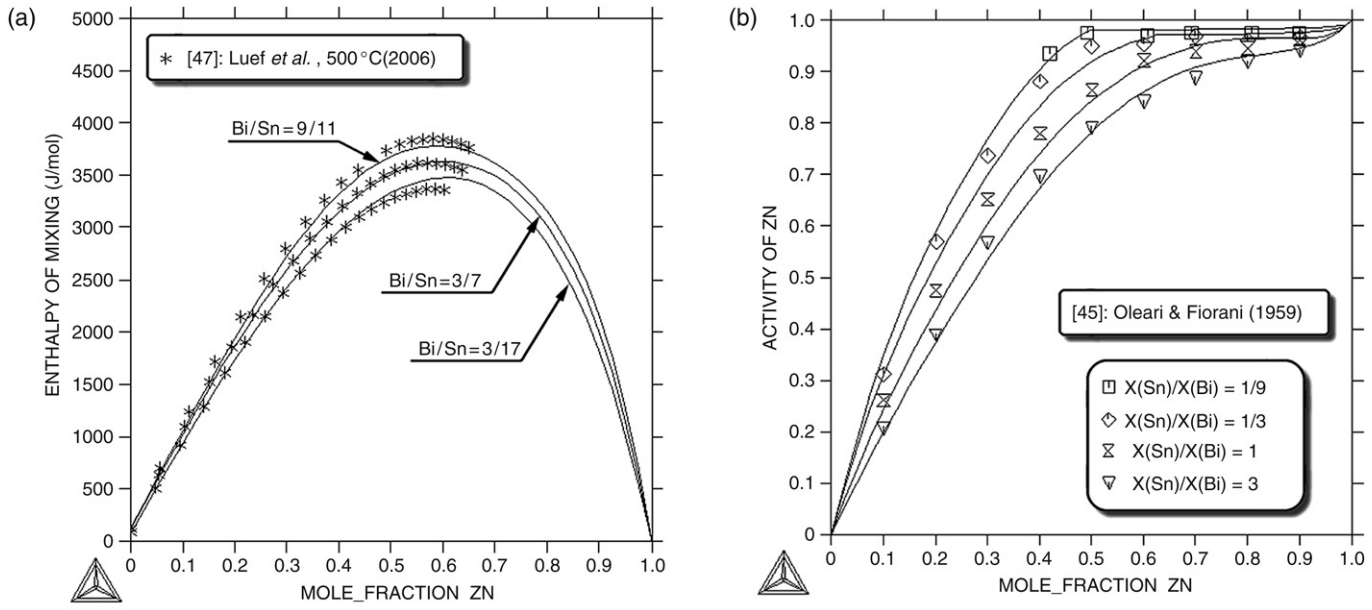

Fig. 8. Calculated (a) integral enthalpies of mixing at 500 °C, compared with the experimental data of Luef et al. [47], and (b) activities of Zn at 450 °C, compared with the experimental data of Oleari and Fiorani [45].

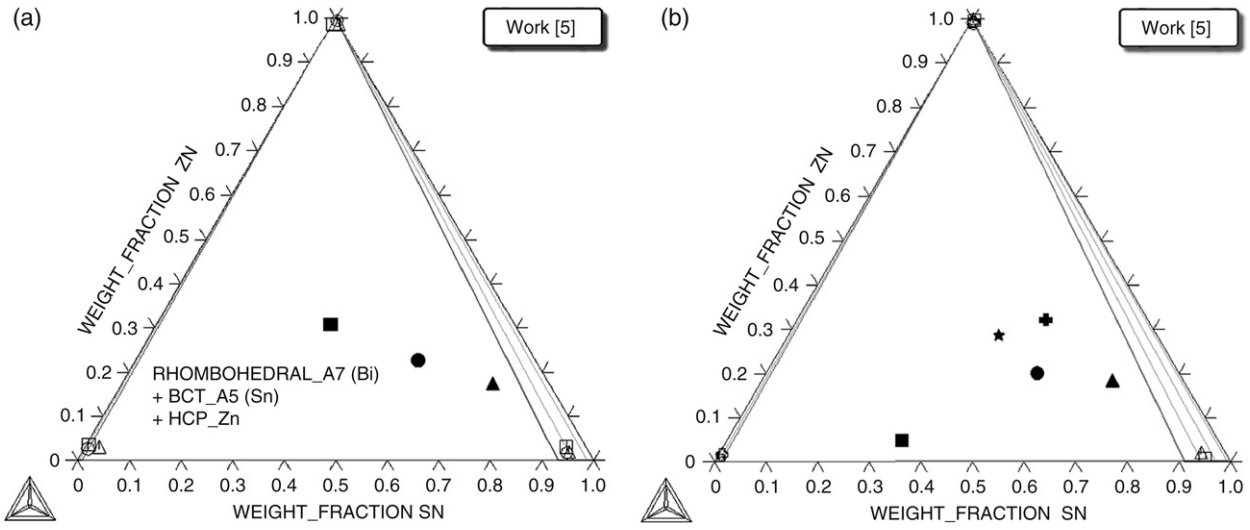

Fig. 9. Calculated isothermal sections at (a) 100 °C and (b) 120 °C in comparison with experimental data from Braga et al. [5].

Table 2
Summary of the ternary corrections for the Bi–Sn–Zn system used in the present assessment

Phase	Thermodynamic parameters (J mol^{-1})
Liquid	${}^{0}L^{\mathrm{Liq}}_{\mathrm{Bi,Sn,Zn}} = -17\,690.6 + 33T$
	${}^{1}L^{\mathrm{Liq}}_{\mathrm{Bi,Sn,Zn}} = -2737.2 - 13T$
	${}^{2}L^{\mathrm{Liq}}_{\mathrm{Bi,Sn,Zn}} = -19\,259.1 + 0.5T$
Rhombohedral_A7 (Bi)	${}^{0}L^{\mathrm{Rhom\_A7}}_{\mathrm{Bi,Sn,Zn}} = +387\,000.0$
	${}^{1}L^{\mathrm{Rhom\_A7}}_{\mathrm{Bi,Sn,Zn}} = 0$
	${}^{2}L^{\mathrm{Rhom\_A7}}_{\mathrm{Bi,Sn,Zn}} = 0$

The results of this assessment have been verified by comparing calculated isopleths with selected phase equilibrium data from Braga et al. [5] and Muzaffar [43] as well as with more recent data from Luef et al. [47]. They are shown in Figs. 8–15.

4. The theoretical results and discussion

4.1. Bi–Sn system

Very good agreement was reached between the calculation and experimental phase and thermodynamic data for this system (Figs. 3 and 4). The calculated solubility of the Bi in the BCT_A5 (Sn) solid solution agreed with the results of SEM measurements and the phase boundaries confirmed by the DTA measurements. The eutectic temperature obtained in the calculation is 138.4 °C, which is in very good agreement with the value measured by Braga et al. [5] (138.6 °C). For

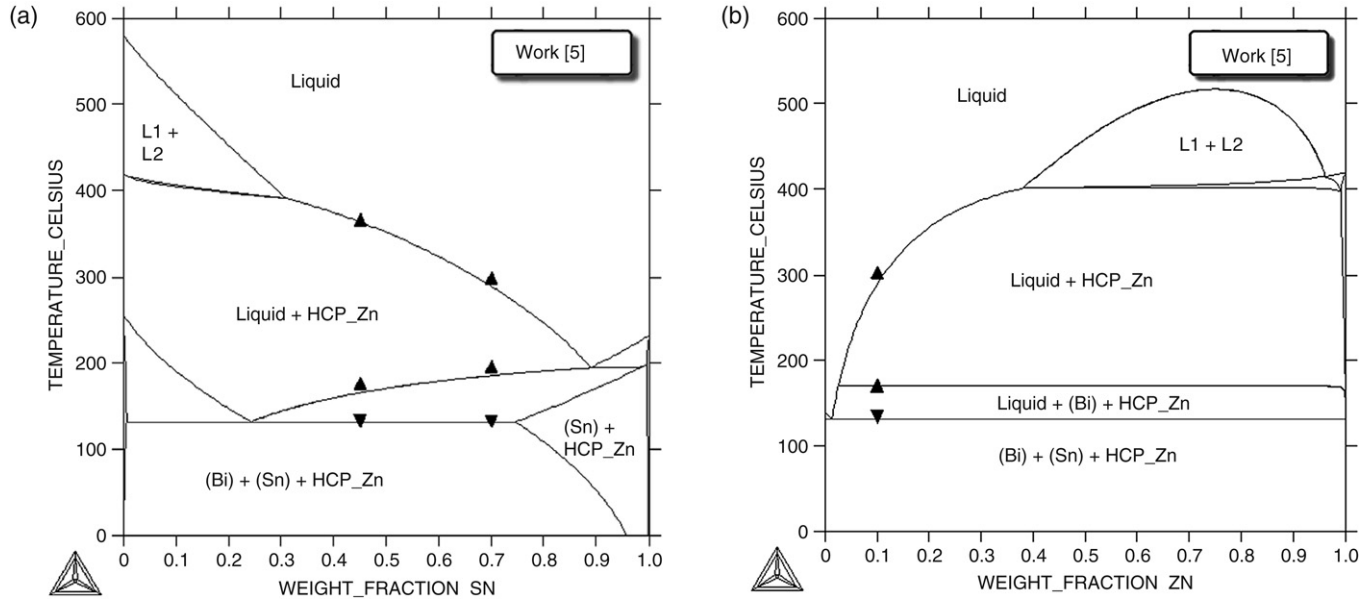

Fig. 10. Calculated vertical sections at constant ratios (a) W(Bi)/W(Zn) = 1/2 and (b) W(Bi)/W(Sn) = 2 in comparison with experimental data from Braga et al. [5].

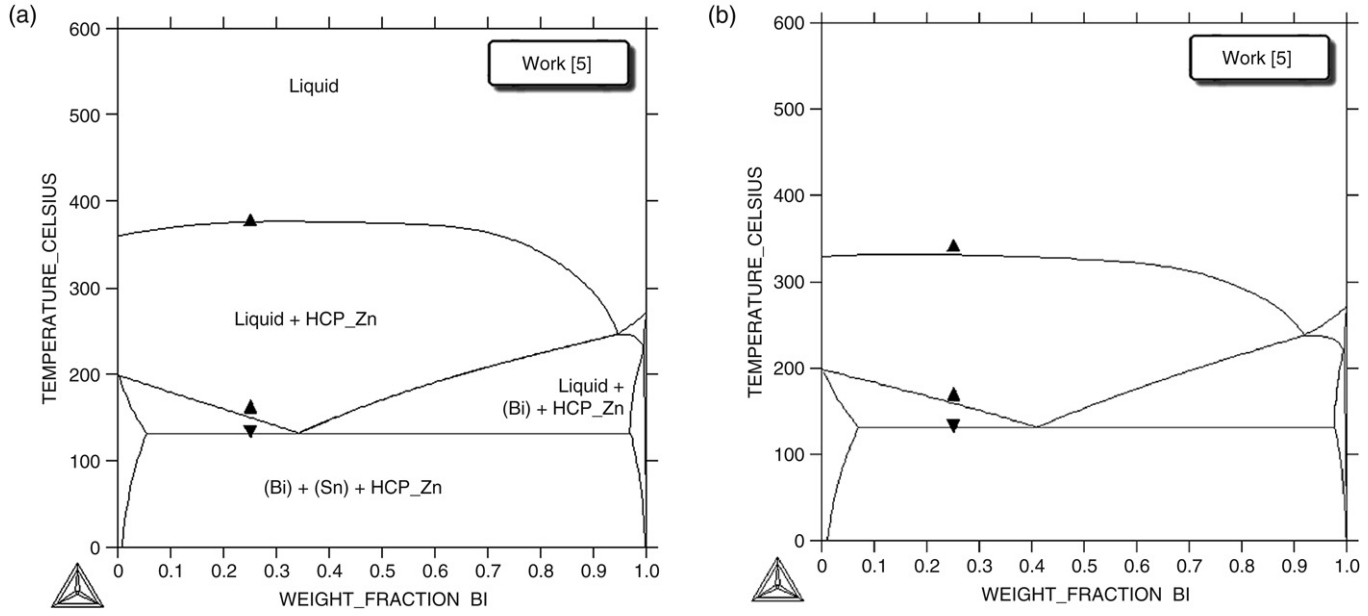

Fig. 11. Calculated vertical sections at constant ratios (a) W(Sn)/W(Zn) = 1 and (b) W(Sn)/W(Zn) = 2 in comparison with experimental data from Braga et al. [5].

comparison, Ohtani and Ishida [10] calculated the eutectic temperature to be 140.7 °C and Lee et al. [19] determined a value of 138.8 °C. A very good agreement between calculated and experimentally measured [15] activities of Sn in liquid Bi–Sn alloys at 450 °C is shown in Fig. 4(a).

The reliability of the new Bi–Sn description was also verified by calculations of the ternary Bi–Sn–Zn system (see Sections 3.5 and 4.3).

4.2. Bi–Zn system

It is clear from the experimental results that the estimated phase boundary [30] in the Bi-rich region is not correct and that the theoretically calculated solubility of Zn in Rhombohedral_A7 (Bi) solid solution using the data from the work of Malakhov [21] is more accurate. The calculated solubility of Bi in HCP_Zn, based on the current reassessment of the relevant interaction parameter, agrees well with experiment; the temperatures and composition of the phases in the invariant reactions are almost unchanged. Further improvement can be achieved by introducing a parameter for temperature dependence, but owing to a lack of experimental data and the spread in the experimentally determined values of the eutectic temperature given in the literature, this would be inappropriate.

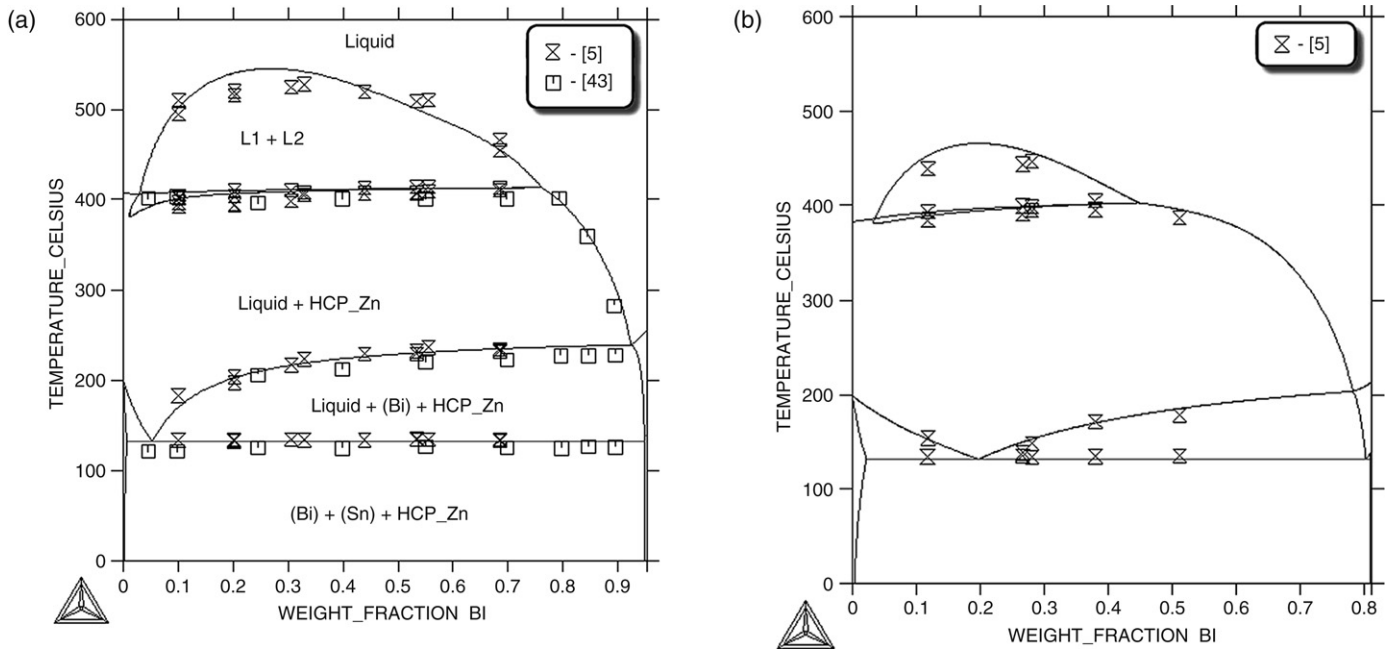

Fig. 12. Calculated vertical sections at (a) 5 wt% of Sn, compared with the experimental data of Braga et al. [5] and Muzaffar [43], and (b) 19 wt% of Sn, compared with experimental data from Braga et al. [5].

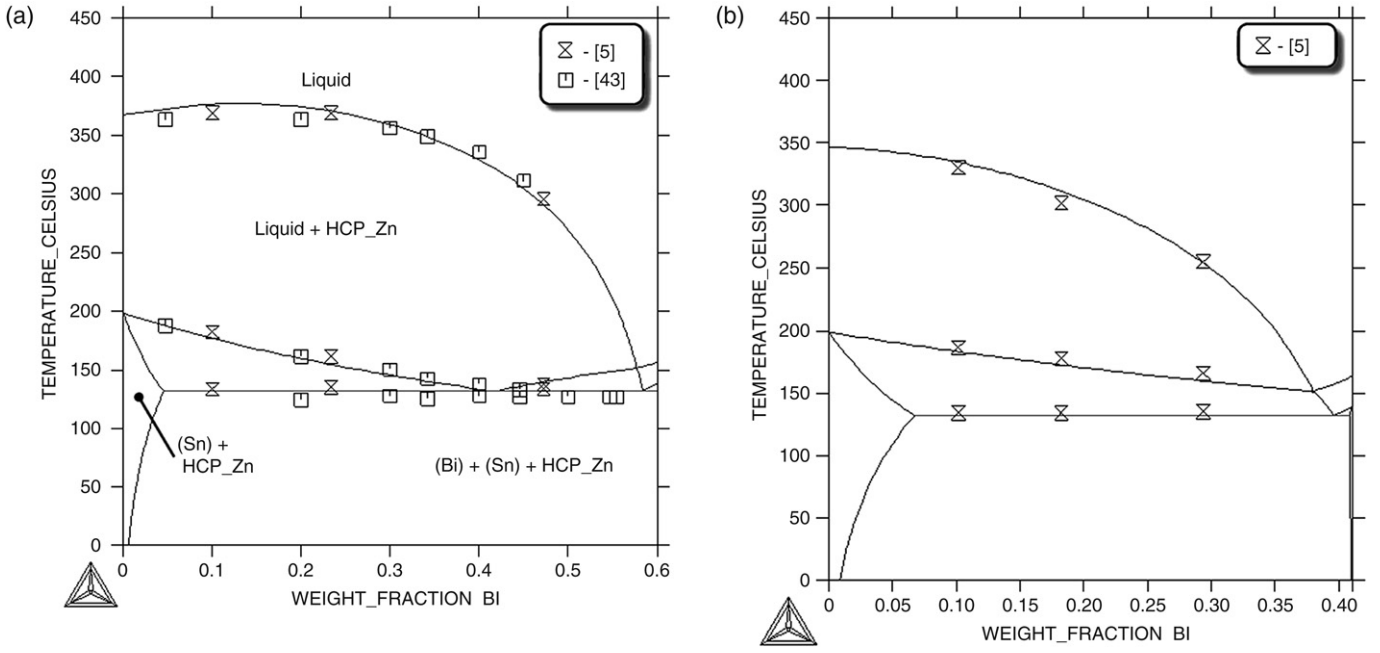

Fig. 13. Calculated vertical sections at (a) 40 wt% of Sn, compared with the experimental data of Braga et al. [5] and Muzaffar [43], and (b) 59 wt% of Sn, compared with the experimental data of Braga et al. [5].

4.3. Bi–Sn–Zn system

The experimentally measured thermodynamic properties and phase equilibria are very well reproduced using the new thermodynamic description in Figs. 8–15. The calculated integral enthalpies of mixing and activities of Zn are compared with experimental data in Fig. 8 (a) and (b), and the agreement is very good.

Fig. 9(a) and (b) show the calculated isothermal sections at 100 and 120 °C, which are in very good agreement with the experimental data [5]. The agreement between the modeling and experimental data (DTA results) from [5] and [43] is also shown in the relevant vertical sections in Figs. 10–14. It should be noted that smaller weight was given to the experimental data of Muzaffar [43] in comparison with the data of Braga et al. [5] in this assessment. The phase equilibrium data from [5] were given priority in the optimization owing to their reliability and consistency. Muzaffar's thermal analysis results are slightly different (e.g. the temperature of invariant reaction), but the

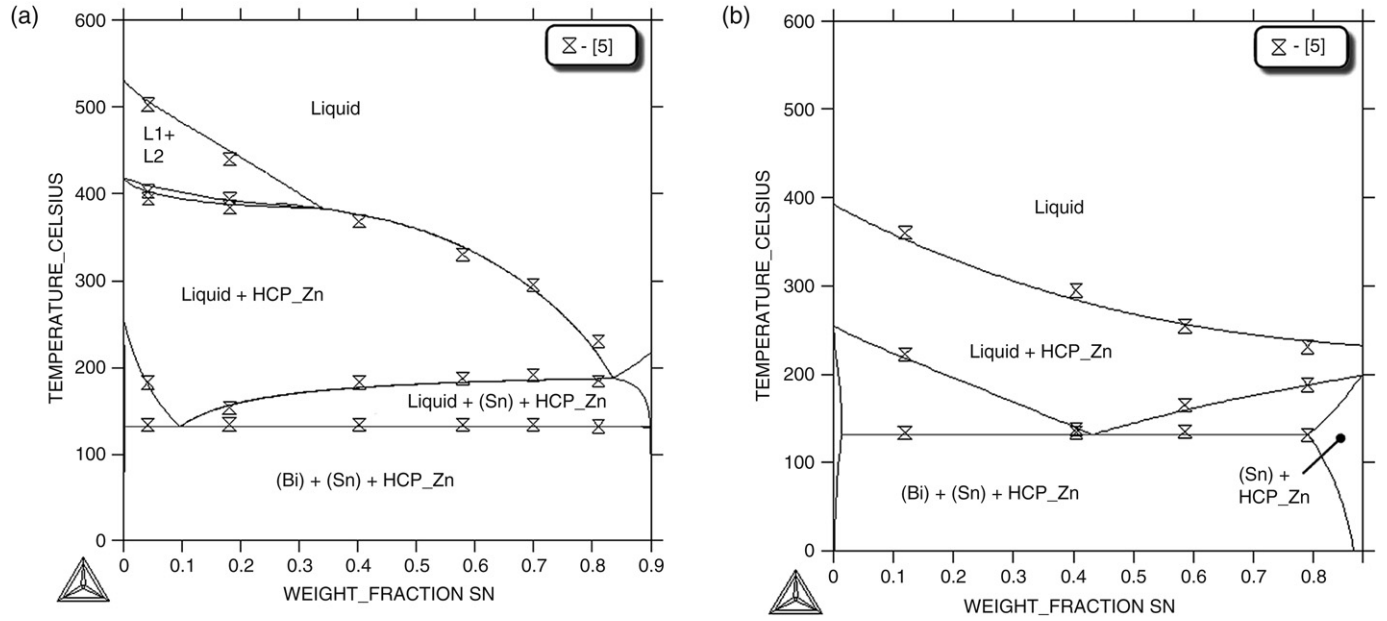

Fig. 14. Calculated vertical sections at (a) 10 wt% of Bi and (b) 12 wt% of Zn, compared with the experimental data of Braga et al. [5].

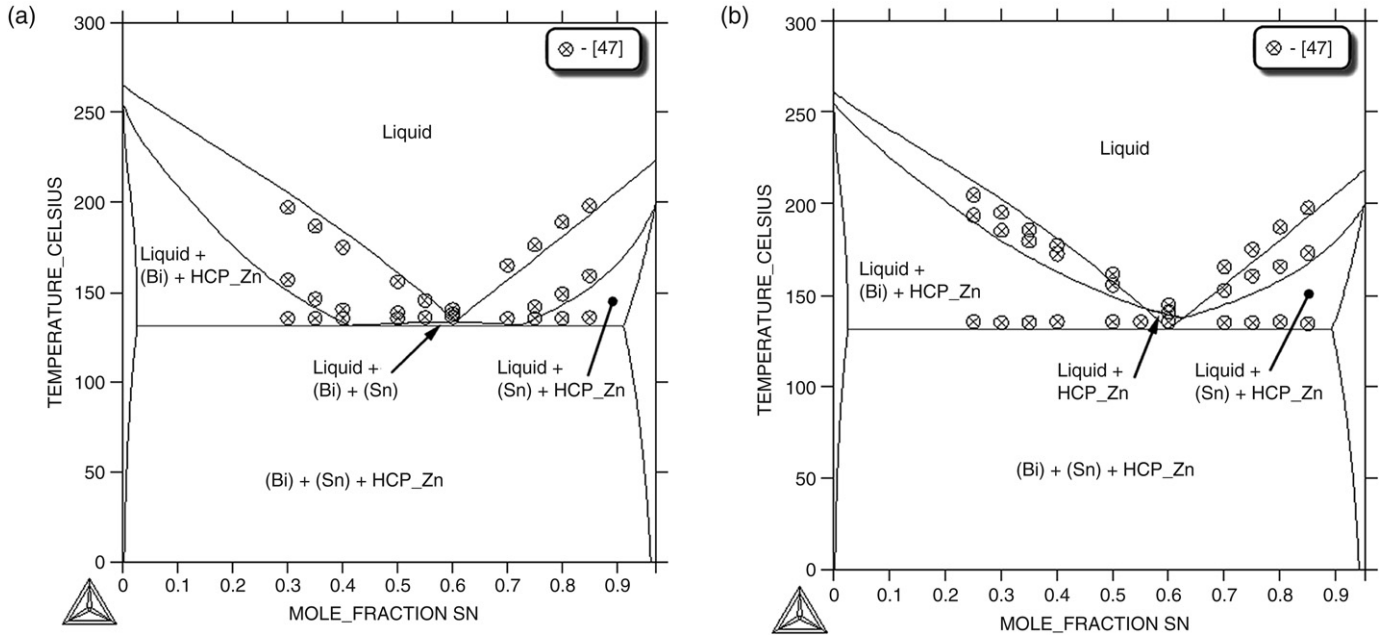

Fig. 15. Calculated vertical sections at (a) 3 at.% of Zn and (b) 5 at.% of Zn, compared with the experimental data of Luef et al. [47].

results are still in reasonable agreement with more recent work. The data of Muzaffar are also very useful because of the number of alloys studied (104!). These alloys covered a major part of the ternary diagram. The ternary eutectic temperature from the work of Muzaffar [43] is 129.87 ± 0.15 °C, but Braga et al. [5] determined this temperature to be 134.1 ± 0.5 °C [5]. The calculated ternary eutectic temperature is 131.7 °C.

We also obtained very good agreement between the calculations and recent experimental results taken from [47] for selected vertical sections. This comparison is shown in Fig. 15.

5. Conclusions

A critical evaluation of the thermodynamic parameters and experimental data available in the literature was carried out for the Bi–Sn, Bi–Zn, Sn–Zn and Bi–Sn–Zn systems.

Our own experimental results [5] led to the verification of the Bi-rich part of the Bi–Zn phase diagram and to a reassessment of the interaction parameter for the HCP_Zn phase in the Zn-rich corner.

In the case of the Bi–Sn system, attention was focused on the Sn-rich part of the diagram, where a different solubility of

Bi in the BCT_A5 (Sn) phase was found in [5] (approximately 10 wt%), and the system was successfully reassessed.

Using the new Bi–Sn system description, the modification of the Bi–Zn system description and the available thermodynamic and phase equilibrium data, the Bi–Sn–Zn ternary system was also completely reassessed.

The reliability of the assessed parameters obtained for the Bi–Sn–Zn system was verified by calculation of thermodynamic properties and isothermal and vertical sections of the phase diagram. These results were compared with experimental data, both from our work [5] and the literature [43, 45,47]. The agreement is excellent for a broad set of experimental measurements carried out by different authors. Therefore, the new datasets for the Bi–Sn and Bi–Sn–Zn systems and the modification of the parameter for the Bi–Zn system were included in the "COST531" database [2].

This database, containing 11 elements (Ag, Au, **Bi**, Cu, In, Ni, Pb, Pd, Sb, **Sn** and **Zn**) was created recently in the scope of the COST 531 project [2]. The reliability of the data in this database is validated both by the modeling of thermodynamic properties of the studied systems (e.g. enthalpies of mixing and their comparison with the experimentally measured data) and by the comparison of theoretical and experimental phase equilibrium data, as shown in this paper.

Acknowledgements

The authors wish to express thanks to Dr. A.T. Dinsdale (NPL, Teddington), coordinator of the database project in the scope of the COST 531 Action, for a fruitful cooperation, and to Prof. A. Paul (Indian Institute of Science) for sharing his unpublished research results.

This work is supported by the COST project No. OC 531.002, financed by the Ministry of Education of the Czech Republic, by the Czech Science Foundation (Project No. 106/05/H008), and by the Research Project AV0Z20410507.

The authors wish also thank to Dr. Andy Watson (University of Leeds) for his kind and significant help with the preparation of this paper for publication.

References

[1] Version 4.4 of the SGTE Unary database.
[2] A.T. Dinsdale, A. Watson, A Kroupa, J. Vrestal, A. Zemanova, J. Vizdal, Version 2.0 of the "COST531" Database for the lead-free solders.
[3] B. Sundman, J. Ågren, J. Phys. Chem. Solids 42 (1981) 297.
[4] Thermo-Calc, version P, software for thermodynamic calculations in multi-component systems, Thermo-Calc AB, Stockholm, Sweden.
[5] M.H. Braga, J. Vizdal, A. Kroupa, J. Ferreira, D. Soares, L.F. Malheiros, The experimental study of the Bi–Sn, Bi–Zn and Bi–Sn–Zn systems, CALPHAD 31 (4) (2007) 468–478.
[6] V.D. Malakhov, X.J. Liu, I. Ohnuma, K. Ishida, J. Phase Equilib. 21 (2000) 514.
[7] N. Moelans, K.C.H. Kumar, P. Wollants, J. Alloys Compounds 360 (2003) 98.
[8] S. Nagasaki, E. Fujita, J. Japan Inst. Met. 16 (1952) 317.
[9] W. Oelsen, K.F. Golücke, Arch. Eisenhüttenwes. 29 (1958) 689.
[10] H. Ohtani, K. Ishida, J. Electron. Mater. 23 (1994) 747–755.
[11] H.O. Samson-Himmelstjerna, Z. Metallk. 28 (1936) 197.
[12] F.E. Wittig, F. Huber, Z. Electrochemie 60 (1956) 1181.
[13] A. Yazawa, T. Kawashima, K. Itagaki, J. Japan Inst. Met. 32 (1968) 1281.
[14] R.L. Sharkey, M.J. Pool, Metall. Trans. 3 (1972) 1773.
[15] N. Asryan, A. Mikula, Z. Metallk. 95 (2004) 132.
[16] A. Yazawa, K. Koike, J. Min. Met. Inst. Jpn. 184 (1968) 1593.
[17] G. Rickert, P. Lamparterand, S. Steeb, Zenaau Z. Natur. Teil A 31 (1976) 711.
[18] H. Seltz, F.J. Dunkerley, J. Am. Chem. Soc. 64 (1942) 1392.
[19] B.-J. Lee, C.-S. Oh, J.-H. Shim, J. Electron. Mater. 25 (1996) 983.
[20] K. Okajima, H. Sakao, Trans. Japan Inst. Met. 21 (1980) 226.
[21] D.V. Malakhov, CALPHAD 24 (2000) 1.
[22] S.S. Kim, T.H. Sanders Jr., Z. Metallk. 94 (2003) 390.
[23] O.J. Kleppa, J. Am. Chem. Soc. 74 (1952) 6052.
[24] M. Kawakami, The Science Reports of the Tóhoku Imperial University 116 (1927) 915.
[25] F.E. Wittig, E. Müller, W. Schilling, Z. Metallk. 62 (1958) 529.
[26] L. Oleari, M. Fiorani, V. Valenti, La Metallurgia Italiana 46 (1955) 773.
[27] C.W. Bale, A.D. Pelton, M. Rigaud, Z. Metallk. 68 (1977) 69.
[28] C. Girard, Ph.D. Thesis, Universite de Provence, Marseille, 1985.
[29] Z.C. Wang, S.K. Yu, F. Sommer, J. Chim. Phys. Phys.-Chim. Biol. 90 (1993) 379.
[30] T.B. Massalski, Binary Alloy Phase Diagrams, ASM International, Ohio, 1990.
[31] Z. Moser, J. Dutkiewicz, W. Gasior, J. Salawa, Bull. Alloy Phase Diagram 6 (1985) 330.
[32] K. Sano, K. Okajima, S. Tatsuo, Mem. Fac. Eng. Nagoya Univ. 5 (1953) 299.
[33] M. Fiorani, V. Valenti, Gazz. Chim. Ital. 85 (1955) 607.
[34] E. Scheil, E.D. Müller, Z. Metallk. 53 (1962) 389.
[35] Z. Kozuka, J. Moriyama, I. Kushima, J. Electrochem. Soc. Jpn. 28 (1960) 167.
[36] O.J. Kleppa, J. Phys. Chem. 59 (1955) 354.
[37] W. Oelson, Z. Metallk. 48 (1957) 1.
[38] E. Schürmann, H. Träger, Arch. Eisenhüttenwes. 32 (1961) 397.
[39] H. Ohtani, M. Miyashita, K. Ishida, J. Japan Inst. Met. 63 (1999) 685.
[40] B.-J. Lee, CALPHAD 20 (1996) 471.
[41] S.G. Fries, H.L. Lukas, System Sn–Zn, in: I. Ansara, A.T. Dinsdale, M.H. Rand (Eds.), COST 507, in: Thermochemical Database for Light Metal Alloys, vol. 2, 1998, p. 288.
[42] A. Bourkba, J.M. Fiorani, C. Naguet, J. Hertz, Z. Metallk. 10 (1996) 773.
[43] S.D. Muzaffar, J. Chem. Soc. 123 (1923) 2341.
[44] J.V. Gluck, R.D. Pehlke, Trans. AIME 239 (1967) 36.
[45] L. Oleari, M. Fiorani, Ric. Sci. 29 (1959) 2219.
[46] W. Ptak, M. Moser, Arch. Hut. 11 (1966) 289.
[47] C. Luef, A. Paul, J. Vizdal, A. Kroupa, A. Kodentsov, H. Ipser, Monatsh. Chem. 137 (2006) 381.

Journal of Mining and Metallurgy 43 B (2) (2007) 151 - 159

Journal of
Mining and
Metallurgy

THE BEHAVIOUR OF THE LATTICE PARAMETERS IN THE Bi-Sn-Zn SYSTEM

M. Helena Braga*#, J. Ferreira and L. F. Malheiros*****

*GMM-IMAT, Dep. of Physics, FEUP, R. Dr. Roberto Frias s/n, 4200-465 Porto, Portugal
**INETI Laboratory, R. da Amieira - P.O. Box 1089, 4466-956 S. Mamede de Infesta, Portugal
***GMM-IMAT, Dep. of Metallurgical and Materials Engineering,
FEUP, R. Dr. Roberto Frias s/n, 4200-465 Porto, Portugal

(Received 18 June 2007; accepted 21 August 2007)

Abstract

Lattice parameters, coefficients of thermal expansion and mass density were determined by means of X-ray powder diffraction between 30 and 180 ºC (or 240 ºC - depending on samples' composition). Rietveld refinement was performed in order to obtain phases' lattice parameters at each temperature. The Panalytical X´Pert Pro MPD was used for room temperature X-ray diffraction experiments (RT-XRD) with bulk samples. The aim was to identify the phases that were present in the sample, as well as, their lattice parameters. For some samples, powder high temperature X-ray diffraction measurements (HT-XRD) were also performed, under a vacuum of 10^{-5} mbar or an argon atmosphere.
It was found that the lattice parameters of (Bi), (Sn) and (Zn) don't change with the composition, at room temperature, as expected since all samples belong to the three phase region. It was also concluded that (Bi) behaves like an isometric crystalline solid on the contrary of (Zn) that has different expansion coefficients for different crystallographic directions a (= b) and c.

Keywords: Bi-Sn-Zn, (RT/HT)-XRD, lattice parameters, expansion coefficients, mass density.

1. Introduction

Health problems (especially neurological and birth malformations) may arise from the excess of lead in human bodies. The excess of lead is due to water contamination. Hence, lead was added to the list of apprehensions with the environment [1].

The objective of COST 531 action "Lead-free Solder Materials" [2] (European

* *Corresponding author: mbraga@fe.up.pt*

DOI:10.2298/JMMB0702151B

Cooperation in the field of Scientific and Technical Research) was the study of systems that may be used as lead-free solders. The selection of these systems was based on technical and health hazard considerations. The crucial technological properties to be analyzed should be: melting temperature, wettability, surface tension, viscosity of the liquid alloys at different temperatures, oxidation behaviour, thermomechanical fatigue, etc.

The evaluation of experimental phase diagrams, measurement of the thermodynamic properties and consequent optimisation of the corresponding phase diagrams (using CALPHAD method) were some of the aims of the COST 531 action.

Bi-Sn-Zn was one of the systems studied in the scope of the above mentioned program.

The coefficient of thermal expansion and mass density are properties that were object of measurements since their knowledge is essential when solders are the issue.

This study complements other previous studies done for the system Bi-Sn-Zn [3, 4].

2. Experimental

Nine samples corresponding to vertical sections with w(Sn) ~ 5 %, 40 % and 59 % were chosen for this study (Fig. 1). They had ~ 20 mm in diameter, ~ 3 mm in high and ~ 2 g in weight. Samples were prepared by mixing pure Bi (> 99.8 %), Sn (> 99.5 %) and Zn (> 99.9 %). The samples were then putted in alumina crucibles and melted in a resistance furnace under an argon atmosphere. The nominal compositions of the samples were confirmed by X-ray Fluorescence (XRF) and Atomic Absorption Spectroscopy (AAS). All samples were homogenized at 120 ºC for 60 minutes and

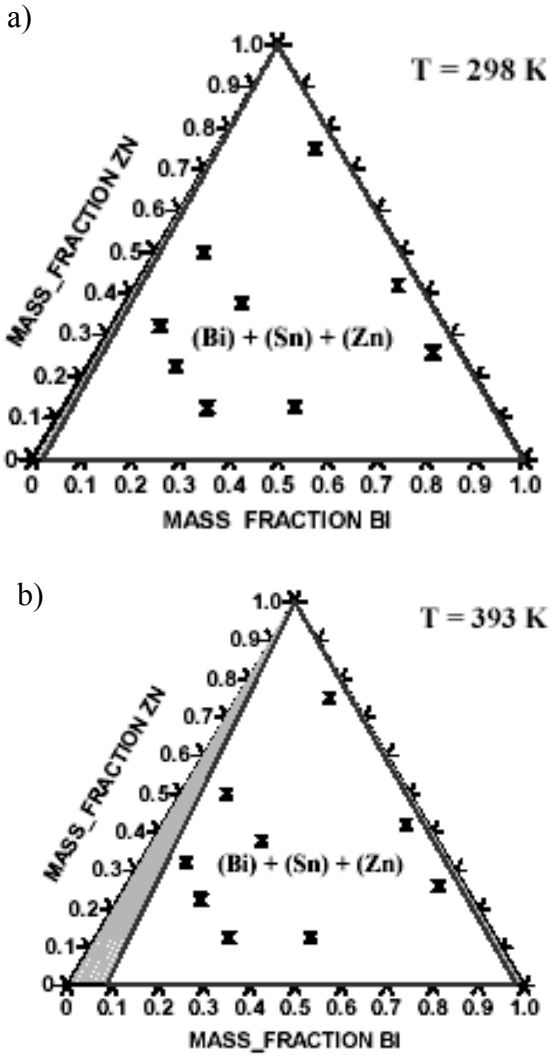

Fig. 1. Compositions of the prepared samples (signed by double triangles) over the calculated phase diagram using the Gibbs equations from [4], a) at 298 K and b) at 393 K.

slowly cooled down to the room temperature in a rate less than 2 ºC/min.

Bulk RT-XRD measurements were performed to identify the present phases. For some samples, powder HT-XRD measurements were also performed, under a vacuum of 10^{-5} mbar or an argon atmosphere. The furnace used is an Anton

Parr Chamber applied to the Panalytical X´Pert Pro MPD. CuKα or primary monochromated CuKα_1 radiations were used. Patterns were collected from 5 to 120º (2θ) with steps of 0.01º and counting time of 10 s.

3. Results

3.1. Room Temperature

RT-XRD data were refined using Rietveld method [5] applied on the Fullprof software [6]. The R_p, R_{wp} and R_B(Bi), R_B(Sn) and R_B(Zn) are of the order of R_p = 13 %, R_{wp} = 14 %, R_B(Bi) = 2 %, R_B(Sn) = 1 % and R_B(Zn) = 1 %. (Bi) was refined as rhombohedral (A7), R-3m, (Sn) was refined as tetragonal (A5), I 4_1/amd (bct) and (Zn) was refined as hexagonal (A3), P 6_3/mmc (hcp). Results for two of the nine samples measured, with compositions w(Bi) = 23.7 %, w(Sn) = 38.5 %, w(Zn) = 37.8 % and w(Bi) = 53.3 %, w(Sn) = 4.9 % , w(Zn) = 41.8 % can be observed in Figs. 2 and 3, respectively.

By the observation of the phase diagram at room temperature (298 K) and at 393 K (Fig. 1), it can be seen that the only phases that show the possibility of having slightly different lattice parameters than the respective pure element, are (Sn) and (Bi). When comparing our Rietveld refinements data with Sn and Bi pure elements data [7], it can be observed that (Sn) and (Bi) are the phases that present some discrepancy (for (Sn) especially for a = b and for (Bi) especially for c) (if [7] is considered), as expected from the phase diagram.

For (Sn), the difference between the average a = b lattice parameter for (Sn) and for pure Sn is 0.162 % of the value of Sn pure and the difference between the average c lattice parameter for (Sn) and the value for Sn pure is 0.088 % of the value for Sn pure

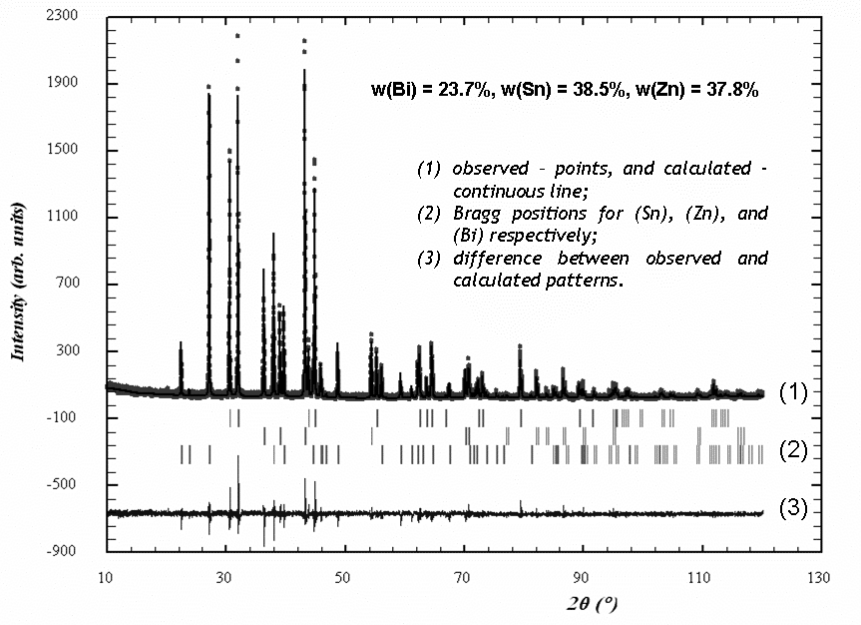

Fig. 2. RT-XRD pattern for a sample with composition w(Bi) = 23.7 %, w(Sn) = 38.5 % and w(Zn) = 37.8 % after Rietveld refinement

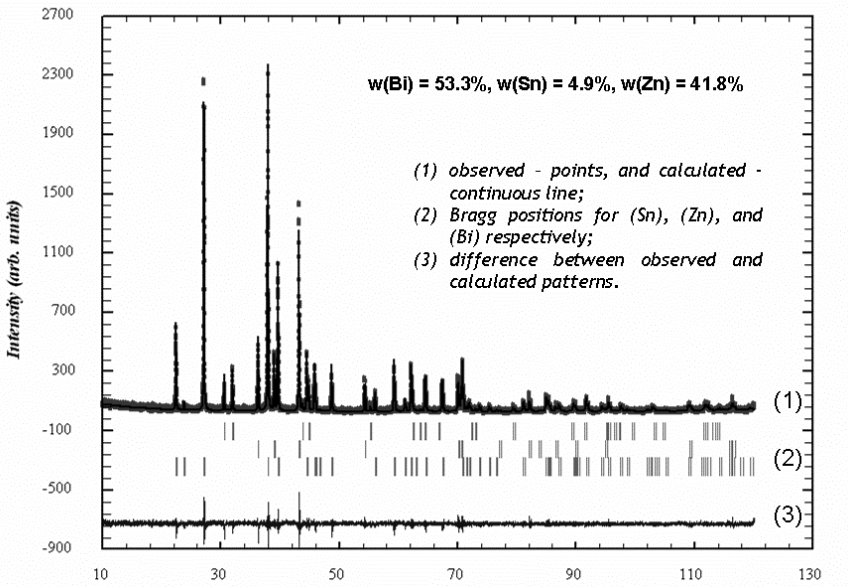

Fig. 3. RT-XRD pattern for a sample with composition w(Bi) = 53.3 %, w(Sn) = 4.9 % and w(Zn) = 41.8 % after Rietveld refinement

(Fig. 4) considering [7].

For (Zn), the difference between the average a = b lattice parameter for (Zn) and the value for Zn pure is 0.038 % of the value for Zn pure and the difference between the average c lattice parameter for (Zn) and the value for Zn pure is 0.061 % of the value for Sn pure (Fig. 5) considering [7].

For (Bi), the difference between the average a = b lattice parameter for (Bi) and the value for Bi pure is 0.095 % of the value for Bi pure and the difference between the average c lattice parameter for (Bi) and the value for Bi pure is 0.238 % of the value for

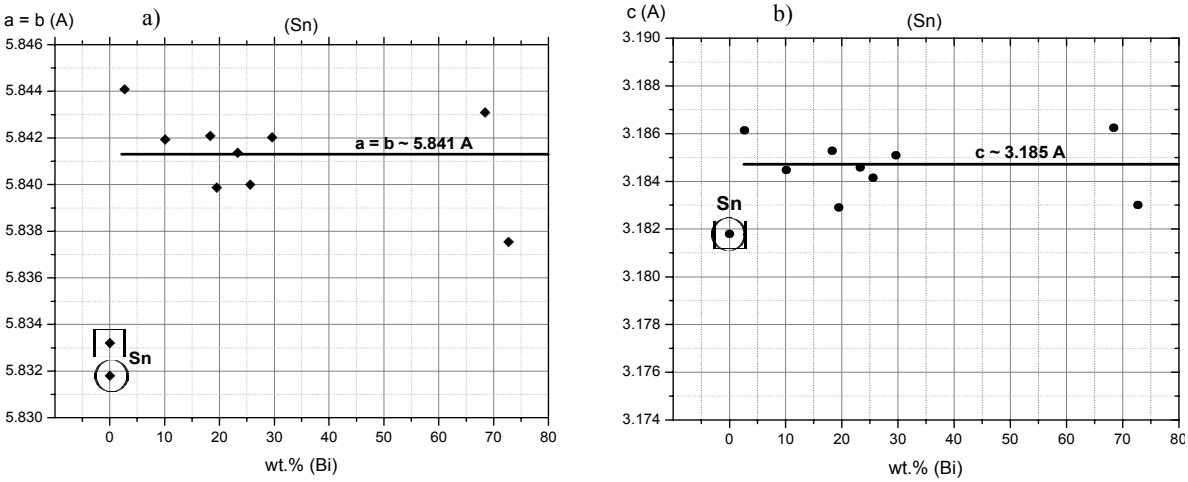

Fig. 4. Lattice parameters for (Sn) found after Rietveld refinement. a) a = b (Å) b) c (Å). Inside the circle the value for pure Sn from [7] and inside the square the value for pure Sn from [8].

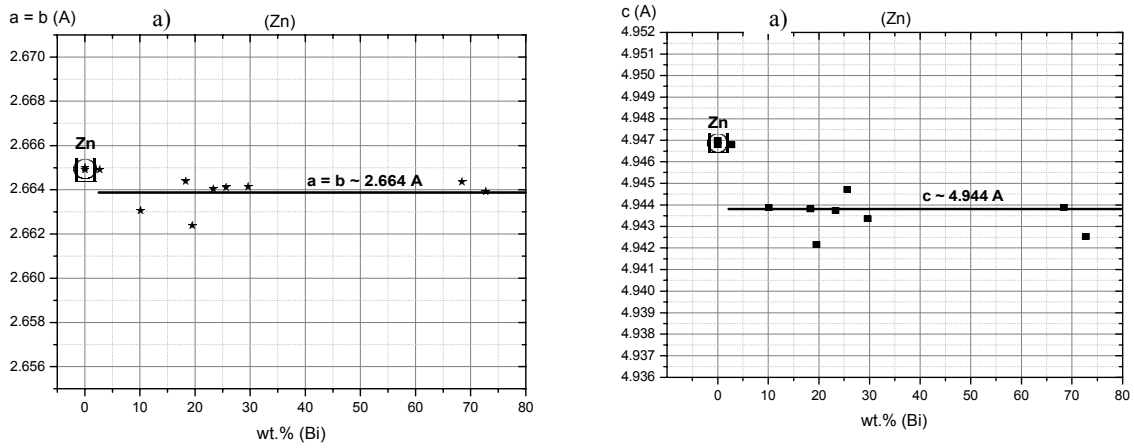

Fig. 5. Lattice parameters for (Zn) found after Rietveld refinement. a) a = b (Å) b) c (Å). Inside the circle the value for pure Zn from [7] and inside the square the value for pure Zn from [9].

Bi pure (Fig. 6) considering [7].

As expected the difference between the measured values of the lattice parameters for (Zn) and Zn [7,9] are of the order of the experimental error (Fig. 5). The major differences between the lattice parameter of the pure element and of the respective phase are for a = b in the case of (Sn) and for c in the case of (Bi). For both cases the value of the experimental lattice parameters are higher than those for the pure elements if [7] is considered. That is expected in what concerns (Sn) since it dissolves Bi and Bi as a higher covalent radius than Sn. If Bi occupies Sn sites in the lattice it is expected that the resulting lattice will be expanded when compared with that from pure Sn. For the latter reason, what is not expected is that

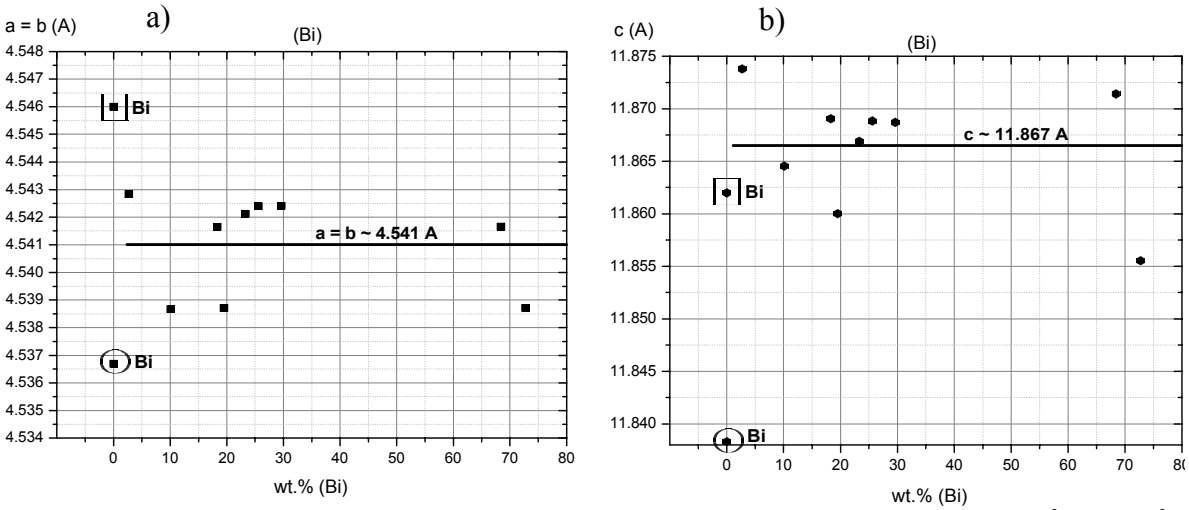

Fig. 6. Lattice parameters for (Bi) found after Rietveld refinement. a) a = b (Å) b) c (Å). Inside the circle the value for pure Bi from [7] and inside the square the value for pure Bi from [10].

the lattice will be contracted (which is what happens in the case of (Bi) if we take [7] into account) when Sn substitutes Bi. Hence, it maybe supposed that the discrepancy found for (Bi), when compared with Bi from [7], is maybe due to two possibilities: the presence of Sn atoms in interstitial spaces (in the c direction) or to experimental inaccuracies. If we take the values for pure Bi from [10], we can consider that the substitution of Bi by Sn results in a contraction of the lattice in the a = b direction.

3.2. High Temperature

If a crystalline solid is isometric (has the same structural configuration throughout), the expansion will be uniform in all dimensions of the crystal. If it is not isometric, there will be different expansion coefficients for different crystallographic directions, and the crystal will change shape as the temperature changes.

The linear expansion coefficient, , is given by equation 1:

$$\alpha_L = \frac{1}{L(T=0^{\circ}C)}\frac{dL}{dT} \qquad (1)$$

L is one of the dimensions of the solid. In this case we've made L has a lattice parameter: a = b or c. dL/dT is the obtained by linear regression of the data obtained experimentally.

If a crystalline solid is isometric, the linear expansion coefficient . (Bi) seems to be isometric $\alpha_{a=b} \cong c$ (Fig. 7 a) and b)) but not (Zn) (Fig. 8 a) and b)). For polycrystalline Zn $\alpha_L = 3.97E\text{-}5K^{-1}$ (for 20º ≤ T ≤ 250 ºC) as it is tabulated in [11]. For a single crystal $\alpha_c = 6.1E\text{-}5K^{-1}$ (for 0º ≤ T ≤ 100 ºC) and $\alpha_{a=b} = 1.5E\text{-}5K^{-1}$ (for 0º ≤ T ≤ 100 ºC) [11]. Our results (Fig. 8 a) and b)) are more in agreement with those for a single crystal, indicating thermal anisotropy.

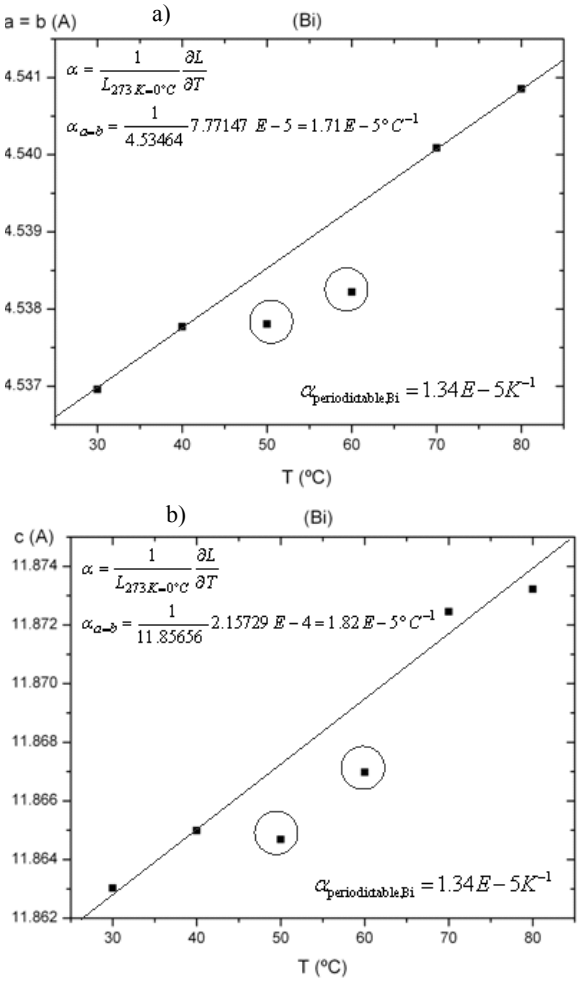

Fig. 7. (Bi) lattice parameters as a function of temperature a) a = b(T) b) c(T) obtained with a sample with w(Bi) = 68.4 %, w(Sn) = 6.0 % and w(Zn) = 25.6 %. Experimental expansion coefficient in comparison with that from [13]. Points surrounded by a circle were not considered for the calculus

(Zn) has a hexagonal structure in which d (interplanar distance) is related with h, k, l (the Miller indices) and with the lattice parameters a = b and c, as follows:

$$\frac{1}{d^2} = \frac{4}{3}\frac{h^2 + hk + k^2}{a^2} + \frac{l^2}{c^2} \quad (2)$$

If a reflection corresponds to [002], h = 0, k = 0 and l = 2, equation 2 becomes: $1/d = \pm \ell /c$. In this case, it can be written: c = d/2. By analysing the reflection [002] (Fig. 9) we can have a direct measure of the c lattice parameter. We've compared c obtained by the analysis of [002] and by Rietveld refinement in Fig. 10. We've also compared obtained by both ways.

In Fig. 11 it can be observed the volume of the unit cell of (Zn) as a function of the temperature as well as the experimental expansion coefficient.

In Fig. 12 it was plotted the mass density as a function of temperature that was calculated using the equation:

$$\rho = \frac{nM}{V_{\text{unit cell}} N_A} \quad (3)$$

In which *n* is the number of atoms per unit cell, *M* the atomic weight, the volume of the unitary cell and N_A the Avogadro's number.

Using the equation that resulted from the linear fit (Fig. 12), we could calculate the mass density at 250ºC as ρ_{250^oC} = 6.929 gcm^{-3} and compare it with the experimental result from [12], ρ_{250^oC} = 6.674 gcm^{-3}, which corresponds to a difference of 3.8 % (in comparison with the value in [12]). It was also calculated the value at 750 ºC, for Zn liquid, ρ_{750^oC} = 6.423 gcm^{-3} and compared with ρ_{750^oC} = 6.265 gcm^{-3} from [12]. It corresponds to a difference of 2.5 % (in comparison with the value in [12]). For Zn liquid, the data from [12] was linear fitted and it was obtained: $\rho(kgm^{-3}) = 6877 - 0.8199 \cdot T(^oC)$ that is comparable with that from Fig. 12.

It was also possible to compare our result, at 20 ºC, ρ_{20^oC} = 7.162 gcm^{-3} , with that from [13] ρ_{20^oC} = 7.140 gcm^{-3} , which corresponds to a difference of 0.3 % (in comparison with the value in [13]).

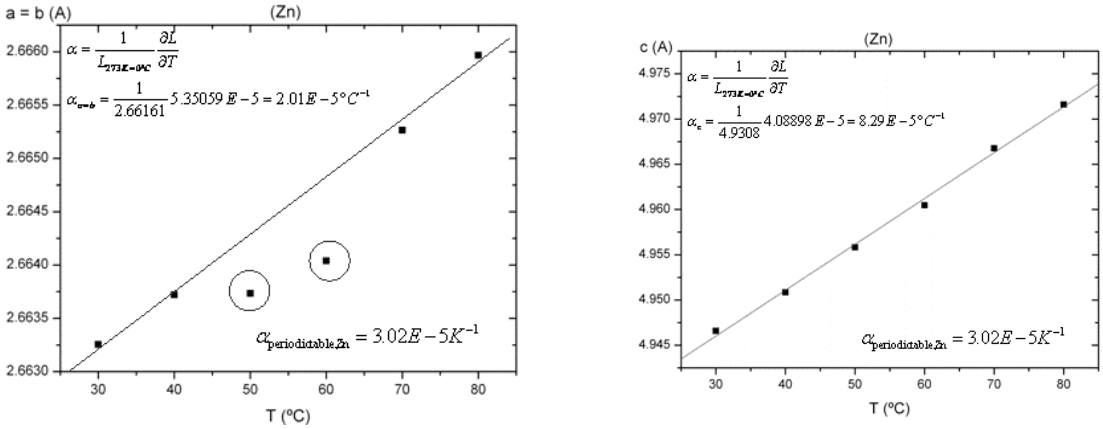

Fig. 8. (Zn) lattice parameters as a function of temperature a) a = b(T) b) c(T) obtained with a sample with w(Bi) = 68.4 %, w(Sn) = 6.0 % and w(Zn) = 25.6 %. Experimental expansion coefficient in comparison with that from [13]. Points surrounded by a circle were not considered for the calculus.

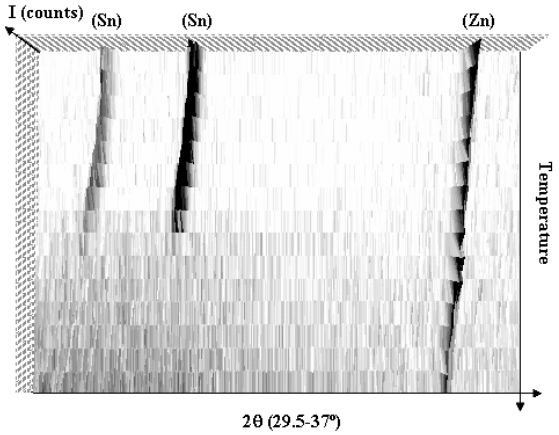

Fig. 9. Zoom of the HT-XRD diffraction patterns as a function of the temperature obtained for a sample with w(Bi) = 68.5 %, w(Sn) = 5.7 % and w(Zn) = 25.8 %. At T > 120 ºC, Sn peaks cannot be distinguished anymore. For (Zn) the reflection corresponding to [002] suffers a deflection with the increasing temperature

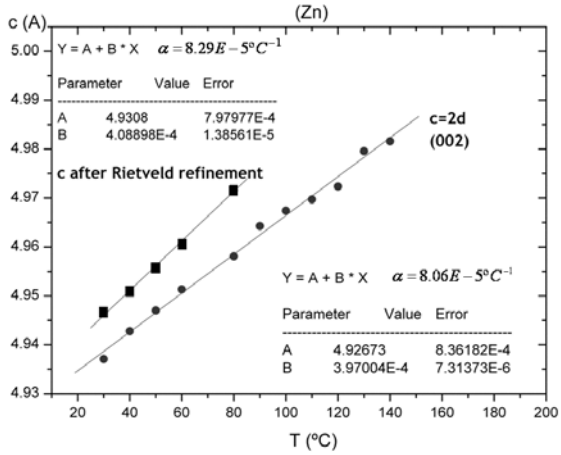

Fig. 10. (Zn) c lattice parameter as a function of temperature obtained with a sample with w(Bi) = 68.4 %, w(Sn) = 6.0 % and w(Zn) = 25.6. c parameter was found after Rietveld refinement (squares) and after the analysis of the reflection corresponding to [002] (circles).

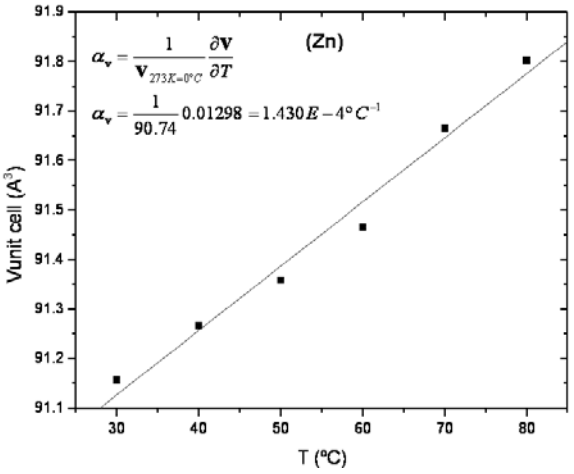

Fig. 11. (Zn) unit cell volume as a function of temperature obtained with a sample with w(Bi) = 68.4 %, w(Sn) = 6.0 % and w(Zn) = 25.6 after Rietveld refinement. Experimental calculated expansion coefficient.

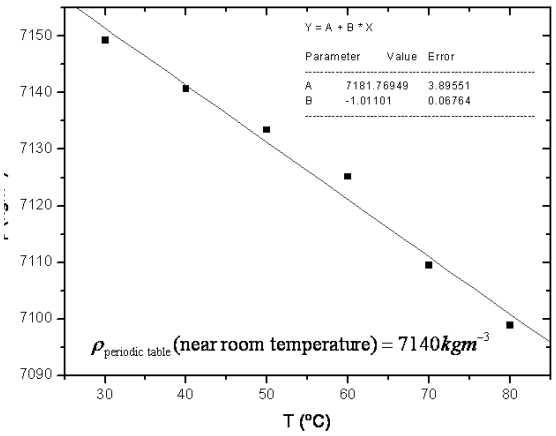

Fig. 12. (Zn) mass density as a function of temperature obtained with a sample with w(Bi) = 68.4 %, w(Sn) = 6.0 % and w(Zn) = 25.6 after Rietveld refinement. Mass density of Zn at a temperature near room temperature [13]

4. Conclusions

Both results at room temperature and at high temperature are in good agreement with what was expected by the observation of the phase diagram and by analysis of the available references.

At room temperature, the dissolution of Bi in (Sn) will make the lattice expand. The interpretation of the dissolution of Sn in (Bi) depends on the values considered for Bi pure.

At high temperatures, (Bi) behaves as an isometric solid but (Zn) shows thermal anisotropy, since $\alpha_c(Zn) > \alpha_{a=b}(Zn)$ as it is expected for a single crystal but not for a polycrystalline solid. Nevertheless, the calculated mass density is in agreement with the published data for room temperature, 250ºC and 750 ºC.

References

1. G. Poupon,http://www.sansplomb.org/doc_presentation/pbissue.pdf, 2004.

2. COST 531 - site, http:// www.univie.ac.at/cost531/, 2007.

3. M. H. Braga, D. Soares, J. Vizdal, J. Ferreira, L.F. Malheiros, A. Kroupa, *CALPHAD*, doi:10.1016/j.calphad.2007.04.004

4. J. Vizdal, M. H. Braga, A. Kroupa, K. W. Richter, D. Soares, L. F. Malheiros, J. Ferreira, *CALPHAD*, doi:10.1016/j.calphad.2007.05.002

5. H. Rietveld, *J. Appl. Cryst.* 2(1969)65-71

6. J. Rodriguez-Carvajal, Program Fullprof (version 3.0 - Nov 2004). D. B Wiles, R. A. Young, A. Sakthivel, *J. Appl. Cryst.* 14(1981)149-151.

7. D. R. Lide (Ed.), CRC Handbook of Chemistry and Physics, 84th Edition. CRC Press. Boca Raton, Florida, 2003; Section 12, Properties of Solids; Thermal and Physical Properties of Pure Metals.

8. 03-065-0296 ICDD PDF-2 2003; from NIST using POWD-12++ after M. Liu, L.-G. Liu, High Temp. High Pressures, 18(1986)79-85.

9. 01-087-0713 ICDD PDF-2 2003; from ICSD using POWD-12++ after H. E. Swanson, E. Tatge, Natl. Bur, Stand. (U.S.), circ. 539, 359(1953)I1.

10. 01-085-1329 ICDD PDF-2 2003; from ICSD using POWD-12++ after P. Cucka, C. S. Barrett, *Acta Crystallogr.*, 15(1962)865-872.

11. American Galvanizers Association, http://www.galvanizeit.org/showContent,302,346.cfm (2007).

12. J. Pstrus, Z. Moser, W. Gasior, TOFA 2004, Discussion Meeting on Thermodynamics of Alloys, Book of Abstracts, Vienna, Austria, September 12-17. SURDAT - Database of Pb - free soldering materials is available on web site http://www.imim.pl (2007).

13. M. Winter. The University of Sheffield and WebElements Ltd, UK, http:// www.webelements.com/ (2007).

CALPHAD: Computer Coupling of Phase Diagrams and Thermochemistry 33 (2009) 237–243

Contents lists available at ScienceDirect

CALPHAD: Computer Coupling of Phase Diagrams and Thermochemistry

journal homepage: www.elsevier.com/locate/calphad

Phase field simulations in miscibility gaps

M.H. Braga [a,*], J.C.R.E. Oliveira [b], L.F. Malheiros [c], J.A. Ferreira [d]

[a] CEMUC, Department of Eng. Physics, FEUP, R. Dr. Roberto Frias s/n, 4200-465 Porto, Portugal
[b] CFP, Department of Eng. Physics, FEUP, R. Dr. Roberto Frias s/n, 4200-465 Porto, Portugal
[c] CEMUC, Department of Metall. and Mat. Eng., FEUP, R. Dr. Roberto Frias s/n, 4200-465 Porto, Portugal
[d] LNEG Laboratory, R. da Amieira - Apartado 1089, S. Mamede Infesta, Portugal

ARTICLE INFO

Article history:
Received 19 May 2008
Received in revised form
29 September 2008
Accepted 6 October 2008
Available online 6 November 2008

Keywords:
Spinodal
Phase field simulations
Bi–Zn
Vycor
Sol–gel

ABSTRACT

Using phase field simulations, it is possible to simulate the dynamics and morphology of immiscible liquids/solids appearing at the miscibility gap of any system. These simulations may also be used to determine the asymptotic compositions of the fluids for a given Gibbs energy. Even more, it is known that different parameters of the excess Gibbs energy of a certain phase may exhibit different asymptotic morphologies, in spite of the similarity of the associated equilibrium curves. This method can be used to choose the best excess Gibbs energy' parameters for the liquid (or solid) phase of a system that will suffer spinodal decomposition. It can also be important (like in the sol–gel process) to choose the best composition, temperature and time to obtain a certain wanted morphology, just by means of the Gibbs energy of the respective phase. In this work, we have performed phase field simulations of the two liquid's separation occurring in the Bi–Zn system, for different temperatures, concentrations and times. We have found a rich diversity of asymptotic morphologies for different points of the Bi–Zn phase diagram. Two different Gibbs energies were used to show how the morphologies will be affected by different parameters of the excess Gibbs energy.

1. Introduction

There are many systems that present miscibility gaps in the liquid or solid phase. These systems are, for example, Bi–Zn, Li–Zr, Mg–Mn, S–Sb, Sn–P, Ti–W, Cu–Ni–Sn or even glasses, such as Vycor®, that contains approximately 75 wt% SiO_2, 20 wt% B_2O_3 and 5 wt% Na_2O.

In the ternary phase diagram of B_2O_3–SiO_2–Na_2O, Vycor® corresponds to a composition in which at a given temperature, two immiscible liquid phases are formed, one of them rich in SiO_2. When the sample is quenched from the miscibility gap, the two phases corresponding to the immiscible liquids are kept. For industry and for most of the applications only the SiO_2 rich phase is important, and so the other phase will be leach out leaving a porous, high-silica skeleton [1].

In this paper, the dynamics of a thermodynamically unstable solution with respect to composition variations is studied. In such a regime, nucleation of the new phase is not necessary. The phase transformation occurs spontaneously by spinodal decomposition and may result in a multi-phase microstructure in which phases are highly interconnected (for a certain range of compositions and temperatures of the spinodal region). The latter microstructures have numerous applications: one of them already mentioned is Vycor® glass, whose silica structure can be the matrix for other applications such as the study of superfluids [2].

Another very important and up-to-date application concerns the sol–gels for the production of nanoparticles [3] and membranes, with applications in health and in food technology [4].

The spinodal decomposition may also be used to improve the mechanical properties of certain materials since, in general, spinodally decomposed materials can exhibit very fine scale composition modulations, resulting in very high strength materials. The phase field simulations of solid or liquid miscibility gaps may be used to determine how the mechanical properties (local stress, strain fields or Young's modulus) depend on the composition of the blend. For example, Cu–Ni–Sn alloys can be hardened by spinodal transformation and are used in electrical contact materials that grip by elastic springback, such as in computer connectors [5].

Lead free solder materials are under investigation for environmental reasons. Structural and mechanical properties are also of great importance in what concerns solders. In order to study the mechanical properties of amorphous solders alloys, it is crucial to study the liquid phase.

The phase field method is a subject of interest since a long time ago. Based on the Ginzburg–Landau theory of phase

* Corresponding author. Tel.: +351 225081420; fax: +351 225081447.
E-mail addresses: mbraga@fe.up.pt (M.H. Braga), jespain@fe.up.pt (J.C.R.E. Oliveira), lfmf@fe.up.pt (L.F. Malheiros), Jorge.Ferreira@ineti.pt (J.A. Ferreira).

0364-5916/$ – see front matter © 2008 Elsevier Ltd. All rights reserved.
doi:10.1016/j.calphad.2008.10.004

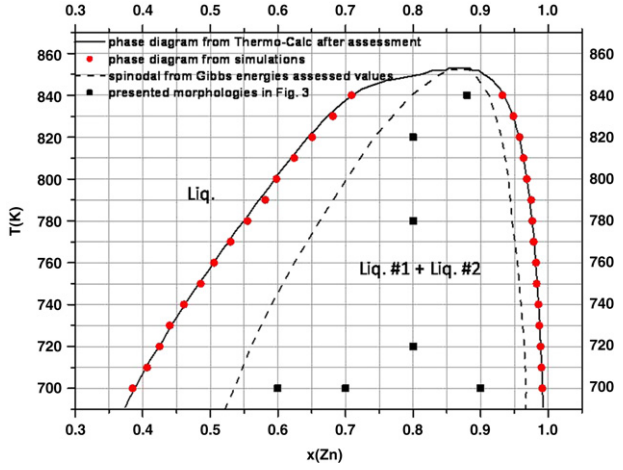

Fig. 1. The zoom of the miscibility gap occurring in the liquid region as well as its spinodal region obtained from Gibbs energy by [16] after [14]. The scale limits, which are the values of ϕ for each temperature obtained with the simulations, are represented by the two opposing circles in the phase diagram miscibility gap curve (x(Liquid#1, Zn) and x(liquid#2, Zn)); points in squares present variations of the simulated asymptotic morphology at different temperatures and compositions shown in Fig. 3.

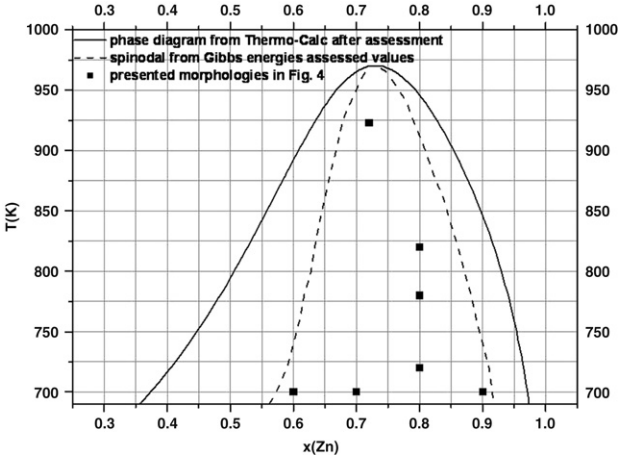

Fig. 2. The zoom of the miscibility gap occurring in the liquid region as well as its spinodal region obtained from Gibbs energy by [15]; points in squares present variations of the simulated asymptotic morphology at different temperatures and compositions shown in Fig. 4.

transitions, one of the first applications of phase field method was developed by Cahn–Hilliard [6] which describes the process of phase separation, by which the two components of a binary solution spontaneously separate. The main feature of this method is to substitute boundary conditions at the interface by a partial differential equation for the evolution of an auxiliary field (the phase field) that takes the role of an order parameter. Since the seventies [7] and mostly on the nineties, the multiphase field concept has been developed by [8–13].

Using phase field simulations, it is possible to simulate the dynamics of immiscible liquids appearing at the miscibility gap of an alloy, just by having access to the Gibbs energy of the liquid phase for each composition and temperature. These simulations may be used to determine the asymptotic compositions of the fluids for a given Gibbs energy. Even more, it is known that different parameters of the excess Gibbs energy of a certain phase may exhibit different asymptotic morphologies, in spite of the similarity of the associated equilibrium curves. Hence, these morphological studies may be an efficient method to distinguish between different Gibbs energies that give approximately the same equilibrium compositions, in spite of having different corresponding parameters of the excess Gibbs energy.

In this work we have performed phase field simulations for the two liquids separation occurring in the miscibility gap of the Bi–Zn system, for different temperatures and concentrations. We have used the Bi–Zn Gibbs energy previously calculated using the CALPHAD method and found a rich diversity of asymptotic morphologies for different points of the Bi–Zn phase diagram. It was also possible to determine the asymptotic compositions of Liq.#1 and Liq.#2. The latter calculations were performed for two different Gibbs energies representing the liquid phase of the Bi–Zn system obtained by two different authors [14,15] using the CALPHAD method.

2. Theory and calculation

2.1. Determination of the Gibbs energies using the CALPHAD method

The CALPHAD method was used prior to this work to obtain the Gibbs energy of the liquid phase [16].

The method for the calculation of thermodynamic equilibrium is based on modeling the Gibbs energies of all coexisting phases and minimizing the total Gibbs energy of the system. The system Bi–Zn was assessed by Malakhov [14] but some changes were introduced in the first assessment by [16].

The Gibbs energy of mixing of the substitutional solution (liquid phase mixture in this case) is expressed by [17], as:

$$G_{mix} = G^{id} + G^{E} \tag{1}$$

where $G^{id} = RT\sum_i x_i \ln(x_i)$ is the ideal mixing contribution, x_i is the molar fraction of the component i with $\sum_i x_i = 1$ and $G^{E} = \sum_i \sum_{i>j} x_i x_j L_{ij}$ (with $L_{ij} = \sum_{\nu=0}^{k}(x_i - x_j)^{\nu} \cdot {}^{\nu}L_{ij}$ where ${}^{\nu}L_{ij} = a_\nu + b_\nu + c_\nu T\ln T$) the contribution due to non-ideal interactions between the components (also known as the excess Gibbs energy of mixing) where x_i and x_j are the molar fractions of the components i and j ($x_j = 1 - x_i$).

In this work we have used the assessments of two different authors: Vizdal et al. [16], after Malakhov [14], and Djaballah et al. [15].

Vizdal et al. [16], after Malakhov [14], assessed the liquid phase using the excess Gibbs energy written as:

$$G^{E} = x_{\mathrm{Bi}}x_{\mathrm{Zn}}[{}^{0}L_{\mathrm{Bi,Zn}} + (x_{\mathrm{Zn}} - x_{\mathrm{Bi}}) \cdot {}^{1}L_{\mathrm{Bi,Zn}} + (x_{\mathrm{Zn}} - x_{\mathrm{Bi}})^2 \cdot {}^{2}L_{\mathrm{Bi,Zn}} + \cdots + (x_{\mathrm{Zn}} - x_{\mathrm{Bi}})^6 \cdot {}^{6}L_{\mathrm{Bi,Zn}}]$$

with ${}^{\nu}L_{\mathrm{Bi,Zn}} = a_\nu + b_\nu T$ (a and b where determined using the CALPHAD method and experimental data).

Djaballah et al. [15] assessed the liquid phase using the excess Gibbs energy written as follows:

$$G^{E} = x_{\mathrm{Bi}}x_{\mathrm{Zn}}[{}^{0}L_{\mathrm{Bi,Zn}} + (x_{\mathrm{Zn}} - x_{\mathrm{Bi}}) \cdot {}^{1}L_{\mathrm{Bi,Zn}} + (x_{\mathrm{Zn}} - x_{\mathrm{Bi}})^2 \cdot {}^{2}L_{\mathrm{Bi,Zn}} + (x_{\mathrm{Zn}} - x_{\mathrm{Bi}})^3 \cdot {}^{3}L_{\mathrm{Bi,Zn}}]$$

with ${}^{\nu}L_{\mathrm{Bi,Zn}} = a_\nu + b_\nu T + c_\nu \ln T$ (a, b and c where determined using the CALPHAD method and experimental data).

3. Phase field simulations

During the phase separation occurring at the spinodal region of Bi–Zn system, a mixture of Liq.#1 and Liq#2 is formed. Because the mixture is incompressible we can characterize the system by one order parameter, ϕ, which is defined as $\phi = x_{\mathrm{Zn}} - x_{\mathrm{Bi}}$. The free energy of the system can be written, phenomenologically, as the Landau functional [6,18],

$$F[\phi] = \int \mathrm{d}\vec{r}\left[k(\nabla\phi)^2 + G^{\mathrm{liquid}}(\phi)\right], \tag{2}$$

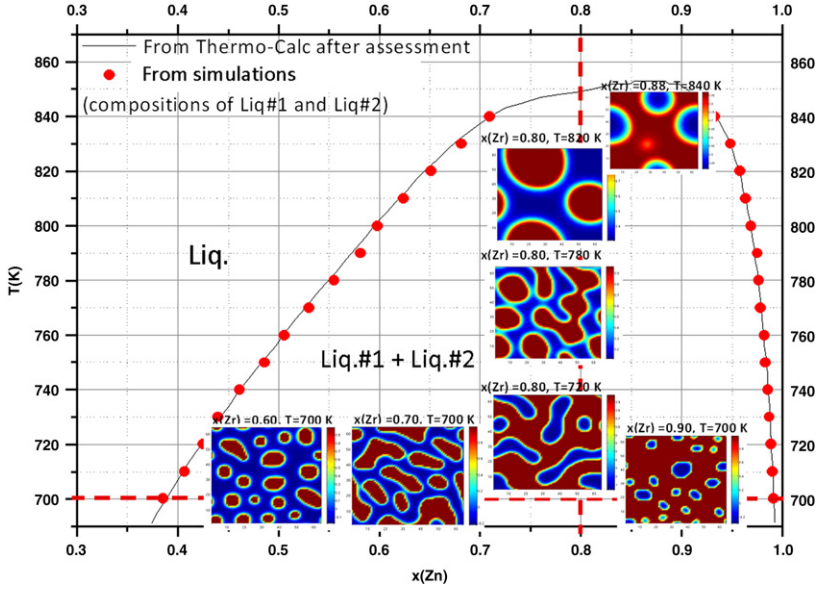

Fig. 3. The zoom of the miscibility gap occurring in the liquid region; simulations' pictures present variations of the asymptotic morphology at different temperatures and compositions for the Gibbs energy obtained by [16] after [14]. The scale limits, that are the values of ϕ for each temperature, are represented by the two corresponding circles in the phase diagram miscibility gap curve (x(Liquid#1, Zn) and x(liquid#2, Zn)). Note that the cubic anisotropy that is seen in some of the simulations is a low resolution effect with no physical meaning.

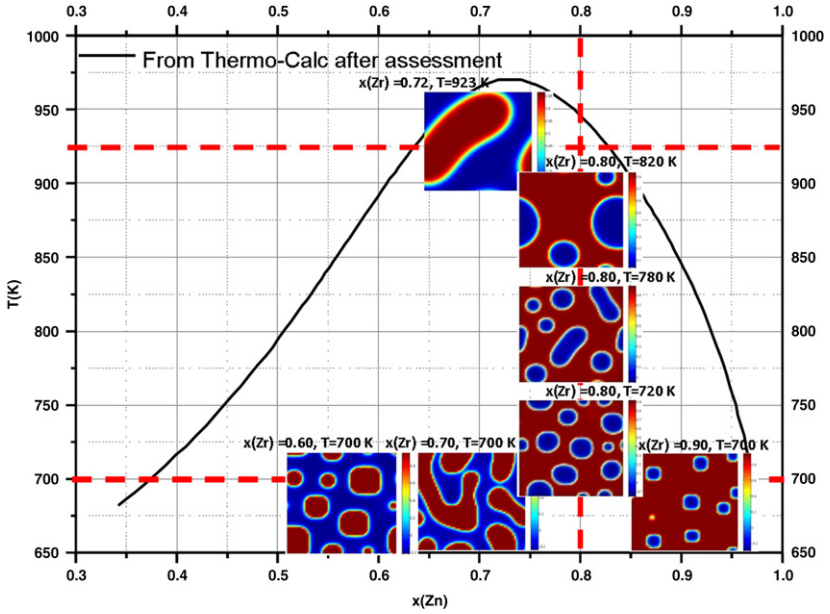

Fig. 4. The zoom of the miscibility gap occurring in the liquid region; simulations' pictures present variations of the asymptotic morphology at different temperatures and compositions for the Gibbs energy obtained by [15]. Note that the cubic anisotropy that is seen in some of the simulations is a low resolution effect with no physical meaning.

where $G^{\text{liquid}}(\phi)$ is the Gibbs energy G_{mix}, presented in (1) (making $\phi = x_{\text{Zn}} - x_{\text{Bi}}$). The surface tension corresponds to the energy of the flat interface per unit length and is given by $\sigma = k\int \mathrm{d}n \left(\frac{\partial\phi}{\partial n}\right)^2$, where the integral is performed across the interface and in the direction normal to it. The functional derivative of F is $\delta F/\delta\phi = k\nabla^2\phi - \frac{\partial G^{\text{liquid}}}{\partial\phi}$.

The time evolution of the order parameter can be described by Cahn–Hilliard equation for the phase separation in isotropic solids or liquids at the diffusive regime [6,18], which can be written in the form of a continuity equation $\partial\phi/\partial t = -\nabla\vec{j}$, with current $\vec{j} = -\nabla(\delta F/\delta\phi)$. Since ϕ is conserved in the total volume, $\partial\phi/\partial t$ is the divergence of a flux $\vec{j}$,

$$\frac{\partial\phi}{\partial t} = -\nabla\cdot\vec{j} = \nabla^2\left(\frac{\partial G^{\text{liquid}}}{\partial\phi} - k\nabla^2\phi\right). \tag{3}$$

The asymptotic growth regime for phase separation in binary liquids, in the diffuse regime, is given by $L \propto t^{1/3}$, where L is the characteristic length of the phase boundaries. Thus, the asymptotic evolution is very slow leading to almost stationary morphologies for large evolution times. The time that is needed to reach the asymptotic growth regime in a given sample will in general depend on the mobility of the alloy species. In a future work we intend to calibrate the key parameters characterizing the

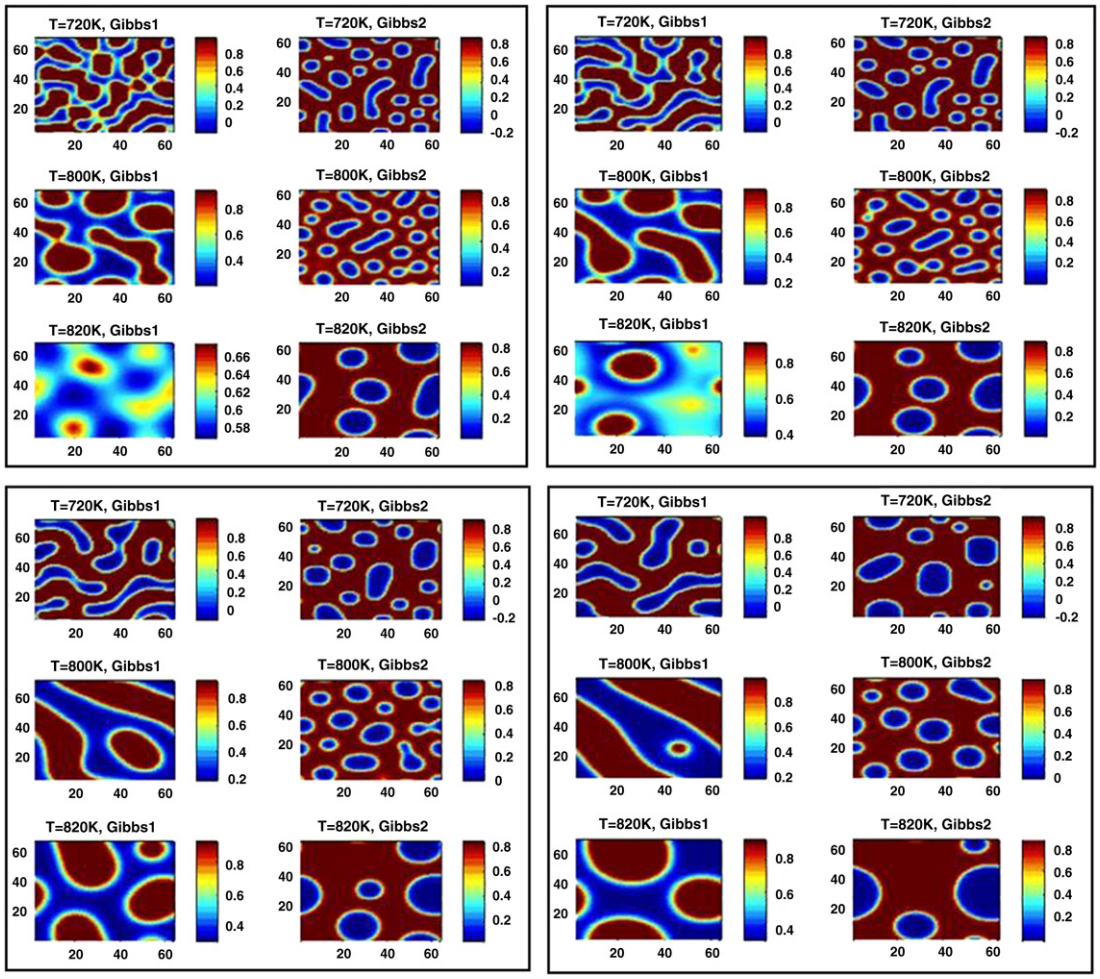

Fig. 5. Different morphologies obtained for the same composition $x(\mathrm{Zn}) = 0.8$ and time, at different indicated temperatures, to allow a comparison between the morphologies obtained with different Gibbs energies (Gibbs1 by [14,16] and Gibbs2 [15]). Time increases from left to right starting above (time in each large square is the same). The scales correspond to the values of ϕ.

system by performing a detailed quantitative study of the time evolution of L in the simulations and a subsequent comparison with the observed one in different system samples.

In Eq. (3) changing the time scale can scale out k. In fact the same dynamics can be obtained with a different surface tension by changing the size of the simulation box accordingly. Hence, the asymptotic morphology of the system is just a function of the Gibbs energy and not of the value of k.

In the alloy system, the atoms of A and B (Bi and Zn in this case) can exchange position only locally (not over large distances), leading then to a diffusive transport of the order parameter.

We have integrated (3) using a standard finite-difference method [19]. In all simulations we have used initial random conditions for ϕ and $k = 1$.

4. Results and discussion

In Figs. 1 and 2 both the miscibility gap and spinodal curves, obtained after the assessments of [14,16] and [15] respectively, can be observed. In Fig. 1 the points corresponding to the asymptotic values of x(Liq.#1, Zn) and x(Liq.#2, Zn), obtained in this work by phase field simulations, can also be observed.

In Fig. 3, the miscibility gap curve of the Bi–Zn system is shown. A good agreement, between the equilibrium curve calculated in [16] and the one obtained by the simulations was found as expected. Here, the simulations' images for different compositions and temperatures represent the asymptotic morphologies of the Bi–Zn system near the equilibrium configuration. It can be seen that the size and shape of the domains change considerably with temperature for the same concentration, and with the concentration, for the same temperature.

In Fig. 4 equivalent results to those of Fig. 3 are shown. It can be observed that the morphologies corresponding to the same temperatures and compositions are considerably different. For instance, interconnected structures may appear in a region of the miscibility gap of Fig. 4 where in Fig. 3 round shaped domains appear.

By the analysis of the asymptotic morphologies shown inside the miscibility gap, it can be seen that for the compositions near each side of the spinodal line (Figs. 1–4), there is a matrix of the more abundant liquid and inside this matrix, isolated round shaped domains of the other liquid phase appear. Concerning the system' compositions that are more in the middle of the spinodal region, for the same temperature as the previously referred morphologies, interconnected domains can be observed. These interconnected domains have many applications and the identification of the compositions for which they appear is crucial [20,21].

Note for example that, for $x(\mathrm{Zn}) = 0.8$ in Fig. 3, interconnected domains appear at least for $T \leq 780$ K. Only round shaped domains can be observed for $x(\mathrm{Zn}) = 0.8$ in Fig. 4. If the phase diagrams and spinodal lines are compared, it can be seen that the latter composition in the miscibility gap of Fig. 1 corresponds to the center of the spinodal region and that at $T = 720$ K it is clear

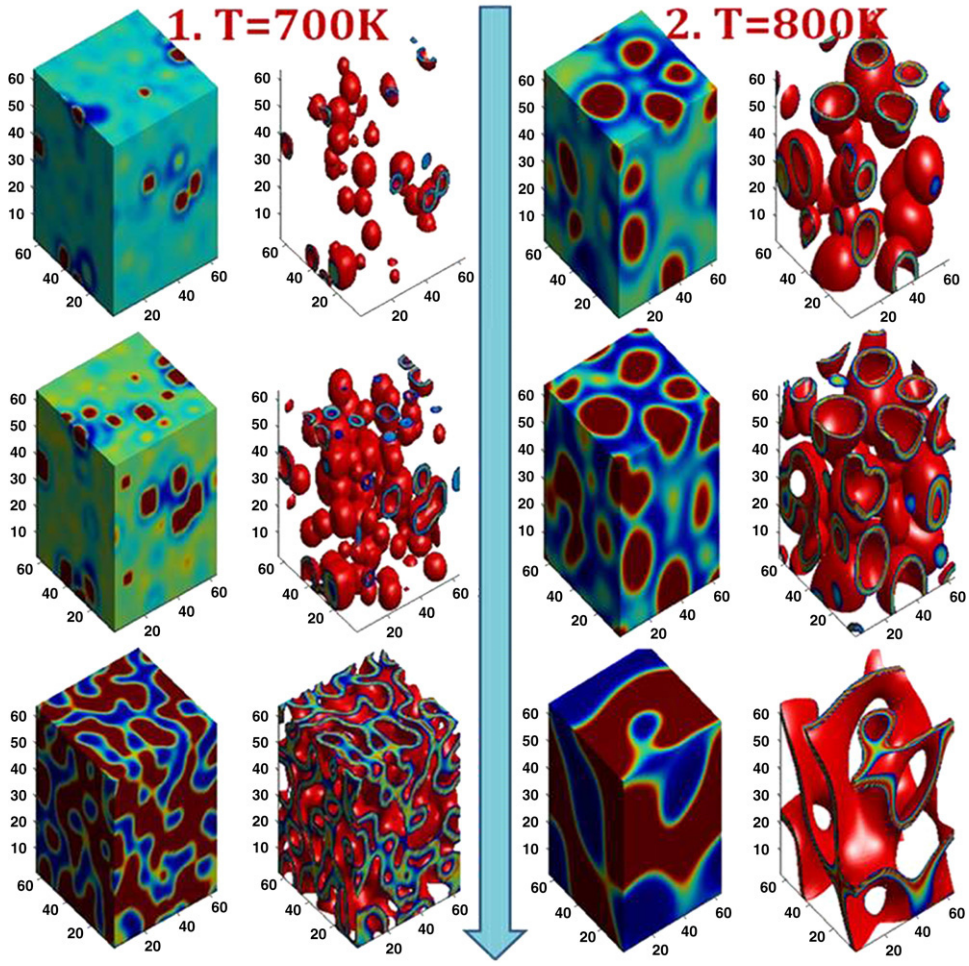

Fig. 6. 3D diagrams showing the evolution of the two immiscible liquids in the Bi–Zn phase diagram for an alloy with $x(\mathrm{Zn}) = 0.8$ at 700 K and at 800 K. The arrow points the direction of time evolution. The Gibbs energy used was determined by [14,16].

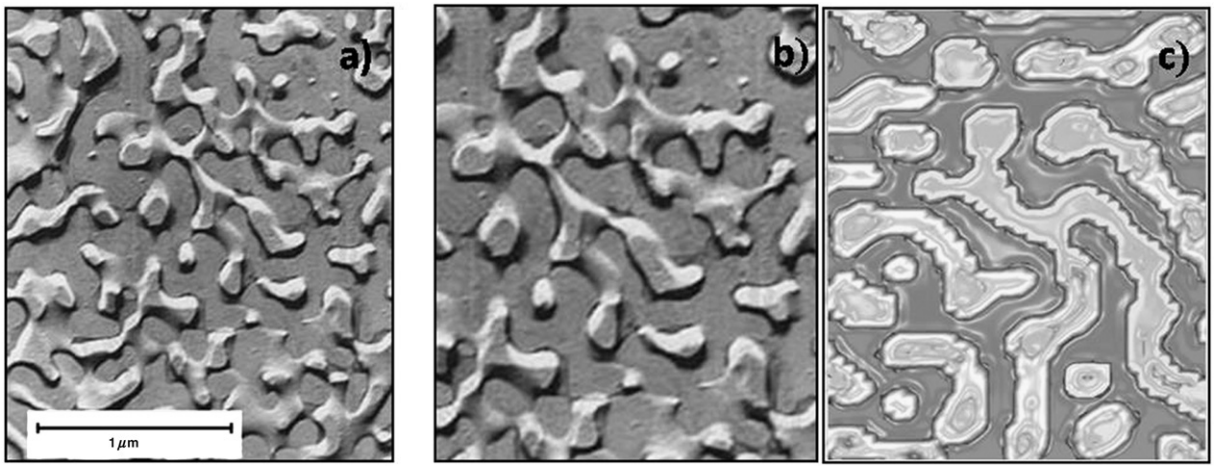

Fig. 7. The Vycor® glass (a) and (b). SEM microphotograph by Vogel [20]. (c) is a simulation obtained for the Bi–Zn system using the Gibbs energy determined by [14,16]. The simulation was obtained for the condition $T = 700$ K, $x(\mathrm{Zn}) = 0.8$ and the figure was graphically modified to be easily compared with the real one obtained with the glass. The objective is to show that the morphologies obtained using phase field simulations and Gibbs energies, assessed by the CALPHAD method, can be very similar to the real ones for different systems.

that Liq.#1 is more abundant (matrix is Liq.#1). On the contrary, by the observation of Fig. 2, it can be seen that $x(\mathrm{Zn}) = 0.8$ does not correspond to the center of the spinodal and that at $T = 720$ K it is clear that Liq.#2 is more abundant (matrix is Liq.#2).

The analysis of the morphologies as a function of temperature also reveals that the interconnected domains will change to spheres as the temperature rises to the upper limit of the miscibility gap.

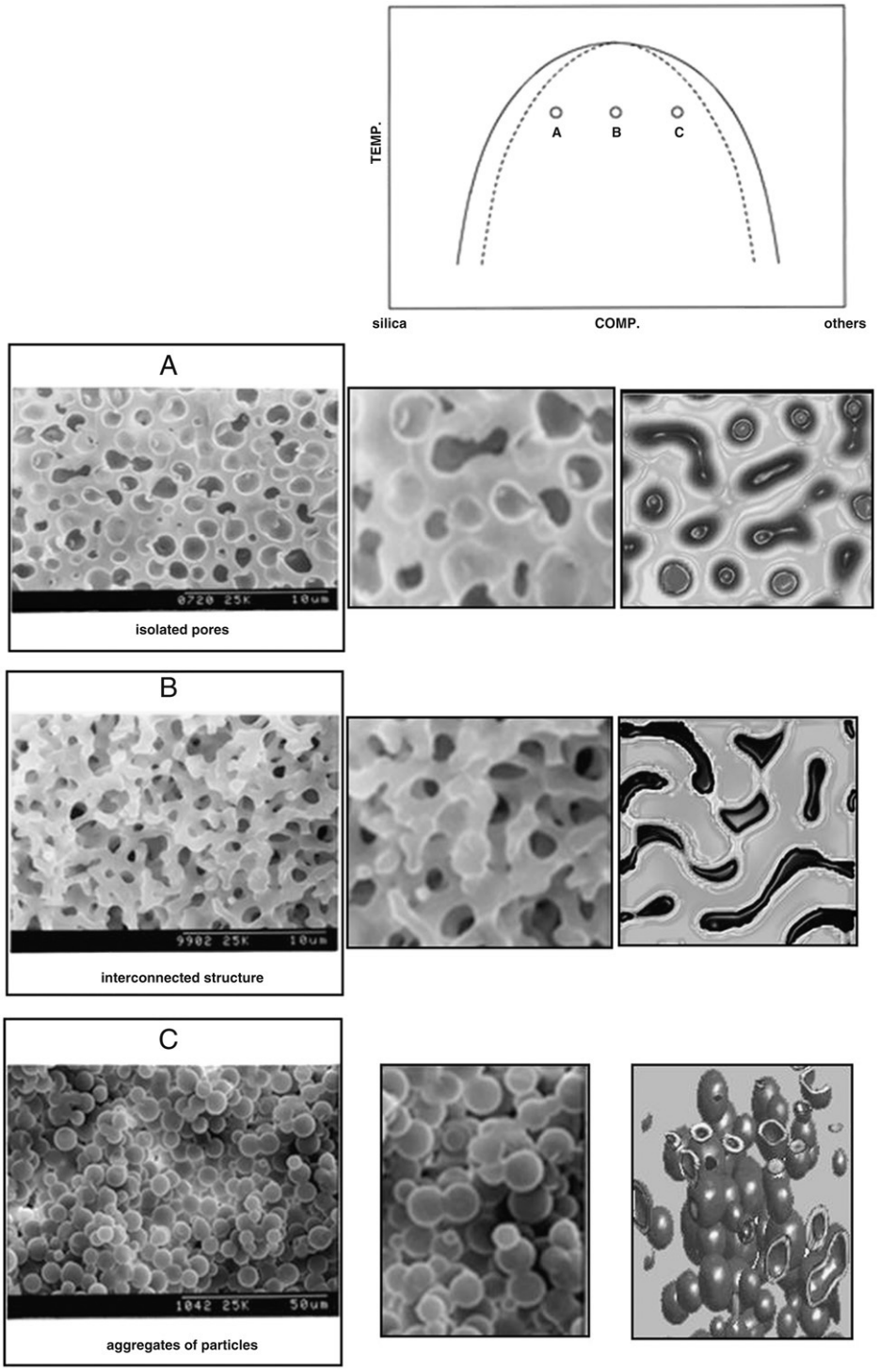

Fig. 8. Schematic phase diagram of the miscibility gap (solid line) and spinodal (broken line) of the sol–gel system (SiO_2/others) and SEM micrographs of the dried sol–gels obtained by Nakamura et al. [21]. A – isolated pores – (the base is silica and pores were left by the other phase belonging to the miscibility gap). At the middle the zoom of the real microphotograph and on the right the 2D simulation obtained for Bi–Zn that was treated graphically to be easily compared with real structures. B – interconnected structure – (the base is silica and pores were left by the other phase belonging to the miscibility gap). At the middle the zoom of the real microphotograph and on the right the 2D simulation obtained for Bi–Zn that was treated graphically to be easily compared with real structures. C — aggregates of particles (the particles are from silica and space around them was left by the other phase belonging to the miscibility gap). At the middle the zoom of the real microphotograph and on the right the 3D simulation obtained for Bi–Zn that was treated graphically to be easily compared with real structures. The same type of variation of structure with composition for a given temperature, that can be seen in A, B, and C, can also be observed on the simulations of the Bi–Zn (Figs. 3 and 4) at $T = 700$ K.

The same type of composition and temperature morphologies dependence was found in [20,21].

It can also be seen in Fig. 5 that the dynamics toward equilibrium also differs when different Gibbs energies are considered. We have performed 3D simulations of the phase separation for the Gibbs energy of [14,16], as it can be observed in Fig. 6, where the evolution of the phase boundaries is presented for two different temperatures.

Although Vycor and sol–gel cannot be directly compared with Bi–Zn, it is relevant to show that, in spite of their different Gibbs

energies, similar morphologies can be observed in corresponding relative positions of the miscibility gap and spinodal regions. This fact enhances the possible applications of the method.

Figs. 7 and 8 show comparisons between our Bi–Zn simulated morphologies (obtained with the Gibbs energy [14,16]) and similar ones for observed samples of Vycor® [20] and sol–gel [21], respectively.

5. Conclusions

Using phase field simulations, the dynamics of the two immiscible liquids appearing on the phase diagram of the Bi–Zn system was studied. Good agreement between the miscibility gap curve determined by the simulations and the one obtained by the CALPHAD method was found, as expected.

It was found a rich diversity of asymptotic morphologies for different points of the Bi–Zn phase diagram.

We have compared the morphologies for two different Gibbs energies determined by Calphad method and found very different morphologies for the same times, concentrations and temperatures. Thus, it can be concluded that the different morphologies and the time it takes to reach them is a signature of the calculated excess Gibbs energy parameters for a given system.

It could also be verified the similarities between the simulated structures and those observed in different real systems, such as Vycor® glass and sol–gel.

It can be pointed out, that for a given temperature, the morphologies of the Bi–Zn system depend on the composition in a similar way as those observed in the sol–gel system, especially the morphologies obtained with one of the Gibbs energies.

The results obtained in this work show that using the Gibbs energies, obtained for example with the CALPHAD method and phase field simulations, we have a straightforward method to determine the morphologies of the miscibility gap as a function of the concentration, temperature and time. This method may be useful to find the best structures, depending on the applications and purposes; for instance, for the fabrication of nanoparticles.

Acknowledgements

The authors would like to acknowledge the COST MP0602 action: "Advanced Solder Materials for High-Temperature Application — their nature, design, process and control in a multiscale domain".

References

[1] M.H. Bartl, K. Gatterer, H.P. Fritzer, S. Arafa, Spectrochim. Acta A 57 (2001) 1991–1999.
[2] B. Peter, B. Paul, L. Gavin, C. Lee, M. Akira, I. Osamu, M. Pinaki, Phys. Lett. A 310 (4) (2003) 311–321.
[3] A. Bouchara, G. Mosser, G.J.A.A. Soler-Illia, J.-Y. Chane-Ching, C. Sanchez, J. Mater. Chem. 14 (2004) 2347–2354.
[4] P. Schurtenberger, Nanotech 2005, California, U.S.A., May 8–12, 2005.
[5] S.M. Allen, E.L. Thomas, The Structure of Materials, Wiley MIT, 1999, pp. 374.
[6] J.W. Cahn, J.E. Hilliard, J. Chem. Phys. 28 (2) (1958) 258.
[7] J.S. Langer, H. Müller-Krumbhaar, Acta Metall. 26 (1978) 1681, 1689, 1697.
[8] L.Q. Chen, A.G. Khachaturyan, Acta Metall. Mater 39 (11) (1991).
[9] A.A. Wheeler, W.J. Boettinger, G.B. Mc Fadden, Phys. Rev. A 45 (10) (1992) 7424.
[10] G. Caginalp, E. Socolovsky, SIAM J. Sci. Comput. 15 (1) (1994) 106.
[11] R. Kobayashi, Physica D 63 (3,4) (1993) 410.
[12] A.A. Wheeler, B.T. Murray, R.J. Schaefer, Physica D 66 (1,2) (1993) 243.
[13] J. Steinbach, F. Pezzolla, B. Nestler, M. Seeßelberg, R. Prieler, G.J. Schmitz, J.L.L. Rezende, Physica D 94 (1996) 135.
[14] D.V. Malakhov, CALPHAD 24 (2000) 1–14.
[15] Y. Djaballah, L. Bennour, F. Bouharkat, A. Belgacem-Bouzida, Modeling. Simul. Mater. Sci. Eng. 13 (2005) 361–369.
[16] J. Vizdal, M.H. Braga, A. Kroupa, K.W. Richter, D. Soares, L.F. Malheiros, J. Ferreira, CALPHAD 31 (2007) 438–448.
[17] O. Redlich, A. Kister, Ind. Eng. Chem. 40 (1948) 411–420.
[18] A.J. Bray, Adv. Phys. 43 (1994) 357–458.
[19] J.C.R.E. Oliveira, C.J.A.P. Martins, P.P. Avelino, Phys. Rev. D 71 (2005) 083509.
[20] W. Vogel, Chemistry of the Glass, The American Ceramics Society, 1985, pp. 83.
[21] N. Nakamura, R. Takahashi, S. Sato, T. Sodesawa, S. Yoshida, Phys. Chem. Chem. Phys. 2 (2000) 4983–4990.

Chapter 5 - Al-Fe-Ti SYSTEM

Chapter 5.

Al-Fe-Ti SYSTEM

5.1. Introduction

Aluminum-based intermetallic alloys with transition metals are of high interest for their complex crystalline and quasicrystalline structures, formed primarily with late transition metals, and their technologically useful compounds (Mihalkovic & Widom, 2012). Experimental phase diagram determination is difficult because many structures usually exist within small composition ranges; many are intrinsically exhibiting mixed or partial site occupancy.

First principles calculations can help resolve some uncertainties in the phase diagrams but are challenging themselves, for many of the same reasons. Intrinsic disorder requires studying alternative realizations of specific site occupancy. Some of the nearby competing phases may have unknown or poorly known structures. The large unit cells pose computational difficulties. Further complicating the study is the prevalence of magnetism among late transition metals.

The Al-Fe-Ti system was object of our study as one of the goals of the COST 535 EU action, "Thermodynamics of Alloyed Aluminides", 2004-2007. We have performed X-ray diffraction at room (RT-XRD), high temperature (HT-XRD) Differential Scanning Calorimetry (DSC) and Electron Probe Micro Analysis (EPMA) with samples belonging to the system.

In this chapter only the study of the Al-Fe system is going to be described, since this system was studied both experimentally and theoretically. In the nearest future, we will be studying the Al-Fe-Ti by means of first principles theoretical calculations to complement the experimental study we've developed already.

5.2. Al-Fe system

Recently, a paper from (Stein et al., 2010) described the ε phase of the Al-Fe system to have body-centered cubic structure of the Hume-Rothery Cu_5Zn_8-type (space group I-43m), formula Al_8Fe_5, and lattice parameter a = 0.89757(2) nm at 1393K, which is 3.02 times that of cubic AlFe (B2) at the same temperature.

Previously, in 1993, the system was assessed by Kattner & Burton (Fig. 5.1).

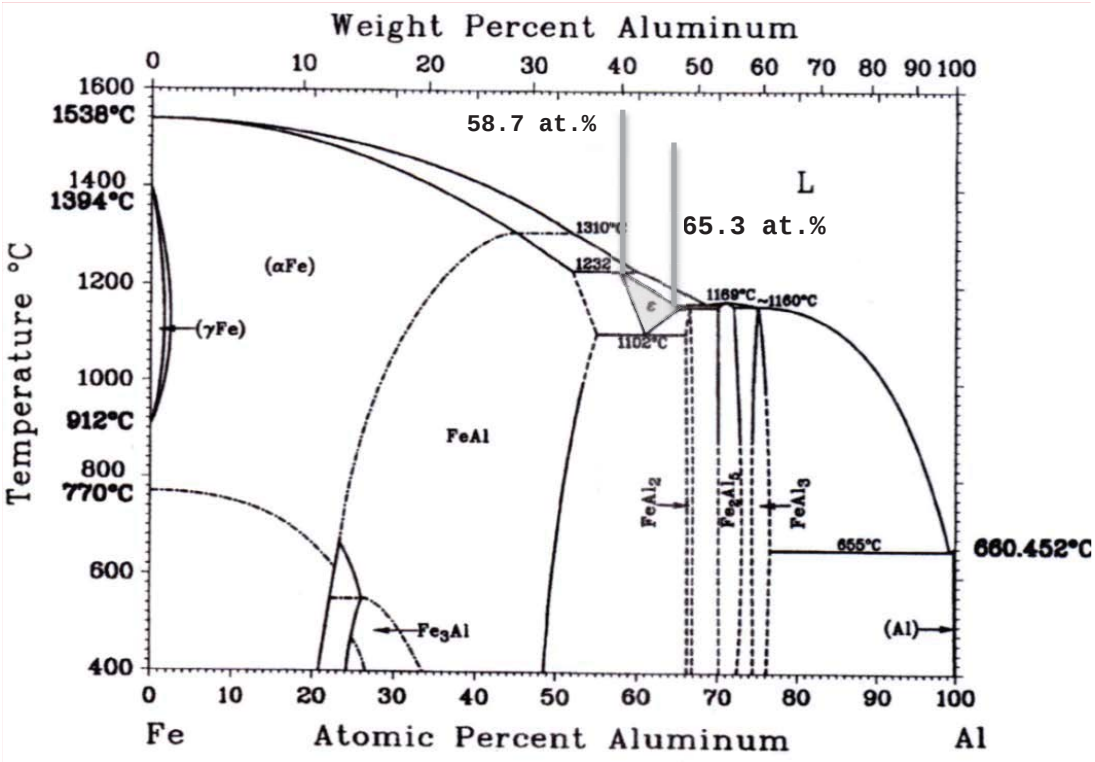

Fig. 5.1 The Fe-Al system according to the assessment by Kattner & Burton, 1993.

We have performed Differential Scanning Calorimetry (DSC) experiments to define the whole range of stability of the ε phase. The experiments were executed at 10 K/60s and under an Ar flux (Fig. 5.2). We've used Alumina crucibles with lids. The samples were prepared from the pure elements, in an arc melting furnace, annealed at 1273 K for 43200s. and cooled down at 0.5 K/60s. The DSC results here presented are in very good agreement with Kattner & Burton, 1993 (Fig. 5.2) and Table 5.1.

At room temperature, the latter samples (that were subsequently submitted to the DSC measurement cited before) presented a two phase region constituted by AlFe and Al_2Fe, as the Electron Probe Micro Analysis (EPMA) has shown in Fig. 5.3.

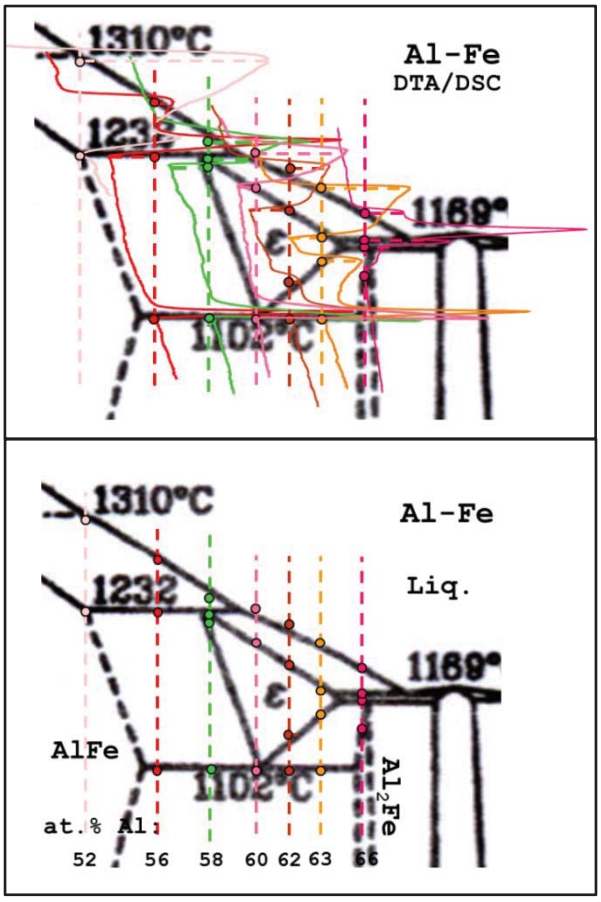

Fig. 5.2 DSC curves obtained in this work (above) were superimposed to the phase diagram in a region centered on the stability range of the ε phase of the Fe-Al system (Kattner & Burton, 1993). Dots and dashed lines (below) show the transformation temperatures correspondent to each signalized composition. They were obtained from the DSC curves shown above.

Subsequently to that of Kattner & Burton, 1993, other assessments were performed (e. g. Sundman et al., 2009). In the latter reference, the ε phase was modeled recurring to a two sublattice model based on the work of Stein et al., 2010 (Fig. 5.4) that was initially presented in a COST – 535 meeting in 2008. Nonetheless, the experimental data on the phase diagram are not fully described by the assessed Al_8Fe_5-ε phase. Furthermore the invariant temperature of the eutectoid reaction Al_8Fe_5-ε → AlFe + Al_2Fe, which was found to be 1375 K in (Kattner & Burton, 1993) and that is in agreement with our DSC data (1371 K), was assessed to be 1362 K in (Sundman et al., 2009) (Fig. 5.5).

x(Al)	ε → AlFe + Al_2Fe **T(K), inv.**	ε→ ε + AlFe **T(K)**	AlFe + Liq. → ε **T(K), inv.**	ε → ε + Al_2Fe **T(K)**	ε + Al_2Fe → Al_2Fe **T(K)**	ε + Al_5Fe_2 → Al_2Fe **T(K), inv.**	Liq → ε + Al_5Fe_2 **T(K), inv.**	ε + Liq. */Liquidus* **T(K)**
0.52	--	--	**1500**	--		--	--	1575
0.56	**1371**	--	**1502**	--		--	--	1544
0.58	**1371**	1488	--	--		--	--	1512/1514
0.60	**1371**	--	--	--		--	--	1474/1505
0.62	**1372**	--	--	1401		--	--	1452/1488
0.63	**1372**	--	--	1419		--	--	1438/1479
0.65	--	--	--	--	1407	**1429**	**1435**	1458

Table 5.1 Transformation temperatures obtained by means of DSC. In bold, the invariant temperatures.

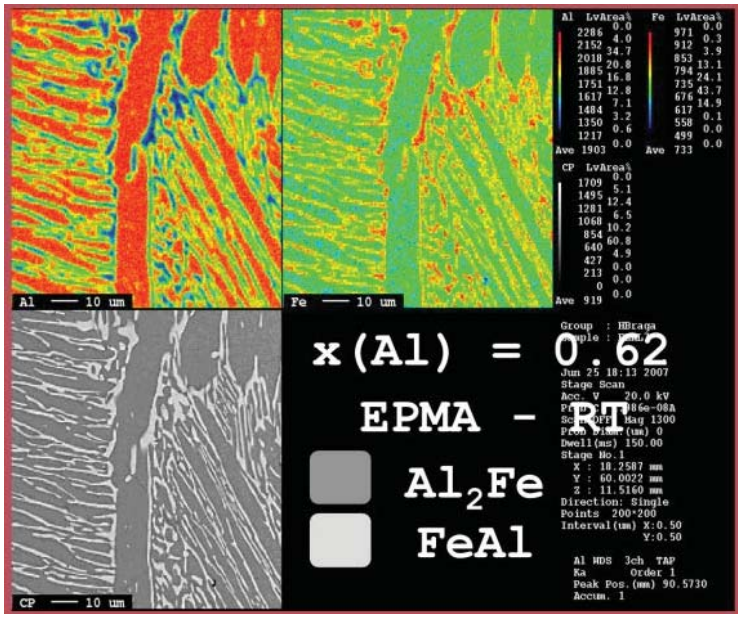

Fig. 5.3 EPMA photography and quantitative X-ray analysis of a sample of the Al-Fe system containing x(Al) = 0.62. Results are in agreement with the Al-Fe assessment by Kattner & Burton, 1993.

We have calculated the enthalpies of formation, and the Gibbs energies, as a function of the temperature, as well as the mechanical properties of the AlFe, Al_2Fe and of several

compositions and structures that can represent the ε phase (Fig. 5.6). We have compared our results with the *ab initio* data from Mihalkovic, Widom and coworkers, 2006, with Stein et al., 2010, and Mihalkovic & Widom, 2012.

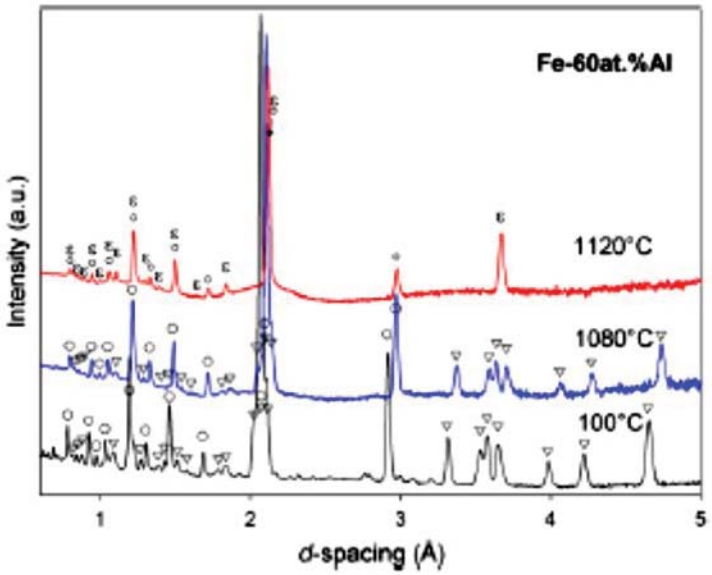

Fig. 5.4 High temperature neutron diffraction data obtained by Stein et al., 2010. The 1393K was refined including two phases, Al_8Fe_5-ε, cubic I-43m and AlFe, cubic, Pm-3m.

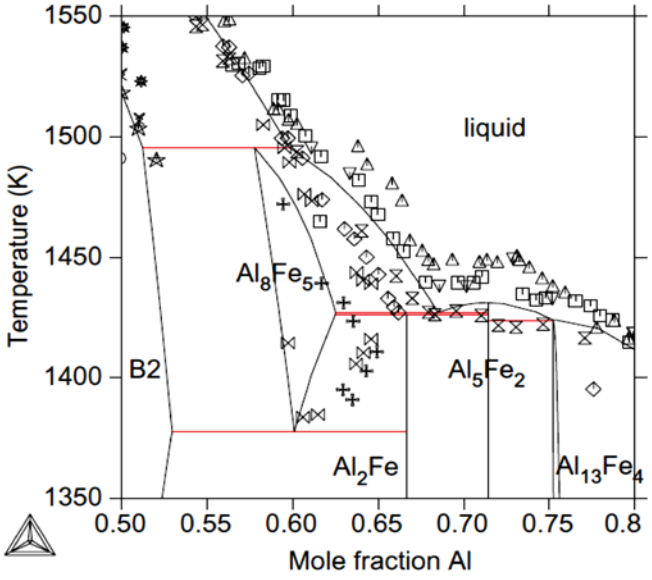

Fig. 5.5 Sundman et al., 2009, assessed Al-Fe phase diagram. Zoom in the vicinity of the stability range of the Al_8Fe_5-ε phase.

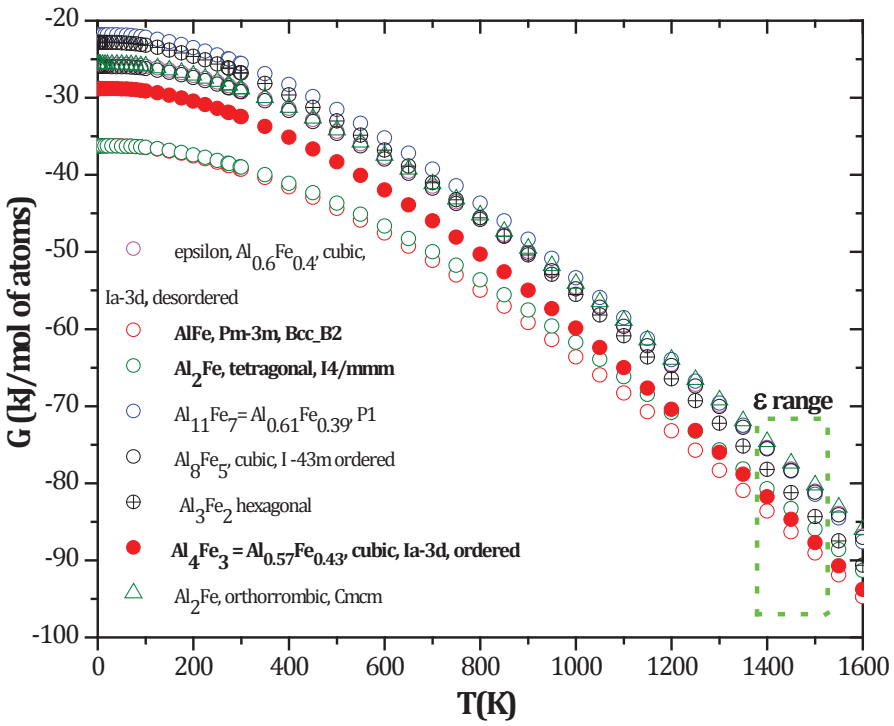

Fig. 5.6 Gibbs energies for several possible compositions and crystal structures of the ε phase and Al_2Fe phase.

It can be observed that Al_4Fe_3, x(Al) = 0.57, cubic, Ia-3d, is the most stable structure for the ε phase and that the tetragonal, I4/mmm, is the most stable for Al_2Fe. We haven't calculated Al_2Fe as triclinic, P-1, yet, although this structure was considered by Mihalkovic & Widom, 2012, to be the stable structure of Al_2Fe above 380 K. We are in trends of making these calculations. The ε phase should be the most stable in the ε range, however, we still find AlFe to be more stable. The difference between the Gibbs energy of formation of AlFe and the most stable Al_4Fe_3-ε phase is within the calculation errors, nonetheless, we are still calculating the Gibbs energy of formation of the ε phase with other compositions and structures.

In the nearest future we will compile and publish our results.

5.3. References

Ansara, I., Effenberg, G., (1998). (ed.), the COST507 database,. COST 507, Definition of thermochemical and thermophysical properties to provide a database for the development of new light Alloys, Vol. 1, pp. 273, ISBN 9282839001

Kattner, U., Burton, B., (1993). Phase diagrams of binary iron alloys. Materials Park, Ohio ASM International, Ed., Okamoto, H., Vol. 1, pp. 12-28, ISBN 0-87170-469-2

Katrych, S., Mihalkovic, M.,. Gramlich, V, Widom, M.& Steurer, W., (2006). X-ray diffraction study and theoretical calculations on the X-phase, $Al_9(Co,Ni)_4$, Philosophical Magazine, Vol. 86, No. 3–5, pp. 451-456 ISSN 1478-6443

Mihalkovic, M., & Widom, M., (2012). Structure and stability of Al_2Fe and Al_5Fe_2: First-principles total energy and phonon calculations, Vol. 85, No. 1, pp. 014113-5, ISSN 1550-235X

Stein F., Vogel S., Eumann, M., & Palm, M., (2010). Determination of the crystal structure of the ε phase in the Fe–Al system by high-temperature neutron diffraction, Intermetallics, Vol. 18, No. 1, pp. 150-156, ISSN 0966-9795

Sundman, B., Ohnuma, I., Dupin, N., Kattner, U., & Fries, S., (2009). An assessment of the entire Al–Fe system including $D0_3$ ordering, Acta Materialia, Vol. 57, No.10, pp. 2896-2908, ISSN 1359-6454

Chapter 6. Final Conclusions and Future work

6. Final Conclusions and Future work

6.1 Final Conclusions

The study performed on the Cu-Sb-S system aims to improve its knowledge by comparing synthetic with natural materials. The compositional variation and thermodynamic properties of the synthetic phases help to establish relations with the natural equivalent composition. The synthetic Tetrahedrite type structure, in its reduced composition $Cu_{12}Sb_4S_{13}$, and $Ag_6Cu_6Sb_4S_{13}$ was studied within the Cu-Sb-S system. Tetrahedrite crystallises in the cubic system space group (I-43m). Moreover in the latter compound Cu can be replaced by other atoms assuming the general $M_{12}X_4S_{13}$ formula in which M = Cu, Ag, Bi, Hg, Fe, Zn, Pb and X = Sb, As. This phase is very important due to economical reasons. It can carry in its structure precious minor elements. The understanding of the mobility and accommodation of minor elements, like Ag, Bi, Hg, Fe, Zn, Pb, … that can replace copper positions or form an independent nanostructure in the Tetrahedrite lattice, will allow us to explore the practical applications of this structure.

In this study, we've also presented *ab initio* calculations for plain and doped Tetrahedrite, using density functional theory. The selection of a particular doping element/ion is of paramount importance to obtain new and optimized photovoltaic materials from the Tetrahedral type of structures. Using the electronic band structures, density of states and correspondent orbital energies, the probability of certain electrons to be excited from the valence to the conduction band can be inferred. It can also be determined the energy cost of such a jump. Our results for the band structure and density of states for $Cu_{12}Sb_4S_{13}$ and $Ag_6Cu_6Sb_4S_{13}$ show that both compounds have similar band gaps even if the electrons that will jump to the conduction band are from atoms occupying different sites. The energy to overcome the band gap of these semiconductors – Tetrahedrites – falls within the photovoltaic operational range of 1.0 - 2.2 eV and the band gaps can be considered direct, as required.

Concerning the Cu–Li–Mg system, we present some work to respond to the problem of efficient hydrogen storage. This problem remains a major technological obstacle towards the development of a hydrogen-based energy economy.

The fundamental data that supports this work was mainly obtained by neutron diffraction and neutron spectroscopy, differential scanning calorimetry, X-ray diffraction and first-principles calculations.

Based in this data and calculations, it was possible to show that the composition of the ternary compound is $CuLi_xMg_{2-x}$ (x=0.08). By neutron data analysis, especially by pair distribution function fittings and first-principles calculations we were able to determine that Li occupies Mg1 sites (1/2, 0, z).

After analyzing the data obtained by neutron diffraction and neutron spectroscopy, differential scanning calorimetry and first principles calculations we concluded that it is very likely that $CuLi_{0.08}Mg_{1.92}$ will react with hydrogen to form $CuLi_{0.08}Mg_{1.92}H_5$. Nonetheless, according to differential scanning calorimetry results, it is also possible that the stoichiometry of the product is $CuLi_{0.08}Mg_{1.92}H_6$. The structure of the hydride is likely to be monoclinic C2/c which is in agreement with the results obtained both by neutron scattering techniques and first principles calculations. Furthermore, it can be determined the presence of MgH_2, formed after hydrogen uptake, even for those samples that did not initially contain $CuMg_2$. We think that $CuLi_{0.08}Mg_{1.92}H_5$ will disproportionate to form MgH_2 and another hydride. In this work it also possible to determine the roll of the Cu-Li-Mg-(H) as a catalyst for both $CuMg_2$ and MgH_2 during absorption and desorption.

Regarding the Bi–Sn–Zn system, the principal results are based on data obtained from differential scanning calorimetry, X-ray diffraction at high and room temperature, scanning electron microscopy and electron microprobe. New values for the liquidus surface of the ternary miscibility gap have also been obtained.

A critical evaluation of the thermodynamic parameters and experimental data available in the literature was carried out for the Bi–Sn, Bi–Zn, Sn–Zn and Bi–Sn–Zn systems. The consistency of the assessed parameters obtained for the Bi–Sn–Zn system was verified by calculation of thermodynamic properties and isothermal and vertical sections of the phase diagram. These results were compared with experimental data, both from our work and the literature. The agreement is excellent for a broad set of experimental measurements carried out by different authors.

Using phase field simulations, the dynamics of the two immiscible liquids appearing on the phase diagram of the Bi-Zn system was studied. Good agreement between the miscibility gap curve determined by the simulations and the one obtained by the Calphad (calculation of phase diagrams) method was found, as expected. It was also found a rich diversity of

asymptotic morphologies for different points of the Bi-Zn phase diagram, and we have compared the morphologies for two different Gibbs energies determined by Calphad method and found very different morphologies for the same times, concentrations and temperatures. Thus, it was concluded that the different morphologies and the time it takes to reach them, is a signature of the calculated excess Gibbs energy parameters for a given system. The latter method may be useful to find the best structures, depending on the applications and purposes; for instance, for the fabrication of nanoparticles.

For the system Al-Fe-Ti, it was observed that Al_4Fe_3, cubic, Ia-3d, is the most stable structure for the ε phase and that the tetragonal, I4/mmm, is the most stable for Al_2Fe at the ε phase stability range of temperatures. Nonetheless in the ε phase range of stability temperatures, AlFe, Pm-3m, is still more stable than any other calculated structure for the ε phase, including Al_4Fe_3. This shows that probably Al_4Fe_3 it is not the crystal structure of the ε phase, in spite of the fact that the difference between the Gibbs energy of formation of AlFe and Al_4Fe_3-ε is within the calculation errors. We will calculate the Gibbs energies for other possible ε phase's crystal structures and compare them with that for AlFe, Pm-3m, to obtain the most stable solution.

6.2. Future work

Due to my background in Geology, structures like Chalcopyrite and Tetrahedrite will be object of my interest and will be deeply studied. We will not develop the studies of the Cu-Sb-S system much further, since Sb is toxic. Nonetheless, I will invest future time in the Cu-(Fe,Sn)-S system which will be an interesting system with relation to applications and for which the previous background will be useful.

6.3. Cu-(Fe,Sn)-S system

The Cu-(Fe,Sn)-S system (with Zn, Li, Mn, Ni, In, Ge, Se, Sb… as dopants) with structures of the type **Chalcopyrite** – Stannite – Kesterite – **Tetrahedrite** will be the focus of our future work.

We want to synthesize these materials at ambient and at high pressure. High pressure synthesis allows structural changes as those taking place in $CuInSe_2$, which is tetragonal at

ambient pressure and becomes cubic, NaCl-like, at 7.6 GPa. On further compression, another structural transition is observed at 39 GPa (Pauporté & Lincot, 1995).

Furthermore, we want to synthesize these materials as nanoflakes. Traditionally, multinary Chalcogenides were synthesized by solid-state reaction, which requires high temperature, inert atmosphere protection, and a long time. We want to use a low temperature solution synthesis route, using ethanol, which can produce nanoflakes on a large scale (An, 2003).

The latter nanoflakes will be the basis of an "ink" that we want to develop in order to maximize solar cell absorber areas facilitating the deposition of the photovoltaic material. This will add further possibilities to the thin-films applications.

First principles calculations will allow us, as until now, to choose the best doping elements, by determining as well as controlling the structural and electronic properties. The determination of the mechanical properties will be possible as well. They will provide important information for further mesoscale simulations. To understand the "whole picture", we will simulate the microstructure from solar irradiation to charge collection using a novel mechanical formalism, which we will develop from scratch using phase field. This study will allow us to visualize and measure the microstructure and develop optimized systems/processes.

The $Cu(In,Ga)(Se,S)_2$ Chalcopyrite type of alloy system provides absorber materials for the most efficient thin-film photovoltaic technology to date (Rau & Schock, 2001). Thin-films based on ZnO/CdS/Chalcopyrite type solar cells are especially outstanding due to their low cost (Dimmler & Schock, 1998), radiation resistance (Dimmler & Schock, 2001), long-term stability (Guillemoles, 2000), and record power conversion efficiencies of over 19% (Contreras et al., 1999).

Traditional solar cell production techniques are usually time consuming and require expensive vacuum systems or toxic chemicals. Depositing chemical compounds such as CIGS on a substrate using vapor phase deposition wastes most of the expensive material in the process (Green, 1982). Chae et al., 2010, have developed a process to create CIGS solar cells based in inkjet printing technology that allows for precise patterning to reduce raw material waste by 90% and significantly lower the cost of producing solar cells with promising, yet expensive compounds.

The work is focused on material based Chalcopyrite type. A layer of this compound with one or two microns thick has the ability to capture the energy from photons about as

efficiently as a 50-micron-thick layer made of silicon (Chae et al., 2010). This is very promising and could be an important new technology to add to the solar energy field, allowing to create working CIGS solar devices with inkjet technology (Chae & al 2010). In particular, they have used the $CuGaS_2$ compound due to the fact that this material presents a direct band gap in the desirable range.

The copper indium/gallium diselenide $Cu(In,Ga)Se_2$ (CIGS) thin-film solar cells (Rau, 2001) have emerged as a technology that could challenge the current hegemony of silicon solar panels. This is possible thanks to the peculiar optical and structural properties of CIGS, which possess an extraordinary stability under operating conditions.

However, among ternary Chalcopyrite semiconductors, $CuGaS_2$ is maybe the most promising material for photovoltaic applications (Chae et al., 2010) due to its bandgap energy (Eg) of 2.43 eV (Siebentritt, 2002) which matches perfectly the solar spectrum for energy conversion and to its large absorption coefficient above Eg. Accurate knowledge of the electronic and optical properties of these materials is very important for many of these applications. In spite of the considerable amount of research devoted to these materials, this knowledge is still incomplete.

The Sulfides can also be mentioned as Chalcogenides, this designation is used when chemical compound containing at least one chalcogen ion (Oxygen, Sulfur, Selenium or Tellurium) and one or more elements with a more electropositive behavior.

Chalcogenide glasses provide a wide range of materials with sufficient stability which transmission of for optical fiber applications at infrared wavelengths (Brady et al., 1998). Some of the earliest demonstrations with Chalcogenide fibers were made with the simple binary glass of arsenic sulfide, AsS, which provided a broad glass formation region and with transmission across the mid infrared (Sanghera & Aggarwal, 1998), and the precedent work involving selenide and telluride glasses provided transmission capabilities at longer wavelengths (Herberholz, et al. 1997). However, even today, the manufacture of Chalcogenide glasses and nanofibers is not straightforward and continues to rely on conventional melting/quenching techniques to produce them

Recently, Chemical Vapor Deposition (CVD) techniques have been implemented in Chalcogenide fibers fabrication, as it was shown in recent works from (Huang & Hewak, 2004) and (Hewak, 2011). This fabrication has the potential to radically improve the manufacturing process. Hewak, 2011, describes the first phase of a project to adapt the

current fiber manufacture to novel chemical vapor deposition chemistry for application in the next generation of Chalcogenide fibers.

In contrast with silica fibers, which is predominantly a passive material, Chalcogenides exhibit active properties and some are highly nonlinear (Hewak, 2011).

Hewak, 2011, presents the potential applications of the Chalcogenide glasses. These materials can be used in the form of thin-films in the production of highly efficient solar cells and are already used in optical data storage.

Chalcogenide fibers can be used for the transmission of light at wavelengths beyond those possible with silica since glass purity is of the utmost importance for both the scientific study and practical application of Chalcogenides (Huang & Heawak, 2004).

This new process is capable of producing high purity glasses at low cost because it relies on liquid-metal chloride precursors and operates at atmospheric pressure. However, this technique involves a slow growth rate and the required precursors are often impure and expensive.

Some other applications of Chalcogenides are presented by (Harrington, 2004). These compounds are also useful for medical applications such as laser surgery, which requires a wavelength of around 3 μm. Gallium lanthanum sulfide fibers transmit well at this wavelength and their non-toxic components and high melting temperature suits invasive surgery. At similar wavelengths, Chalcogenide fibers have several atmospheric transmission windows (Bureau et al., 2004) and can be applied in spectroscopy and satellites remote sensing (Anne et al., 2009).

6.4. Cu-Li-Mg (H,D) system

The Cu-Li-Mg (H,D) system has been thoroughly studied by the group. At this moment we are studying this system as the base of the negative electrode of a Li battery cell. We expect to have further developments concerning this application soon.

Other ways to explore this system are related with the catalytic effect over other elements and hydrides.

6.5. Al-Fe-Ti system

The Al-Fe system near the ε phase is close to be further understood, both theoretically and experimentally.

We plan to make a bibliography search for being updated with the last studies on the Al-Fe-Ti the system. We will gather all our experimental data and complete it in accordance the publish one.

We want to complement the experimental study with theoretical results for certain phases that compose the system.

6.6. References

An C., Jin Y., Tang K., & Qian Y., (2003). Selective Synthesis and Characterization of Famatinite Nanofibers and Tetrahedrite Nanoflakes, Journal Materials Chemistry, Vol.13, No.2, pp. 301-303 ISSN 1364-5501

Anne, M-L., Keirsse J.,, Nazabal V.,, Hyodo, K.,, Inoue, S.,, Boussard-Pledel C.,, Lhermite H., Charrier J.,, Yanakata K.,, Loreal O., Le Person J., Colas F., Compère C., & Bureau, B., (2009). *Sensors*, Chalcogenide Glass Optical Waveguides for Infrared Biosensing, Vol. 9, No. 9, pp 7398-7411, ISSN 1424-8220

Brady, D., Schweizer, T., Wang, J., & Hewak D., (1998). Minimum loss predictions and measurements in gallium lanthanum sulphide based glasses and fibre, Journal of Non-Crystalline Solids, Vol. 242, No.2-3, pp. 92-98, ISSN 0022-3093

Bureau, B., Hua, X., Smektala, F., Adam, J-L., Troles, J., Ma, H., Boussard-Plèdel, C., Lucas, J., Lucas, P., Le Coq, D., Riley M., & Simmons, J., (2004). Journal of Non-Crystalline Solids, Recent advances in chalcogenide glasses, Vol. 345-346, pp. 276-283, ISSN 0022-3093

Chae, R., Seung, Y., Chih, H., Tae, J., & Si O., (2010). Synthesis and characterization of CuInSe2 thin films for photovoltaic cells by a solution-based deposition method, Current Applied Physics Vol.10, No.3, pp. 383-386, ISSN 1567-1739

Contreras, M., Egaas, B., Ramanathan, K., Hiltner, J., Swartzlander, A., Hasoon, F., & Noufi, R. (1999). Progress toward 20% efficiency in Cu(In,Ga)Se_2 polycrystalline thin-film solar cells, Progress in Photovoltaics: Research and Applications, Vol. 7, No. 4, pp. 311–316, ISSN 1099-159X

Dimmler, B., & Schock, W. (1998). Scalability and pilot operation in solar cells of $CuInSe_2$ and their alloys. Progress in Photovoltaics: Research and Applications, Vol.6, No. 3, pp. 193–199, ISSN 1099-159X

Dimmler, B., Schock, W., (2001). Defect generation in Cu(In,Ga)Se_2 heterojunction solar cells by high-energy electron and proton irradiation, Journal of Applied Physics, Vol. 90, No.2, pp.650–658, ISSN 1089-7550

Green M. (1982). Solar cells: Operating principles, technology, and system applications Englewood Cliffs, NJ, Prentice-Hall, Inc., ISBN 0-85823-580-3

Guillemoles, J., (2000). Stability of Cu(In,Ga)Se_2 solar cells: a thermodynamic approach, Thin Solid Films, Vol. 361–362, No.1 , pp.338–345, ISSN 0040-6090

Harrington, J., (2004). Infrared Fibers and Their Applications, SPIE Press, Bellingham, Washington USA, ISBN 0-8194-5218-1

Herberholz, R., Nadenau, V., Rühle, U., Köble, C., Schock, H., & Dimmler, B. (1997). Prospects of wide-gap chalcopyrites for thin film photovoltaic modules, Solar Energy Materials and Solar Cells, Vol. 49, No. 1-4, pp.227–237, ISSN 0927-0248

Hewak, D., (2011). The Promise of Chalcogenides, Nature Photonics, Vol. 5, No.8, pp.474, ISSN 1749-4885

Huang, C., & Hewak, D., (2004). High purity germanium sulphide glass for optoelectronic applications synthesized by chemical vapour deposition, Electronics Letters, Vol. 40, No.14, pp. 863-865, ISSN 0013-5194

Rau, U., & Schock, H., (2001). Cu(In,Ga)Se_2 solar cells, Clean Electricity from Photovoltaics, Imperial College Press, London, ISBN-13 978-1860941610

Rau, U. (2003). Electronic properties of wide-gap Cu(In,Ga)$(Se,S)_2$ solar cells. Proceedings of the 3rd World Conference on Photovoltaic Energy Convention, Osaka, ISBN 4-9901816-0-3

Sanghera J., & Aggarwal, I., (1998). Infrared Fiber Optics, CRC Press, Boca Raton, Florida, ISBN-10 3-540-20785-6

Siebentritt, S., (2002). Wide gap chalcopyrites: material properties and solar cells, Thin Solid Films, Vol. 403–404, No.3 pp. 1–8, ISSN 0040-6090